BEILSTEIN JOURNAL OF NANOTECHNOLOGY

Nanotechnology for cross-scale analysis: comprehensive evaluation of water environments

Edited by Yui Sasaki and Tsuyoshi Minami

Generated on 10 November 2026, 20:53

Imprint

Beilstein Journal of Nanotechnology
www.bjnano.org
ISSN 2190-4286
Email: journals-support@beilstein-institut.de

The *Beilstein Journal of Nanotechnology* is published by the Beilstein-Institut zur Förderung der Chemischen Wissenschaften.

Beilstein-Institut zur Förderung der Chemischen Wissenschaften
Trakehner Straße 7–9
60487 Frankfurt am Main
Germany
www.beilstein-institut.de

The copyright to this document as a whole, which is published in the *Beilstein Journal of Nanotechnology*, is held by the Beilstein-Institut zur Förderung der Chemischen Wissenschaften. The copyright to the individual articles in this document is held by the respective authors, subject to a Creative Commons Attribution license.

BEILSTEIN JOURNAL OF NANOTECHNOLOGY

Electrochemical determination of ciprofloxacin using a MIL-101/reduced graphene oxide-modified electrode

Nguyen Quang Man[1], Nguyen Ngoc Nghia[*2,3], Nguyen Vinh Phu[1], Vo Thi Khanh Ly[1], Le Lam Son[2], Pham Khac Lieu[2], Le Thi Hong Phong[4], Nguyen Dinh Luyen[5] and Dinh Quang Khieu[*2]

Full Research Paper

Open Access

Address:
[1]University of Medicine and Pharmacy, Hue University, 530000, Vietnam, [2]University of Sciences, Hue University, 530000, Vietnam, [3]Department of Education and Training, Hue City, 530000, Vietnam, [4]Institute of Materials Sciences, Vietnam Academy of Science and Technology, 18 Hoang Quoc Viet, Cau Giay, Hanoi City,100000, Vietnam and [5]University of Education, Hue University, 530000, Vietnam

Email:
Nguyen Ngoc Nghia[*] - nnnghia.al@hue.edu.vn;
Dinh Quang Khieu[*] - dqkhieu@hueuni.edu.vn

* Corresponding author

Keywords:
ciprofloxacin; electrochemical analysis; MIL-101; reduced graphene oxide

Beilstein J. Nanotechnol. **2026,** *17,* 541–554.
https://doi.org/10.3762/bjnano.17.35

Received: 08 January 2026
Accepted: 02 April 2026
Published: 21 April 2026

This article is part of the thematic issue "Nanotechnology for cross-scale analysis: comprehensive evaluation of water environments".

Guest Editors: Y. Sasaki and T. Minami



© 2026 Man et al.; licensee Beilstein-Institut.
License and terms: see end of document.

Abstract

An electrochemical sensor for the determination of ciprofloxacin (CPR) was developed using a glassy carbon electrode modified with MIL-101/reduced graphene oxide (MIL-101/rGO). MIL-101/rGO was synthesized via a facile ultrasonic-assisted method and characterized by various physicochemical techniques. The synergistic combination of MIL-101 with rGO significantly enhanced the electrocatalytic activity toward CPR oxidation. The electrochemical behavior of CPR on the MIL-101/rGO-modified electrode was systematically investigated using cyclic voltammetry and differential pulse voltammetry. Under optimized experimental conditions, the proposed sensor exhibited a linear response over 0.25–9.41 μM and a detection limit of 0.11 μM for CPR determination. The sensor also demonstrated good selectivity, satisfactory repeatability, and long-term stability. Furthermore, the method's practical applicability was validated by the determination of CPR in pharmaceutical samples, yielding acceptable recoveries. These results indicate that the MIL-101/rGO-modified electrode provides a promising and efficient platform for the electrochemical sensing of CPR in pharmaceutical and environmental analysis.

Introduction

Ciprofloxacin ($C_{17}H_{18}FN_3O_3$, CPR) is a fluoroquinolone antibiotic widely used in human and veterinary medicine to treat various bacterial infections [1]. Due to its high usage, incomplete metabolism, and environmental persistence, CPR residues are often found in pharmaceutical products, biological fluids, and aquatic environments [2,3]. The uncontrolled presence

of ciprofloxacin not only poses risks to human health but also promotes the development of antibiotic-resistant bacteria, raising significant environmental and public health concerns [4]. Therefore, developing sensitive, selective, and affordable analytical methods for detecting ciprofloxacin is very important.

Conventional analytical techniques for CPR determination, including a fluorescence sensor based on $CsPbBr_3$ quantum dots embedded in a molecularly imprinted polymer [5], and ultrasound-assisted magnetic dispersive micro-solid phase extraction based on carbon quantum dots/zeolite imidazolate framework-90/polyvinyl pyrrolidone/iron(II,III) oxide with high-performance liquid chromatography [6,7] or chromatography–tandem mass spectrometry [8] offer high accuracy and reliability. However, these techniques often need expensive equipment, complex sample preparation, skilled operators, and lengthy analysis times, which restrict their use for quick or in situ testing. In contrast, electrochemical sensors have become appealing alternatives because of their inherent benefits such as simplicity, low cost, rapid response, high sensitivity, and potential for miniaturization and field use.

The performance of electrochemical sensors heavily relies on the electrode's surface properties. Recently, metal–organic frameworks (MOFs) have attracted significant interest in electrochemical sensing due to their highly ordered porous structures, very high surface areas, tunable pore sizes, and numerous active sites. Among these, MIL-101, a chromium-based MOF, is notable for its large pore volume, excellent chemical stability, and strong ability to adsorb organic molecules [9-11].

However, the poor electrical conductivity inherent to MIL-101 limits its direct use in electrochemical sensing. To address this limitation, hybridizing MOFs with conductive carbon materials has been extensively studied. Reduced graphene oxide (rGO) is especially appealing due to its high electrical conductivity [12], large specific surface area, mechanical stability [13], and strong π–π interactions with aromatic compounds like ciprofloxacin [14,15].

Integrating MIL-101 with rGO aims to combine the high surface area and adsorption capacity of MIL-101 with the excellent electrical conductivity and electron-transfer ability of rGO, creating a synergistic effect that boosts the electrochemical performance of the composite material. This combination can promote efficient analyte adsorption and fast charge transfer at the electrode interface. Consistent with this idea, Gu et al. reported that MIL-101/rGO composites exhibit enhanced electrocatalytic activity toward the reduction of metronidazole and the anodic stripping detection of Cd^{2+} and Pb^{2+}, demonstrating a strong synergistic effect between MIL-101 and rGO in electrochemical sensing [16].

In this work, a MIL-101/rGO hybrid was successfully synthesized and used as a modifier for a glassy carbon electrode to develop a sensitive electrochemical sensor for CPR detection. The electrochemical behavior of CPR on the MIL-101/rGO-modified electrode was examined. The proposed sensor demonstrated enhanced electrocatalytic activity, high sensitivity, and a low detection limit for CPR. Additionally, the practical utility of the sensor was confirmed through its application in analyzing real samples, highlighting its potential for pharmaceutical and environmental monitoring.

Experimental

Materials

Ciprofloxacin (CPR) was obtained from a commercial supplier and used without additional purification. Chromium(III) nitrate nonahydrate ($Cr(NO_3)_3{\cdot}9H_2O$), terephthalic acid (H_2BDC), graphite powder, potassium permanganate ($KMnO_4$), sodium borohydride ($NaBH_4$), sulfuric acid (H_2SO_4), hydrogen peroxide (H_2O_2), and other analytical-grade reagents were purchased from standard chemical suppliers. Britton–Robinson (BR) buffer solutions at different pH levels were prepared using a mixture of acetic acid, phosphoric acid, and boric acid, with pH adjusted using 0.2 M NaOH solution.

Synthesis of reduced graphene oxide (rGO), MIL-101, and MIL-101/rGO

Graphene oxide (GO) was synthesized from natural graphite using a modified Hummers' method, as described in [17]. MIL-101(Cr) was prepared through a hydrothermal reaction by dissolving terephthalic acid (H_2BDC, 1.66 g) and chromium(III) nitrate nonahydrate ($Cr(NO_3)_3{\cdot}9H_2O$, 4.0 g) in 48 mL of deionized water, followed by the addition of 2 mL of hydrofluoric acid. The mixture was transferred to a Teflon-lined stainless-steel autoclave and heated at 200 °C for 8 h [18]. After cooling to room temperature, a highly crystalline green chromium terephthalate powder (MIL-101(Cr)) was collected by filtration, thoroughly washed with deionized water, and dried before use.

The MIL-101/rGO composites were synthesized following a reported procedure with slight modifications [18]. Briefly, dried MIL-101(Cr) (0.1 g) was dispersed in 20 mL of deionized water and ultrasonicated for 30 min to obtain a homogeneous suspension. Subsequently, a predetermined amount of GO was added to the MIL-101 suspension under continuous stirring, followed by ultrasonication for 30 min. Sodium borohydride ($NaBH_4$) was then introduced into the mixture, which was heated at

60 °C and stirred continuously for 12 h to reduce GO and form the MIL-101/rGO composite (Table 1).

Table 1: The composition for MIL-101/rGO.

Notation	MIL-101 (mg)	GO (mg)	$NaBH_4$ (mg)
MIL-101/rGO(10)	100	10	35
MIL-101/rGO(5)	100	20	70
MIL-101/rGO(3.3)	100	30	105
MIL-101/rGO(2.5)	100	40	140
MIL-101/rGO(2)	100	50	175

After the reaction was completed, the product was collected by filtration, washed several times with deionized water to remove residual reagents, and dried at 60 °C for 24 h before use. The resulting composites were labeled as MIL-101/rGO(10), MIL-101/rGO(5), MIL-101/rGO(3.3), MIL-101/rGO(2.5), and MIL-101/rGO(2), where the numbers in parentheses indicate the mass ratio of MIL-101 to GO. For comparison, reduced graphene oxide (rGO) was also prepared using the same reduction process without MIL-101.

Equipment

The X-ray diffraction analyses were conducted using a D8 Advance Bruker (Germany). Morphology and elemental mapping were measured with a Hitachi S-4800 FESEM (Japan) equipped with an energy-dispersive X-ray (EDX) system. Raman spectroscopy was performed on an Xplora Plus instrument (Horiba, Japan) with a stimulating light wavelength of 785 nm. Electrochemical impedance spectra (EIS) were recorded using an Autolab PGSTAT302N system. Electrochemical experiments were carried out on a CPA-HH5 workstation (Vietnam). A platinum wire served as the counter electrode, and a glassy carbon electrode was used as the working electrode.

Preparation of the modified electrode

Before modification, the glassy carbon electrode (GCE) was polished successively with alumina slurry (0.05 μm) on a polishing cloth, thoroughly rinsed with deionized water, and sonicated in ethanol and water to remove residual impurities. To prepare the modified electrode, a specific amount of MIL-101/rGO composite was dispersed in deionized water using ultrasonication to create a uniform suspension (1 $mg{\cdot}mL^{-1}$). An aliquot of this suspension (5 μL) was drop-cast onto the cleaned GCE surface and allowed to dry naturally at room temperature to form the MIL-101/rGO-modified electrode. The modified electrode was then gently rinsed with deionized water before conducting electrochemical measurements.

Electrochemical measurements

Electrochemical measurements were conducted using a standard three-electrode setup connected to an electrochemical workstation. Cyclic voltammetry (CV) and differential pulse voltammetry (DPV) were employed to analyze the electrochemical behavior of CPR. All tests took place in BR buffer solution at room temperature under optimized pH conditions. DPV parameters, including accumulation potential (E_{acc}), accumulation time (t_{acc}), pulse amplitude (ΔE), and voltage step (U_{step}), were optimized before conducting the analytical measurements.

Real sample preparation

Pharmaceutical samples containing CPR were prepared by carefully weighing and finely grinding the tablets (or powder for oral suspension). A suitable amount of the powdered sample was dissolved in deionized water and sonicated to ensure complete dissolution. The resulting solution was filtered to remove insoluble excipients and properly diluted with BR buffer (pH 4) before electrochemical analysis. The CPR content in the pharmaceutical samples was measured using the standard addition method.

Data analysis

All electrochemical measurements were performed in triplicate. Calibration curves were constructed from DPV peak currents versus CPR concentrations. The limit of detection (LOD) was calculated based on the formula $3S/b$ where S is the standard deviation of the blank signal (or the standard deviation of the intercept of the calibration curve), and b is the slope of the calibration curve [19]. Repeatability, reproducibility, selectivity, and stability of the sensor were evaluated using relative standard deviation (RSD) values.

Results and Discussion

Materials characterization

Figure 1a presents the XRD patterns of GO, rGO, and pristine MIL-101, while Figure 1b shows the diffraction patterns of MIL-101/rGO composites prepared with different MIL-101/rGO mass ratios (as indicated in parentheses). In Figure 1a, GO exhibits characteristic diffraction peaks at 2θ values of 10.9° and 42.7°, corresponding to the (001) plane, which arise from the increased interlayer spacing caused by abundant oxygen-containing functional groups [20]. After reduction, this peak disappears, and broad reflections centered at 2θ values of 25.8° and 43.1° appear for rGO, attributed to the (002) and (100) planes of graphitic carbon, confirming the successful reduction of GO and partial restoration of the sp^2 carbon network [21].

The XRD pattern of the synthesized MIL-101 shows several characteristic diffraction peaks located at 2θ ≈ 5.2°, 5.6°, 5.9°, 8.1°, 8.4°, 9.1°, 10.3°, 16.5°, and 18.0°, which can be indexed

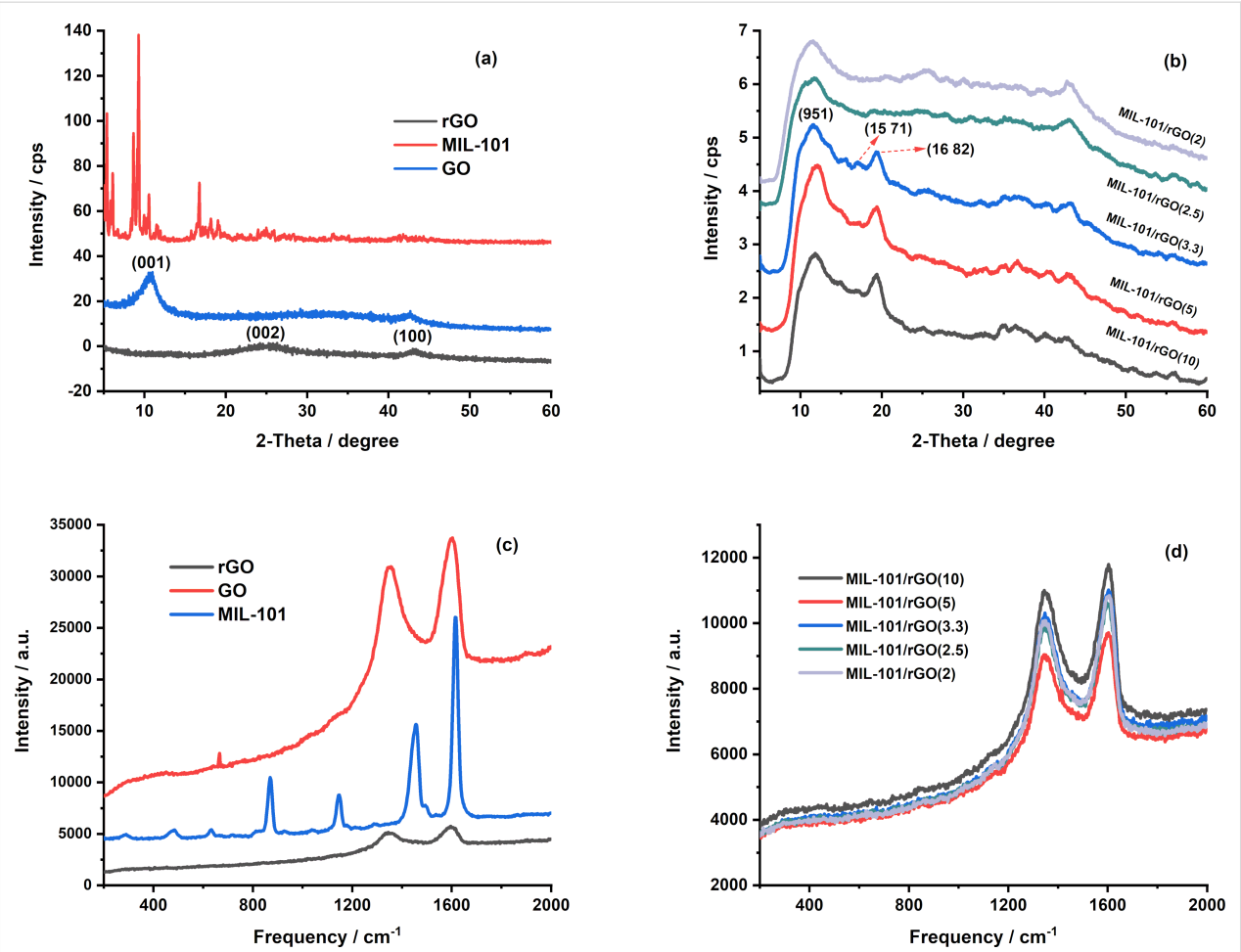


Figure 1: (a) X-ray diffraction (XRD) patterns of graphene oxide (GO), reduced graphene oxide (rGO), and MIL-101, (b) X-ray patterns of MIL-101/rGO with various mass ratios, (c) Raman spectra of GO, rGO and MIL-101, and (d) Raman spectra of MIL-101/rGO with various mass ratios.

to the (333), (440), (442), (733), (660), (911), (951), (15 7 1), and (16 8 2) crystal planes of MIL-101(Cr) according CCCD No. 605510 (Supporting Information File 1, Figure S1) confirming the successful formation of the crystalline MOF framework. As shown in Figure 1b, all MIL-101/rGO composites retain the characteristic angle diffraction peaks of MIL-101 at 2θ = 11.7°, 15.6°, 17.0°, and 19.3°, consistent with [22], indicating that the crystalline framework of MIL-101 remains intact after mixing with rGO, regardless of the mass ratio. Meanwhile, the broad diffraction feature associated with rGO becomes more prominent with increasing rGO content, reflecting the growing contribution of the disordered graphitic phase. The XRD results from both figures confirm the successful formation of MIL-101/rGO composites. This structural combination is beneficial for electrochemical applications because rGO improves electrical conductivity and promotes charge transfer.

The Raman spectra of GO, rGO, MIL-101, and the MIL-101/rGO composites are presented in Figure 1a,c. As shown in Figure 1c, GO exhibits two characteristic bands at ≈1345 cm^{-1} (D band) and ≈1599 cm^{-1} (G band), which are associated with structural defects/disorder and the in-plane vibration of sp^2-bonded carbon atoms, respectively [23]. After chemical reduction, rGO shows a slight shift of these bands to ≈1340 cm^{-1} (D) and ≈1592 cm^{-1} (G), accompanied by an increase in the intensity ratio I_D/I_G from 0.91 (GO) to 0.99 (rGO). This increase indicates the partial restoration of sp^2 carbon domains together with the generation of new, smaller graphitic domains, which is typical for reduced graphene oxide. In contrast, pristine MIL-101 displays multiple Raman bands in the low- and mid-frequency regions (280, 473, 629, 809, 866, 925, 1037, 1145, 1283, 1454, and 1611 cm^{-1}), which can be assigned to lattice vibrations of the metal–oxygen clusters and organic linker modes, confirming the successful formation of the MIL-101 framework [24]. For the MIL-101/rGO composites (Figure 1d), the Raman spectra are dominated by the D and G bands of rGO located at ≈1340 and ≈1600 cm^{-1}, while the characteristic bands of MIL-101 become much weaker or partially over-

lapped due to the strong Raman response of the carbon phase. The I_D/I_G ratios of the composites range from 0.89 to 0.94, depending on the rGO content. Notably, these values are slightly lower than that of pure rGO, suggesting that the incorporation of MIL-101 can partially promote better ordering of sp^2 domains through interfacial interactions between MIL-101 and rGO sheets.

The EDX results confirm the successful formation of the MIL-101/rGO composite through the presence of C, O, and Cr as the main constituent elements. As summarized in the elemental composition table, carbon (C) accounts for 30.42 wt % (42.31 atom %), which mainly originates from the rGO sheets and the organic linker of MIL-101, indicating the effective incorporation of rGO into the composite matrix. Oxygen (O) is the most abundant element with 48.87 wt % (51.03 atom %), consistent with the presence of metal–oxygen clusters in MIL-101 as well as residual oxygen-containing functional groups on rGO. Chromium (Cr), the metal center of MIL-101, is detected at 20.72 wt % (6.66 atom %), confirming the successful introduction of the MIL-101 framework (Figure 2).

The chemical composition and electronic states of the MIL-101/rGO composite were investigated by X-ray photoelectron spectroscopy (XPS). The survey spectrum (Figure 3a) confirms the presence of Cr, C, and O, which is consistent with the expected composition of MIL-101(Cr) integrated with reduced graphene oxide (rGO). No obvious extraneous elemental signals were observed in the survey spectrum, suggesting that the synthesized composite is predominantly composed of the expected elements within the detection limit of XPS. The high-resolution Cr 2p spectrum (Figure 3b) shows two prominent peaks at approximately 577.9 and 589.0 eV, representing the Cr 2p3/2 and Cr 2p1/2 spin–orbit components, respectively. The energy gap between these peaks (≈11.1 eV) is typical of Cr^{3+} species coordinated with oxygen in the Cr–O clusters of the MIL-101 framework [25]. Importantly, no signals related to Cr^{6+} species (usually observed at higher binding energies) are detected, confirming that chromium remains mainly in the trivalent oxidation state. This indicates that the Cr environment in MIL-101 stays intact after integration with rGO. The C 1s spectrum (Figure 3c) can be decomposed into several components representing different carbon bonding environments. The primary peak at about 285.6 eV corresponds to C–C/C=C bonds found in the sp^2-hybridized carbon of the graphene lattice, indicating the presence of rGO sheets. Other components at around 285.9–287.1 eV are assigned to C–O functional groups, such as hydroxy or epoxy groups, while the peak near 287.7 eV can be attributed to O–C=O groups, originating from the carboxylate ligands of the terephthalate linkers in MIL-101 and residual oxygen functionalities on rGO [26]. The presence of these oxygen groups suggests that the reduction of graphene oxide is

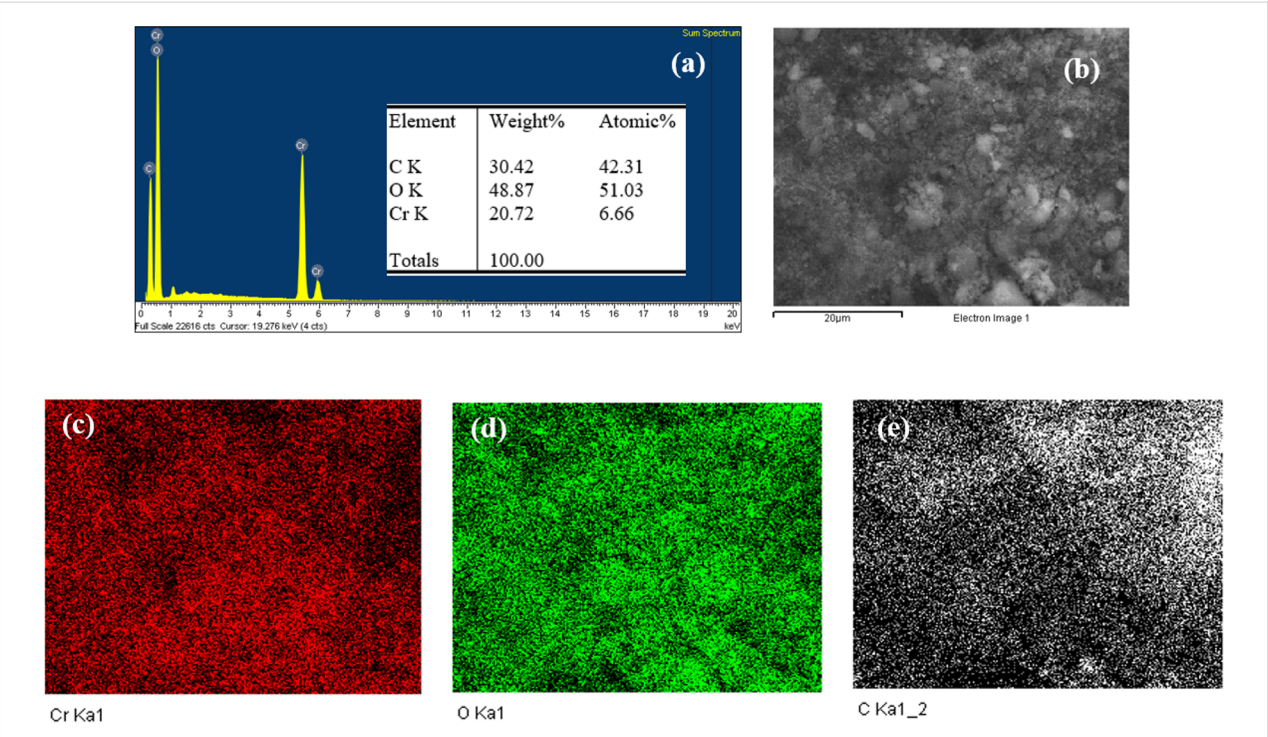


Figure 2: EDX elemental mapping and elemental composition of MIL-101/rGO (3.3), (a) EDX spectrum, (b) electron image, (c) chromium element mapping, (d) oxygen element mapping, and (e) carbon element mapping.

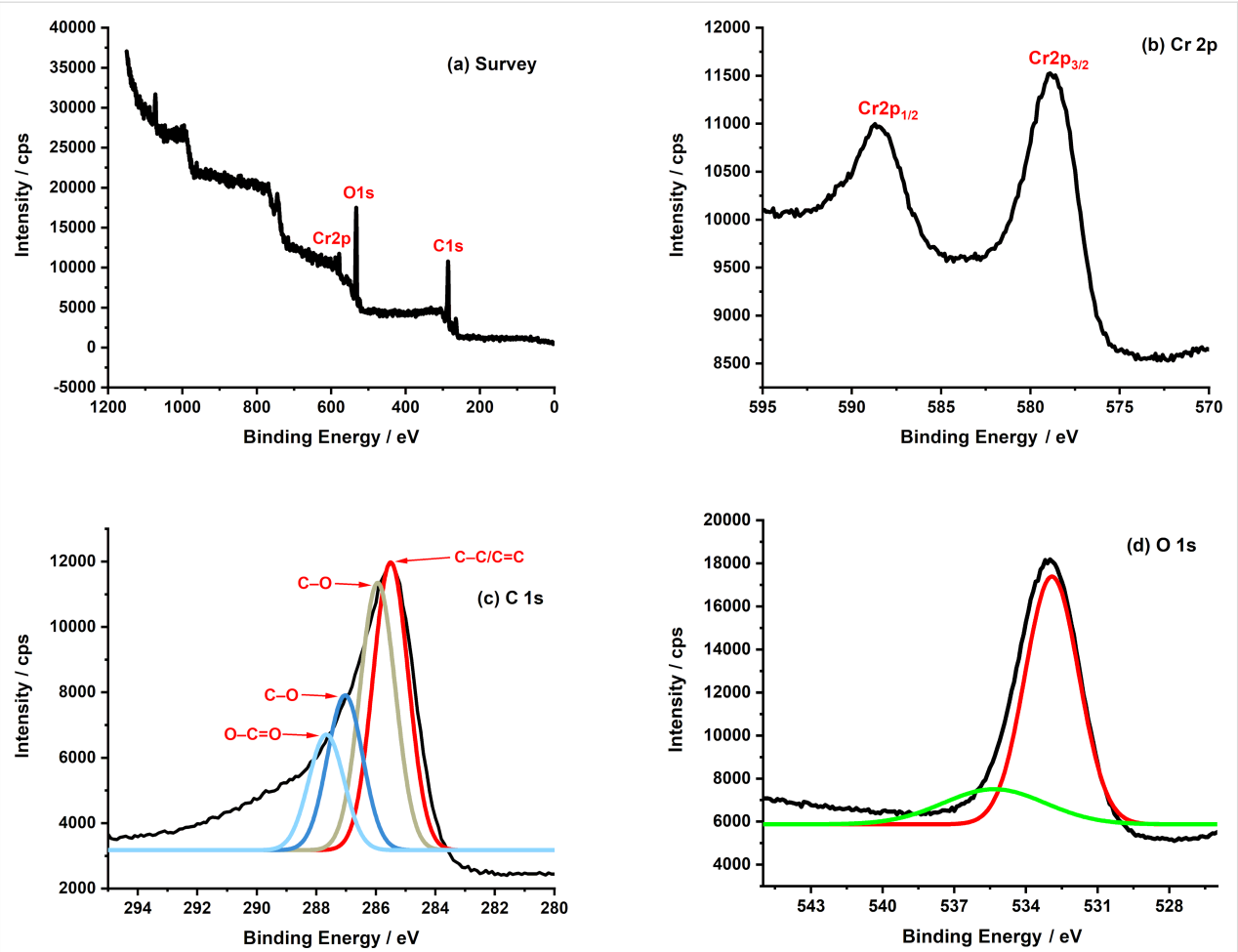


Figure 3: XPS spectra of the MIL-101/rGO (3.3): (a) survey spectrum, (b) high-resolution Cr 2p spectrum, (c) high-resolution C 1s spectrum, and (d) high-resolution O 1s spectrum.

partial and that surface functional groups remain, helping to facilitate interactions between rGO sheets and MIL-101 particles. The O 1s spectrum (Figure 3d) shows two main contributions. The peak around 532.9 eV is due to Cr–O bonds within the metal–oxo clusters of MIL-101(Cr), confirming the formation of the MOF framework. The second feature at approximately 535.8 eV can be attributed to oxygen species in C–O groups, hydroxy groups, or adsorbed water molecules associated with the rGO surface and the porous MOF structure [27]. The presence of these oxygen-containing species further supports the coexistence of MIL-101 and rGO within the composite. Overall, the XPS results confirm the successful integration of MIL-101(Cr) and rGO, while preserving the Cr^{3+} oxidation state and the characteristic coordination environment of the MIL-101 framework.

The SEM images of rGO, MIL-101, and the MIL-101/rGO composite are shown in Figure 4. The rGO sample (Figure 4a) displays a typical wrinkled, sheet-like morphology that offers a large surface area and a conductive substrate for material deposition. The pristine MIL-101 (Figure 4b) consists of irregular polyhedral particles that tend to aggregate, forming relatively compact clusters. In contrast, the MIL-101/rGO composite (Figure 4c) reveals that MIL-101 particles are dispersed on the wrinkled rGO sheets. The rGO sheets serve as a supporting scaffold, helping to separate the MIL-101 particles and reduce their aggregation to some extent. This structural characteristic benefits the dispersion of the MOF particles and enhances electron transfer within the composite material.

Electrochemical determination of ciprofloxacin (CPR) at MIL-101/rGO/GCE

Electrochemical behavior of CPR

Figure 5a compares the cyclic voltammograms of CPR recorded at different electrodes in 0.1 M BR buffer (pH 4) (see Supporting Information File 1, Figure S2). A weak and poorly defined oxidation peak is observed at the bare GCE, indicating sluggish electron-transfer kinetics. Upon modification with

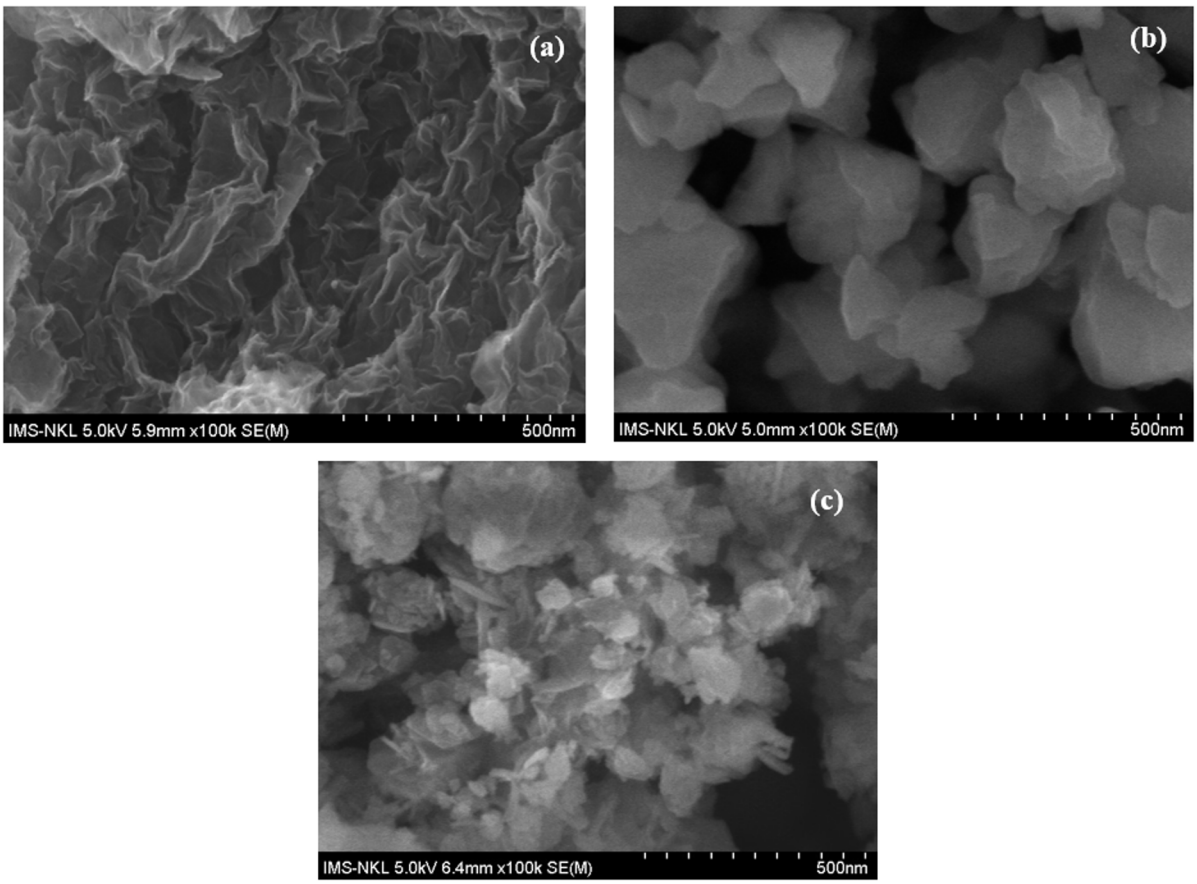


Figure 4: SEM observation of (a) rGO, (b) MIL-101, and (c) MIL-101(Cr)/rGO (3.3).

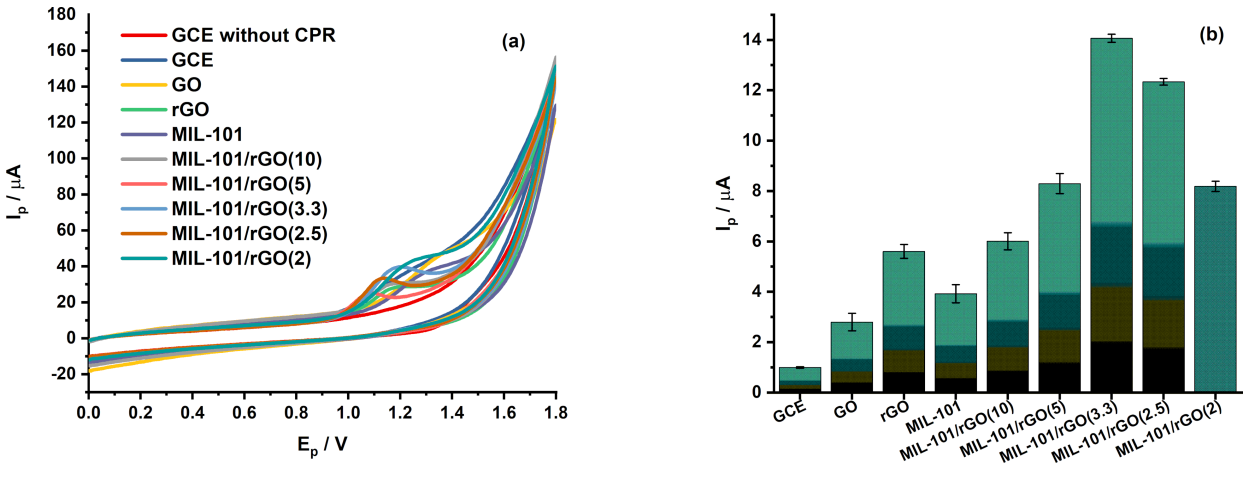


Figure 5: (a) Cyclic voltammograms (CVs) recorded at different electrodes in 0.1 M BRS buffer (pH 4) containing 15 µM CPR at a scan rate of 0.1 V/s and (b) comparison of the corresponding peak currents obtained at various electrodes (n = 3).

MIL-101 or rGO, the anodic peak current increases noticeably, reflecting improved adsorption and conductivity. The obtained peak potentials (E_p) for GCE, GO/GCE, rGO/GCE, MIL-101/GCE, MIL-101/rGO(10)/GCE, MIL-101/rGO(5)/GCE, MIL-101/rGO(3.3)/GCE, MIL-101/rGO(2.5)/GCE, and MIL-101/rGO(2)/GCE were 1.203, 1.150, 1.166, 1.288, 1.153, 1.072, 1.175, 1.125, and 1.219 V, respectively. In general, after modification of the electrode surface with these materials, the oxida-

tion peak potential of CPR shifted to lower potentials compared with bare GCE (1.203 V), accompanied by a significant increase in peak current. This behavior indicates that the modified materials can effectively enhance the electrocatalytic activity toward CPR oxidation. Notably, the MIL-101/rGO composite electrodes exhibit a much higher oxidation response than either MIL-101/GCE or rGO/GCE alone, demonstrating an apparent synergistic effect between the high surface area and adsorption capability of MIL-101 and the excellent electrical conductivity of rGO. Among the investigated compositions, MIL-101/rGO(3.3)/GCE provides the highest and most reproducible peak current (Figure 5b), and was therefore selected for subsequent experiments.

Effect of pH

The impact of solution pH on the electrochemical oxidation of CPR was studied over a pH range of 2–9 (Figure 6). The oxidation peak current rises with pH up to 4, then gradually declines at higher pH levels, showing that both CPR's protonation state and its interaction with the electrode significantly influence the electrochemical response (Supporting Information File 1, Figure S3). As a result, pH 4 was selected as the optimal condition. Additionally, the oxidation peak potential shifts linearly toward less positive values as pH increases. The linear relationship between peak potential and pH indicates that protons participate in the electrode process.

$$E_{\mathrm{CPR}} = (1.4790 \pm 0.0241) + (-0.0663 \pm 0.0041)\,\mathrm{pH};$$
$$r^2 = 0.9778$$

The slope of approximately 0.066 V·pH^{-1} is close to the theoretical Nernstian value, indicating that the number of transferred electrons is similar to that of protons. This result suggests a proton-coupled electron-transfer mechanism for CPR oxidation.

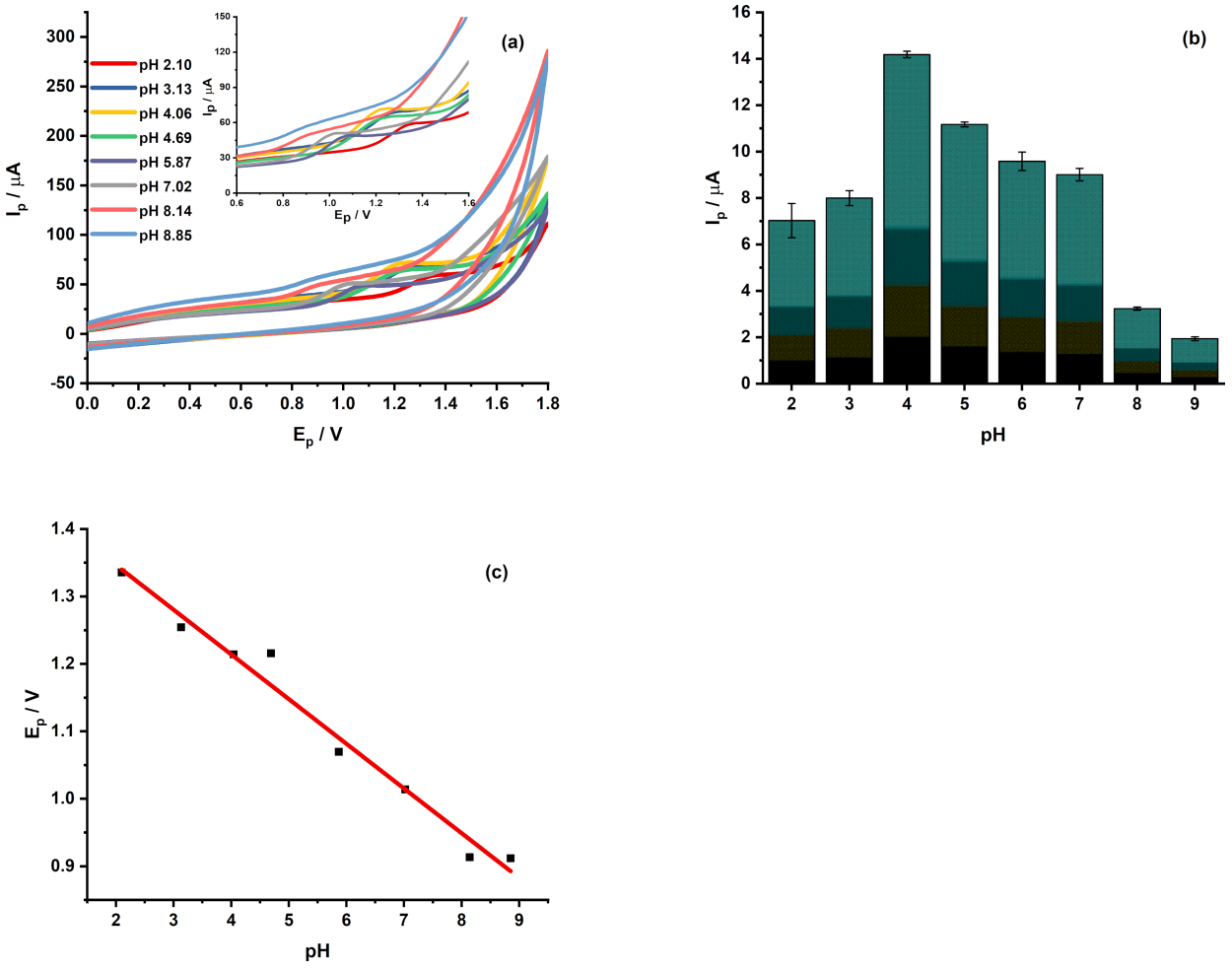


Figure 6: (a) CVs of MIL-101/rGO(3.3)/GCE recorded in 0.1 M BR buffer over the pH range of 2–9 containing 15 µM CPR at a scan rate of 0.1 V·s^{-1} and the inset shows the magnified view of the peak potential region, (b) variation of the oxidation peak current with pH, and (c) dependence of the oxidation peak potential on pH.

Effect of scan rate and kinetic analysis

The effect of scan rate on the electrochemical response of CPR at MIL-101/rGO(3.3)/GCE was examined over the range of 0.05–0.40 $V \cdot s^{-1}$ (Figure 7). The oxidation peak current increases linearly with the square root of the scan rate (Figure 7a), indicating that CPR oxidation is mainly controlled by diffusion [28].

$$I_{CPR} = (-0.7720 \pm 0.4714) + (26.1564 \pm 1.0341) v^{1/2};$$
$$r^2 = 0.9892$$

Furthermore, based on Laviron's theory [29], the linear dependence of peak potential on the natural logarithm of scan rate confirms the irreversible nature of the oxidation process (Figure 7c).

$$E_{CPR} = (1.1274 \pm 0.0024) + (0.0321 \pm 0.0013) \ln v;$$
$$r^2 = 0.9895$$

For an irreversible electrochemical system, the charge-transfer coefficient (α) was assumed to be 0.5, as is common in the literature [30].

From the slope of the E_{CPR}–ln v plot, the product of α and the number of transferred electrons (n) was calculated to be 0.7999, leading to an estimated n value of approximately 1.6. Although this does not correspond to an integer, it reasonably indicates the involvement of two electrons in the oxidation process. When combined with the pH-dependent study, the results further suggest that the electrochemical oxidation of CPR at the modified electrode likely involves a two-electron, two-proton transfer process, aligning with previously reported electrochemical oxidation mechanisms of CPR [31]. The proposed oxidation pathway of CPR is schematically illustrated in Scheme 1.

Optimization of DPV parameters

To achieve maximum sensitivity, the parameters for differential pulse voltammetry (DPV) were systematically optimized. The accumulation potential, accumulation time, pulse ampli-

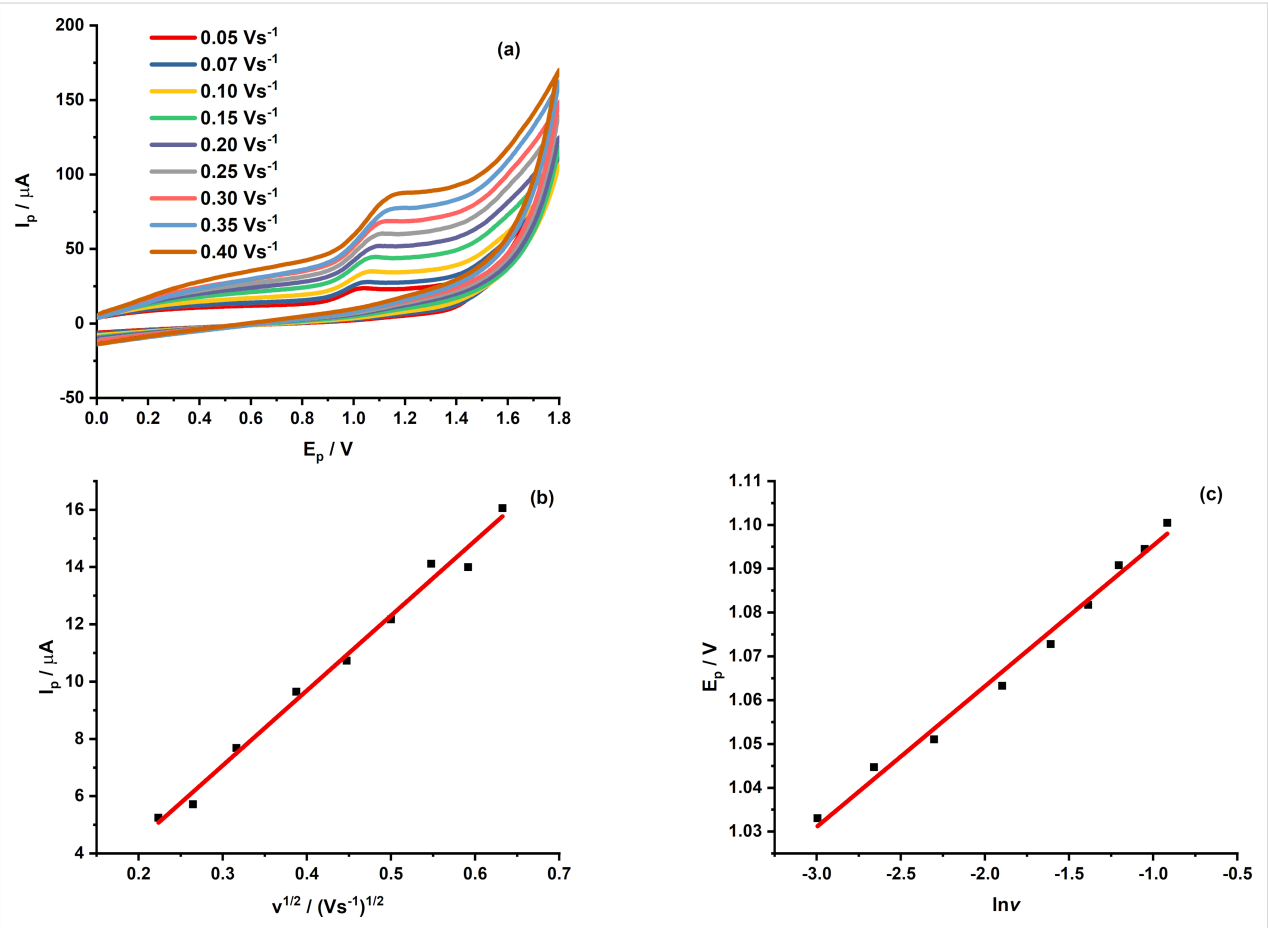
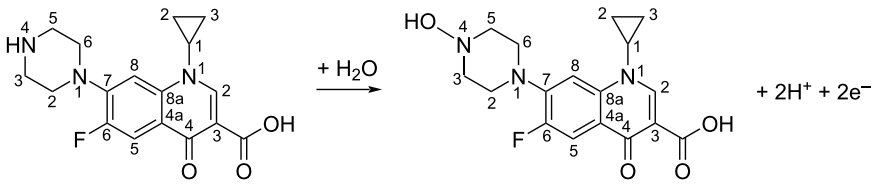


Figure 7: (a) Cyclic voltammograms of MIL-101/rGO(3.3)/GCE recorded in 0.1 M BR buffer (pH 4) containing 15 µM ciprofloxacin at scan rates from 0.05 to 0.40 $V \cdot s^{-1}$; (b) linear relationship between the peak current and the square root of scan rate ($v^{1/2}$), and (c) linear dependence of the peak potential of ciprofloxacin on the natural logarithm of scan rate (ln v).



Scheme 1: The oxidation mechanism of CPR at MIL-101/rGO/CGE.

tude, and potential step were investigated individually (Supporting Information File 1, Figure S4–S7). The optimal conditions were determined to be an accumulation potential of 0 V, an accumulation time of 4 s, a pulse amplitude of 0.11 V, and a voltage step of 0.010 V. Under these conditions, the oxidation peak current of CPR reached its maximum while maintaining a good peak shape and stable signal.

Analytical performance and linear range

The analytical performance of the proposed sensor was evaluated by recording the DPV responses at increasing analyte concentrations (Figure 8a). As the CPR concentration rose, the peak current steadily increased, indicating that the electrochemical signal highly depends on the CPR concentration. The calibration plot of peak current versus concentration is shown in Figure 8b. Two linear regions are observed within the concentration ranges of 0.25–9.41 and 9.41–24.39 μM.

The corresponding regression equations are described as follows

$$\text{Range 1}: 0.25-9.41\,\mu\text{M},$$
$$I_{\text{CPR}} = (0.7790 \pm 0.0226) + (0.7109 \pm 0.0049) C_{\text{CPR}};$$
$$r^2 = 0.9990$$

$$\text{Range 2}: 9.41-24.39\,\mu\text{M},$$
$$I_{\text{CPR}} = (3.3577 \pm 0.0747) + (0.4247 \pm 0.0045) C_{\text{CPR}};$$
$$r^2 = 0.9992$$

The presence of two linear ranges indicates a change in the interaction between the CPR molecules and the electrode surface at higher concentrations. At lower concentrations, CPR molecules are effectively adsorbed onto the active sites of the MIL-101/rGO-modified electrode, resulting in higher sensitivity. However, as the concentration increases, the number of available active sites gradually decreases due to partial surface occupation by CPR molecules. As a result, the slope of the calibration curve decreases slightly in the higher-concentration range. This behavior shows the beginning saturation of active sites on the electrode surface, which is common in adsorption-controlled electrochemical sensing systems. However, a strong linear relationship is still maintained across a wide concentration range, demonstrating the good analytical performance of the proposed sensor for quantitative analysis.

The limit of detection (LOD_{CPR}) and the limit of quantification (LOQ_{CPR}) were 0.11 and 0.36 μM, respectively. Table 2 shows the LOD and linear range of the proposed DPV and compares them with published reports. The LOD of the proposed sensor

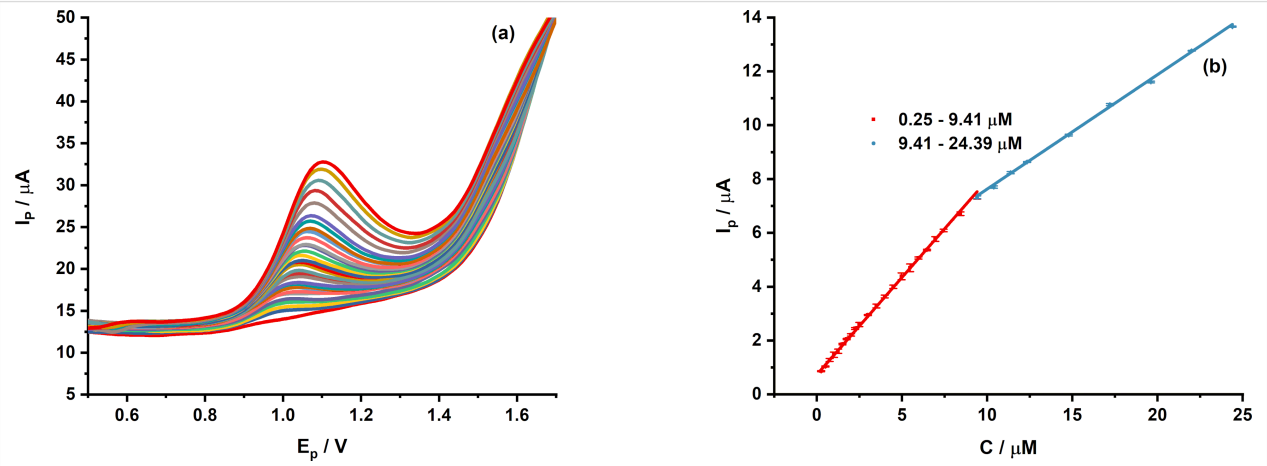


Figure 8: (a) DPV curves of MIL-101/rGO(3.3)/GCE recorded in 0.1 M BRS buffer (pH 4) at CPR concentrations ranging from 0.25 to 24.39 μM and (b) corresponding calibration plots of peak current versus ciprofloxacin concentration.

Table 2: Comparison of the analytical performance of the proposed MIL-101/rGO/GCE with previously reported electrochemical sensors for CPR determination.

Electrodes	Methods	Linear range (μM)	LOD (μM)	Real samples	Ref.
CB–PLA (3D-printed) sensor	–	1.0–12.5	0.3	tap water and synthetic urine	[32]
Poly [Mn(Chr)$_3$]Cl$_2$/PGE	SWV	1–200	0.536	pharmaceutical and urine samples	[33]
AgNPs-CB-Ch/GCE	SWV	3.1–24.8; 36.9–130.3	0.48	synthetic urine samples	[34]
GaTCPP(Ni)-Nafion/SPCE	DPV	200–1000	118	pharmaceutical samples	[35]
MWCNT/GCE	chronoamperometric	40–1000	6	urine and serum samples	[36]
CNSs/GCE	DPV	0.5–5.0	0.15	water sample and medicinal formulations	[37]
{[Co(HL)(bix)]·H$_2$O}$_n$/GCE	DPV	2–20	0.135	water samples	[38]
[Co(HL)(bimb)·H$_2$O]}$_n$/GCE	DPV	1–14	0.082	water samples	[38]
MIL-101/rGO/GCE	DPV	0.25–9.41	0.110	pharmaceutical formulations	this study

was comparable to previous sensors. The advantage of using the MIL-101(Cr)/rGO composite comes from the synergistic combination of its two components. MIL-101(Cr) has a high surface area and abundant porous structure, providing numerous active sites and strong adsorption capability for the target molecules; rGO offers high electrical conductivity, facilitating rapid electron transfer.

Repeatability, reproducibility, and stability

The measurement repeatability of the proposed sensor was evaluated at different CPR concentrations (1.0, 2.5, 5.0, 10.4, and 24.4 μM). Differential pulse voltammetry (DPV) responses were recorded over ten consecutive measurements, and the relative standard deviation (RSD) values were calculated and compared with half of the Horwitz RSD. The obtained RSD values were significantly lower than half of the Horwitz RSD, indicating excellent repeatability and analytical precision of the sensor (Figure 9a).

The reproducibility of the sensor was further assessed using independently prepared MIL-101/rGO-modified electrodes fabricated under identical conditions (Figure 9b). The peak current response was measured as I_{CPR} = 4.29 ± 0.16 μA, corresponding to an RSD of 3.70%. The low RSD value (<5%) confirms the good fabrication reproducibility of the proposed electrode.

The long-term stability of the sensor was evaluated using a single electrode stored in BR buffer at low temperature after use

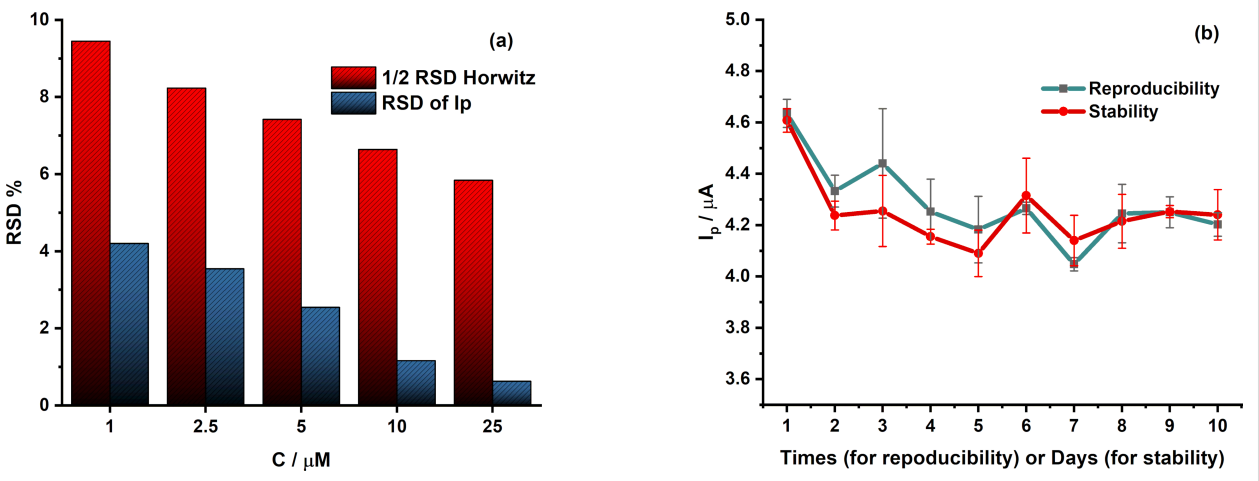


Figure 9: (a) Relative standard deviation of the anodic peak currents obtained from DPV measurements recorded over ten consecutive scans at the MIL-101/rGO(3.3)/GCE in 0.1 M B-R buffer (pH 4) containing CPR at different concentrations (1.0, 2.5, 5.0, 10.4, and 24.4 μM), in comparison with half of the Horwitz RSD (1/2 RSD$_H$) and (b) reproducibility and long-term stability of the MIL-101/rGO(3.3)/GCE evaluated from the peak current response toward ciprofloxacin (5.0 μM) in 0.1 M Britton–Robinson buffer (pH 4), including ten repeated measurements using independently prepared electrodes and the current response recorded over ten days.

and tested over several days (Figure 9b). The peak current was recalled as I_{CPR} = 4.25 ± 0.14 μA with an RSD of 3.33%. After ten days of storage, approximately 92% of the initial current response was retained. The low RSD values together with the high current retention demonstrate the satisfactory long-term stability and reliable performance of the MIL-101/rGO-modified electrode.

Interference study

The selectivity of the proposed sensor toward ciprofloxacin (CPR) was evaluated in the presence of common inorganic ions and organic compounds, including $CaCl_2$ (denoted as C1), NaCl (C2), K_2SO_4 (C3), $Al(NO_3)_3$ (C4), $Mg_3(C_6H_5O_7)_2$ (C5), NH_4Cl (C6), citric acid (C7), saccharine (C8), D-sorbitol (C9), ascorbic acid (C10), D-glucose (C11), and lactose (C12). An interfering species was considered to have a significant effect on the CPR peak current when the absolute relative deviation exceeded 5%.

As shown in Figure 10, no significant interference was observed for most of the tested species, even when their concentrations were more than 100-fold higher than that of CPR. These results demonstrate that the proposed sensor possesses good selectivity and strong anti-interference capability, making it suitable for the determination of CPR in complex sample matrices.

Application to pharmaceutical samples

The proposed DPV method was used to determine CPR in various commercial pharmaceutical formulations using the standard addition method (Table 3). The recovery values obtained ranged from 95.91% to 104.67%, demonstrating good accuracy of the method. The slightly higher recovery for Tablets 2 (104.67%) may be due to excipients in the formulation. Some excipients can produce weak electrochemical responses or contribute to background currents near CPR oxidation potentials, which can slightly raise the measured peak current and cause a minor overestimation of the analyte concentration. However, these recoveries are within the acceptable range for pharmaceutical analysis (90–110%), confirming the reliability of the developed DPV method for analyzing CPR in real samples.

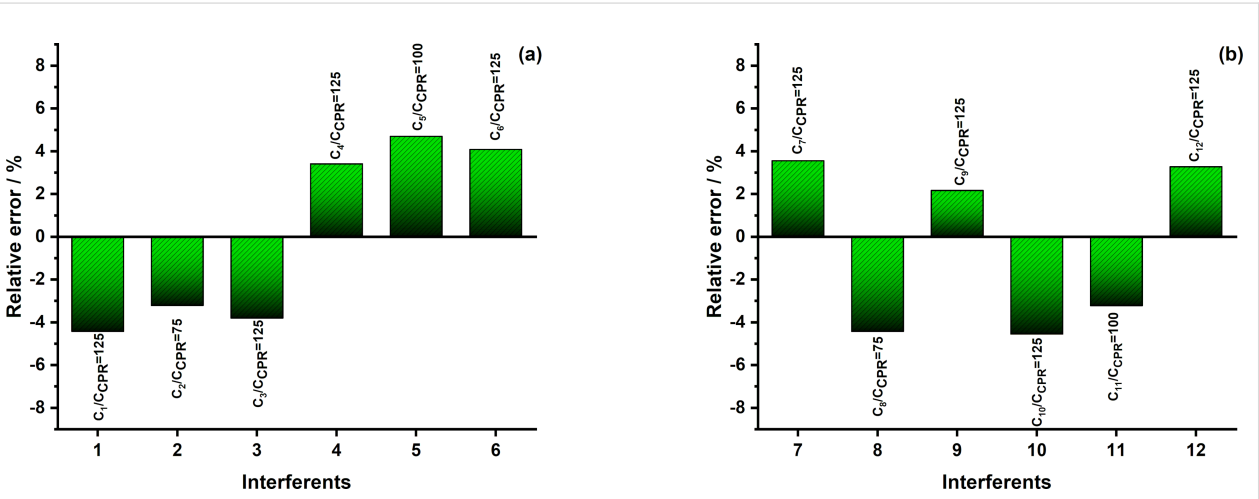


Figure 10: Relative error (RE%) caused by the interference of selected inorganic (a) and organic (b) species at different concentration ratios.

Table 3: Determination and recovery of CPR in commercial pharmaceutical formulations by DPV at MIL-101/rGO(3.3)/GCE.[a]

Notation	CPR content ± SD (μM)[b]	CPR content ± SD (mg)[c]	Spiked (μM)	Found ± SD (μM)[b]	Recovery (%)
Tablets 1 (Label 500 mg CPR/unit)	1.4376 ± 0.0182	479.3 ± 3.0	1.0	2.4089 ± 0.0299	97.13
Tablets 2 (Label 500 mg CPR/unit)	1.5656 ± 0.0281	512.1 ± 7.9	1.0	2.6123 ± 0.0158	104.67
Powder of oral suspension (Label 250 mg CPR/unit)	1.4851 ± 0.0172	245.6 ± 3.9	1.0	2.4442 ± 0.0257	95.91

[a]SD: standard deviation of three repeated measurements; [b]CPR concentration calculated in electrochemical cell; [c]CPR amount calculated in one unit of drug by DPV method.

Conclusion

In this work, an electrochemical sensor based on a MIL-101/reduced graphene oxide (MIL-101/rGO) modified glassy carbon electrode was successfully developed for detecting ciprofloxacin. MIL-101/rGO, synthesized using a simple ultrasonic-assisted method, displayed a favorable microstructure and strong interfacial interaction between MIL-101 and rGO, leading to an improved electrochemical response to ciprofloxacin oxidation. Electrochemical investigations showed that the modified electrode exhibited enhanced electrochemical performance and increased catalytic activity toward CPR oxidation compared to the bare electrode. Under optimal experimental conditions, the proposed sensor demonstrated a broad linear response range with a low detection limit, along with good selectivity against common interfering substances. Additionally, the sensor exhibited excellent repeatability, strong reproducibility in fabrication, and reliable long-term stability. The practical application of the method was confirmed through successful detection of CPR in pharmaceutical products with acceptable recoveries. Overall, the MIL-101/rGO-modified electrode is a reliable and efficient electrochemical sensing platform for CPR detection and shows potential for routine pharmaceutical analysis and related electrochemical sensing research.

Supporting Information

Supporting Information File 1

Additional figures.
[https://www.beilstein-journals.org/bjnano/content/supplementary/2190-4286-17-35-S1.pdf]

Funding

Hue University partially funded this research under the Core Research Program No. NCTB.DHH.2025.05.

Author Contributions

Nguyen Quang Man: conceptualization; funding acquisition; writing – original draft; writing – review & editing. Nguyen Ngoc Nghia: conceptualization; funding acquisition; writing – original draft; writing – review & editing. Nguyen Vinh Phu: investigation; methodology; resources; validation; visualization. Vo Thi Khanh Ly: investigation; methodology; resources; validation; visualization. Le Lam Son: investigation; methodology; resources; validation; visualization. Pham Khac Lieu: investigation; methodology; resources; validation; visualization. Le Thi Hong Phong: investigation; methodology; validation; visualization. Nguyen Dinh Luyen: supervision. Dinh Quang Khieu: writing – review & editing.

ORCID® iDs

Nguyen Quang Man - https://orcid.org/0000-0001-6511-1236
Nguyen Ngoc Nghia - https://orcid.org/0009-0009-9166-7815
Nguyen Vinh Phu - https://orcid.org/0000-0003-2389-3422
Vo Thi Khanh Ly - https://orcid.org/0009-0005-0854-3290
Le Lam Son - https://orcid.org/0000-0002-8693-7472
Pham Khac Lieu - https://orcid.org/0000-0002-9002-1416
Le Thi Hong Phong - https://orcid.org/0000-0001-8825-6243
Nguyen Dinh Luyen - https://orcid.org/0009-0004-3926-9282
Dinh Quang Khieu - https://orcid.org/0000-0003-3473-6377

Data Availability Statement

All data that supports the findings of this study is available in the published article and/or the supporting information of this article.

References

1. Thai, T.; Salisbury, B. H.; Zito, P. M. *Ciprofloxacin;* StatPearls Publishing LLC, 2025.
2. Peñafiel, M. E.; Vanegas, E.; Bermejo, D.; Matesanz, J. M.; Ormad, M. P. *Hyperfine Interact.* **2019,** *240,* 71. doi:10.1007/s10751-019-1612-9
3. Al-howri, B. M.; Ismail, S.; Khajavian, M. *Environ. Monit. Assess.* **2025,** *197,* 1095. doi:10.1007/s10661-025-14454-z
4. Thakur, R.; Singh, A.; Dhanwar, R.; Kadam, S.; Waghmare, U.; Lodha, T.; Lopes, B. S.; Prakash, O. *Discov. Sustain.* **2025,** *6,* 232. doi:10.1007/s43621-025-01048-5
5. Wang, J.; Li, X.; Xu, Z.; Xu, L. *Food Sci. Hum. Wellness* **2025**. doi:10.26599/fshw.2025.9250607
6. Ahmadi, K.; Nasirimoghadam, S.; Mohammadjafar, F.; Hashemi, S. F.; Zeeb, M. *Anal. Lett.* **2026,** *59,* 935–948. doi:10.1080/00032719.2025.2519463
7. Elgendy, K.; Zaky, M.; Alaa Eldin, T.; Fadel, S. *Results Chem.* **2023,** *5,* 100749. doi:10.1016/j.rechem.2022.100749
8. de Vroom, S. L.; Pistorius, M. C. M.; Bijleveld, Y. A.; Geerlings, S. E.; Mathôt, R. A. A.; van Hest, R. M.; Jager, N. G. L. *Ther. Drug Monit.* **2022,** *44,* 552–557. doi:10.1097/ftd.0000000000000969
9. Qiu, S.; Wang, Y.; Wan, J.; Han, J.; Ma, Y.; Wang, S. *Appl. Surf. Sci.* **2020,** *525,* 146511. doi:10.1016/j.apsusc.2020.146511
10. Zorainy, M. Y.; Gar Alalm, M.; Kaliaguine, S.; Boffito, D. C. *J. Mater. Chem. A* **2021,** *9,* 22159–22217. doi:10.1039/d1ta06238g
11. Keshta, B. E.; Yu, H.; Wang, L.; Yi, H.; Jian, S.; Uddin, M. A.; Ouyang, C.; Wang, Y.; Yuan, X.; Zhang, Y.; Jin, Y.; Basit, A.; Owais Malik, M.; Awan, K. M. *npj Clean Water* **2025,** *8,* 15. doi:10.1038/s41545-024-00413-7
12. Öztekin, D.; Arbağ, H.; Yaşyerli, S. *Arabian J. Sci. Eng.* **2025,** *50,* 9905–9918. doi:10.1007/s13369-024-09915-5
13. Mustafa, Z.; Kumar, D.; Swain, B. P.; Pradhan, B. B.; Ghadai, R. K. *Sci. Rep.* **2026,** *16,* 536. doi:10.1038/s41598-025-29897-0
14. Wang, S.; Zou, H.-J.; Sun, J.; Lu, C.; Gao, X.; Han, X. *J. Sol-Gel Sci. Technol.* **2025,** *116,* 2717–2732. doi:10.1007/s10971-025-06994-0
15. Jilani, A.; Dustgeer, M. R.; Ansari, M. O.; Zaka, A.; Mansoor, M. A.; Melaibari, A. A.; Ibrahim, H. *J. Water Process Eng.* **2025,** *80,* 109086. doi:10.1016/j.jwpe.2025.109086
16. Gu, J.; Yin, X.; Bo, X.; Guo, L. *ChemElectroChem* **2018,** *5,* 2893–2901. doi:10.1002/celc.201800588

17. Wu, Y.; Luo, H.; Wang, H.; Wang, C.; Zhang, J.; Zhang, Z. *J. Colloid Interface Sci.* **2013,** *394,* 183–191. doi:10.1016/j.jcis.2012.11.049
18. Wu, Y.; Luo, H.; Zhang, L. *Environ. Sci. Pollut. Res.* **2015,** *22,* 17238–17243. doi:10.1007/s11356-015-5364-z
19. Miller, J. N.; Miller, J. C.; Miller, R. D. *Statistics and Chemometrics for Analytical Chemistry,* 7th ed.; Pearson, 2005.
20. Yasin, G.; Arif, M.; Shakeel, M.; Dun, Y.; Zuo, Y.; Khan, W. Q.; Tang, Y.; Khan, A.; Nadeem, M. *Adv. Eng. Mater.* **2018,** *20,* 1701166. doi:10.1002/adem.201701166
21. Jiao, X.; Qiu, Y.; Zhang, L.; Zhang, X. *RSC Adv.* **2017,** *7,* 52337–52344. doi:10.1039/c7ra10809e
22. Ferey, G.; Mellot-Draznieks, C.; Serre, C.; Millange, F.; Dutour, J.; Surble, S.; Margiolaki, I. *Science* **2005,** *309,* 2040–2042. doi:10.1126/science.1116275
23. Wei, G.; Yu, J.; Gu, M.; Tang, T. B. *J. Appl. Phys.* **2016,** *119,* 224102. doi:10.1063/1.4953357
24. Meneses-Ruiz, E.; Escobar, J.; Mora, R. J.; Montoya, J. A.; Barrera, M. C.; Solís-Casados, D.; Escobar-Alarcón, L.; Del Ángel, P.; Laredo, G. *Oil Gas Sci. Technol.* **2021,** *76,* 56. doi:10.2516/ogst/2021038
25. Huang, X.; Hu, Q.; Gao, L.; Hao, Q.; Wang, P.; Qin, D. *RSC Adv.* **2018,** *8,* 27623–27630. doi:10.1039/c8ra04789h
26. Jiang, J.; Zhu, L.; Chen, H.; Sun, Y.; Qian, W.; Lin, H.; Han, S. *J. Mater. Sci.* **2019,** *54,* 1422–1433. doi:10.1007/s10853-018-2913-0
27. Vo, T. K.; Kim, J.-H.; Kwon, H. T.; Kim, J. *J. Ind. Eng. Chem. (Amsterdam, Neth.)* **2019,** *80,* 345–351. doi:10.1016/j.jiec.2019.08.013
28. Bard, A. J.; Faulkner, L. R. *Russ. J. Electrochem.* **2002,** *38,* 1364–1365. doi:10.1023/a:1021637209564
29. Laviron, E. *J. Electroanal. Chem. Interfacial Electrochem.* **1979,** *101,* 19–28. doi:10.1016/s0022-0728(79)80075-3
30. Li, C. *Colloids Surf., B* **2007,** *55,* 77–83. doi:10.1016/j.colsurfb.2006.11.009
31. Tajik, S.; Beitollahi, H.; Zaeimbashi, R.; Sheikhshoaei, M.; Askari, M. B.; Salarizadeh, P. *J. Mater. Sci.: Mater. Electron.* **2021,** *32,* 17558–17567. doi:10.1007/s10854-021-06288-5
32. Henriques, B. F.; Neumann, A.; Bertolim, L. V.; de Freitas, R. C.; Silva, L. R. G.; Stefano, J. S.; Janegitz, B. C. *Electroanalysis* **2025,** *37,* e12008. doi:10.1002/elan.12008
33. Shitahun, A.; Atlabachew, M.; Aragaw, B. A.; Benor, A.; Metto, M.; Abebe, A. *Int. J. Electrochem. Sci.* **2025,** *20,* 100937. doi:10.1016/j.ijoes.2025.100937
34. Meireles, L. M.; Silva, R. M.; da Silva, R. C.; Okumura, L. L.; Moreira, R. P. L.; Silva, T. A. *J. Solid State Electrochem.* **2025,** *29,* 3111–3122. doi:10.1007/s10008-024-06033-y
35. Shepa, J.; Király, N.; Demeterová, J.; Shepa, I.; Hviščová, P.; Volavka, D.; Kožár, M.; Šišoláková, I.; Oriňaková, R.; Zeleňák, V.; Almáši, M. *Microchem. J.* **2025,** *218,* 115638. doi:10.1016/j.microc.2025.115638
36. Fotouhi, L.; Alahyari, M. *Colloids Surf., B* **2010,** *81,* 110–114. doi:10.1016/j.colsurfb.2010.06.030
37. Ipte, P. R.; Kumar, S.; Satpati, A. K. *J. Environ. Sci. Health, Part A: Toxic/Hazard. Subst. Environ. Eng.* **2020,** *55,* 142–150. doi:10.1080/10934529.2019.1674591
38. Xiang, R.; Qin, T.; Liu, Y.; Lan, L.; Dong, X.; Srivastava, D.; Parvez, M. K.; Al-Dosari, M. S.; Kumar, A.; Pan, Y. *Microchem. J.* **2025,** *209,* 112594. doi:10.1016/j.microc.2024.112594

License and Terms

This is an open access article licensed under the terms of the Beilstein-Institut Open Access License Agreement (https://www.beilstein-journals.org/bjnano/terms), which is identical to the Creative Commons Attribution 4.0 International License (https://creativecommons.org/licenses/by/4.0). The reuse of material under this license requires that the author(s), source and license are credited. Third-party material in this article could be subject to other licenses (typically indicated in the credit line), and in this case, users are required to obtain permission from the license holder to reuse the material.

The definitive version of this article is the electronic one which can be found at:
https://doi.org/10.3762/bjnano.17.35

BEILSTEIN JOURNAL OF NANOTECHNOLOGY

Interface-engineered Caco-2 cell culture on a collagen-coated liquid–liquid interface in a microfluidic device

Satoru Kuriu* and Soo Hyeon Kim*

Full Research Paper

Open Access

Address:
Institute of Industrial Science, The University of Tokyo, 4-6-1 Komaba, Meguro-ku, Tokyo 153-8505 JAPAN

Email:
Satoru Kuriu* - kurius@iis.u-tokyo.ac.jp;
Soo Hyeon Kim* - shkim@iis.u-tokyo.ac.jp

* Corresponding author

Keywords:
Caco-2; collagen; FC-43; gut-on-a-chip; liquid–liquid interface

Beilstein J. Nanotechnol. **2026,** *17,* 760–768.
https://doi.org/10.3762/bjnano.17.53

Received: 10 March 2026
Accepted: 26 May 2026
Published: 11 June 2026

This article is part of the thematic issue "Nanotechnology for cross-scale analysis: comprehensive evaluation of water environments".

Guest Editors: Y. Sasaki and T. Minami.



© 2026 Kuriu and Kim; licensee Beilstein-Institut.
License and terms: see end of document.

Abstract

Epithelial tissues form selective barriers essential for physiological homeostasis. Conventional in vitro models rely on solid substrates, which limit the physicochemical flexibility of the cellular microenvironment. Here, we introduce a microfluidic platform in which a collagen-coated liquid–liquid interface formed between perfluorocarbon (FC-43) and culture medium serves as a substrate for epithelial cell adhesion. By culturing Caco-2 cells in the device, we show that the liquid interface supports cell attachment and the formation of monolayers. Immunofluorescence observation reveals the development of tight junctions and organized actin cytoskeletons, indicating early-stage epithelial maturation. Our new microfluidic system enables the formation of stable liquid–liquid interfaces that serve as viable and flexible substrates for epithelial cell culture, offering new opportunities for multiphase microfluidic models of epithelial barriers.

Introduction

Epithelial tissues form selective barriers that regulate the transport of molecules, ions, and gases; they play an important role in physiological homeostasis [1]. In vitro models of epithelial barriers, particularly culturing Caco-2 cells, have been widely used to study the function of the epithelial tissues [2-4]. The microfluidic culture system known as gut-on-a-chip enables the cultivation of Caco-2 cells under conditions that more closely recapitulate the in vivo intestinal environment. By precisely controlling fluid flow and inducing mechanical stimuli, this platform provides physiologically relevant mechanical cues that are difficult to reproduce in conventional static culture systems [5-7]. Gut-on-a-chip platforms recapitulate the apical-basolateral compartmentalization of the human intestinal epithelium by dividing upper and lower microchannels with a solid porous

membrane, upon which intestinal epithelial cells are cultured to establish a polarized epithelial barrier. Although porous membranes enable compartmentalization, they may also impose non-physiological diffusion barriers and mechanical constraints.

Liquid–liquid interfaces provide a mechanically soft and dynamically reconfigurable environment that more closely mimics native cellular microenvironments than rigid solid substrates. Unlike conventional solid culture surfaces, liquid–liquid interfaces offer a distinct platform for cell culture, enabling a scaffold-free and mechanically tunable environment that eliminates the rigidity and pore-related constraints inherent to synthetic solid membranes [8-10]. Importantly, culturing cells at a liquid–liquid interface provides a unique opportunity to decouple biochemical signaling from substrate-imposed mechanical constraints, thereby enabling more physiologically relevant investigation of epithelial barrier formation, transport functions, and mechanobiological responses that are otherwise difficult to isolate in conventional solid-supported systems. Moreover, when functionalized with extracellular matrix proteins, such interfaces can support uniform epithelial maturation and stable monolayer formation, demonstrating their potential as engineered bioactive substrates [10]. Owing to their dynamic responsiveness to chemical and physical stimuli, such interfaces can also serve as reservoirs or delivery media for gases and hydrophobic molecules [11]. Incorporating a liquid–liquid interfacial strategy into microfluidic cell culture systems may therefore offer an alternative to porous membrane-based designs and mitigate the inherent limitations of synthetic solid membranes in gut-on-a-chip platforms. Among candidate materials, perfluorocarbon liquids such as FC-43 are particularly attractive due to their chemical inertness, immiscibility with aqueous media, and high gas solubility [11], making them well suited for multiphase microfluidic applications.

In this study, we propose a novel microfluidic cell culture system by utilizing a collagen-coated liquid–liquid interface that serves as a cell-adhesion substrate for epithelial cells (Figure 1A). The rectangular cuboid-shaped microfluidic device allows for stable formation of the liquid–liquid interface for cell culture by sequential flow manipulation (Figure 1B). Using Caco-2 cells, a well-known epithelial cell line, we demonstrate that cells can adhere and form monolayers on the liquid–liquid interface. Immunofluorescence images reveal the formation of tight junctions and organized actin cytoskeletons, indicating epithelial early-stage maturation. Our results establish liquid–liquid interfaces as viable and functional substrates for epithelial cell culture and highlight their potential for the development of flexible, multiphase microfluidic models of epithelial barrier.

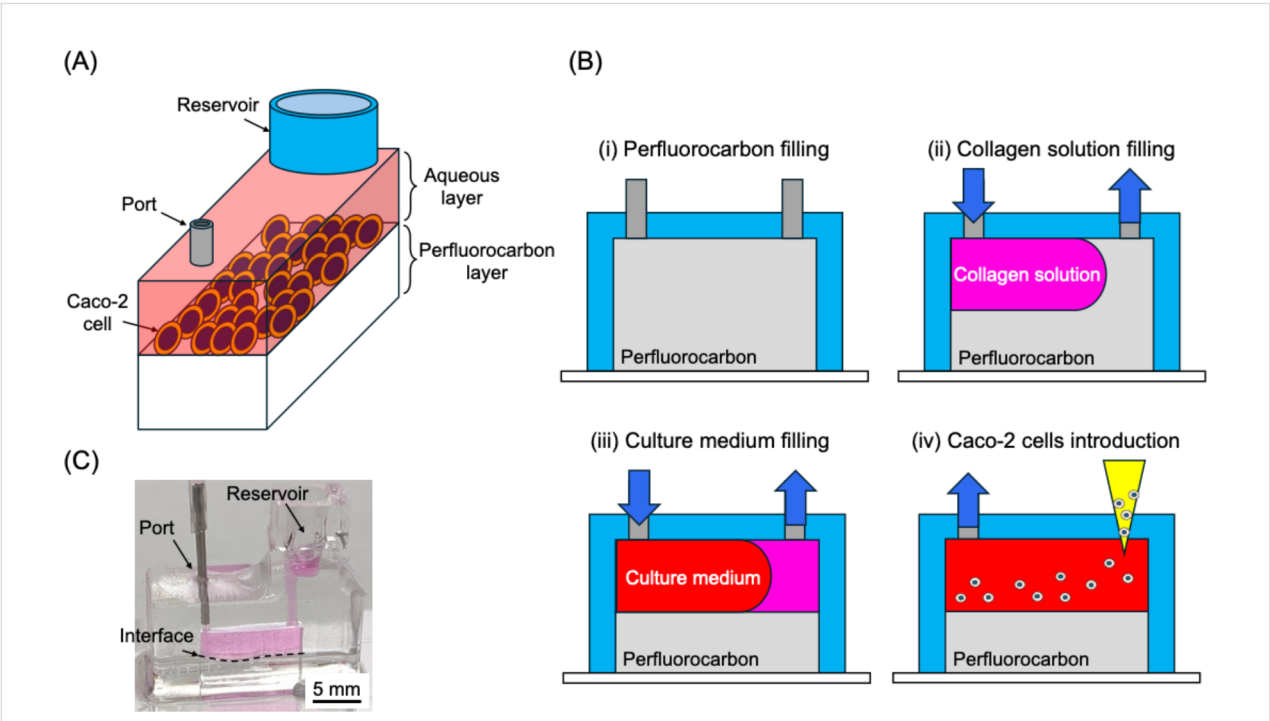


Figure 1: Illustration of the liquid–liquid interface formation. (A) Concept of the microfluidic device. (B) Fluid operation description: (i) FC-43 filling, (ii) collagen solution filling, (iii) culture medium filling, and (iv) Caco-2 cells introduction. (C) Fabricated microfluidic device. The dashed line indicates the boundary of the liquid–liquid interface.

Results and Discussion

Liquid–liquid interface formation in the microfluidic device

The liquid–liquid interface was formed by first filling the microchannel with the perfluorocarbon liquid FC-43, followed by the introduction of an aqueous solution containing collagen (Figure 1B-ii). The effect of channel dimensions on the formation of the liquid–liquid interface was evaluated using the rectangular cuboid-shaped microfluidic device.

First, channel height and length were fixed at 7 and 10 mm, respectively, while the channel width was varied (1.0, 1.5, 2.0, 5.0, and 10.0 mm). Liquid–liquid interfaces were subsequently formed in each channel by introducing collagen solution at 50 µL/min. Here, when forming the liquid–liquid interface, a meniscus develops. To quantify the extent of this meniscus, we introduced rectangularity as an easily interpretable indicator. Rectangularity is calculated using Equation 1 based on the collagen region observed on the channel height × channel length plane of the microfluidic device (i.e., 7 mm × 10 mm in this case, see Figure 2, Figure 3, and Supporting Information File 1, Figures S1–S3) and the minimum bounding rectangle of the collagen solution region.

$$\text{Rectangularity (\%)} = \frac{\text{The area of the collagen solution region}}{\text{The area of the minimum bounding rectangle of the collagen solution region}} \times 100 \quad (1)$$

The rectangularity for each channel size is shown in Figure 3. When the channel width ranged from 1 to 2 mm, the rectangularity of the aqueous layer was 94% or higher; however, when the channel width was 5 or 10 mm, the rectangularity decreased to 88% (Figure 3). These results suggest that channel width affects the formation of the liquid–liquid interface. To analyze this effect, the "Bond number" (B_o), a dimensionless parameter defined as

$$B_0 = \frac{\rho g L^2}{\sigma}, \quad (2)$$

was introduced to evaluate whether gravitational forces or interfacial tension dominate when two fluids of different densities are in contact. Here, ρ denotes the density difference between FC-43 and the collagen solution, g is the gravitational acceleration, L is the channel width, and σ is the interfacial tension coefficient. In this experiment, as the channel width L was varied, its effect on the Bond number was directly assessed. Taking the Bond number for a channel width of 1 mm as a reference, the Bond numbers for channel widths of 1.5, 2, 5, and 10 mm were 2.25, 4, 25, and 100 times greater, respectively. For channel widths of 5 and 10 mm, the Bond number increased by one to two orders of magnitude. As the Bond number increases, gravi-

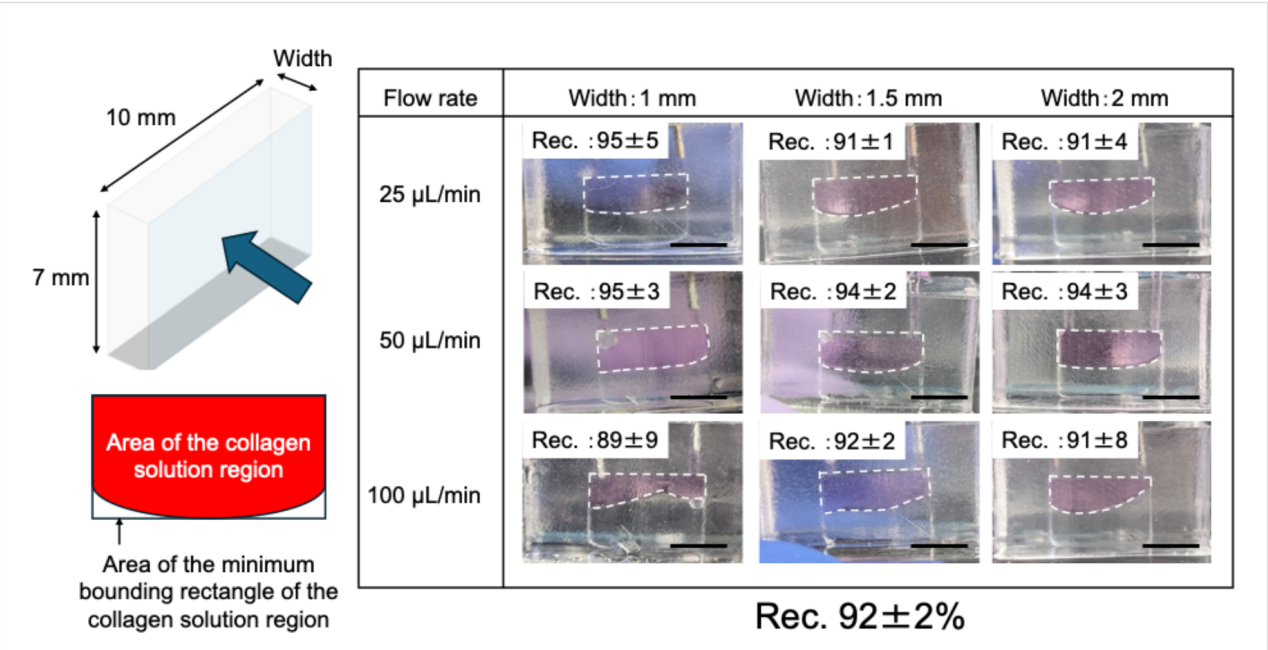


Figure 2: Rectangularity of the collagen solution region with respect to channel dimension (7 mm × 10 mm × width) and collagen solution introduction flow rate. The collagen region was imaged by a smartphone followed by the direction indicated by arrow. Rectangularity is abbreviated as "Rec".

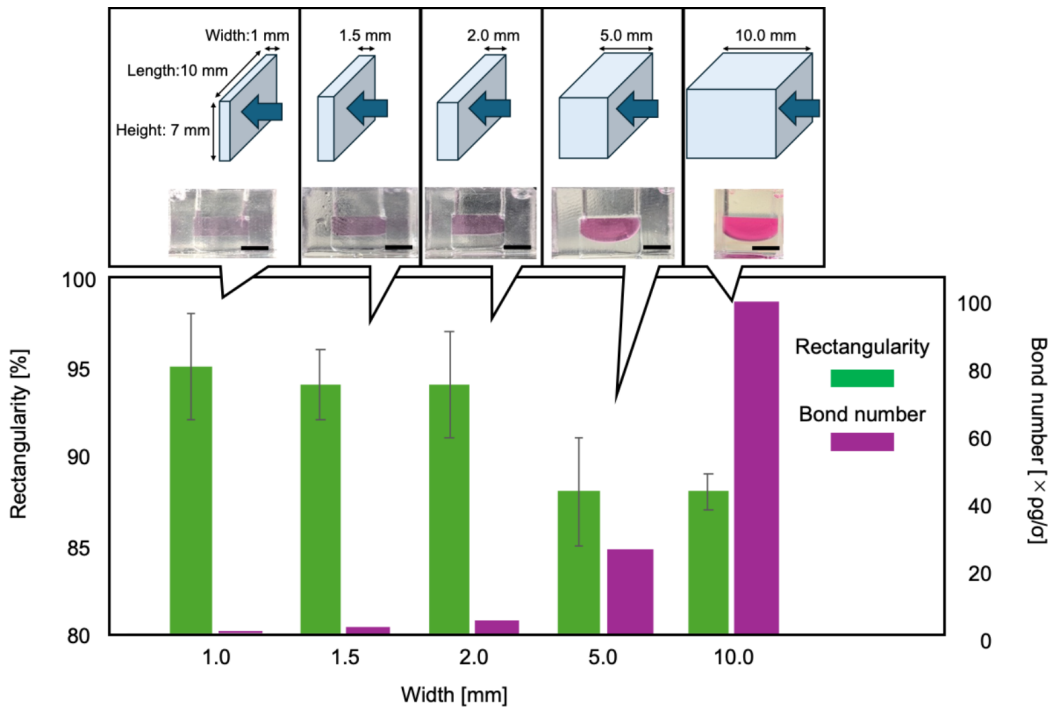


Figure 3: Rectangularity and Bond number as functions of the channel width (1.0, 1.5, 2.0, 5.0, and 10.0 mm). Representative interface images are shown above each bar. The images of the collagen solution region were captured from the direction indicated by the arrows. Scale bars are 5 mm. $n = 3$.

tational forces increasingly dominate over interfacial tension. Thus, for channel widths of 5 and 10 mm, the gravitational effect on the aqueous layer exceeds that of surface tension, resulting in a pronounced meniscus and a reduction in rectangularity. In this study, a high rectangularity was interpreted as indicating an interface nearly parallel to the channel bottom, which is favorable for microscopic observation; accordingly, devices exhibiting high rectangularity were selected for the demonstration. For a practical application, the device with a width of 2 mm was selected for the cell culture experiments because it offered advantages in operation, including easier bubble removal.

In addition, the effect of channel height on the formation of the liquid–liquid interface was evaluated (Figure 4). The channel height was varied at 7, 5, and 4 mm. When the height was 4 mm, the FC-43 layer was almost completely displaced upon the introduction of the collagen solution, preventing interface formation. At a height of 5 mm, the liquid–liquid interface was formed, but the rectangularity decreased to approximately 87%, comparable to the rectangularity observed for aqueous layers in channels 5 and 10 mm wide at a height of 7 mm. These results indicate that channel height is also a critical parameter for the formation of the liquid–liquid interface.

Rectangularity was evaluated by varying both the channel size and the flow rate of the collagen solution (Figure 2, Supporting Information File 1, Figures S1–S3). Our results suggest that interface formation is largely insensitive to the flow rate of the collagen solution, whereas the channel size significantly governs the interfacial shape.

Caco-2 cell culture on the liquid–liquid interface

The feasibility of adhesive cell culture on the liquid–liquid interface with a collagen layer was demonstrated by culturing Caco-2 cells (a human colorectal adenocarcinoma cell line). After forming the liquid–liquid interface using FC-43 and collagen-containing serum-free DMEM, the cell suspension was introduced and seeded at a density of 1.5×10^5 cells/cm^2. The growth of Caco-2 cells on the liquid–liquid interface is shown in Figure 5. The images were captured near the center of the channel. At two days post-seeding, most Caco-2 cells had adhered to the interface, resulting in the formation of a monolayer. This monolayer was maintained for seven days. In this study, Caco-2 cell monolayer culture was performed using three independent devices. As a result, confluency reached 95 ± 3% after seven days of culture. Here, the images of the left, center and right regions of the channel for each device were acquired

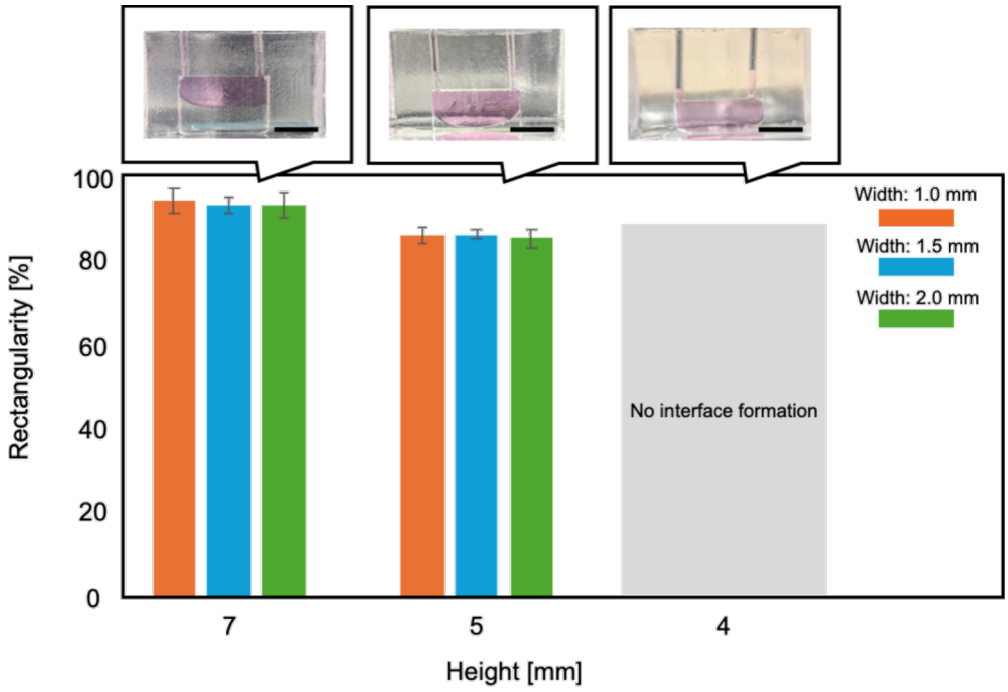


Figure 4: Rectangularity as a function of channel height (7, 5, and 4 mm). Representative interface images are shown above each bar. For a channel height of 4 mm, almost all of the FC-43 was replaced by the collagen solution; therefore, the rectangularity was not calculated, and it is labeled as "No interface formation". Scale bars are 5 mm. n = 3.

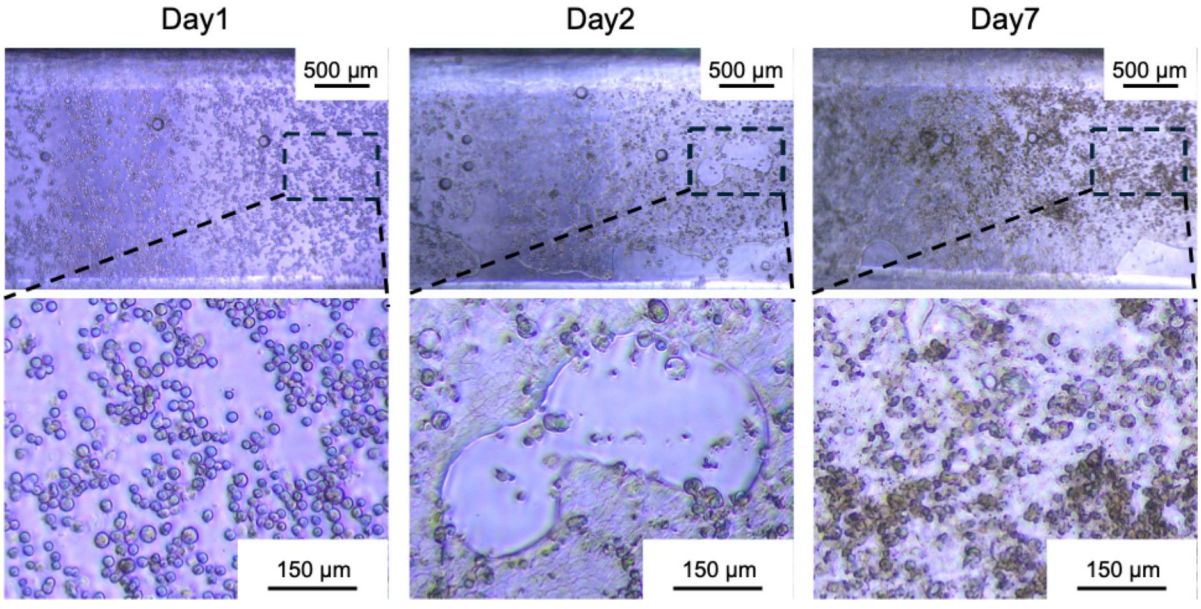


Figure 5: Time-lapse images of the progression of Caco-2 cells at the liquid–liquid interface. Images indicate Day1, Day2 and Day7, respectively. Region with a lower number of cells is magnified to show that Caco-2 cells grow on the interface.

on day seven of culture (see Supporting Information File 1, Figure S4), and confluency was calculated. Previous studies have suggested that Caco-2 cells begin to exhibit early functional characteristics of the intestinal epithelium, such as tight junction formation, after approximately seven days of culture [12]. In the present study, we therefore chose a period of seven

days of culture to assess the early-stage maturation of Caco-2 monolayers from a proof-of-concept perspective. Here, the liquid–liquid interface remained intact and was stably maintained throughout the cell culture period (data is not shown).

To observe whether collagen was coated on the liquid–liquid interface, immunostaining for collagen was performed (Supporting Information File 1, Figure S5). Compared to the device without collagen coating, fluorescence was observed in the collagen-coated device. In addition, to evaluate the effect of collagen coating on the liquid–liquid interface, the behavior of Caco-2 cells seeded onto a liquid–liquid interface without collagen coating is shown in Supporting Information File 1, Figure S6. Caco-2 cells did not adhere on the liquid–liquid interface to form a monolayer; instead, they aggregated and were observed floating on the liquid–liquid interface. Those results indicate that bringing the collagen solution into contact with FC-43 results in the formation of a collagen layer on the liquid–liquid interface that is sufficiently robust to support cell adhesion.

Caco-2 cells monolayer maturation

Immunofluorescence staining was performed to observe the characteristics of cultured Caco-2 cells as an intestinal epithelial model. Figure 6 shows a comparison of immunofluorescence images of ZO-1, F-actin, and nuclei in Caco-2 cells cultured in the microfluidic device and in 96-well plates. Under both conditions, epifluorescence imaging shows that the nuclei, ZO-1, and F-actin signals are localized within the same focal plane and are distributed across the entire liquid–liquid interface formed in the microfluidic device, indicating the formation of a monolayer. Although autofluorescence from FC-43 was observed in the images of the microfluidic devices, ZO-1 localization at cell–cell junctions was confirmed, suggesting the formation of epithelial barrier properties in Caco-2 cells cultured in the microfluidic device [13,14]. F-actin localization was observed under both conditions, suggesting that the cytoskeletal organization supporting the epithelial structure was maintained in Caco-2 cells cultured in the microfluidic device. Colocalization of ZO-1 with F-actin at cell–cell borders indicates the formation of mature tight junctions and the establishment of a functional epithelial barrier. Taken together, these results suggest that Caco-2 cells [15,16] cultured in the microfluidic

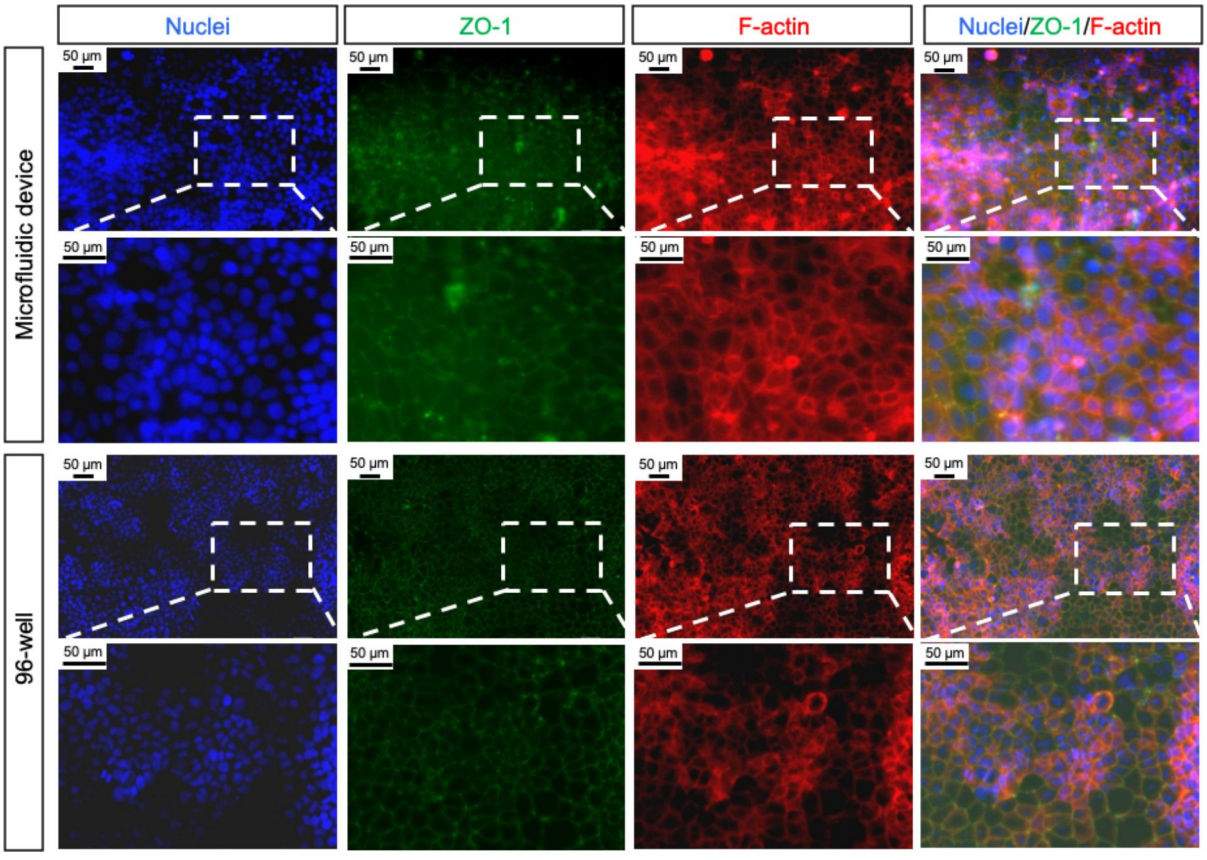


Figure 6: Immunofluorescence images of Caco-2 cells cultured in a microfluidic device and 96-well plates. Nuclei, ZO-1, F-actin and Merge images are displayed.

device formed an epithelial monolayer with tight junctions and supporting cytoskeletal organization, recapitulating intestinal epithelial characteristics. Caco-2 cell culture and immunostaining within the microfluidic device were conducted in triplicate (n = 3), and representative results are shown in this study.

Conclusion

We propose a unique rectangular cuboid-shaped microfluidic device that enables Caco-2 cell culture on a liquid–liquid interface. The collagen-coated liquid–liquid interface was formed by sequentially perfusing collagen-containing aqueous solution into the microfluidic channel filled with perfluorocarbon FC-43. Caco-2 cells were successfully cultured on the interface by forming a monolayer, and immunofluorescence imaging confirmed tight-junction formation and organized actin cytoskeletons, indicating early-stage epithelial maturation. Unlike conventional systems that rely on plastic or silicone rubber substrates for cell adhesion, our system enables direct cell culture on a liquid–liquid interface, offering a novel platform with potential for advanced drug transport studies and co-culture experiments with other cell types. This approach is expected to open new avenues for functional assays, such as transepithelial electrical resistance or drug permeability studies and co-culture experiments with other cell types.

Experimental

Device materials, reagents, and Caco-2 cells

The materials for device fabrication and assembly were obtained from the following suppliers: PDMS (Silpot 184W/C, Dow Corning Toray, Tokyo, Japan) and cover glass (MICRO COVER GLASS, MATSUNAMI GLASS IND., LTD., Osaka, Japan). Reagents for experiments were obtained from the following suppliers: formaldehyde (FA) (Formaldehyde, FUJIFILM Wako Pure Chemical Corporation, Osaka, Japan), Triton X-100 (Triton^{TM}X-100, Sigma-Aldrich, St. Louis, MO, USA), ZO-1 antibody (ZO-1 Monoclonal Antibody [ZO1-1A12], Alexa Fluor^{TM} 488, Thermo Fisher Scientific Inc., Waltham, MA, USA), phalloidin (Phalloidin, Red Fluorescent Dye Conjugate, Acti-stain 555, Cytoskeleton, Inc., CO, USA), Hoechst33342 (Hoecst 33342 solution, Dojindo Laboratories, Kumamoto, Japan), PBS (D-PBS(−) (10×), Nacalai Tesque, Inc., Kyoto, Japan), DMEM (DMEM(1×)+GlutaMAX^{TM}-I, Gibco, Thermo Fisher Scientific Inc., Waltham, MA, USA), FBS (Fetal Bovine Serum, Gibco, Thermo Fisher Scientific Inc., Waltham, MA, USA), Collagen type I-C (Cellmatrix® Type I-C, Nitta Gelatin Inc., Osaka, Japan) and FC-43 (3M, St. Paul, MN, USA).

Device fabrication

The microfluidic device was fabricated by following soft lithography. The polyacetal plate was milled to fabricate the molds, which were designed by three-dimensional computer-aided design software. The fabrication process is shown in Supporting Information File 1, Figure S7. Briefly, PDMS was cast on molds and cured at 85 °C for 5 h (Figure S7i). The cured PDMS was removed from the mold and holes with diameters of 1.0 and 1.5 mm were punched for port and reservoir, respectively (Figure S7ii). Port and reservoir were attached on to the microfluidic device (Figure S7iii). A thin layer of uncured PDMS was applied to the bottom of the device, attached to a coverslip and cured at 85 °C for 2 h (Figure S7iv).

Caco-2 cell culture

The procedure of the Caco-2 cell culture in the microfluidic device is shown in Figure S8. First, the device was filled with FC-43 (Figure S8i). Next, collagen-containing serum-free DMEM (60 μg/mL) was introduced into the channel at a flow rate of 50 μL/min using a syringe pump (KDS, kd Scientific, MA, USA) from the port (Figure S8ii). In this study, the collagen concentration was selected as the optimal condition based on preliminary experiments (data not shown). In brief, excessively low collagen concentrations impede cell adhesion, while excessively high concentrations lead to gelation, making fluid handling impossible. The microfluidic device was put in the refrigerator (4 °C, 2 h) (Figure S8iii). Thereafter, culture medium was introduced into the channel at a flow rate of 10 μL/min for 10 min to replace the existing liquid layer (Figure S8iv). The human large intestinal cancer cell line Caco-2 cells (CACO-2, KAC Co., Ltd., Kyoto, Japan) were harvested and resuspended in culture medium (DMEM/FBS = 9:1) (Figure S8v). A portion of the cell suspension was aspirated using a pipette, and the pipette tip was mounted onto the device reservoir. The cell suspension was then introduced into the channel from the port using a syringe pump at a flow rate of 20 μL/min for 1 min, and Caco-2 cells were seeded onto the liquid–liquid interface at a density of 1.5×10^5 cells/cm^2. The microfluidic device was then put in an incubator (37 °C, 5% CO_2). The culture medium was replaced daily by flowing fresh medium through the channel at a flow rate of 10 μL/min for 10 min. For control experiments, Caco-2 cells were seeded into 96-well plates at a density of 1.5×10^5 cells/cm^2, and the culture medium was replaced daily. The microfluidic device and the 96-well plate were put in an incubator (37 °C, 5% CO_2).

Immunostaining procedure

For immunostaining, Caco-2 cells cultured in the channel device and 96-well plates for seven days were fixed with 4% FA/PBS for 20 min, followed by permeabilization with 0.5% Triton X-100/PBS at room temperature for 20 min (Supporting Information File 1, Figure S9ii,iv). Blocking was performed with 1% BSA/PBS at 4 °C overnight (Figure S9vi). The samples were then incubated at room temperature for 3 h in a solu-

tion containing ZO-1 antibody (5 μg/mL), phalloidin (0.1 μM), and Hoechst33342 (2 μg/mL). Between each procedure, PBS was filled to wash the channel or wells (Figure S9i,iii,v,vii).

For immunostaining, the collagen layer coated on the liquid–liquid interface was fixed with 4% FA/PBS for 20 min at room temperature for 20 min (Figure S10v). Blocking was performed with 1% BSA/PBS at 4 °C overnight (Figure S10vii). The samples were then incubated at room temperature for 3 h in a solution containing collagen antibody (5 μg/mL) (Figure S10ix). In the negative control experiment without collagen coating, the procedure was carried out in the same manner, except for the step shown in Figure S10ii.

Image acquisition and quantification

The appearance of the aqueous layer was captured using a smartphone (Google Pixel 9a, Google LLC, CA, USA). Bright-field images of the cells were acquired using an inverted microscope (Leica DMil, Leica Microsystems, Wetzlar, Germany) equipped with a FLEXACAM camera. Fluorescence images were acquired using an all-in-one fluorescence microscope (BZ-X700, Keyence Corporation, Osaka, Japan). The fluorescence images were saved in 14-bit TiFF format, and the images were processed using the ImageJ software (NIH).

Supporting Information

Supporting Information File 1

Additional figures.
[https://www.beilstein-journals.org/bjnano/content/supplementary/2190-4286-17-53-S1.pdf]

Funding

This work was supported by JSPS KAKENHI Grant Number JP23H03865, JP24K03302.

Author Contributions

Satoru Kuriu: conceptualization; data curation; formal analysis; investigation; methodology; validation; visualization; writing – original draft; writing – review & editing. Soo Hyeon Kim: funding acquisition; project administration; supervision; writing – review & editing.

ORCID® iDs

Satoru Kuriu - https://orcid.org/0000-0001-9328-4134

Data Availability Statement

All data that supports the findings of this study is available in the published article and/or the supporting information of this article.

Preprint

A non-peer-reviewed version of this article has been previously published as a preprint: https://doi.org/10.3762/bxiv.2026.10.v1

References

1. Zihni, C.; Mills, C.; Matter, K.; Balda, M. S. *Nat. Rev. Mol. Cell Biol.* **2016,** *17,* 564–580. doi:10.1038/nrm.2016.80
2. Wang, X.; Li, L.; Zhang, G. *RSC Adv.* **2019,** *9,* 34607–34616. doi:10.1039/c9ra06222j
3. Yokoi, F.; Deguchi, S.; Takayama, K. *Regener. Ther.* **2025,** *29,* 541–550. doi:10.1016/j.reth.2025.04.023
4. Xian, C.; Zhang, J.; Zhao, S.; Li, X.-G. *J. Tissue Eng.* **2023,** *14,* 20417314221149882. doi:10.1177/20417314221149882
5. Kim, H. J.; Huh, D.; Hamilton, G.; Ingber, D. E. *Lab Chip* **2012,** *12,* 2165–2174. doi:10.1039/c2lc40074j
6. Valiei, A.; Aminian-Dehkordi, J.; Mofrad, M. R. K. *APL Bioeng.* **2023,** *7,* 011502. doi:10.1063/5.0126541
7. Donkers, J. M.; van der Vaart, J. I.; van de Steeg, E. *Biomimetics* **2023,** *8,* 226. doi:10.3390/biomimetics8020226
8. Jia, X.; Minami, K.; Uto, K.; Chang, A. C.; Hill, J. P.; Ueki, T.; Nakanishi, J.; Ariga, K. *Small* **2019,** *15,* 1804640. doi:10.1002/smll.201804640
9. Ueki, T.; Uto, K.; Yamamoto, S.; Tamate, R.; Kamiyama, Y.; Jia, X.; Noguchi, H.; Minami, K.; Ariga, K.; Wang, H.; Nakanishi, J. *Adv. Mater. (Weinheim, Ger.)* **2024,** *36,* 2310105. doi:10.1002/adma.202310105
10. Sonoi, R.; Kamihira, M. *Sci. Rep.* **2024,** *14,* 12314. doi:10.1038/s41598-024-63115-7
11. Ariga, K. *Small* **2024,** *20,* 2305636. doi:10.1002/smll.202305636
12. Valenzano, M. C.; DiGuilio, K.; Mercado, J.; Teter, M.; To, J.; Ferraro, B.; Mixson, B.; Manley, I.; Baker, V.; Moore, B. A.; Wertheimer, J.; Mullin, J. M. *PLoS One* **2015,** *10,* e0133926. doi:10.1371/journal.pone.0133926
13. Ross, A. M.; Walsh, D. R.; Cahalane, R. M.; Marcar, L.; Mulvihill, J. J. E. *Biochem. Biophys. Rep.* **2021,** *27,* 101096. doi:10.1016/j.bbrep.2021.101096
14. Putt, K. K.; Pei, R.; White, H. M.; Bolling, B. W. *Food Funct.* **2017,** *8,* 406–414. doi:10.1039/c6fo01592a
15. Mazzei, A.; Pagliara, P.; Del Vecchio, G.; Giampetruzzi, L.; Croce, F.; Schiavone, R.; Verri, T.; Barca, A. *Biology (Basel, Switz.)* **2022,** *12,* 36. doi:10.3390/biology12010036
16. Nakajima, T.; Sasaki, K.; Yamamori, A.; Sakurai, K.; Miyata, K.; Watanabe, T.; Matsunaga, Y. T. *Biomater. Sci.* **2020,** *8,* 5615–5627. doi:10.1039/d0bm00763c

License and Terms

This is an open access article licensed under the terms of the Beilstein-Institut Open Access License Agreement (https://www.beilstein-journals.org/bjnano/terms), which is identical to the Creative Commons Attribution 4.0 International License (https://creativecommons.org/licenses/by/4.0). The reuse of material under this license requires that the author(s), source and license are credited. Third-party material in this article could be subject to other licenses (typically indicated in the credit line), and in this case, users are required to obtain permission from the license holder to reuse the material.

The definitive version of this article is the electronic one which can be found at:
https://doi.org/10.3762/bjnano.17.53

BEILSTEIN JOURNAL OF NANOTECHNOLOGY

Cross-scale design of chemosensor arrays: from molecular self-assembly in water to paper-based devices for metal ion detection

Yui Sasaki[1,2] and Tsuyoshi Minami[*3]

Perspective

Open Access

Address:
[1]Research Center for Advanced Science and Technology, The University of Tokyo, 4-6-1, Komaba, Meguro-ku, Tokyo 153-8904, Japan, [2]JST PRESTO, 4-1-8 Honcho, Kawaguchi, Saitama 332-0012, Japan, and [3]Institute of Industrial Science, The University of Tokyo, 4-6-1 Komaba, Meguro-ku, Tokyo 153-8505, Japan

Email:
Tsuyoshi Minami[*] - tminami@g.ecc.u-tokyo.ac.jp

* Corresponding author

Keywords:
chemosensor; metal ion; paper device; pattern recognition; self-assembly

Beilstein J. Nanotechnol. **2026,** *17,* 828–838.
https://doi.org/10.3762/bjnano.17.59

Received: 19 March 2026
Accepted: 22 May 2026
Published: 24 June 2026

This article is part of the thematic issue "Nanotechnology for cross-scale analysis: comprehensive evaluation of water environments".

Associate Editor: S. A. Claridge

© 2026 Sasaki and Minami; licensee Beilstein-Institut.
License and terms: see end of document.

Abstract

Monitoring metal ions in aquatic environments is essential for understanding ecosystem dynamics and assessing water quality. Chemosensors have emerged as powerful analytical tools at the molecular level that transduce ion-recognition events into optical signals. In particular, coordination with metal ions enables cross-reactive sensing, allowing for simultaneous detection of multiple analytes based on pattern recognition. This perspective summarizes advances in self-assembled chemosensor systems for metal ion detection and further developments to solid-state chemosensor array devices based on nanotechnologies. In practical chemosensor designs, dynamic covalent bonds between catechol and phenylboronic acid derivatives have been employed to provide a versatile strategy for the spontaneous preparation of chemosensor elements without extensive synthetic effort. Furthermore, integration of these self-assembled chemosensors into paper substrates enables portable detection platforms for on-site analysis without using stationary laboratory instruments. This cross-scale design strategy provides a promising approach for simultaneous detection of metal ions in various water environments across microscopic and macroscopic scales.

Introduction

Metal ions are essential species in biological systems; however, heavy metal ions act as pollutants and can damage organs and the immune system through the intake of contaminated food [1,2]. Globally, the monitoring of metal ion levels in water environments is significant.

Chemosensors are analytical tools at the molecular level that exhibit optical responses through colorimetric and fluorescence signals [3-5]; they have been widely applied to metal ion detection [6-11]. The detection principle of chemosensors relies on ion and molecular recognition chemistry [3]. Target metal ions

have various sizes and valencies; thus, simultaneous detection of multiple metal ions is desired [1,2]. In this regard, chemosensors provide multivalent interactions toward analytes, which allow the simultaneous detection of metal ions based on pattern recognition [12-16].

Chemosensor design relies on molecular-recognition chemistry, dye chemistry, and photochemistry [3]. Conventional chemosensors based on covalent bond chemistry require organic synthetic approaches in the chemosensor preparations [6-9]. Meanwhile, molecular self-assembly serves as a driving force for easy-to-obtain chemosensors through spontaneous preparation without a synthetic burden [17]. Moreover, the optical properties of chemosensors are tuned during association and dissociation upon analyte detection [18,19]. The performance of chemosensors has been widely evaluated in the solution state using conventional spectroscopic instruments [12-16], whereas the practical implementation of sensing systems remains challenging in on-site analysis [20,21]. Thus, the development of a solid-state chemosensor device is necessary for facile analyte detection.

To implement the cross-scale design concept, chemosensor elements should be highly dispersed on solid support materials possessing nanoarchitectures such as fiber structures. Paper substrates, which are commonly used in daily life, are eco-friendly and highly processable materials for disposable analytical devices [20-25]. In particular, the fiber structures of paper substrates provide unique functional nanoarchitectures [26,27]. Regarding analytical devices, such fiber-like nanostructures contribute to the homogeneous dispersion of chemosensor molecules through office printing technologies [28,29]. The printed chemosensor arrays on a paper substrate exhibit optical changes upon analyte capture, which are detected using portable recording apparatuses (e.g., smartphones, digital cameras, and flatbed scanners) [21,30]. Approaches using paper substrates as solid supports for chemosensor array devices enable on-site analysis without using stationary laboratory facilities.

Previous reviews have discussed chemosensors for metal ions [6-9], approaches for self-assembled chemosensors [17,19,31], chemosensor arrays (nanoparticles [32,33], polymers [34,35], and self-assembled elements [36]), solid-state analytical devices using gels [37,38] and paper substrates [21], and chemometric techniques [39] and their principles [40,41], independently. However, the conceptual connection between molecular-scale recognition events and device-level sensing architectures remains insufficiently explored. In this perspective, we propose a cross-scale design that bridges ion and molecular recognition chemistry with solid-state sensing devices incorporating nanoscale architectures for environmental monitoring of metal ions. This perspective introduces the principles of metal ion detection using chemosensors and the design strategy based on molecular self-assemblies for sensing multiple analytes based on pattern recognition [13,15]. After the discussion of the potential of self-assembled chemosensors and their arrays for simultaneous detection of metal ions in solution states, the concept is expanded to a paper-based chemosensor array device [20]. In this perspective, we introduce the new concept "cross-scale design", defined as an approach connecting molecular sensing in solution states and solid-state sensing, while maintaining or enhancing chemosensor behaviors compared with those in solution (Figure 1). In this context, the concept of cross-scale design refers to the hierarchical integration of

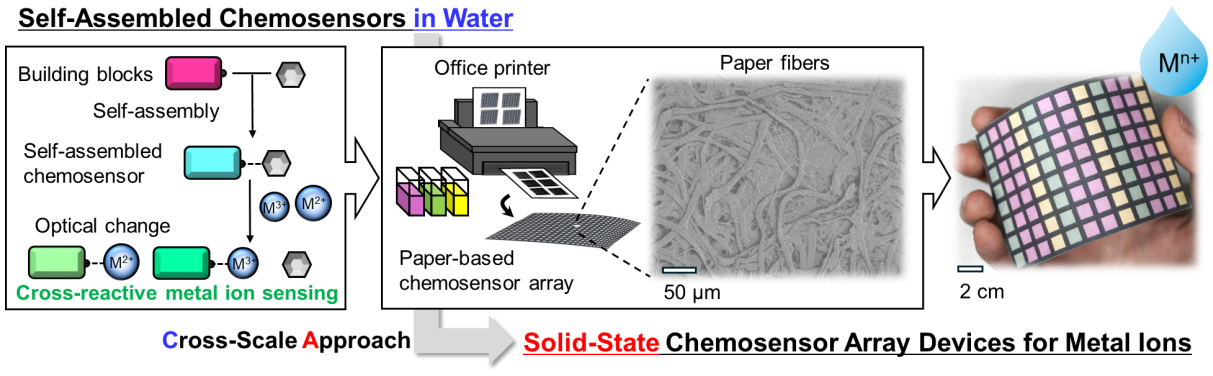


Figure 1: Conceptual figure showing this perspective on simultaneous metal ion detection based on self-assembled chemosensors and their devices through a cross-scale design. The middle panel of Figure 1 was adapted from [28] ("Nanoarchitectonics of highly dispersed polythiophene on paper for accurate quantitative detection of metal ions", © 2024 Y. Sasaki et al., published by the Royal Society of Chemistry, distributed under the terms of the Creative Commons Attribution 3.0 Unported License, https://creativecommons.org/licenses/by/3.0/). The rightmost panel of Figure 1 was adapted from [20] (© 2023 Y. Sasaki et al., distributed under the terms of the Creative Commons Attribution 4.0 International License, https://creativecommons.org/licenses/by/4.0).

sensing processes across multiple levels, from supramolecular chemosensors and pattern-recognition-based sensing to device-level architectures for practical environmental monitoring.

Discussion

Designs and preparation of chemosensors for the simultaneous detection of metal ions

As described in the Introduction, we aim to simultaneously discriminate multiple metal ions based on pattern recognition. In pattern recognition-driven chemical sensors, various response patterns including absorbance, fluorescence intensities, and wavelength changes are used as input data for pattern recognition [36]. To perform accurate analysis, appropriate designs of chemosensors are required. This section focuses on the design strategies based on molecular self-assemblies and the candidates for building blocks for chemosensor elements.

Categorization of chemosensor designs

In the simultaneous detection of multiple metal ions in aqueous media, chemosensors should satisfy the following requirements: They must exhibit different optical properties depending on the types of metal ions and their concentrations to obtain fingerprint-like response patterns, and they must be highly soluble [17]. Typical chemosensor molecules are covalently linked among the binding sites for analytes, optical units (chromophores and fluorophores), and manipulator units, if necessary (Figure 2A) [42]. To construct a chemosensor array, the variation of optical properties is significant, while the modification of chemosensor properties is limited by the synthetic effort required. Molecular self-assembly is a valid approach to spontaneously obtain an ensemble in aqueous media by mixing building blocks and to tune optical properties by changing the combination of building blocks [17,19,31].

One representative self-assembly-driven chemosensing system is an indicator-displacement assay (IDA) [31,43]. In this system, an indicator and a receptor unit spontaneously form a self-assembled chemosensor in aqueous media, accompanied by an optical change. Upon analyte addition, the indicator is released from the chemosensor ensemble, which induces optical recovery (Figure 2B). To further tune the optical properties of indicators, building blocks acting as optical manipulators are an appropriate strategy in self-assembled chemosensing. The chemosensor is formed using optical units (and the target binding site) and optical manipulators [13,15]. In contrast to the typical IDA, the approach using the optical unit serving as the target binding site and the optical manipulator induces distinct optical changes upon analyte capture (Figure 2C). This approach offers the advantage of facile preparation of chemosensors that display a variety of optical patterns, even with a small number of building blocks.

Selection of building blocks of chemosensors for metal ion sensing

The general strategy of metal-ion recognition primarily relies on multivalent coordination between target metal ions and donor atoms (e.g., nitrogen, oxygen, and sulfur) of binding sites [44]. Upon metal ion capture, the chemical information is visualized using optical units and further amplified by optical manipula-

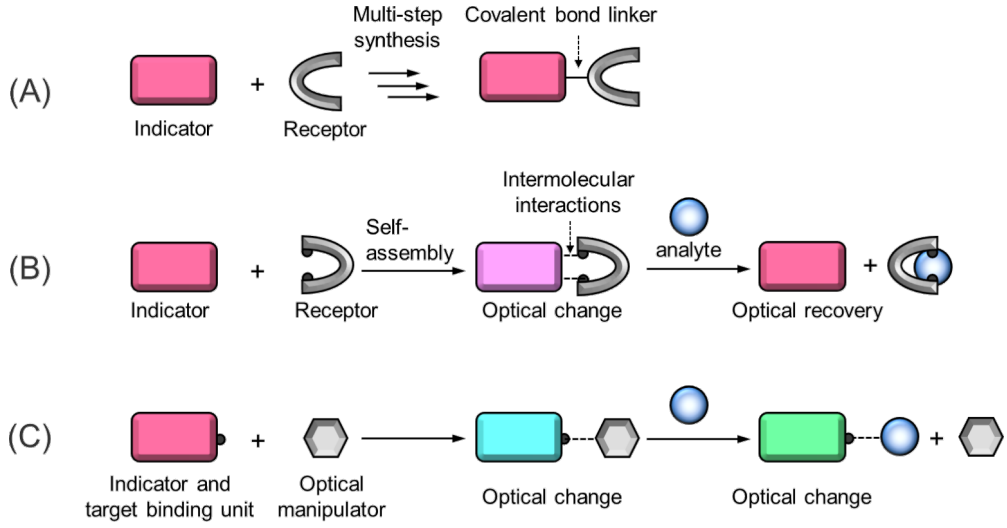


Figure 2: Categorization of chemosensor preparation and detection principles. (A) An indicator–spacer–receptor-based chemosensor based on covalent bond chemistry, (B) an indicator displacement assay for analyte capture based on a competitive reaction among the indicator, the receptor, and the analyte, and (C) a self-assembled chemosensing system based on a competitive reaction among the indicator (and target binding unit), the optical manipulator, and the analyte. Figure 2 was adapted from [17] (© 2023 Y. Sasaki & T. Minami. *ChemNanoMat* published by Wiley-VCH GmbH, distributed under the terms of the Creative Commons Attribution 4.0 International License, https://creativecommons.org/licenses/by/4.0).

tors. To induce recognizable optical responses, molecular dynamics during the association and dissociation of color manipulators are significant [36].

Dynamic covalent bonds are key motifs that contribute to the formation of self-assembled chemosensors and analyte detection [45,46]. Phenylboronic acid derivatives have been widely used as the building blocks for versatile supramolecular architectures [47-49]. The inherent reversibility derived from dynamic covalent bonds endows unique functions to the self-assembled structures. In the field of analytical chemistry, beneficial molecular behavior based on boronate esterification has been applied to reversible and continuous analyte detection [48]. In conventional chemosensor designs, phenylboronic acid derivatives are widely used as receptor units for analytes with cis-diol moieties [47-49]. Also, the favorable binding affinity of phenylboronic acid derivatives enables the formation of ensembles with indicators bearing cis-diol units [50-52].

Catechol derivatives demonstrate favorable metal-ion recognition abilities, owing to the presence of two adjacent hydroxy groups [53]. The optical properties of catechol derivatives correspond to the protonation and deprotonation forms [54]. The coordination with metal ions promotes the deprotonation of catechol derivatives from neutral structures [53]. Herein, we focus on phenylboronic acid as an optical manipulator of catechol derivatives that act as indicators and binding sites for metal ions and discuss the usability of this combination in the simultaneous detection of metal ions.

Dynamic covalent bond-based chemosensors for metal ion detection in solution states

In this chemosensor design, catechol derivatives (i.e., alizarin red S (**1**), bromopyrogallol red (**2**), pyrogallol red (**3**), and pyrocatechol violet (**4**)) and a phenylboronic acid derivative (i.e., 3-nitrophenylboronic acid (**5**)) are employed (Figure 3) [13,20]. These building blocks are assembled through boronate esterification, which induces an optical change. For example, the catechol dye **1** showed blueshifts in the UV–vis absorption spectra with an increase in concentration of **5**, which supported the spontaneous formation of a boronate ester (Figure 4A). The nitrophenyl moiety acting as an electron-withdrawing group of **5** increases the Lewis acidity of boronic acid and facilitates the formation of boronate esters [11]. Meanwhile, the colorimetric ensemble of **1** and **5** exhibited redshifts in the UV–vis absorption spectra in the presence of a target metal ion (Ni^{2+}). The optical changes suggested the coordination between **1** and the metal ion, along with the release of **5**, according to a competitive reaction among **1**, **5**, and the metal ion (Figure 4B). In this sensing approach, the catechol derivative served as the binding site for metal ions, resulting in a unique spectral profile. Consequently, this method induces versatile optical patterns beyond simple signal recovery and, thus, enables simultaneous discrimination of various metal ions even with a small number of chemosensor elements.

Scheme of pattern recognition-driven chemical sensing

The process of simultaneous detection comprises several steps, namely, design and preparation of chemosensors, recording chemosensor responses to analytes, collection and preparation of input data, data processing using chemometric techniques, and visualization of chemical information (Figure 5) [36]. The optical responses of chemosensors and their arrays are acquired using spectrophotometers and portable recording apparatuses. The recorded optical responses as spectral profiles and digital images are summarized into a data matrix, according to the categories of types of chemosensor elements, analytes, and their concentrations. To validate the reproducibility of the sensing performance, replicate measurements are carried out. Therefore, the data matrix contains multidimensional chemical information, which can be processed using chemometric methods to classify and predict chemical information and to visualize the results as two- and three-dimensional outputs [39].

Herein, the assays are categorized into three types, namely, qualitative (i.e., discrimination among analyte types), semiquan-

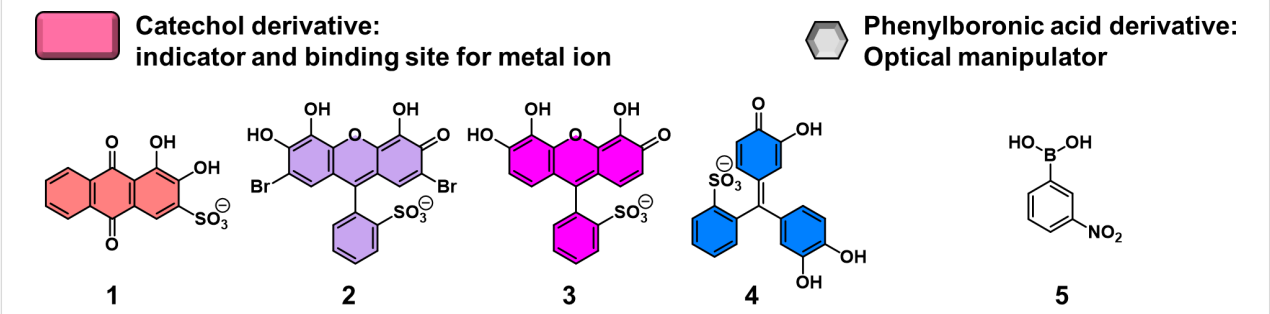


Figure 3: Chemical structures of catechols **1**–**4** and phenylboronic acid derivative **5**.

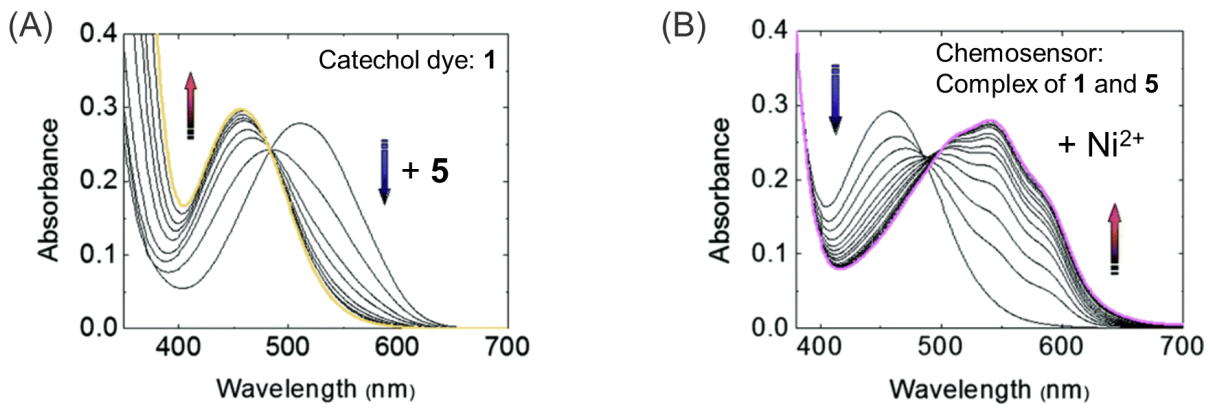


Figure 4: Colorimetric changes of a catechol dye **1** derived from (A) association with **5** through boronate esterification and (B) competitive coordination with Ni^{2+} in the presence of **5** in aqueous media. Figure 4, panels A and B were used with permission of The Royal Society of Chemistry, from [13] ("A molecular self-assembled colorimetric chemosensor array for simultaneous detection of metal ions in water" by Y. Sasaki et al., *Chem. Commun.*, Vol. 53, Issue 49, © 2017). This content is not subject to CC BY 4.0.

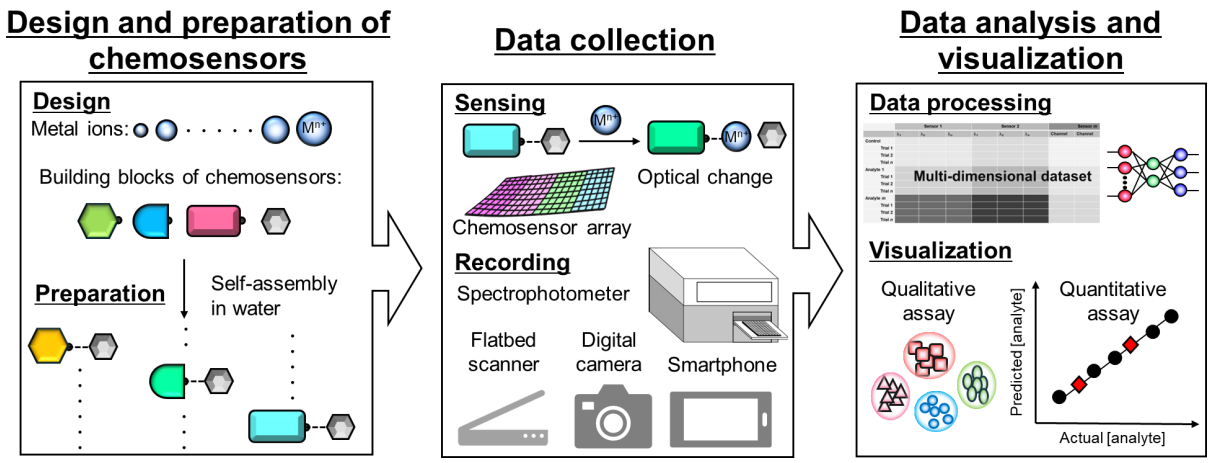


Figure 5: Conceptual scheme for pattern recognition-driven chemical sensing.

titative (i.e., discrimination among analyte types and concentration levels), and quantitative detection (i.e., prediction of unknown analytes and their concentrations in real samples) [36]. Next, data processing is performed using supervised and unsupervised methods, depending on the purpose of the analysis. Unsupervised methods include principal component analysis (PCA) and hierarchical clustering analysis (HCA), while supervised methods include linear discriminant analysis (LDA), support vector machine (SVM), and artificial neural network (ANN). The details of each method have already been summarized in previous reviews [39]. In this perspective, simultaneous detection using LDA and SVM is introduced as an example [39]. LDA reduces the dimensionality of the input data and classifies each component based on its differences [39]. In the following sections, LDA is introduced for qualitative discrimination, whereas SVM is used for quantitative assays [55]. Thus, the analytical method can be used for quantitative assays in complicated media, such as mixtures of analytes and real samples in the presence of interfering species.

Colorimetric chemosensor arrays for qualitative detection of eleven metal ions

To explore the potential of colorimetric self-assembled chemosensors, the three catechol dyes **1**–**3** and the color manipulator **5** were selected as components of an array for the simultaneous discrimination of eleven types of metal ions (i.e., Pb^{2+}, Cu^{2+}, Zn^{2+}, Ni^{2+}, Cd^{2+}, Co^{2+}, Fe^{2+}, Hg^{2+}, Al^{3+}, Ga^{3+}, and Ca^{2+}) [13]. As described in Figure 6A, the various colorimetric patterns were obtained on an array, according to the combination of the colorimetric ensembles and target metal ions. Importantly, the magnitude of the color changes of the catechol dyes in response to the metal ions was significant in the presence of

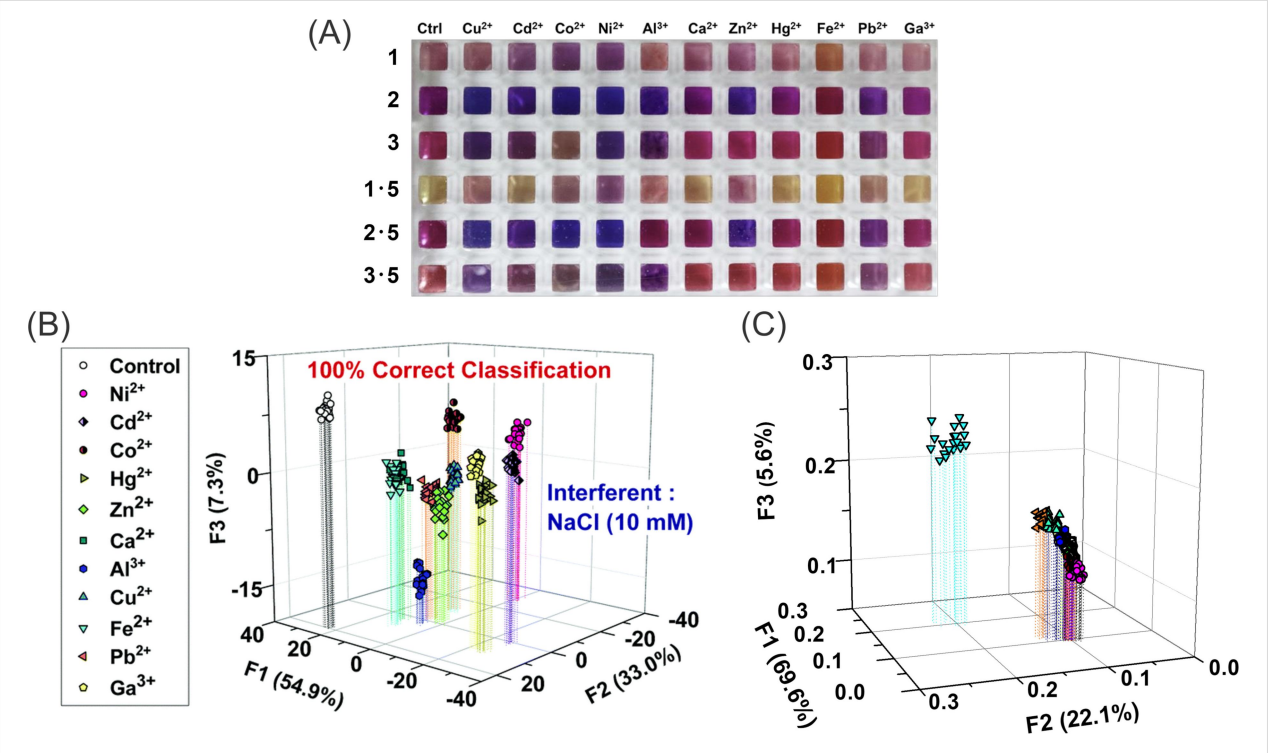


Figure 6: (A) Colorimetric patterns of a stand-alone dye array and the self-assembled chemosensor array in the presence or absence of metal ions. LDA canonical score plots for the qualitative assay of eleven metal ions using (B) the self-assembled chemosensor array and (C) the stand-alone dye array in aqueous media. Figure 6, panels A and B were used with permission of The Royal Society of Chemistry, from [13] ("A molecular self-assembled colorimetric chemosensor array for simultaneous detection of metal ions in water" by Y. Sasaki et al., *Chem. Commun.*, Vol. 53, Issue 49, © 2017). This content is not subject to CC BY 4.0. Figure 6, panel (C) was reproduced with permission from [56]. © 2018 Institute of Industrial Science, The University of Tokyo. This content is not subject to CC BY 4.0.

5, unlike without the color manipulator (i.e., stand-alone dye array). Indeed, the qualitative detection with 100% correct classification was achieved for eleven types of metal ions, even with excess amounts of sodium chloride (NaCl) (Figure 6B). In this assay, the input data for LDA were constructed using UV–vis absorption spectra of chemosensors upon analyte addition. The dimensionality of the input data depends on the number of chemosensors, analytes, and replicate measurements, which is decreased using LDA. Each axis (i.e., factor, F) corresponds to the contribution derived from the multidimensional colorimetric response dataset [39]. The stand-alone dye array did not show accurate discrimination of the same metal ions (Figure 6C) [56]. Overall, the spontaneous preparation approaches using the catechol and the phenylboronic acid derivatives suggested the feasibility of simultaneous detection of metal ions in solution states, based on cross-reactivity and reversibility of self-assembled chemosensors.

Solid-state chemosensor array device toward on-site metal ion detection

Based on the concept described above, a paper-based chemosensor array device was fabricated by printing self-assembled chemosensor elements onto paper substrates. To demonstrate the concept of cross-scale design, this section introduces a paper-based chemosensor array device embedded with the colorimetric ensembles that have already been evaluated in solution states. Herein, the key aspect of this concept is the retention of sensing performance of the self-assembled chemosensors even on the paper substrates.

Design and fabrication of the paper-based chemosensor array device

The uniformity of the sensing layer significantly affects the reproducibility and accuracy of analyte detection. Therefore, a printed pattern with 96 microwells was designed to avoid coffee ring effects [57]. Device designs (well design and area length and width), printing conditions and process (printing cycles of chemosensor inks), and sensing process (analyte solution volume) were optimized using a central composite design [58].

The selection of appropriate paper substrates also plays a significant role in reproducible sensing [59]. The mechanical properties of paper substrates depend on their thickness, pore size, and liquid absorbability [21]. In particular, the thickness of the substrates influences the magnitude of optical changes [60]. In addition, the fiber structures of paper substrates effec-

tively contribute to the high dispersion of chemosensor elements [28].

The fabrication process in Figure 7A begins with patterning a hydrophobic layer using an office wax printer. The printed wax layer melts on a hot plate during annealing. Next, an inkjet printer is employed to deposit chemosensor solutions onto predefined regions of the paper substrate. The fiber structures of paper substrates contribute to highly dispersed chemosensor elements, resulting in uniform solid-state sensing layers (Figure 7B). Upon exposure to metal ions in aqueous solutions, the immobilized chemosensors interact with the analytes and induce optical changes on the paper substrate. These optical patterns are rapidly recorded using portable devices. Subsequently, the captured digital photographs are processed using imaging analysis to extract color information (e.g., RGB values) and further analyzed using pattern-recognition methods. Indeed, each chemosensor on the paper device showed different colorimetric responses to metal ions, indicating the fingerprint-like patterns containing multidimensional optical information.

Solid-state simultaneous detection of metal ions

Next, the 96-well microtiter paper-based chemosensor array device embedded with four types of colorimetric ensembles using building blocks **1**–**5** was employed for the qualitative discrimination of nine types of metal ions. Although the same sensor molecules were applied, the sensing environments are significantly different in solution and in the solid state. Therefore, in contrast to solution-based chemosensors, an additional ensemble made of **4** and **5** was included in the chemosensor library as an array component to increase optical response patterns. The obtained colorimetric changes on the device were rapidly recorded using a flatbed scanner [20]. The fabricated device demonstrated 100% correct classification of nine types of metal ions (Figure 8B). From the sensitivity aspect, the detectable ranges of the paper-based device were comparable to those of the solution-based chemosensor array. The concept can also be extended to polymer-based chemosensor elements. In a previous study, a polythiophene derivative immobilized chemosensor array on a paper substrate achieved highly sensitive detection of metal ions at tens of parts per billion levels, which was comparable to the detection range of an analytical method based on a stationary spectrophotometer [28].

Applicability of the paper-based chemosensor array to real-sample analysis

Herein, the usability of the paper-based chemosensor array device in real-sample analysis is introduced [20]. To realize the concept of cross-scale design, the sensor performance of chemosensor elements in solution states should be maintained or improved on the paper substrates. In environmental assessment, metal ion levels in river water indicate the state of ecological systems [1,2]. The colorimetric responses in the presence of interferents show non-linearity. Therefore, a powerful machine-learning method, SVM, was employed to build a linear calibration line from datasets constructed by color channels. Spike-and-recovery tests toward Zn^{2+} and Cu^{2+} demonstrated reliable analytical performance with recovery rates of 89–125%, even without sample purification (Figure 8C,D). To compare the sensing performance of the paper-based analytical device, recent paper-based colorimetric sensor devices for metal ion detection are summarized in Table 1. As shown, many paper-based analytical devices enable real-sample analysis with simple operation and minimal sample pretreatment. Indeed, the

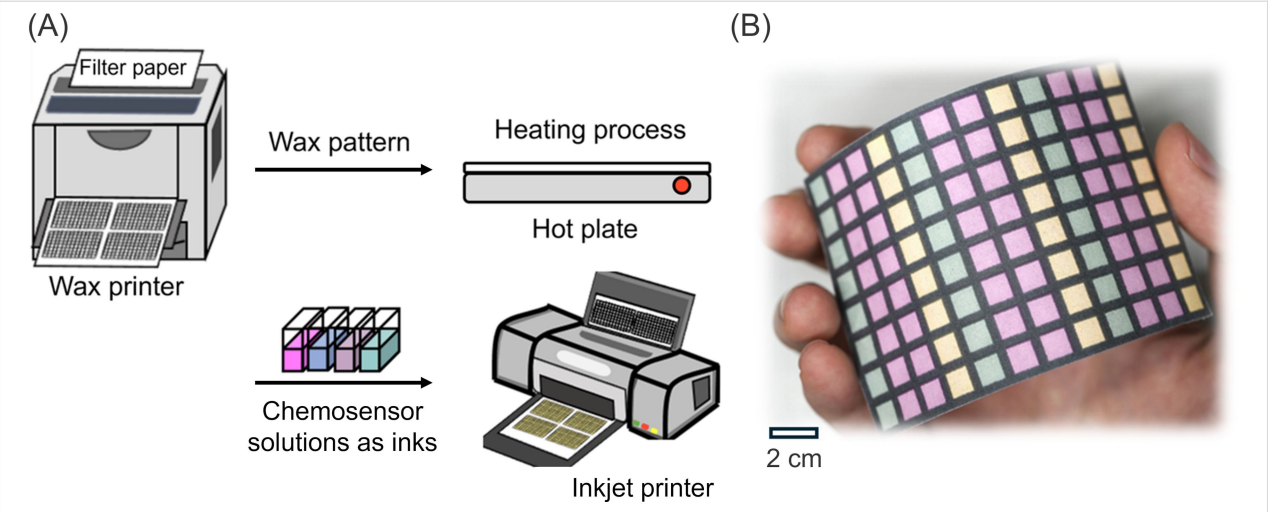


Figure 7: (A) Schematic of device fabrication using office printers and apparatus. (B) Photograph of the 96-well microtiter paper-based chemosensor array device. Figure 7 was adapted from [20] (© 2023 Y. Sasaki et al., distributed under the terms of the Creative Commons Attribution 4.0 International License, https://creativecommons.org/licenses/by/4.0).

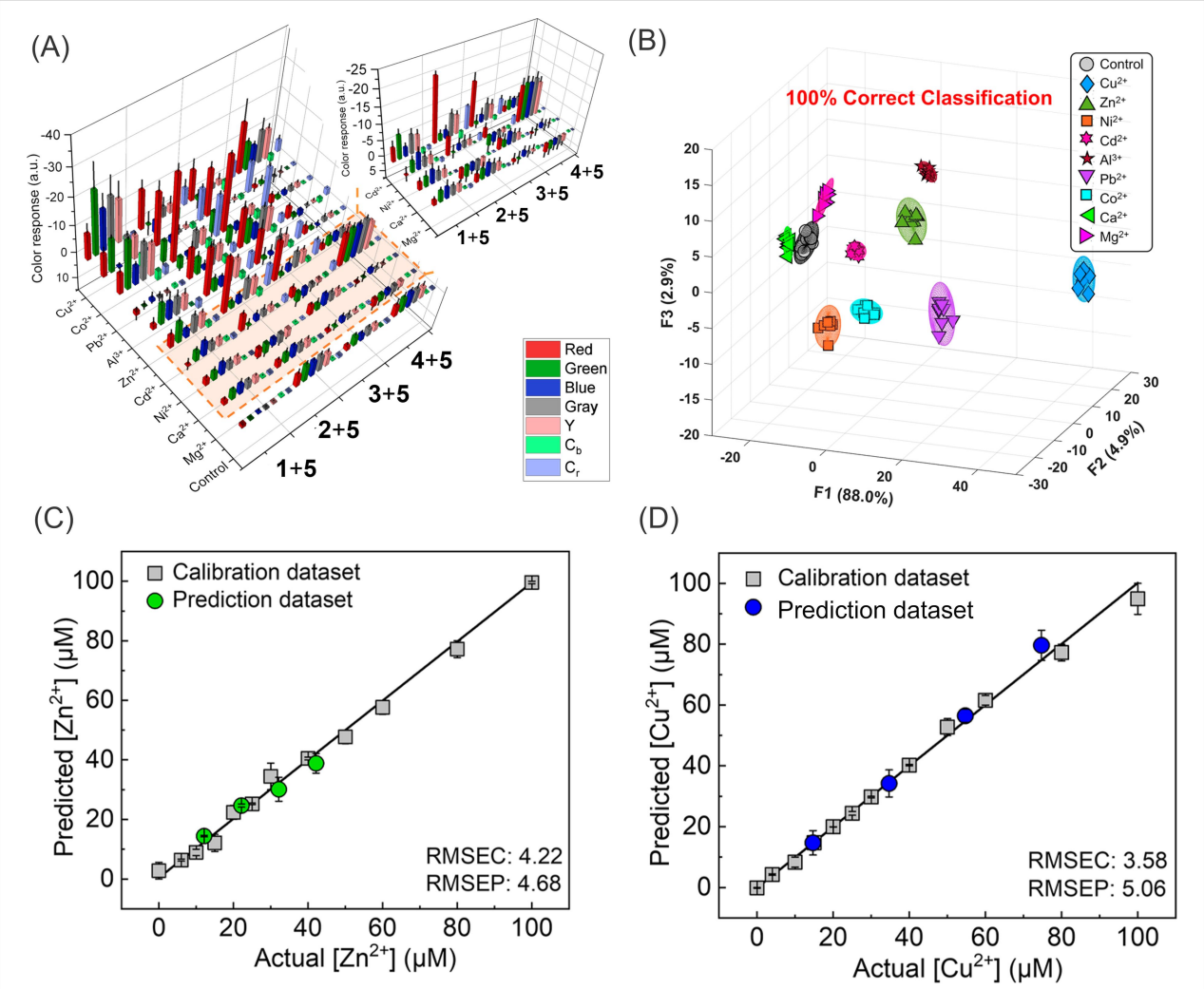


Figure 8: (A) Color response profile of the paper-based chemosensor array device upon adding target metal ions. (B) LDA canonical score plot for the qualitative assay of nine types of metal ions using the paper-based chemosensor array device. Results of the SVM regression for (C) Zn^{2+} and (D) Cu^{2+} in a river water sample. The values of the root-mean-square errors of calibration (RMSEC) and prediction (RMSEP) suggest the accuracy of the established model and prediction results. Figure 8, panels A–D were reproduced from [20] (© 2023 Y. Sasaki et al., distributed under the terms of the Creative Commons Attribution 4.0 International License, https://creativecommons.org/licenses/by/4.0).

sensor performance from the viewpoint of usability and applicability is beyond that of solution-based chemosensors in metal ion sensing.

Conclusion

In this perspective, we described the concept of cross-scale design for metal ion detection by integrating self-assembled chemosensors with solid-state analytical devices. Self-assembled chemosensor systems based on dynamic covalent bonds between catechol and phenylboronic acid derivatives provide a versatile platform for the spontaneous preparation of chemosensor elements without extensive synthetic effort. The reversible formation of boronate esters enables cross-reactive sensing behavior, providing fingerprint-like response patterns for various metal ions and their concentrations. By applying chemometric methods, multidimensional chemical information can be visualized qualitatively and quantitatively.

To address the challenges of metal ion analysis outside laboratories, paper-based platforms are attractive owing to their compatibility with office-printing technologies and portable imaging tools. Importantly, the paper-based chemosensor array device demonstrated reliable analytical performance in river water samples without the need for stationary analytical instruments or sample preparation.

The combination of molecular self-assembly, pattern-recognition sensing, and printable analytical devices provides a promising strategy for bridging molecular sensing systems in solution and solid-state analytical devices toward practical metal ion

Table 1: Comparison of representative paper-based colorimetric sensing devices for metal-ion detection.

Probe/device	Medium	LOD (μM)[a]	Key metrics	Ref.
plug-and-play μPAD with colorimetric reagents (bathophenanthroline, dimethylglyoxime, and bathocuproine)	river water	Fe^{2+} 1.79, Ni^{2+} 5.11, Cu^{2+} 3.15	recovery rate (76–121%) agrees with AAS	[61]
inkjet-printed paper optode	drinking and environmental water	Pb^{2+} N.R.[b]; dynamic range 1–10	quick sensor response (<5 min)	[62]
mesoporous silica nanosphere-coated paper chemosensor	water	Cd^{2+} 0.22, Co^{2+} 0.28, Ni^{2+} 0.44, Fe^{3+} 0.54	reusability (for five cycles) after chelate treatment	[63]
silica nanoparticle-modified rhodamine B paper strip	drinking water	Cu^{2+} 11.0	sensor performance validated by ICP-OES	[64]
imidazole–dithiocarbamate derivative-coated tissue-paper strip	water samples	Cu^{2+} 0.0151, Hg^{2+} 1.17	different optical properties depending on the target metal ions	[65]
chemosensor array device functionalized with ensembles of catechol dyes and a phenylboronic acid derivative	river water	Cu^{2+} 2.36, Zn^{2+} 2.60, Ni^{2+} 4.77	qualitative and quantitative assays in metal-ion mixtures; recovery rate: 89–125% for Zn^{2+} and Cu^{2+} in river water	[20]
capillary-flow microfluidic paper device functionalized with colorimetric reagents (dimethylglyoxime, bathocuproine, and bathophenanthroline)	water	Ni^{2+} 34.1, Cu^{2+} 4.72, Fe^{3+} 19.7	recovery rates of 80–110% for >90% of collected samples	[66]
sodium rhodizonate-attached paper device	drinking, tap, and Ilam platform water samples	Ba^{2+} 26.5, Sr^{2+} 54.2	smartphone-assisted assay applying a masking strategy	[67]
bi-ligand cobalt-MOF nanozyme with 3,3′,5,5′-tetramethylbenzidine/H_2O_2 chromogenic system	environmental water	Cu^{2+} 0.130	smartphone-assisted sensor for on-site analysis	[68]
paper device immobilized with eriochrome black T (EBT) and bromothymol blue (BTB)	aqueous medium	Pb^{2+} (BTB) 29.0, Pb^{2+} (EBT) 86.9	high selectivity against other ions; thermal stability at 25–90 °C	[69]
dithizone colorimetric reagent immobilized on paper using a polyvinyl chloride matrix plasticized with dibutyl phthalate	water	Pb^{2+} 6.08, Cd^{2+} 0.890	rapid detection (150 s for Pb^{2+} and 60 s for Cd^{2+})	[70]
naphthylamine–quinolinol azo chemosensor-attached test strip	water and food samples[c]	Cd^{2+} 0.0262	reusability for six cycles with a chelate agent	[71]
dual-sided capillary microfluidic paper device immobilized with colorimetric reagents (dimethylglyoxime, bathocuproine, and bathophenanthroline)	river, tap, pond, drinking water	Ni^{2+} 22.1, Fe^{3+} 5.37, Cu^{2+} 3.15	recovery rate: 86–112%; stable for >4 weeks	[72]
paper strips using chromogens (cuprizone, 1,5-diphenylcarbazide, zincon monosodium salt, and 1-(2-pyridylazo)-2-naphthol)	environmental water	Cu^{2+} 4.72, Cr(VI) 5.00, Zn^{2+} 11.0, Mn^{2+} 5.10	comparable sensing performance with AAS	[73]

[a]LOD values were converted to "μM" for direct comparison. Reported ppm values were treated as "mg·L^{-1}" for dilute aqueous samples. Atomic weights used for conversion were Fe 55.845, Co 58.933, Ni 58.693, Cu 63.546, Zn 65.38, Cd 112.414, Ba 137.327, Sr 87.62, Cr 51.996, Mn 54.938, Hg 200.59, and Pb 207.2 g·mol^{-1}. For Cr(VI), conversion was based on the atomic weight of Cr. [b]N.R.: not reported; the corresponding study reported a dynamic range rather than an explicit LOD. [c]Food samples included potato, mushroom, apple, carrot, corn, barley, cashew, and sunflower seeds.

assessment. We believe that such cross-scale design approaches will contribute to on-site detection of chemical species in water environments across microscopic to macroscopic scales. More broadly, the cross-scale design strategy presented here may provide a general framework for bridging molecular recognition systems into practical sensing technologies that operate across molecular, nanoscale, and device levels.

Funding

Y. S. gratefully acknowledges the financial support from the Japan Society for the Promotion of Science (JSPS) KAKENHI (Grant No. JP24K17667) and JST PRESTO (Grant No. JPMJPR23H2). T. M. thanks JSPS KAKENHI (Grant Nos. JP23H03864, JP24K01315, JP25K22200, and JP25K24718).

Author Contributions

Yui Sasaki: funding acquisition; writing – original draft. Tsuyoshi Minami: conceptualization; funding acquisition; project administration; supervision; writing – review & editing.

ORCID® iDs

Yui Sasaki - https://orcid.org/0000-0003-4185-569X
Tsuyoshi Minami - https://orcid.org/0000-0001-8331-378X

Data Availability Statement

Data sharing is not applicable as no new data was generated or analyzed in this study.

References

1. Aragay, G.; Pons, J.; Merkoçi, A. *Chem. Rev.* **2011,** *111,* 3433–3458. doi:10.1021/cr100383r
2. Malik, L. A.; Bashir, A.; Qureashi, A.; Pandith, A. H. *Environ. Chem. Lett.* **2019,** *17,* 1495–1521. doi:10.1007/s10311-019-00891-z
3. Wang, B.; Anslyn, E. V., Eds. *Chemosensors: Principles, Strategies, and Applications;* Wiley, 2011. doi:10.1002/9781118019580
4. Wang, Y.-Y.; Kong, Y.; Zheng, Z.; Geng, W.-C.; Zhao, Z.-Y.; Sun, H.; Guo, D.-S. *Beilstein J. Org. Chem.* **2019,** *15,* 1394–1406. doi:10.3762/bjoc.15.139
5. Gharibzahedi, S. M. T.; Altintas, Z. *Beilstein J. Nanotechnol.* **2025,** *16,* 2207–2244. doi:10.3762/bjnano.16.153
6. Prodi, L.; Bolletta, F.; Montalti, M.; Zaccheroni, N. *Coord. Chem. Rev.* **2000,** *205,* 59–83. doi:10.1016/s0010-8545(00)00242-3
7. Patil, A.; Salunke-Gawali, S. *Inorg. Chim. Acta* **2018,** *482,* 99–112. doi:10.1016/j.ica.2018.05.026
8. Ghosh, P.; Roy, P. *Chem. Commun.* **2023,** *59,* 5174–5200. doi:10.1039/d3cc00651d
9. Zhang, H.; Song, J.; Wang, S.; Song, Q.; Guo, H.; Li, Z. *Dyes Pigm.* **2023,** *216,* 111380. doi:10.1016/j.dyepig.2023.111380
10. Pal, R.; Das, R.; Pal, A.; Kapoor, B. S.; Kundu, K.; Thakur, A.; Mukhopadhyay, S. S.; Banerjee, P. *Microchem. J.* **2024,** *207,* 111739. doi:10.1016/j.microc.2024.111739
11. Chattopadhyay, M. K.; Mondal, A.; Hazra, A.; Tarai, S. K.; Kapoor, B. S.; Mukhopadhyay, S. S.; Sarkar, S.; Banerjee, P. *Sens. Actuators Rep.* **2024,** *8,* 100215. doi:10.1016/j.snr.2024.100215
12. Palacios, M. A.; Wang, Z.; Montes, V. A.; Zyryanov, G. V.; Anzenbacher, P., Jr. *J. Am. Chem. Soc.* **2008,** *130,* 10307–10314. doi:10.1021/ja802377k
13. Sasaki, Y.; Minamiki, T.; Tokito, S.; Minami, T. *Chem. Commun.* **2017,** *53,* 6561–6564. doi:10.1039/c7cc03218h
14. Ihde, M. H.; Tropp, J.; Diaz, M.; Shiller, A. M.; Azoulay, J. D.; Bonizzoni, M. *Adv. Funct. Mater.* **2022,** *32,* 2112634. doi:10.1002/adfm.202112634
15. Sasaki, Y.; Ohshiro, K.; Zhou, Q.; Lyu, X.; Tang, W.; Okabe, K.; Takizawa, S.-y.; Minami, T. *Chem. Commun.* **2023,** *59,* 7747–7750. doi:10.1039/d3cc00949a
16. Yang, R.-P.; Huang, S.-Z.; Wei, K.-N.; Tang, Q.; Tao, Z.; Huang, Y.; Zhao, A.-T. *Dalton Trans.* **2023,** *52,* 7279–7289. doi:10.1039/d3dt00995e
17. Sasaki, Y.; Minami, T. *ChemNanoMat* **2024,** *10,* e202300335. doi:10.1002/cnma.202300335
18. Praveen, V. K.; Vedhanarayanan, B.; Mal, A.; Mishra, R. K.; Ajayaghosh, A. *Acc. Chem. Res.* **2020,** *53,* 496–507. doi:10.1021/acs.accounts.9b00580
19. Wu, J.; Kwon, B.; Liu, W.; Anslyn, E. V.; Wang, P.; Kim, J. S. *Chem. Rev.* **2015,** *115,* 7893–7943. doi:10.1021/cr500553d
20. Sasaki, Y.; Lyu, X.; Minami, T. *Front. Chem. (Lausanne, Switz.)* **2023,** *11,* 1134752. doi:10.3389/fchem.2023.1134752
21. Mohan, B.; Sasaki, Y.; Minami, T. *Anal. Chim. Acta* **2024,** *1313,* 342741. doi:10.1016/j.aca.2024.342741
22. Wang, S.; Chen, W.-J.; Du, A.; Kou, Y.; Xu, X.; Hu, D.; Lu, Z. *Adv. Compos. Hybrid Mater.* **2025,** *8,* 260. doi:10.1007/s42114-025-01333-x
23. Zhang, Q.; Yan, J.; Ma, X.; Zhao, L.; Song, P.; Xia, L. *J. Hazard. Mater.* **2024,** *480,* 136195. doi:10.1016/j.jhazmat.2024.136195
24. Devadhasan, J. P.; Kim, J. *Sens. Actuators, B* **2018,** *273,* 18–24. doi:10.1016/j.snb.2018.06.005
25. Datta, S.; Dey, S.; Sinha, C.; Dutta, B.; Banerjee, P.; Mir, M. H. *Dalton Trans.* **2024,** *53,* 2859–2866. doi:10.1039/d3dt03939k
26. Alahmad, W.; Cetinkaya, A.; Kaya, S. I.; Varanusupakul, P.; Ozkan, S. A. *Trends Environ. Anal. Chem.* **2023,** *40,* e00220. doi:10.1016/j.teac.2023.e00220
27. Díaz-Liñán, M. C.; García-Valverde, M. T.; Lucena, R.; Cárdenas, S.; López-Lorente, A. I. *Anal. Methods* **2020,** *12,* 3074–3091. doi:10.1039/d0ay00702a
28. Sasaki, Y.; Lyu, X.; Kawashima, T.; Zhang, Y.; Ohshiro, K.; Okabe, K.; Tsuchiya, K.; Minami, T. *RSC Adv.* **2024,** *14,* 5159–5166. doi:10.1039/d3ra08429a
29. Yamada, K.; Shibata, H.; Suzuki, K.; Citterio, D. *Lab Chip* **2017,** *17,* 1206–1249. doi:10.1039/c6lc01577h
30. Geng, Z.; Miao, Y.; Zhang, G.; Liang, X. *Sens. Actuators, A* **2023,** *349,* 114056. doi:10.1016/j.sna.2022.114056
31. Sedgwick, A. C.; Brewster, J. T.; Wu, T.; Feng, X.; Bull, S. D.; Qian, X.; Sessler, J. L.; James, T. D.; Anslyn, E. V.; Sun, X. *Chem. Soc. Rev.* **2021,** *50,* 9–38. doi:10.1039/c9cs00538b
32. Geng, Y.; Peveler, W. J.; Rotello, V. M. *Angew. Chem., Int. Ed.* **2019,** *58,* 5190–5200. doi:10.1002/anie.201809607
33. Lu, X.; Suslick, K. S.; Li, Z. *Analysis Sensing* **2023,** *3,* e202200050. doi:10.1002/anse.202200050
34. Shimizu, K. D.; Stephenson, C. J. *Curr. Opin. Chem. Biol.* **2010,** *14,* 743–750. doi:10.1016/j.cbpa.2010.07.007
35. Ke, Y.; Sun, Y.; Liao, A.; Zhao, F.; Tan, Y.; Tan, C. *ACS Appl. Mater. Interfaces* **2025,** *17,* 16396–16409. doi:10.1021/acsami.4c22848
36. Sasaki, Y.; Kubota, R.; Minami, T. *Coord. Chem. Rev.* **2021,** *429,* 213607. doi:10.1016/j.ccr.2020.213607
37. Anzenbacher, P., Jr.; Liu, Y.-l.; Kozelkova, M. E. *Curr. Opin. Chem. Biol.* **2010,** *14,* 693–704. doi:10.1016/j.cbpa.2010.08.011
38. Ikeda, M.; Ochi, R.; Hamachi, I. *Lab Chip* **2010,** *10,* 3325–3334. doi:10.1039/c004908e
39. Anzenbacher, P., Jr.; Lubal, P.; Buček, P.; Palacios, M. A.; Kozelkova, M. E. *Chem. Soc. Rev.* **2010,** *39,* 3954–3979. doi:10.1039/b926220m
40. Albert, K. J.; Lewis, N. S.; Schauer, C. L.; Sotzing, G. A.; Stitzel, S. E.; Vaid, T. P.; Walt, D. R. *Chem. Rev.* **2000,** *100,* 2595–2626. doi:10.1021/cr980102w
41. Li, Z.; Askim, J. R.; Suslick, K. S. *Chem. Rev.* **2019,** *119,* 231–292. doi:10.1021/acs.chemrev.8b00226
42. Guo, C.; Sedgwick, A. C.; Hirao, T.; Sessler, J. L. *Coord. Chem. Rev.* **2021,** *427,* 213560. doi:10.1016/j.ccr.2020.213560

43. Nguyen, B. T.; Anslyn, E. V. *Coord. Chem. Rev.* **2006,** *250,* 3118–3127. doi:10.1016/j.ccr.2006.04.009
44. Hay, B. P.; Hancock, R. D. *Coord. Chem. Rev.* **2001,** *212,* 61–78. doi:10.1016/s0010-8545(00)00366-0
45. Sasaki, Y.; Kojima, S.; Hamedpour, V.; Kubota, R.; Takizawa, S.-y.; Yoshikawa, I.; Houjou, H.; Kubo, Y.; Minami, T. *Chem. Sci.* **2020,** *11,* 3790–3796. doi:10.1039/d0sc00194e
46. You, L. *Chem. Commun.* **2023,** *59,* 12943–12958. doi:10.1039/d3cc04022d
47. Nishiyabu, R.; Kubo, Y.; James, T. D.; Fossey, J. S. *Chem. Commun.* **2011,** *47,* 1124–1150. doi:10.1039/c0cc02921a
48. Bian, Z.; Liu, A.; Li, Y.; Fang, G.; Yao, Q.; Zhang, G.; Wu, Z. *Analyst* **2020,** *145,* 719–744. doi:10.1039/c9an00741e
49. António, J. P. M.; Roque, I. L.; Santos, F. M. F.; Gois, P. M. P. *Acc. Chem. Res.* **2025,** *58,* 673–687. doi:10.1021/acs.accounts.4c00691
50. Springsteen, G.; Wang, B. *Chem. Commun.* **2001,** 1608–1609. doi:10.1039/b104895n
51. Kubo, Y.; Ishida, T.; Kobayashi, A.; James, T. D. *J. Mater. Chem.* **2005,** *15,* 2889–2895. doi:10.1039/b501243k
52. Tomsho, J. W.; Benkovic, S. J. *J. Org. Chem.* **2012,** *77,* 2098–2106. doi:10.1021/jo202250d
53. Zhang, L.; Dong, S.; Zhu, L. *Chem. Commun.* **2007,** 1891–1893. doi:10.1039/b618413h
54. Carta, L.; Biczysko, M.; Bloino, J.; Licari, D.; Barone, V. *Phys. Chem. Chem. Phys.* **2014,** *16,* 2897–2911. doi:10.1039/c3cp50499a
55. Minami, T.; Esipenko, N. A.; Zhang, B.; Kozelkova, M. E.; Isaacs, L.; Nishiyabu, R.; Kubo, Y.; Anzenbacher, P., Jr. *J. Am. Chem. Soc.* **2012,** *134,* 20021–20024. doi:10.1021/ja3102192
56. Sasaki, Y.; Minami, T. *Seisan Kenkyu* **2018,** *70,* 193–196. doi:10.11188/seisankenkyu.70.193
57. Lyu, X.; Hamedpour, V.; Sasaki, Y.; Zhang, Z.; Minami, T. *Anal. Chem. (Washington, DC, U. S.)* **2021,** *93,* 1179–1184. doi:10.1021/acs.analchem.0c04291
58. Hamedpour, V.; Oliveri, P.; Malegori, C.; Minami, T. *Sens. Actuators, B* **2020,** *322,* 128571. doi:10.1016/j.snb.2020.128571
59. Xu, Y.; Bonizzoni, M. *Analyst* **2020,** *145,* 3505–3516. doi:10.1039/d0an00137f
60. Pratiwi, R.; Septyani, R. N.; Febriany, R.; Saputri, F. A.; Nuwarda, R. F. *Int. J. Anal. Chem.* **2019,** *2019,* 4682839. doi:10.1155/2019/4682839
61. Silva-Neto, H. A.; Cardoso, T. M. G.; McMahon, C. J.; Sgobbi, L. F.; Henry, C. S.; Coltro, W. K. T. *Analyst* **2021,** *146,* 3463–3473. doi:10.1039/d1an00176k
62. Cui, Y.; Wang, R.; Brady, B.; Wang, X. *Anal. Bioanal. Chem.* **2022,** *414,* 7585–7595. doi:10.1007/s00216-022-04286-y
63. El-Sewify, I. M.; Radwan, A.; Azzazy, H. M. E.-S. *RSC Adv.* **2023,** *13,* 6433–6441. doi:10.1039/d3ra00369h
64. Sannok, T.; Wechakorn, K.; Jantra, J.; Kaewchoay, N.; Teepoo, S. *Anal. Bioanal. Chem.* **2023,** *415,* 4703–4712. doi:10.1007/s00216-023-04754-z
65. Thangaraj, B.; Ponram, M.; Ranganathan, S.; Sambath, B.; Cingaram, R.; Iyer, S. K.; Natesan Sundaramurthy, K. *RSC Adv.* **2023,** *13,* 26023–26030. doi:10.1039/d3ra03764a
66. Aryal, P.; Brack, E.; Alexander, T.; Henry, C. S. *Anal. Chem. (Washington, DC, U. S.)* **2023,** *95,* 5820–5827. doi:10.1021/acs.analchem.3c00378
67. Ezoji, H.; Neshati, J.; Esmaeili, N. *J. Iran. Chem. Soc.* **2024,** *21,* 2713–2723. doi:10.1007/s13738-024-03103-w
68. Amalraj, A.; Ayyanu, R.; Pavadai, R.; Govindaraj, T. S.; Aham, E. C.; Li, X.; Deng, Y.; Zhang, Z. *J. Environ. Chem. Eng.* **2024,** *12,* 113522. doi:10.1016/j.jece.2024.113522
69. Poovadichalil, N. M.; Ullah, A.; Maurya, M. R.; Hasan, A.; Sadasivuni, K. K. *Int. J. Environ. Sci. Technol.* **2025,** *22,* 15467–15478. doi:10.1007/s13762-025-06636-6
70. Solhtalab, M.; Majdinasab, M.; Zarei, S.; Majdinasab, E. *J. Hazard. Mater. Adv.* **2025,** *19,* 100867. doi:10.1016/j.hazadv.2025.100867
71. Mousavi, S. H.; Mohammadi, A.; Zanjanchi, M. A.; Fallah Moafi, H. *Anal. Methods* **2025,** *17,* 9365–9380. doi:10.1039/d5ay01326g
72. Punnoy, P.; Aryal, P.; Hefner, C. E.; Brack, E.; Rodthongkum, N.; Potiyaraj, P.; Henry, C. S. *Anal. Chim. Acta* **2025,** *1356,* 344031. doi:10.1016/j.aca.2025.344031
73. Malik, S.; Singh, J.; Umar, A.; Ibrahim, A. A.; Baskoutas, S. *J. Photochem. Photobiol., A* **2026,** *471,* 116675. doi:10.1016/j.jphotochem.2025.116675

License and Terms

This is an open access article licensed under the terms of the Beilstein-Institut Open Access License Agreement (https://www.beilstein-journals.org/bjnano/terms), which is identical to the Creative Commons Attribution 4.0 International License (https://creativecommons.org/licenses/by/4.0). The reuse of material under this license requires that the author(s), source and license are credited. Third-party material in this article could be subject to other licenses (typically indicated in the credit line), and in this case, users are required to obtain permission from the license holder to reuse the material.

The definitive version of this article is the electronic one which can be found at:
https://doi.org/10.3762/bjnano.17.59

BEILSTEIN JOURNAL OF NANOTECHNOLOGY

Supramolecular one-dimensional conducting nanofibers from a C_3-symmetric tetrathiafulvalene derivative

Yoko Tatewaki*[1], Fumiya Hirose[1], Sadafumi Nishihara[2], Tomoyuki Akutagawa[3], Takayoshi Nakamura[2,4] and Tsuyoshi Minami[5]

Full Research Paper

Open Access

Address:
[1]Department of Applied Chemistry, Tokyo University of Agriculture and Technology, 2-24-16 Nakacho, Koganei-shi, Tokyo, 184-8588 Japan, [2]Graduate School of Advanced Science and Engineering, Hiroshima University, 1-3-1, Kagamiyama, Higashi-hiroshima 739-8526, Japan, [3]Institute of Multidisciplinary Research for Advanced Materials (IMRAM), Tohoku University, Sendai 980-8577, Japan, [4]Research Institute for Electronic Science, Hokkaido University, Sapporo, Japan and [5]Institute of Industrial Science, The University of Tokyo, 4-6-1 Komaba, Meguro-ku, Tokyo 153-8505, Japan

Email:
Yoko Tatewaki* - ytatewa@cc.tuat.ac.jp

* Corresponding author

Keywords:
charge-transfer complex; conducting nanofibers; one-dimensional nanostructures; supramolecular self-assembly; tetrathiafulvalene

Beilstein J. Nanotechnol. **2026,** *17,* 872–881.
https://doi.org/10.3762/bjnano.17.63

Received: 31 March 2026
Accepted: 18 June 2026
Published: 10 July 2026

This article is part of the thematic issue "Nanotechnology for cross-scale analysis: comprehensive evaluation of water environments".

Associate Editor: S. A. Claridge

© 2026 Tatewaki et al.; licensee Beilstein-Institut.
License and terms: see end of document.

Abstract

This study reports the design and synthesis of a C_3-symmetric discotic tetrathiafulvalene (TTF) derivative, MeS-TTF-Ts, as a molecular platform for the self-assembly of one-dimensional conductive nanostructures. The molecular architecture contains three TTF units radially arranged around a rigid C_3-symmetric core, enabling the formation of highly ordered one-dimensional assemblies through cooperative π–π stacking and directional intermolecular interactions. Solution casting of MeS-TTF-Ts produced nanorod and nanofiber structures with morphologies strongly dependent on the solvent conditions. AFM and SEM observations revealed that distinct supramolecular structures were formed depending on the solvent and substrate used, suggesting that molecular interactions and assembly processes play important roles in determining the resulting morphologies. Furthermore, MeS-TTF-Ts was combined with the strong electron acceptor F4TCNQ to form a charge-transfer complex, (MeS-TTF-Ts)(F4TCNQ)$_3$, which yielded well-defined one-dimensional nanofibers. UV–vis and FTIR spectroscopic analyses confirmed substantial charge transfer from MeS-TTF-Ts to F4TCNQ through the formation of $F4TCNQ^-$ and TTF^+ species. These results indicate the formation of a highly charge-transferred donor–acceptor assembly in the nanofibers. Electrical conductivity measurements revealed that the (MeS-TTF-Ts)(F4TCNQ)$_3$ nanofibers exhibit a conductivity of 1.24×10^{-2} S·cm^{-1}. These findings demonstrate that rational molecular design combined with controlled supramolecular self-assembly provides an effective strategy for constructing one-dimensional conductive nanostructures based on organic charge-transfer systems.

Introduction

Supramolecular gels have been developed as organized soft materials that form anisotropic nanostructures such as ribbons and fibers within their networks [1,2]. These materials have attracted considerable attention in the fields of materials science and nanotechnology because of their diverse functionalities, including luminescence, sensing, charge transport, and drug delivery [3-6]. Supramolecular gels are formed through bottom-up self-assembly driven by weak intermolecular interactions such as hydrogen bonding, π–π stacking, and donor–acceptor interactions, resulting in three-dimensional interconnected nanofibrous networks [7,8]. Such one-dimensional nanostructures can be precisely controlled in terms of morphology and physical properties through molecular design, making them promising platforms for the development of functional nanomaterials [9,10].

In particular, when electroactive molecules are employed, one-dimensional structures formed through self-assembly are expected to be applicable as nanowire materials in molecular electronic devices. Among them, tetrathiafulvalene (TTF) derivatives are representative redox-active molecules capable of forming charge-transfer complexes, and their charge-transfer salts have long been known to exhibit high electrical conductivity [11-14].

In recent years, TTF derivatives functionalized with amide groups or long alkyl chains have been reported to form highly ordered one-dimensional stacked structures through cooperative hydrogen bonding and π–π stacking interactions, leading to the formation of nanowires via self-assembly [15-20]. These assemblies can be partially oxidized through charge-transfer interactions with iodine or strong electron acceptors, thereby generating TTF radical cation species that serve as charge transport pathways. As a result, their electrical properties can be tuned from semiconducting to metallic behavior, depending on the doping level [21-24].

The realization of nanoscale conductive structures requires precise control of intermolecular interactions and rational molecular design capable of directing the spontaneous formation of one-dimensional stacked assemblies [25-28]. In particular, for molecules incorporating redox-active units, it has been reported that one-dimensional structures formed through self-assembly can directly function as charge transport pathways [29,30].

C_3-symmetric discotic molecules, which possess a rigid central core and three-directional interaction sites, are well known as molecular platforms that readily form highly ordered columnar stacking structures [31-33]. Furthermore, expansion of the π-conjugated framework enhances electronic interactions between stacked units, and the cooperative incorporation of noncovalent interactions such as directional hydrogen bonding enables the construction of stable one-dimensional nanostructures while facilitating efficient linear stacking of conductive units [34-36].

Experimental

General

Nuclear magnetic resonance (NMR) spectra were recorded on a JEOL ECX-400 spectrometer operating at 400 MHz for ^{1}H NMR and 100.6 MHz for ^{13}C NMR. Chemical shifts are reported in parts per million (ppm) relative to external tetramethylsilane (TMS) and are given downfield.

Mass spectrometry measurements were carried out using a JEOL JMS instrument. Elemental analyses were performed at the Research Support Center, Okayama University.

Materials

Mercury(II) acetate, triethyl phosphite, lithium bromide (anhydrous), lithium hydroxide monohydrate, oxalyl chloride, and pyridine were purchased from Kanto Chemical Co., Inc. 2,6-Diaminopyridine and 1,3,5-benzenetricarbonyl trichloride were purchased from Tokyo Chemical Industry Co., Ltd. (TCI). All reagents were used as received without further purification unless otherwise noted.

Synthesis of compounds

4,5-Bis(methylthio)-1,3-dithiole-2-thione (**2**)

Iodomethane (790 mg, 5.56 mmol) was added to a solution of zinc chelate **1** (1.000 g, 1.39 mmol) in acetone (25 mL). The reaction mixture was stirred at 25 °C overnight. After removal of the solvent under reduced pressure, the residue was extracted with chloroform and washed with brine. The organic layer was dried over $MgSO_4$, filtered, and concentrated under reduced pressure. The crude product was purified by recrystallization from acetone to afford compound **2** as yellow needle crystals. Yield 401.0 mg (63.7%) [37,38]. ^{1}H NMR (400 MHz, $CDCl_3$) δ 2.50 (s, 6H); ^{13}C NMR (100.6 MHz, $CDCl_3$) δ 211.0, 136.0, 19.4; MS (FAB) *m/z*: $[M + H]^+$ calcd for $C_5H_6S_5$, 226.91; found, 227.

Dimethyl 1,3-dithiole-2-oxo-4,5-dicarboxylate (**3**)

Mercury(II) acetate (3.824 g, 12.0 mmol) was added to a solution of dimethyl 1,3-dithiole-2-thioxo-4,5-dicarboxylate (999.6 mg, 3.99 mmol) in chloroform (40 mL). The reaction mixture was stirred at 25 °C for 1 h. The mixture was filtered through Celite and washed with chloroform. The solvent was removed under reduced pressure, and the residue was purified

by column chromatography (chloroform) to afford compound **3** as a white solid. Yield 898.7 mg (96.1%) [39,40]. ^{1}H NMR (400 MHz, $CDCl_3$) δ 3.91 (s, 6H); ^{13}C NMR (100.6 MHz, $CDCl_3$) δ 186.4, 159.2, 129.1, 53.6; MS (FAB) *m/z*: $[M + H]^+$ calcd for $C_7H_6O_5S_2$, 234.97; found, 235.

MeS-TTF(COOMe)$_2$ (**4**)

Compounds **2** (358.6 mg, 1.58 mmol) and **3** (373.4 mg, 1.59 mmol) were dissolved in a mixture of triethyl phosphite (10 mL) and toluene (10 mL). The reaction mixture was refluxed at 110 °C for 2 h. After removal of the solvent under reduced pressure, toluene (100 mL) was added to the residue and evaporated under reduced pressure. This procedure was repeated several times. The crude product was purified by column chromatography (chloroform) to afford compound **4** as a dark brown solid. Yield 381.0 mg (57.9%) [38,41,42]. ^{1}H NMR (400 MHz, $CDCl_3$) δ 3.85 (s, 6H), 2.43 (s, 6H); ^{13}C NMR (100.6 MHz, $CDCl_3$) δ 159.9, 132.0, 127.7, 112.5, 99.9, 53.4, 19.3; MS (FAB) *m/z*: $[M + H]^+$ calcd for $C_{12}H_{12}O_4S_6$, 411.91; found; 412.

MeS-TTF-COOMe (**5**)

A solution of **4** (360.0 mg, 0.873 mmol) and lithium bromide (1.600 g, 18.4 mmol) in dry DMF (15 mL) was stirred at 85 °C for 3.5 h. After cooling to room temperature, brine was added, and the mixture was extracted with ethyl acetate. The combined organic layers were washed with brine, dried over $MgSO_4$, filtered, and concentrated under reduced pressure. The crude product was purified by column chromatography (chloroform) to afford compound **5** as a brown solid. Yield 130.8 mg (42.3%) [43,44]. ^{1}H NMR (400 MHz, $CDCl_3$) δ 7.34 (s, 1H), 3.85 (s, 3H), 2.43 (s, 6H); ^{13}C NMR (100.6 MHz, $CDCl_3$) δ 159.7, 132.0, 127.9, 127.1, 112.9, 109.4, 52.7, 19.2; MS (FAB) *m/z*: $[M + H]^+$ calcd for $C_{10}H_{10}O_2S_6$, 353.90; found, 354.

MeS-TTF-COOH (**6**)

An aqueous solution of lithium hydroxide (82.0 mg, 1.95 mmol) was added to a solution of **5** (130.8 mg, 0.369 mmol) in 1,4-dioxane (8.5 mL). The reaction mixture was stirred at room temperature overnight. The mixture was then acidified with 5 M HCl (ca. 1.0 mL), during which the solution turned red. After stirring for 30 min, diethyl ether (6.0 mL) and water (2.0 mL) were added to form a biphasic system. Additional 5 M HCl was added until the pH reached 1–2. The layers were separated, and the aqueous phase was extracted with diethyl ether. The combined organic layers were dried over $MgSO_4$, filtered, and concentrated under reduced pressure to afford compound **6** as a red solid. Yield 115.7 mg (92.1%) [44,45]. ^{1}H NMR (400 MHz, DMSO-d_6) δ 11.8–14.6 (br, 1H), 7.71 (s, 1H), 2.43 (s, 6H); ^{13}C NMR (100.6 MHz, DMSO-d_6) δ 160.3, 133.0, 128.8, 126.4, 113.8, 106.8, 18.6; MS (FAB) *m/z*: $[M + H]^+$ calcd for $C_9H_8O_2S_6$, 339.88; found, 340.

MeS-TTF-COCl (**7**)

Oxalyl chloride (113.7 µL, 1.32 mmol) was added dropwise to a solution of **6** (113.0 mg, 0.332 mmol) and pyridine (0.45 µL) in dry THF (10 mL). The reaction mixture was stirred at 45 °C for 2 h. The solvent and excess oxalyl chloride were removed under reduced pressure, and the residue was washed with pentane to afford compound **7** as a purple solid in quantitative yield. The product was used in the next step without further purification [46,47].

MeS-TTF-CONHPy (**8**)

A solution of **7** (47.8 mg, 0.133 mmol) in dry THF was added to a solution of 2,6-diaminopyridine (16.80 mg, 0.154 mmol) and triethylamine (24.0 µL, 0.172 mmol) in dry THF (1.0 mL) at 0 °C. The reaction mixture was stirred at 0 °C for 2 h and then at room temperature overnight. The solvent was removed under reduced pressure, and the residue was purified by column chromatography (chloroform/methanol = 47:3) to afford compound **8** as a red-brown solid. Yield 25.0 mg (43.5%) [46]. ^{1}H NMR (400 MHz, $CDCl_3$) δ 7.89 (s, 1H), 7.50 (m, *J* = 24.8 Hz, 2H), 7.24 (s, 1H), 6.30 (d, *J* = 7.6 Hz, 1H), 4.40 (s, 2H), 2.43 (s, 6H); ^{13}C NMR (100.6 MHz, $CDCl_3$) δ 157.0, 148.9, 140.4, 132.2, 128.0, 127.2, 127.1, 111.9, 110.4, 105.0, 103.6, 19.2; MS (FAB) *m/z*: $[M + H]^+$ calcd for $C_{14}H_{13}N_3OS_6$, 430.94; found, 431.

MeS-TTF-Ts

A solution of **8** (25.0 mg, 57.9 µmol) and triethylamine (7.65 µL, 54.9 µmol) in dry THF (1.0 mL) was cooled to 0 °C. A solution of trimesoyl chloride (5.33 mg, 20.1 µmol) in dry THF (1.0 mL) was added dropwise to the stirred solution at 0 °C. The reaction mixture was stirred at 0 °C for 2 h and then at room temperature overnight. Hexane was added to the mixture to induce precipitation, and the resulting solid was collected and washed with ethyl acetate, methanol, and hexane to afford MeS-TTF-Ts as a brown solid. Yield 14.65 mg (55.9%) [48,49]. ^{1}H NMR (400 MHz, DMSO-d_6) δ 10.74 (m, *J* = 24.0 Hz, 3H), 8.67 (t, *J* = 13.6 Hz, 3H), 8.05 (d, *J* = 7.6 Hz, 3H), 7.93 (m, *J* = 15.6 Hz, 6H), 7.67 (m, *J* = 4.8 Hz, 3H), 2.45 (s, 18H); ^{13}C NMR (100.6 MHz, DMSO-d_6) δ 157.8, 150.2, 149.7, 149.4, 140.4, 134.6, 133.2, 131.7, 128.1, 126.1, 112.8, 106.0, 90.7, 79.2, 18.6; FTIR (ATR, νmax/cm^{-1}): 2970, 2930, 2873, 1698, 1584, 1512, 1445, 1292, 1236, 773, 699. The FTIR spectrum of MeS-TTF-Ts is shown in Figure S1 in Supporting Information File 1. MS (APCI) *m/z*: $[M + H]^+$ calcd for $C_{51}H_{39}N_9O_6S_{18}$, 1449.80; found, 1449.8082; Anal. calcd for $C_{51}H_{39}N_9O_6S_{18}$: C, 42.21; H, 2.71; N, 8.69; found: C, 42.12; H, 2.66; N, 8.63.

Measurements

AFM measurements

The structures formed on mica substrates were observed using an atomic force microscopy (AFM) system (Bruker Multi Mode 8). Measurements were performed in non-contact mode using a silicon cantilever with a spring constant of approximately 0.8 $N \cdot m^{-1}$.

Optical spectra

UV–vis absorption spectra were recorded in the range of 300–1200 nm using a JASCO V-650 spectrophotometer. A mixed solvent of dimethyl sulfoxide (DMSO) and acetonitrile was used for the measurements. Fourier-transform infrared (FTIR) spectra were recorded using a JASCO FT/IR-4200 spectrometer. Spectra were obtained either by the ATR method or from cast films deposited on quartz substrates, depending on the sample form.

Conductivity measurements

Electrical conductivity was measured by a direct current (DC) two-probe method. Gold electrodes with a thickness of 100 nm were deposited on mica substrates by vacuum evaporation. Electrical contacts were made by attaching gold wires (25 μm in diameter) using silver paste.

Temperature-dependent DC conductivity was measured using a Keithley 6517 electrometer, with an applied voltage in the range of −100 to +100 V. The electrode gap and electrode length were 60 μm and 0.6 cm, respectively.

Results and Discussion

Synthesis

The synthetic strategy employed for the preparation of MeS-TTF-Ts in this study is similar to that reported by John D. Wallis and co-workers [50,51]. In the final step, an acylation reaction between compound **7** and compound **8** was carried out (Scheme 1).

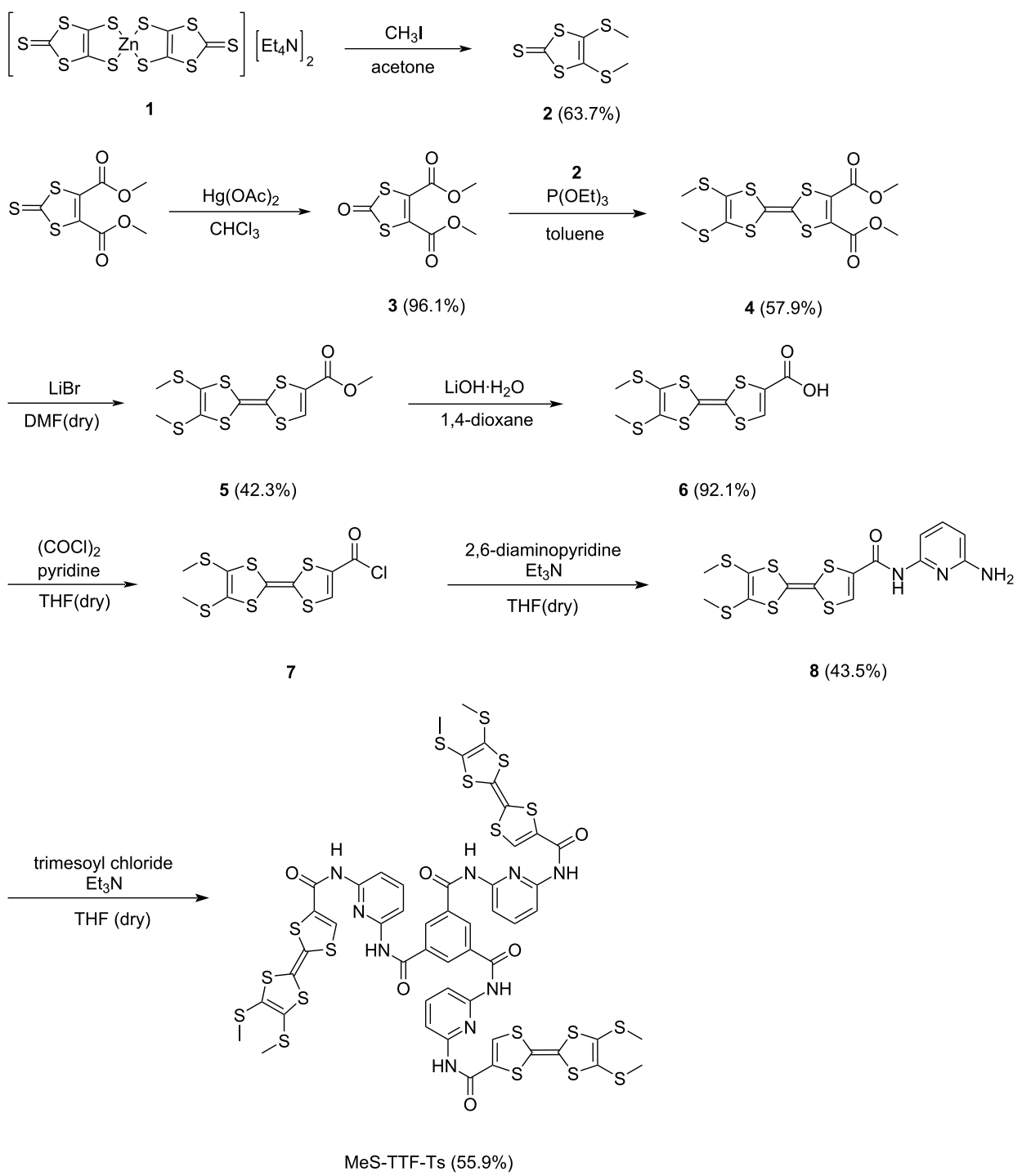
Formation of nanofibers from C_3-symmetric MeS-TTF-Ts and the (MeS-TTF-Ts)$(F4TCNQ)_3$ charge-transfer complex

In order to form conductive fibers using MeS-TTF-Ts, it was necessary to identify suitable conditions for controlling the formation of supramolecular structures. Atomic force microscopy (AFM) observations of cast films of MeS-TTF-Ts revealed the formation of well-defined one-dimensional nanostructures with relatively uniform morphology.

Specifically, dimethylformamide (DMF) solution of MeS-TTF-Ts (6 mM) was dripped onto a mica substrate, and the solvent was allowed to evaporate, resulting in the formation of nanorod-like structures with a width of 100 nm, a height of 30 nm, and a length of 3 μm (Figure 1). These nanorods were observed to be distributed across the substrate without significant aggregation, suggesting that the self-assembly process proceeds in a controlled manner under these conditions. The formation of such anisotropic nanostructures is attributed to directional π–π stacking interactions between the TTF cores, together with the cooperative effect of intermolecular interactions, which promote one-dimensional growth along a preferred direction. These results indicate that the solvent casting process in DMF provides suitable conditions for inducing ordered supramolecular organization of MeS-TTF-Ts.

When the casting solvent was changed to DMSO at the same concentration, a mesh-like structure composed of interconnected fibers with different sizes was observed (Figure 2). The fibers exhibited dimensions of approximately 50 nm in width, 5 nm in height, and lengths exceeding 10 μm. Compared with the nanorod structures obtained from DMF, a markedly different morphology was observed in the DMSO system, highlighting the important role of solvent conditions in determining the self-assembled structures. Although the detailed mechanism of the assembly formation remains unclear, the observed differences in morphology may arise from differences in intermolecular interactions and molecular packing during the self-assembly process. In particular, the formation of different polymorphic assembly states may contribute to the distinct morphologies observed in DMF and DMSO systems. These results suggest that solvent-dependent molecular organization strongly influences the resulting supramolecular structures. Internal structures were also observed within these assemblies, suggesting that the fibers are composed of bundles of thinner fibrils forming a hierarchical structure. Such hierarchical organization is considered to arise from directional π–π stacking interactions between the TTF cores together with cooperative intermolecular interactions, which promote lateral association of one-dimensionally grown fibrils. However, due to the highly entangled nature of the fibrous network, precise statistical evaluation was difficult.

A charge-transfer complex solution of (MeS-TTF-Ts)$(F4TCNQ)_3$ was prepared by mixing a DMSO solution of the donor molecule MeS-TTF-Ts with an acetonitrile solution of the acceptor molecule F4TCNQ at a molar ratio of 1:3. AFM observations of the cast films of the resulting (MeS-TTF-Ts)$(F4TCNQ)_3$ solution revealed the formation of well-defined one-dimensional nanofiber structures. Specifically, a mixed solution of MeS-TTF-Ts in DMSO and F4TCNQ in acetonitrile was prepared at a final concentration of 6 mM and dripped onto a mica substrate, followed by solvent evaporation. As a result, nanofibers with a width of 140 nm, a height of



Scheme 1: Synthesis of C_3-symmetric MeS-TTF-Ts.

6 nm, and lengths exceeding 5 μm were formed (Figure 3). These fibers were continuously distributed over the substrate, forming a relatively uniform network structure.

Furthermore, compared with the nanofibers formed from MeS-TTF-Ts alone, a significant increase in fiber diameter was observed. This result suggests that the introduction of F4TCNQ induces donor–acceptor charge-transfer interactions, leading to the formation of one-dimensional stacked structures composed of MeS-TTF-Ts and F4TCNQ. These results suggest that charge-transfer interactions enhance intermolecular interactions, thereby promoting the formation of thicker fibrous structures.

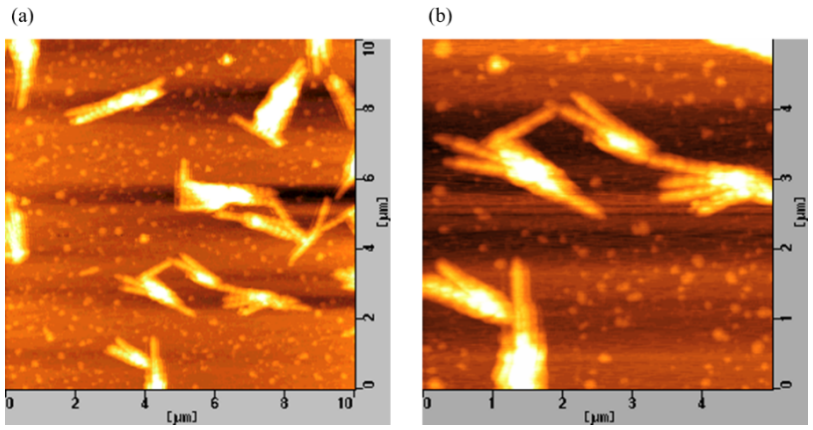


Figure 1: AFM images of nanorods composed of C_3-symmetric MeS-TTF-Ts deposited from DMF on a mica substrate. (a) 10 µm × 10 µm; (b) 5 µm × 5 µm.

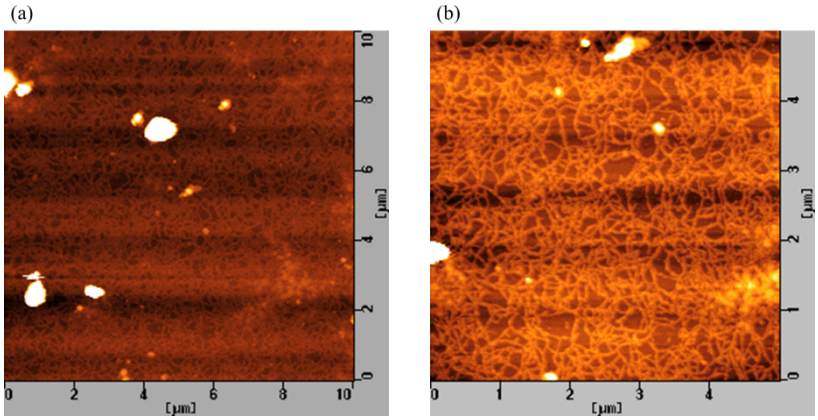


Figure 2: AFM images of nanofibers composed of C_3-symmetric MeS-TTF-Ts deposited from DMSO on a mica substrate. (a) 10 µm × 10 µm; (b) 5 µm × 5 µm.

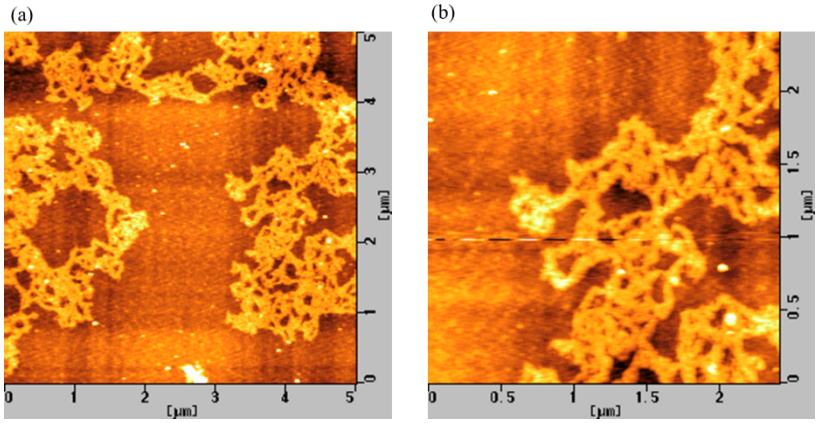


Figure 3: AFM images of nanofibers composed of the C_3-symmetric (MeS-TTF-Ts)$(F4TCNQ)_3$ charge-transfer complex deposited from a mixed solvent of DMSO and acetonitrile on a mica substrate. (a) 5 µm × 5 µm; (b) 2.5 µm × 2.5 µm.

In contrast, when a mixed solution of MeS-TTF-Ts in DMF and F4TCNQ in acetonitrile was prepared at a final concentration of 6 mM and cast onto a mica substrate followed by solvent evaporation, no nanofiber structures were formed, and aggregated structures were observed instead. These aggregates exhibited a relatively uniform height of 140 nm. This result suggests that under these mixed solvent conditions, one-dimensional self-assembly does not proceed efficiently and the molecules tend to aggregate in a disordered manner. Furthermore, as observed for MeS-TTF-Ts alone, the morphology of the molecular assemblies in the (MeS-TTF-Ts)(F4TCNQ)$_3$ system is strongly dependent on the solvent conditions. The observed differences may originate from variations in molecular organization, intermolecular interactions, and molecular packing during the self-assembly process. In other words, variations in solvent conditions lead to a competition between one-dimensional anisotropic growth and disordered aggregation, resulting in marked differences in the observed morphologies.

In addition to AFM observations, scanning electron microscopy (SEM) measurements were performed for representative samples deposited on HOPG substrates. Representative SEM images are provided in Supporting Information File 1 (Figures S2–S4). The morphologies observed by SEM differed from those obtained by AFM on mica substrates, showing more aggregated structures. This difference may originate from the distinct surface properties of the substrates used for the measurements. Although the detailed mechanism remains unclear, these results suggest that the self-assembly behavior of MeS-TTF-Ts and its charge-transfer complex is influenced by the substrate surface as well as the solvent conditions.

Optical spectra of nanofibers formed from MeS-TTF-Ts and the (MeS-TTF-Ts)(F4TCNQ)$_3$ charge-transfer complex

Figure 4 shows the UV–vis spectra of nanofiber cast films deposited on quartz substrates. The samples were prepared by drop-casting a DMSO solution of MeS-TTF-Ts and a mixed solution of MeS-TTF-Ts in DMSO and F4TCNQ in acetonitrile onto quartz substrates, followed by solvent evaporation. The final concentration of each solution was adjusted to 6 mM.

For the (MeS-TTF-Ts)(F4TCNQ)$_3$ nanofibers, characteristic absorption bands were observed at 682 and 875 nm. These absorption bands are in good agreement with those previously reported for intramolecular transitions of the F4TCNQ radical anion (F4TCNQ$^-$). In addition, the absorption bands observed at 462 and 333 nm are assigned to intramolecular transitions of the TTF radical cation (TTF$^+$) and F4TCNQ$^-$, respectively [13,14,52-55]. The appearance of these absorption bands suggests the formation of a charge-transfer state through electron transfer from the donor MeS-TTF-Ts to the acceptor F4TCNQ.

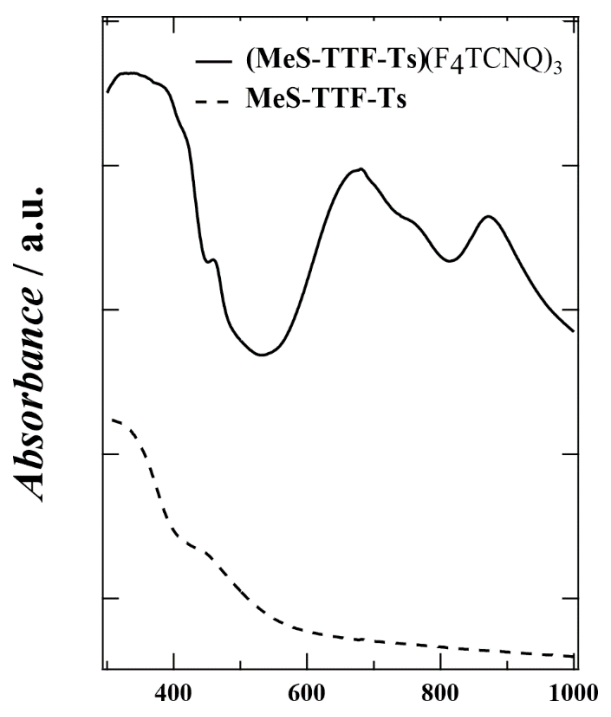


Figure 4: UV–vis spectra of nanofiber films on quartz substrates formed from MeS-TTF-Ts and the (MeS-TTF-Ts)(F4TCNQ)$_3$ charge-transfer complex.

Figure 5 shows the FTIR spectra of neutral F4TCNQ and the (MeS-TTF-Ts)(F4TCNQ)$_3$ charge-transfer complex thin film deposited on a CaF_2 substrate. The thin film was prepared by drop-casting a mixed solution of MeS-TTF-Ts in DMSO and F4TCNQ in acetonitrile onto a CaF_2 substrate, followed by solvent evaporation. The final concentration of the solution was adjusted to 6 mM.

To further investigate the electronic state of the charge-transfer complex, FTIR measurements were performed. The C≡N stretching bands observed at 2227 and 2214 cm^{-1} for neutral F4TCNQ shifted to 2194 and 2157 cm^{-1}, respectively, upon complex formation. Such pronounced downshifts indicate an increase in electron density on the F4TCNQ moiety resulting from electron transfer from MeS-TTF-Ts to F4TCNQ, supporting the formation of charge-transfer interactions.

Since the samples obtained in this study are supramolecular nanofibers rather than single crystals, the vibrational frequencies may be influenced by molecular packing and local molecular environments. Nevertheless, the characteristic absorption bands assigned to F4TCNQ$^-$ and TTF$^+$ in the UV–vis spectra,

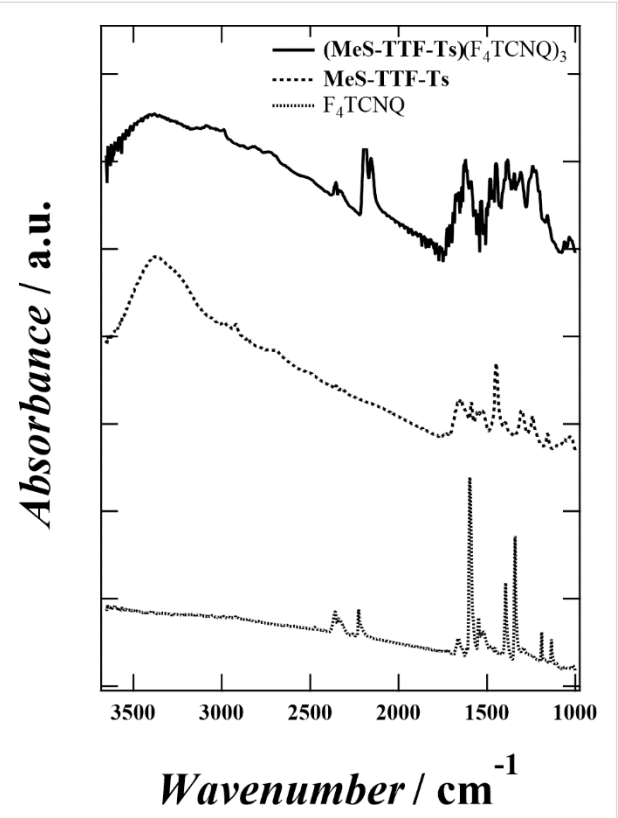


Figure 5: FTIR spectra of neutral F4TCNQ and the (MeS-TTF-Ts)(F4TCNQ)$_3$ charge-transfer complex thin film deposited on a CaF_2 substrate.

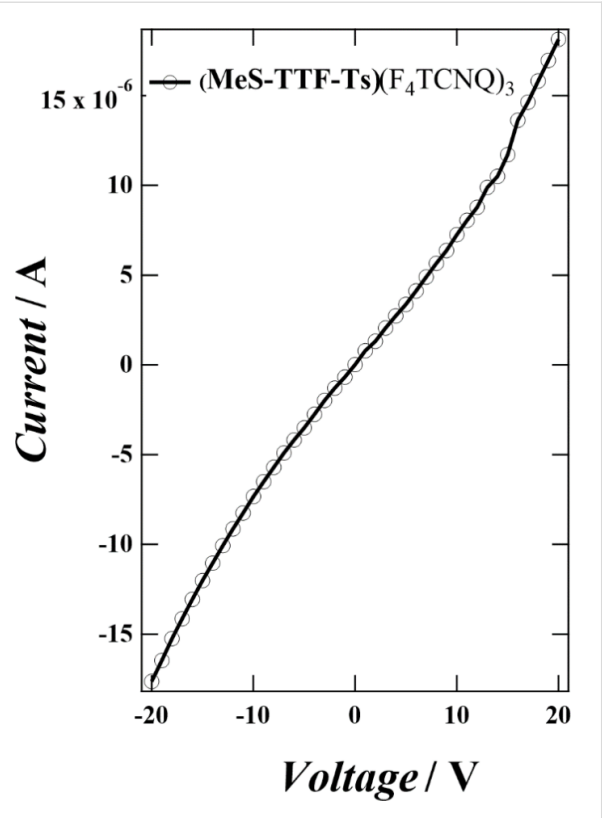


Figure 6: *I–V* curves of nanofibers composed of the (MeS-TTF-Ts)(F4TCNQ)$_3$ charge-transfer complex deposited on a mica substrate.

together with the pronounced downshifts of the C≡N stretching bands observed in the FTIR spectra, provide strong evidence for substantial electron transfer from MeS-TTF-Ts to F4TCNQ and suggest the formation of a highly charge-transferred state in the nanofibers.

Electrical conductivity of nanofibers formed from the (MeS-TTF-Ts)(F4TCNQ)$_3$ charge-transfer complex

Figure 6 shows the current–voltage (*I–V*) characteristics of nanofibers composed of the (MeS-TTF-Ts)(F4TCNQ)$_3$ charge-transfer complex deposited on a mica substrate. The sample solution was prepared by mixing DMSO solution of MeS-TTF-Ts with an acetonitrile solution of F4TCNQ at a molar ratio of 1:3, with a final concentration of 6 mM.

The solution (4 µL) was cast onto a mica substrate equipped with gold electrodes (gap: 50 µm, electrode length: 6 mm) fabricated by vacuum deposition, followed by solvent evaporation to form nanofiber structures. Electrical conductivity measurements of the resulting nanofibers exhibited a clear current response, indicating good electrical conduction behavior. The electrical conductivity (σ) of the nanofibers composed of the (MeS-TTF-Ts)(F4TCNQ)$_3$ complex was determined to be 1.24×10^{-2} S·cm^{-1}. This result suggests that the one-dimensional stacked structure formed through donor–acceptor charge-transfer interactions functions as an effective charge transport pathway.

Conclusion

In this study, a C_3-symmetric discotic tetrathiafulvalene (TTF) derivative, MeS-TTF-Ts, was designed and synthesized as a molecular platform for constructing one-dimensional conductive nanostructures based on self-assembly. The molecular architecture features three TTF units radially arranged around a rigid C_3-symmetric core and incorporates hydrogen-bonding sites, enabling the formation of highly ordered one-dimensional stacked structures through cooperative π–π stacking and directional intermolecular interactions.

Solution casting of MeS-TTF-Ts resulted in the formation of nanorod and nanofiber structures. These morphologies strongly depended on the solvent conditions, which influenced molecular organization and intermolecular packing during the self-assembly process. In particular, the use of DMSO resulted in the formation of uniform interconnected fibrous networks.

These findings demonstrate that hierarchical control of supramolecular structures can be achieved through solvent modulation.

Furthermore, combining MeS-TTF-Ts with the strong electron acceptor F4TCNQ led to the formation of a charge-transfer complex, (MeS-TTF-Ts)$(F4TCNQ)_3$, which successfully generated well-defined one-dimensional nanofiber structures. Spectroscopic measurements confirmed the formation of charge-transfer states, while morphological observations suggested the formation of one-dimensional stacked structures driven by donor–acceptor interactions. These results indicate that charge-transfer interactions can be effectively incorporated into self-assembled architectures through rational molecular design.

Electrical conductivity measurements revealed that the nanofibers exhibited a conductivity of 1.24×10^{-2} $S \cdot cm^{-1}$, demonstrating their potential as self-assembled organic nanowire materials. This conductivity is attributed to the one-dimensional stacked structure formed through donor–acceptor charge-transfer interactions, which functions as an efficient charge transport pathway.

Overall, this study demonstrates that the combination of molecular design and controlled self-assembly enables the construction of conductive supramolecular nanostructures with integrated structural and functional properties. These findings provide important insights into the relationship between molecular structure, supramolecular organization, and charge transport, and offer a useful design strategy for the development of organic conductive nanomaterials based on self-assembly.

Supporting Information

Supporting Information File 1

Additional figures.
[https://www.beilstein-journals.org/bjnano/content/supplementary/2190-4286-17-63-S1.pdf]

Funding

This work was financially supported by the Japan Society for the Promotion of Science (JSPS) KAKENHI (Grant no. JP23H03864). The authors gratefully acknowledge this support.

ORCID® iDs

Yoko Tatewaki - https://orcid.org/0000-0002-8311-1325
Fumiya Hirose - https://orcid.org/0009-0007-6831-4822
Tsuyoshi Minami - https://orcid.org/0000-0001-8331-378X

Data Availability Statement

All data that supports the findings of this study is available in the published article and/or the supporting information of this article.

References

1. Adams, D. J. *J. Am. Chem. Soc.* **2022,** *144,* 11047–11053. doi:10.1021/jacs.2c02096
2. Smith, D. K. *Soft Matter* **2024,** *20,* 10–70. doi:10.1039/d3sm01301d
3. Okesola, B. O.; Smith, D. K. *Chem. Soc. Rev.* **2016,** *45,* 4226–4251. doi:10.1039/c6cs00124f
4. Das, T.; Häring, M.; Haldar, D.; Díaz Díaz, D. *Biomater. Sci.* **2018,** *6,* 38–59. doi:10.1039/c7bm00882a
5. Bianco, S.; Hallam Stewart, F.; Panja, S.; Zyar, A.; Bowley, E.; Bek, M.; Kádár, R.; Terry, A.; Appio, R.; Plivelic, T. S.; Maguire, M.; Poptani, H.; Marcello, M.; Sonani, R. R.; Egelman, E. H.; Adams, D. J. *Nat. Synth.* **2024,** *3,* 1481–1489. doi:10.1038/s44160-024-00623-4
6. Draper, E. R.; Adams, D. J. *Chem* **2017,** *3,* 390–410. doi:10.1016/j.chempr.2017.07.012
7. van Esch, J. H.; Feringa, B. L. *Angew. Chem., Int. Ed.* **2000,** *39,* 2263–2266. doi:10.1002/1521-3773(20000703)39:13<2263::aid-anie2263>3.0.co;2-v
8. Terech, P.; Weiss, R. G. *Chem. Rev.* **1997,** *97,* 3133–3160. doi:10.1021/cr9700282
9. Estroff, L. A.; Hamilton, A. D. *Chem. Rev.* **2004,** *104,* 1201–1218. doi:10.1021/cr0302049
10. Yan, X.; Zhu, P.; Li, J. *Chem. Soc. Rev.* **2010,** *39,* 1877–1890. doi:10.1039/b915765b
11. Ferraris, J.; Cowan, D. O.; Walatka, V.; Perlstein, J. H. *J. Am. Chem. Soc.* **1973,** *95,* 948–949. doi:10.1021/ja00784a066
12. Massetti, M.; Jiao, F.; Ferguson, A. J.; Zhao, D.; Wijeratne, K.; Würger, A.; Blackburn, J. L.; Crispin, X.; Fabiano, S. *Chem. Rev.* **2021,** *121,* 12465–12547. doi:10.1021/acs.chemrev.1c00218
13. Torrance, J. B.; Scott, B. A.; Kaufman, F. B. *Solid State Commun.* **1975,** *17,* 1369–1373. doi:10.1016/0038-1098(75)90605-5
14. Torrance, J. B.; Scott, B. A.; Welber, B.; Kaufman, F. B.; Seiden, P. E. *Phys. Rev. B* **1979,** *19,* 730–741. doi:10.1103/physrevb.19.730
15. Nalluri, S. K. M.; Shivarova, N.; Kanibolotsky, A. L.; Zelzer, M.; Gupta, S.; Frederix, P. W. J. M.; Skabara, P. J.; Gleskova, H.; Ulijn, R. V. *Langmuir* **2014,** *30,* 12429–12437. doi:10.1021/la503459y
16. Wang, X.-J.; Xing, L.-B.; Cao, W.-N.; Li, X.-B.; Chen, B.; Tung, C.-H.; Wu, L.-Z. *Langmuir* **2011,** *27,* 774–781. doi:10.1021/la103686n
17. Puigmartí-Luis, J.; Laukhin, V.; Pérez del Pino, Á.; Vidal-Gancedo, J.; Rovira, C.; Laukhina, E.; Amabilino, D. B. *Angew. Chem., Int. Ed.* **2007,** *46,* 238–241. doi:10.1002/anie.200602483
18. Jain, A.; Rao, K. V.; Mogera, U.; Sagade, A. A.; George, S. J. *Chem. – Eur. J.* **2011,** *17,* 12355–12361. doi:10.1002/chem.201101813
19. Kitamura, T.; Nakaso, S.; Mizoshita, N.; Tochigi, Y.; Shimomura, T.; Moriyama, M.; Ito, K.; Kato, T. *J. Am. Chem. Soc.* **2005,** *127,* 14769–14775. doi:10.1021/ja053496z
20. Iyoda, M.; Yamakawa, J.; Rahman, M. J. *Angew. Chem., Int. Ed.* **2011,** *50,* 10522–10553. doi:10.1002/anie.201006198
21. Avarvari, N.; Wallis, J. D. *J. Mater. Chem.* **2009,** *19,* 4061–4076. doi:10.1039/b820598a
22. Martín, N.; Sánchez, L.; Herranz, M. Á.; Illescas, B.; Guldi, D. M. *Acc. Chem. Res.* **2007,** *40,* 1015–1024. doi:10.1021/ar700026t
23. Bendikov, M.; Wudl, F.; Perepichka, D. F. *Chem. Rev.* **2004,** *104,* 4891–4946. doi:10.1021/cr030666m

24. Frère, P.; Skabara, P. J. *Chem. Soc. Rev.* **2005,** *34,* 69–98. doi:10.1039/b316392j
25. Elemans, J. A. A. W.; Rowan, A. E.; Nolte, R. J. M. *J. Mater. Chem.* **2003,** *13,* 2661–2670. doi:10.1039/b304972h
26. Bushby, R. J.; Lozman, O. R. *Curr. Opin. Colloid Interface Sci.* **2002,** *7,* 343–354. doi:10.1016/s1359-0294(02)00085-7
27. Aida, T.; Meijer, E. W.; Stupp, S. I. *Science* **2012,** *335,* 813–817. doi:10.1126/science.1205962
28. Lehn, J.-M. *Angew. Chem., Int. Ed.* **2015,** *54,* 3276–3289. doi:10.1002/anie.201409399
29. Facchetti, A. *Chem. Mater.* **2011,** *23,* 733–758. doi:10.1021/cm102419z
30. Sirringhaus, H. *Adv. Mater. (Weinheim, Ger.)* **2014,** *26,* 1319–1335. doi:10.1002/adma.201304346
31. Sergeyev, S.; Pisula, W.; Geerts, Y. H. *Chem. Soc. Rev.* **2007,** *36,* 1902–1929. doi:10.1039/b417320c
32. Kumar, S. *Chem. Soc. Rev.* **2006,** *35,* 83–109. doi:10.1039/b506619k
33. Pisula, W.; Feng, X.; Müllen, K. *Adv. Mater. (Weinheim, Ger.)* **2010,** *22,* 3634–3649. doi:10.1002/adma.201000585
34. Hunter, C. A.; Sanders, J. K. M. *J. Am. Chem. Soc.* **1990,** *112,* 5525–5534. doi:10.1021/ja00170a016
35. Desiraju, G. R. *Acc. Chem. Res.* **2002,** *35,* 565–573. doi:10.1021/ar010054t
36. Whitesides, G. M.; Grzybowski, B. *Science* **2002,** *295,* 2418–2421. doi:10.1126/science.1070821
37. Simonsen, K. B.; Svenstrup, N.; Lau, J.; Simonsen, O.; Mørk, P.; Kristensen, G. J.; Becher, J. *Synthesis* **1996,** 407–418. doi:10.1055/s-1996-4216
38. Hasegawa, M.; Iyoda, M. *Bull. Chem. Soc. Jpn.* **2020,** *93,* 154–162. doi:10.1246/bcsj.20190283
39. Fesun, I. N.; Timoshenko, V. M.; Chernega, A. N.; Shermolovich, Y. G. *Russ. J. Org. Chem.* **2006,** *42,* 124–130. doi:10.1134/s1070428006010192
40. Zhao, J.; Jin, J.; Wu, C.; Jiang, H.; Zhou, Y.; Zuo, J.; Wang, X. *Analyst* **2010,** *135,* 2965–2969. doi:10.1039/c0an00338g
41. Enozawa, H.; Takahashi, T.; Nishinaga, T.; Kato, T.; Hasegawa, M.; Iyoda, M. *Bull. Chem. Soc. Jpn.* **2012,** *85,* 1120–1137. doi:10.1246/bcsj.20120135
42. Gomar-Nadal, E.; Rovira, C.; Amabilino, D. B. *Tetrahedron* **2006,** *62,* 3370–3379. doi:10.1016/j.tet.2006.01.056
43. Surpateanu, G. G.; Lungu, C. N.; Fourmentin, S.; Landy, D.; Surpateanu, G.; Avarvari, N. *Supramol. Chem.* **2009,** *21,* 372–378. doi:10.1080/10610270802017673
44. Bogdan, A.; Moraru, I.-T.; Auban-Senzier, P.; Grosu, I.; Pop, F.; Avarvari, N. *Molecules* **2022,** *27,* 6926. doi:10.3390/molecules27206926
45. Heuzé, K.; Fourmigué, M.; Batail, P. *J. Mater. Chem.* **1999,** *9,* 2373–2379. doi:10.1039/a902852h
46. Boumedjout, M.; Bendjeddou, A.; Abbaz, T.; Kaboub, L.; Gouasmia, A.; Villemin, D. *Phosphorus, Sulfur Silicon Relat. Elem.* **2016,** *191,* 891–897. doi:10.1080/10426507.2015.1114485
47. Lu, H.; Xu, W.; Zhang, D.; Zhu, D. *Chem. Commun.* **2005,** 4777–4779. doi:10.1039/b509133k
48. Lai, T.-L.; Pop, F.; Melan, C.; Canevet, D.; Sallé, M.; Avarvari, N. *Chem. – Eur. J.* **2016,** *22,* 5839–5843. doi:10.1002/chem.201600072
49. Rajput, L.; Banerjee, R. *Cryst. Growth Des.* **2014,** *14,* 2729–2732. doi:10.1021/cg500439f
50. Danila, I.; Riobé, F.; Puigmartí-Luis, J.; Pérez del Pino, Á.; Wallis, J. D.; Amabilino, D. B.; Avarvari, N. *J. Mater. Chem.* **2009,** *19,* 4495. doi:10.1039/b822884a
51. Danila, I.; Riobé, F.; Piron, F.; Puigmartí-Luis, J.; Wallis, J. D.; Linares, M.; Ågren, H.; Beljonne, D.; Amabilino, D. B.; Avarvari, N. *J. Am. Chem. Soc.* **2011,** *133,* 8344–8353. doi:10.1021/ja202211k
52. Jacobsen, C. S. Optical Properties. In *Semiconductors and Semimetals;* Conwell, E., Ed.; Academic Press: New York, NY, USA, 1988; pp 293–384. doi:10.1016/s0080-8784(08)62545-4
53. Akutagawa, T.; Abe, Y.; Nezu, Y.-i.; Nakamura, T.; Kataoka, M.; Yamanaka, A.; Inoue, K.; Inabe, T.; Christensen, C. A.; Becher, J. *Inorg. Chem.* **1998,** *37,* 2330–2331. doi:10.1021/ic971623p
54. Akutagawa, T.; Abe, Y.; Hasegawa, T.; Nakamura, T.; Inabe, T.; Christensen, C. A.; Becher, J. *Chem. Lett.* **2000,** *29,* 132–133. doi:10.1246/cl.2000.132
55. Tatewaki, Y.; Noda, Y.; Akutagawa, T.; Tunashima, R.; Noro, S.-i.; Nakamura, T.; Hasegawa, H.; Mashiko, S.; Becher, J. *J. Phys. Chem. C* **2007,** *111,* 18871–18877. doi:10.1021/jp074829c

License and Terms

This is an open access article licensed under the terms of the Beilstein-Institut Open Access License Agreement (https://www.beilstein-journals.org/bjnano/terms), which is identical to the Creative Commons Attribution 4.0 International License (https://creativecommons.org/licenses/by/4.0). The reuse of material under this license requires that the author(s), source and license are credited. Third-party material in this article could be subject to other licenses (typically indicated in the credit line), and in this case, users are required to obtain permission from the license holder to reuse the material.

The definitive version of this article is the electronic one which can be found at:
https://doi.org/10.3762/bjnano.17.63

BEILSTEIN JOURNAL OF NANOTECHNOLOGY

Materials challenges in solid-state sensors for continuous monitoring of ions in water

Maryam Darestani-Farahani and Peter Kruse*

Review

Open Access

Address:
Department of Chemistry and Chemical Biology, McMaster University, 1280 Main Street West, Hamilton, Ontario L8S 4M1, Canada

Email:
Maryam Darestani-Farahani - mary.df90@gmail.com; Peter Kruse* - pkruse@mcmaster.ca

* Corresponding author

Keywords:
aqueous ion sensors; biosensors; chemical sensors; nanomaterials; water quality monitoring

Beilstein J. Nanotechnol. **2026,** *17,* 935–973.
https://doi.org/10.3762/bjnano.17.66

Received: 13 March 2026
Accepted: 01 July 2026
Published: 27 July 2026

This article is part of the thematic issue "Nanotechnology for cross-scale analysis: comprehensive evaluation of water environments".

Guest Editors: Y. Sasaki and T. Minami



© 2026 Darestani-Farahani and Kruse; licensee Beilstein-Institut.
License and terms: see end of document.

Abstract

Accurate detection of ions in aqueous environments, ranging from trace to high concentrations, is essential for monitoring natural water resources, treatment facilities, and wastewater systems. Solid-state sensors have emerged as versatile platforms for this purpose due to their adaptability in geometry, compatibility with electronic integration, portability, and low energy requirements. A wide variety of active materials have been investigated, including metal oxides, graphene, carbon nanotubes, silicon nanowires, AlGaN/GaN, MXenes, transition metal dichalcogenides, and organic polymers all of which can be tailored for sensor development. Sensor selectivity and functionality can be enhanced through strategies such as defect engineering, nanoparticle doping, surface functionalization with organic molecules, or incorporation of advanced recognition elements like metal–organic frameworks, covalent organic frameworks, ion-imprinted polymers, and biomaterials. Hybrid nanocomposites and ion-selective membranes further expand the design space, enabling customized performance for specific applications. This review systematically examines the materials employed in solid-state ion sensors, their transduction mechanisms, and analyte interactions with sensing media, while critically evaluating advantages, limitations, fabrication approaches, and performance metrics. In addition, recent advances in sensor arrays are highlighted to demonstrate progress toward multiplexed detection. By consolidating these developments, this work provides a comprehensive framework to guide the rational selection of active and sensing materials for designing electrochemical and electrical devices capable of reliable, real-time ion monitoring in water.

Introduction

Access to clean water is critical for public health and ecosystem integrity. Traditionally, water quality monitoring has relied on periodic grab sampling and laboratory analyses. While useful, these methods only offer brief snapshots and may miss sudden changes or localized chemical shifts. For example, ion levels in natural, treated, or distributed water can change rapidly, within

minutes or hours, due to factors like storm runoff, treatment plant issues, pipe leaks, or ion exchange processes such as those in softening systems. Continuous online monitoring provides significant benefits in these situations. Without frequent monitoring, these fluctuations might go unnoticed until routine checks reveal a problem [1]. Additionally, many regulations such as WHO guideline values, the U.S. EPA National Primary Drinking Water Regulations and European Union set strict limits on ion concentrations, and real-time monitoring allows for early warnings and quick corrective actions [2-5]. In large-scale water systems, integrating widely deployed sensors with telemetry creates intelligent networks that enhance efficiency, identify issues like contamination or corrosion, and inform infrastructure decisions. Ultimately, online monitoring transforms water systems from passive sampling regimes to active management systems [1].

Electronic ion-sensing platforms including electrochemical (ion-selective electrodes (ISEs) [6,7], amperometric and voltammetric sensors) and electrical (field-effect transistors (FETs) [8-10] and chemiresistors [11]) are promising for online deployment due to their portability, low power, and amenability to automation and networking. To be fit for purpose in online monitoring, sensors must meet requirements that extend beyond laboratory figures of merit. (i) Selectivity is essential to discriminate targets in complex matrices containing abundant co-ions and natural organic matter; this requires an understanding of unwanted interferences for the system [8-10] and smart design, modification, and protection of the active surface according to the system. (ii) Sensitivity, limit of detection (LOD), and dynamic range must satisfy regulatory thresholds, for trace metals often in the low-micrograms-per-liter regime; for nutrients, typically milligrams per liter or lower [2,3,12]. (iii) Calibration stability and drift control are central for continuous operation because frequent recalibration is impractical. Sensors must maintain their performance over extended periods (weeks to months or even years) with minimal drift, or include self-calibration or diagnosis capability [7,13-15]. (iv) Response times should be fast to capture transients without excessive averaging. (v) Accuracy in a variable sensing matrix and with temperature fluctuations is required because real samples (biological fluids, environmental solutions, or industrial streams) differ widely in composition and operating conditions. In practice, this means the device must tolerate variations in ionic strength, pH, temperature, and fluid flow since these factors influence ion activity, binding equilibria, charge screening, and the electrical response of the transducer. (vi) Fouling resilience and mechanical stability are also important parameters. In real water systems, sensors are exposed to biofilm growth, particulate loading, scaling, and mechanical stress. Designs must mitigate fouling and maintain performance in spite of these conditions [16]. Finally, (vii) the sensor should be suitable for in situ (on-site) measurements and operate with low power requirements to support long-term use. It should also allow for automatic data recording and wireless data transmission, be housed in a durable and weather-resistant enclosure and operate reagent-free and with little or no routine maintenance. Ideally, the system should also support network connectivity to enable remote access and continuous monitoring [17].

In summary, electronic ion sensors especially ISEs, FETs, and chemiresistive devices, are central to next-generation online water quality monitoring. They offer sensitivity and selectivity aligned with regulatory thresholds, fast response to capture transient events, and the potential for dense spatial networks. Given these advantages, there are recent reviews highlighting rapid advances in all-solid-state ISEs [18], FET devices and electrochemical sensors for ion detection in water [19-21], and integrated systems that couple sensing with communications and analytics for field-deployable monitoring [22-24]. These are not going to be covered in this review. This review aims to critically assess the diverse classes of nanomaterials as active layer for electrodes, FETs, and chemiresistors, and as sensing element for these solid-state electronic sensors; this is to understand how different materials influence performance, stability, and applicability of the devices in continuous water quality monitoring. Here we provide an overview of application and device geometry of electrical sensors employed for online monitoring of ions in aqueous environments, with a focus on recent advancements in the materials utilized in water quality monitoring. Furthermore, the specific challenges associated with each class of sensing materials will be examined, followed by discussion of emerging strategies and innovative approaches to enhance their performance in water quality monitoring.

Review

Applications

The desired properties of sensor materials are driven both by the need for selective interaction with the analyte of interest in the relevant concentration range and the need for tolerating the presence of the analyte matrix. We therefore start with a brief overview of relevant areas of application for aqueous ion sensors. The rapid and continuous assessment of ionic species in natural water systems and drinking water, industrial water, wastewater, and swimming pools has become increasingly critical for ensuring water quality, detecting contamination events, and supporting process control in treatment facilities. Among the ions of primary concern, nutrients are widely monitored due to their roles in nutrient cycling, eutrophication, and as indicators of agricultural runoff and wastewater contamination [14,25,26]. Common cations and anions behave like persistent

fingerprints that can be used to track source water mixing, intrusion, or salinity variations [4,14,26,27]. Transition metal ions are important for evaluating corrosion, leaching, and industrial contamination in distribution systems and natural waters [28-30]. Continuous monitoring of these ionic species can provide early warnings of pollution events, treatment failures, or changes in source water chemistry, enabling rapid management responses. Recent developments in sensing technologies have made real-time and in situ measurements of these ions increasingly feasible, advancing toward integrated, data-driven water quality management [14,25,31].

Nutrients

Continuous monitoring of nitrate, nitrite, and ammonium is increasingly essential in drinking water, domestic wastewater, and industrial wastewater because these nitrogen species are contaminants that are subject to regulatory limits and serve as real-time indicators of treatment performance. In drinking water, nitrate and nitrite are regulated due to methemoglobinemia risks [32], with limits of 50 mg/L nitrate and 3 mg/L nitrite according to the WHO (Table 1) [2]. Ammonium is not universally regulated but is widely monitored because its presence promotes nitrification and indicates contamination or chloramination instability; online sensors typically require detection limits of 0.005–0.05 mg/L for nitrate and nitrite and ≈0.01 mg/L for ammonium to provide early warning in distribution systems (Table 1) [33,34]. In domestic wastewater, ammonium is the primary pollutant removed through nitrification, while nitrate and nitrite serve as operational markers of biological nitrogen removal; effluent limits commonly target 1–5 mg/L NH_4^+–N or 10–15 mg/L total nitrogen, necessitating online detection limits of 0.05–0.1 mg/L for nitrite and nitrate and 0.1–0.5 mg/L for ammonium to support aeration and carbon-dosing control [35-37]. In industrial wastewater, nitrogen moni-

Table 1: A list of nutrients and common cations and anions with their sources and their health and environmental effects together with the WHO guideline maximum value for drinking water.

Ion	Sources	Health and environmental effects	WHO guideline	Ref.
nitrate (NO_3^-)	fertilizers, septic leakage, agricultural runoff	high levels cause methemoglobinemia (blue-baby syndrome) in infants	50 mg/L	[2,57]
nitrite (NO_2^-)	intermediate in nitrification/denitrification, contaminated pipes	more toxic than nitrate; causes methemoglobinemia and blood oxygen transport issues	3 mg/L	[2,57]
ammonium (NH_4^+)	biological decay, sewage, fertilizers	indicates pollution; affects chlorination efficiency; high levels may affect taste/odor	0.5 mg/L (Rec)	[2,57]
sodium (Na^+)	natural minerals, seawater intrusion, softeners	high sodium intake is of concern for individuals with hypertension	200 mg/L (Rec)	[2,43]
potassium (K^+)	natural sources, fertilizers, softening processes	essential nutrient; toxic only at extremely high intake; no typical water toxicity	—	[2,43]
calcium (Ca^{2+})	natural minerals (limestone, gypsum)	essential mineral; contributes to water hardness; no known toxicity in water	—	[2,42]
magnesium (Mg^{2+})	natural minerals, seawater intrusion	essential mineral; excessive levels contribute to water hardness and laxative effects	—	[2,42]
fluoride (F^-)	natural groundwater, industrial emissions	prevents dental caries at low levels; causes fluorosis at high levels	1.5 mg/L	[2]
chloride (Cl^-)	natural salts, seawater intrusion, industrial waste	not toxic at normal levels; affects taste and corrosion	250 mg/L (Rec)	[2]
bromate (BrO_3^-)	formed during ozonation of water with bromide	carcinogenic (kidney tumors observed in animals)	0.01 mg/L	[49]
carbonate/hydrogen carbonate (CO_3^{2-}/HCO_3^-)	natural rock weathering; alkalinity	nontoxic; important for buffering capacity and pH stability	—	[51]
sulfate (SO_4^{2-})	natural minerals, mining, industrial discharge	high levels can cause diarrhea (especially with Mg/Na) and taste effects	500 mg/L (Rec)	[2]
phosphate (PO_4^{3-})	fertilizers, detergents, wastewater	not typically toxic at drinking-water levels; contributes to eutrophication in surface water	—	[56,57]

toring is particularly crucial in fertilizer and chemical production, food and beverage processing, aquaculture, mining, metal finishing, and semiconductor manufacturing, where ammonium, nitrite, or nitrate may represent regulated pollutants, corrosive agents, or indicators of process losses. Industrial analyzers therefore combine low detection limits (0.01–0.1 mg/L) with wide analytical ranges extending to hundreds of milligrams per liter, enabling control of both high-strength process streams and low-concentration effluents [38-40].

Common cations

Real-time, continuous monitoring of the major cations, sodium, potassium, magnesium, and calcium, is important because these ions control both salinity and hardness, which in turn affect health-related guidelines, aesthetics, and treatment performance. Regarding drinking water, the EU Drinking Water Directive and the WHO set a recommended value of 200 mg/L for sodium (primarily for taste and for individuals with hypertension, heart disease, or kidney problems). While there are no EU-wide limits for calcium and magnesium, they are managed via hardness and taste thresholds; WHO and related reviews report calcium taste thresholds of roughly 100–300 mg/L (as $CaCO_3$) and note that hardnesses above 200–500 mg/L as $CaCO_3$ are generally considered poor or unacceptable from an operational and consumer perspective (Table 1). Continuous cation monitoring in drinking water systems therefore benefits from low-milligram-per-liter detection limits (0.5–1 mg/L for Na^+ and K^+; 0.1–1 mg/L for Ca^{2+} and Mg^{2+}) so that utilities can detect deviations well below these operational thresholds and manage blending, softening, or desalination processes in real time [2,5,41-43]. In domestic wastewater, Na^+, Ca^{2+}, and Mg^{2+} govern bulk salinity and hardness, which strongly influence activated-sludge flocculation, nitrification, and sludge dewatering; experimental studies show that increased NaCl loads can alter flocculation and, at higher levels, inhibit biological treatment, while hardness (mostly Ca^{2+} and Mg^{2+}) can improve sludge flocculation strength and dewaterability. Here, online cation sensors with milligram-per-liter-level detection limits, with ranges extending to several grams per liter, are appropriate to follow storm-driven dilution and episodic saline shocks [44,45]. In industrial wastewater, continuous monitoring of these common cations is especially critical in high-salinity sectors, such as textile dyeing, tanning, petroleum and petrochemical processing, food and beverage production, desalination brine management, and coastal plants impacted by seawater intrusion, where Na^+, Ca^{2+}, and Mg^{2+} dominate salinity, affect membrane fouling, drive corrosion and scaling, and can inhibit biological nitrogen removal at elevated concentrations. In these applications, real-time cation measurements with broad dynamic ranges (from few milligrams per liter up to several tens of grams per liter as total dissolved salts) provide the resolution needed for proactive process control, early detection of saline upsets, and demonstration of compliance with site-specific salinity and hardness criteria [46-48].

Common anions

Common anions, including fluoride, chloride, bromate, sulfate, carbonate/hydrogencarbonate, and phosphate, strongly influence corrosivity, scaling, eutrophication risk, disinfection by-product formation, salinity, and regulatory compliance. In drinking water, several anions have strict health-based or operational limits under the EU Drinking Water Directive and WHO guidelines, including fluoride (1.5 mg/L) and chloride (250 mg/L), while bromate, a carcinogenic disinfection by-product, has a stringent maximum of 10 µg/L, requiring submicrogram-per-liter detection for early warning of ozone or advanced-oxidation-process upsets [2,5,49]. Continuous monitoring of alkalinity species (carbonate/hydrogencarbonate, phosphate) is also essential for controlling corrosion, buffering capacity, and softening processes (Table 1) [2,50-53]. In domestic wastewater, anions such as sulfate and chloride are key drivers of salinity that can inhibit nitrification at elevated levels [54,55], while phosphate is a regulated nutrient contributing to eutrophication; typical effluent limits in Europe and international guidelines require total phosphorus levels of ≤1–2 mg/L, making online orthophosphate monitoring with sub-milligram-per-liter detection limits vital [37,50,56-59]. In industrial wastewater, anion monitoring is especially critical in semiconductor manufacturing (fluoride, chloride, sulfate) [60,61], pulp and paper (chloride, sulfate) [62], textile dyeing (chloride, sulfate) [63], petrochemical and refinery operations (chloride, sulfate) [64], fertilizer and food industries (phosphate), and desalination plants (bromide/bromate and chloride) [5,65]. These sectors face both regulatory discharge requirements and process-control challenges, often necessitating continuous analyzers with detection ranges from low microgram per liter (e.g., bromate) to thousands of milligrams per liter (e.g., chloride or sulfate in industrial brines) [5]. Thus, real-time anion monitoring provides essential high-resolution data for maintaining regulatory compliance, protecting infrastructure, optimizing treatment processes, and mitigating environmental impacts across all water sectors.

Heavy metals

Lead, mercury, arsenic, chromium, cadmium, manganese, iron, nickel, and copper are important heavy metals. Lead, iron, and copper may enter drinking water due to the corrosion of plumbing materials in the distribution system. Mercury can also appear in the form of methylmercury, the most toxic and environmentally prevalent species, alongside its ionic form. Arsenic can naturally occur in groundwater and unlike most of metals,

which are typically present as cations, arsenic commonly exists as oxoanions (arsenite or arsenate). Other metals occur as oxoanions only in their higher oxidation states, notably chromium(VI) and manganese(VII), which form chromate (or dichromate) and permanganate [4,42,66,67].

Because toxicity, mobility, and regulatory relevance of many metals depend strongly on their oxidation state, it is essential to distinguish these species explicitly in both discussion and tabulated summaries. For example, Cr^{6+} is a carcinogenic ion with high mobility and strong oxidizing character, whereas Cr^{3+} is far less toxic, less mobile, and even an essential micronutrient at trace levels. A similar contrast exists for arsenic, where As^{3+} is more toxic, more mobile, and more weakly adsorbed, while As^{5+} is comparatively less toxic and more strongly retained by mineral surfaces. Iron and manganese also exhibit oxidation-state-dependent behavior: Fe^{2+} and Mn^{2+} are soluble under reducing conditions, whereas Fe^{3+} and Mn^{4+} readily precipitate as oxides, influencing both their detectability and their appearance or operational impacts in water systems. These distinctions are critical for sensor design because the target oxidation state determines the required detection chemistry and redox environment.

Their online monitoring is essential in drinking water, mining effluents, and domestic and industrial wastewater due to their toxicity and stringent regulatory limits. In drinking water, the EU Drinking Water Directive imposes very low maximum acceptable concentrations (MACs) such as for lead (10 µg/L), arsenic (10 µg/L), mercury (1 µg/L), chromium (50 µg/L), nickel (20 µg/L), manganese (50 µg/L), and copper (2 mg/L), necessitating online or high-frequency monitoring solutions with low-microgram-per-liter detection limits for early detection of contamination events, corrosion-release episodes, and treatment failures [5]. In domestic wastewater, heavy metals entering from sewer networks and industrial contributions can inhibit biological nutrient removal, impair sludge quality, and cause biosolids to fail land-application standards; although municipal effluent limits vary by Member State, typical discharge permits restrict metals to ranges of 1–100 µg/L for highly toxic species (Cd^{2+}, Hg^{2+}, Pb^{2+}, As^{3+}/As^{5+}) and 0.1–2 mg/L for Fe^{2+}/Fe^{3+}, Mn^{2}/Mn^{4+}, Ni^{2+}, Cu^{2+}, or Cr^{6+}/Cr^{3+} ions, requiring sensors capable of tracking both trace concentrations and episodic spikes [68-70]. In industrial wastewater, continuous heavy-metal monitoring is particularly critical in electroplating, battery manufacturing, semiconductor production, mining/metallurgy, chemical synthesis, pulp and paper, fertilizer production, petroleum refining, and textile dyeing, where metal concentrations can fluctuate rapidly and effluent limits are often extremely stringent (frequently <10–50 µg/L for Cd^{2+}, Hg^{2+}, Pb^{2+}, As^{3+}/As^{5+}, Cr^{6+}/Cr^{3+} ions). Monitoring ranges must therefore span from sub-microgram per liter for high-toxicity metals to tens of milligrams per liter for Fe^{2+}/Fe^{3+}, Mn^{2}/Mn^{4+}, Ni^{2+}, Cu^{2+} ions in industrial streams. Across all sectors, continuous heavy-metal monitoring enhances regulatory compliance, enables rapid response to contamination events, and supports process optimization and environmental protection in ways that intermittent grab sampling cannot [37,66] (Table 2).

Device geometries

To meet the increasing demand for real-time and in situ analysis, electrical and electrochemical sensors have gained prominence owing to their portability, low power consumption, and adaptability to complex aqueous matrices. Several device geometries of potentiometric, voltammetric, amperometric, field-effect transistor (FET)-based, and chemiresistive sensors have been explored for online water monitoring (Figure 1). Each sensor type differs in its transduction mechanism, structural configuration, and material composition, which ultimately influence its analytical performance, stability, and ease of integration into autonomous systems [22].

Potentiometric sensors, particularly ion-selective electrodes (ISEs), remain among the most established technologies for the detection of ionic species in water. As illustrated in Figure 1a, an ISE generally consists of a disk or planar electrode coated with a polymeric ion-selective membrane (ISM) containing an ionophore [75]. In ISEs, the potential changes at the membrane–sample interface against a reference electrode follow the Nernst equation allowing for selective detection of specific ions such as nitrate, potassium, and calcium [76]. For a monovalent ion at 25 °C, the theoretical Nernstian slope is ≈59.16 mV/decade of activity change, decreasing proportionally with temperature and scaling as 59.16/z for ions of charge z [77]. Modern solid-contact ISEs (SC-ISEs) replace the inner reference solution with a solid electron–ion transducer, typically based on conducting polymers or nanostructured carbon materials [76,78]. SC-ISEs convert the ionic potential formed at the membrane–sample interface into an electronic signal through one of three principal mechanisms: (1) Capacitive (electrostatic) transduction relies on high double-layer or pseudocapacitive charge storage at the solid contact; carbon nanotubes (CNTs) are a widely used material, which provides a large interfacial capacitance and excellent potential stability. (2) Redox (faradaic) transduction uses redox-active materials in which reversible electron-transfer reactions buffer potential changes, for example ferrocene-doped conducting polymers whose Fe^{2+}/Fe^{3+} redox couple provides a stable and reproducible interfacial potential. (3) Mixed ionic–electronic conduction occurs in materials such as PEDOT:PSS, which supports simultaneous ion and electron transport and transduces potential

Table 2: A list of dangerous heavy metals with their sources, their health and environmental effects, and the WHO guideline values for drinking water.

Metal ion	Sources of contamination	Health and environmental effects	WHO guideline value	Reference
lead (Pb^{2+})	corroding pipelines, batteries, industrial effluents, paints, mining	strong neurotoxin; lowers IQ in children; cardiovascular, kidney, and reproductive toxicity	0.01 mg/L	[2,71,72]
mercury (Hg^{2+})	mining, coal combustion, industrial waste, dental/medical waste	severe neurotoxicity; kidney damage; bioaccumulates as methylmercury in aquatic life	0.006 mg/L	[2,71,72]
arsenic (As^{3+})	natural groundwater leaching, mining, pesticides, industrial waste	carcinogenic (skin, bladder, lung); skin lesions; cardiovascular disease; developmental toxicity	0.01 mg/L for total arsenic	[2,71,72]
arsenic (As^{5+})	oxidized groundwater, industrial discharge, agricultural chemicals	less toxic than As^{3+} but still carcinogenic with long-term exposure; associated with skin, bladder, and lung cancers; more strongly adsorbed in soils, making it comparatively less mobile	0.01 mg/L for total arsenic	[2,71,72]
chromium (Cr^{6+})	leather tanning, electroplating, stainless steel industry, pigments	Cr^{6+} is carcinogenic; causes DNA damage, skin irritation, gastrointestinal injury	0.05 mg/L for total chromium	[2,71,72]
chromium (Cr^{3+})	natural minerals, steel industry, leather tanning	essential trace nutrient at low levels, but excessive exposure may cause skin irritation and organ toxicity; considerably less toxic and less mobile than Cr^{6+}	0.05 mg/L for total chromium	[2,71,72]
cadmium (Cd^{2+})	mining, batteries, fertilizers, electroplating, waste disposal	kidney damage, bone demineralization, carcinogenic, bioaccumulative	0.003 mg/L	[2,71,72]
manganese (Mn^{2+})	natural geology, mining, wastewater, industrial runoff	essential nutrient but toxic at high levels; neurological impacts; affects childrens' cognitive development	0.08 mg/L	[2,73]
manganese (Mn^{4+})	oxidized water systems; strong oxidants used in water treatment; industrial discharge	occurs as insoluble MnO_2 in oxidized waters, less toxic than Mn^{2+}, elevated Mn^{4+} particulates can cause discoloration, turbidity, and deposition in pipes, and may release Mn^{2+} under reducing conditions	0.08 mg/L for total manganese	[2,73]
iron (Fe^{2+})	natural soil/rock erosion; corroded iron pipes; groundwater under reducing conditions	not highly toxic but causes aesthetic issues, promotes bacteria, can cause oxidative stress when very high	(Rec) 0.3 mg/L for total iron	[2,66]
iron (Fe^{3+})	oxidized water systems, industrial discharge, corroded infrastructure	less soluble than Fe^{2+} and tends to precipitate as iron oxides; lower direct toxicity, but excessive levels can cause turbidity, pipe scaling, discoloration, and ecological imbalance in aquatic systems	(Rec) 0.3 mg/L for total iron	[2,66]
nickel (Ni^{2+})	electroplating, stainless-steel corrosion, industrial discharge	dermatitis, respiratory problems, possible carcinogenicity; toxic to aquatic organisms	0.07 mg/L	[2,74]
copper (Cu^{2+})	corroded copper pipes, mining, industrial effluents	essential nutrient but harmful at high levels; liver/kidney damage; toxic to fish and aquatic life	2 mg/L	[2,66,72]

changes via modulation of the polymer oxidation state. Together, these mechanisms enable SC-ISEs to achieve stable, Nernstian ion detection without an internal liquid junction. These sensors are cost-effective and energy-efficient for continuous field operation, although potential drift and water-layer formation can affect long-term stability [79]. The requirement for a reference electrode, however creates severe challenges in stability, miniaturization, and long-term maintenance [13]. Solid-contact nitrate-selective electrodes and valinomycin-based K^+ ISEs integrated on chips for environmental waters are some examples of ISEs [7].

As shown in Figure 1b, voltammetric and amperometric devices share a three-electrode geometry, comprising a working, reference, and counter electrode, often implemented as planar screen-printed electrodes suitable for integration in flow

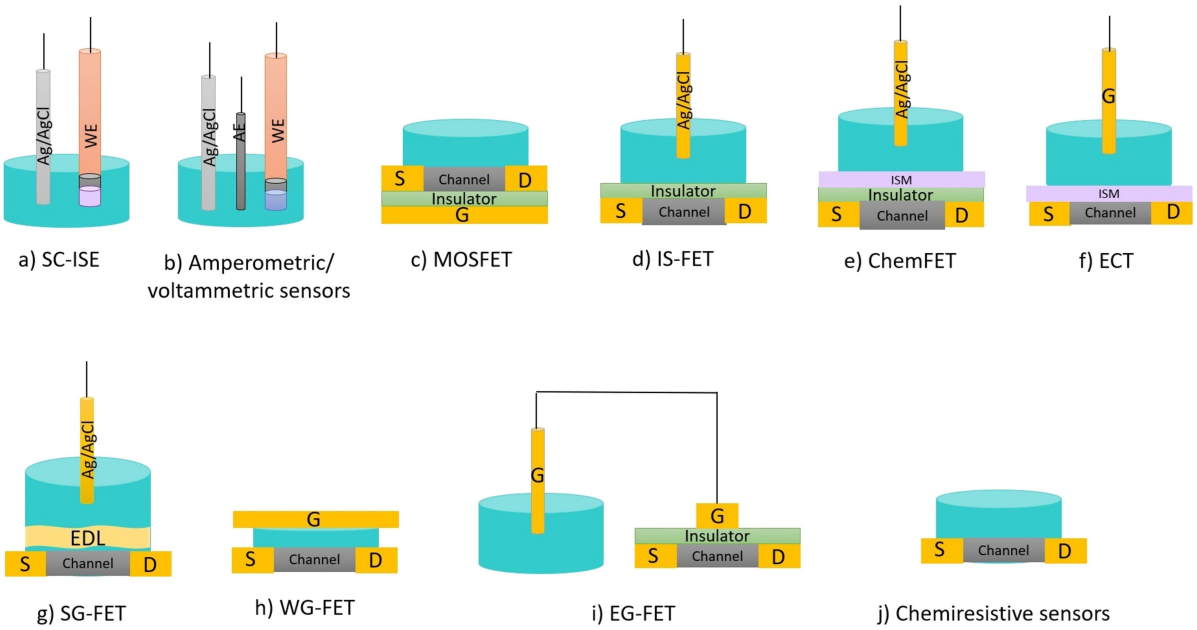


Figure 1: Schematic overview of major electrochemical and electrical sensor geometries for ion detection. (a) Solid-contact ion-selective electrodes (SC-ISEs) with no internal filling solution in working electrode covered with a layer of ISM (ion-selective membrane in purple color; uses solid transducer, (b) amperometric/voltametric sensors, (c) metal-oxide-semiconductor FETs (MOSFETs) with back-gated geometry, (d) ion-sensitive FETs (IS-FETs) which oxide surface directly exposed to electrolyte, (e) chemical FETs (ChemFETs) with ion-selective membrane on top of IS-FET, (f) electrochemical transistors (ECTs) that volumetric ion penetration modulates channel, (g) solution-gated FETs (SG-FETs) with EDL gating at channel–electrolyte interface, (h) water-gated FETs (WG-FETs) in which thin water layer acts as gate dielectric, (i) extended-gate FETs (EG-FETs) with an external sensing electrode connected to the MOSFET gate, and (j) chemiresistive sensors. Used symbols are S = source; D = drain; G = gate; Ag/AgCl = reference electrode; WE = working electrode; AE = auxiliary electrode; ISM = ion-selective membrane; EDL = electric double layer.

systems. In voltammetry, the applied potential is scanned, and the resulting current response indicates the redox behavior of the analyte [80]. Amperometric sensors, by contrast, operate at a fixed potential and measure a steady-state current proportional to analyte concentration [81]. These sensors are particularly effective for redox-active species or, when coupled with enzymatic films, for indirectly measuring ions such as nitrate or phosphate. While they offer fast response times and high sensitivity, electrode fouling and matrix interference can limit their durability in continuous operation. Anodic stripping voltammetry (ASV) sensors build upon this principle, employing thin-film working electrodes (e.g., bismuth or gold films) that enable preconcentration of trace metal ions before measurement [82]. The ASV process involves two stages: (1) deposition, where metal ions are reduced and plated onto the electrode surface, and (2) stripping, where oxidation peaks are recorded and quantified [82,83]. This approach allows for detection at nanomolar levels and is widely applied for Pb^{2+}, Cd^{2+}, and Cu^{2+} monitoring in natural waters. The geometry is typically planar and flow-through compatible, but periodic electrode renewal and electrolyte control are necessary for consistent field use [82]. Pb^{2+} and Cd^{2+} determination in natural waters using bismuth-based ASV electrodes is an example of this method for ion detection [84].

Field-effect transistor (FET)-based sensors represent a different class of solid-state devices in which the conductivity of a semiconductor channel is modulated by changes in the surface potential at an electrolyte–gate interface [85]. FET platforms can lead to fast, miniaturized, CMOS-compatible devices (complementary metal-oxide-semiconductor, a common fabrication process for integrated circuit chips) [8-10]. Figure 1c–i illustrates the major FET geometries, each differing in how the gate potential is applied and how the analyte interacts with the channel. It includes metal-oxide-semiconductor FETs (MOSFETs), ion-sensitive FETs (IS-FETs), chemical FETs (ChemFETs), electrochemical transistors (ECTs), solution-gated FETs (SG-FETs), water-gated FETs (WG-FETs), and extended-gate FETs (EG-FETs). In MOSFET-based devices, the gate terminal, typically a metal or another conductive material, is coated with an insulating layer, often the corresponding metal oxide, and the semiconductor channel is exposed to the solution. A gate voltage is externally applied perpendicular to the channel and can be tuned or swept. Interactions between the analyte and the channel modify the electrostatic environment of the channel. This modification alters the channel conductance and changes its dependence on the applied gate voltage. Consequently, variations in the device transfer characteristics can be correlated with the analyte concentration (Figure 1c). An ion-

sensitive FET (ISFET) is a modified MOSFET designed so that its insulator (often a metal oxide) on top of the channel is directly exposed to the solution. The electrolyte and a reference electrode form the gate (Figure 1d). The sensor directly responds to surface chemical reactions (protonation/deprotonation of –OH groups) that change oxide surface potential and shift the threshold voltage. Due to this mechanism, highly sensitive and stable IS-FETs for pH monitoring are reported that are CMOS-compatible and can be miniaturized, but this type of FET suffers from poor selectivity to other ions present in water [86-89]. Chemical FETs (ChemFETs or ISM-FETs) incorporate ISMs (containing ionophores) on top of the metal oxide of IS-FETs to solve this problem (Figure 1e). Target ions bind to ionophores in the membrane and generate a membrane potential relative to the fixed potential of a reference electrode, thus modulating the underlying IS-FET threshold voltage. ChemFETs are selective and sensitive devices. For example, Joly et al. developed a ChemFET microsensors to detect NO_3^- and NH_4^+ achieving near-Nernstian slopes in liquid and soil phases [90]. It should be considered that incorporating a membrane, as opposed to allowing direct analyte interaction with the sensing surface, tends to increase signal drift due to membrane aging and ionophore leaching, while it can also reduce the sensor's response speed and its lifetime.

Electrochemical transistors (ECTs) are another type of FETs that translate ionic activity in a solution directly into amplified electronic signals. Their channels are commonly coated with ISMs to increase their selectivity (Figure 1f). ECTs rely on volumetric ion penetration into an active channel (often a mixed ionic–electronic conductor), which modulates its conductivity through redox or doping/de-doping processes. This typically yields high transconductance, strong signal amplification, and excellent sensitivity at low operating voltages, though it can introduce slower response times and long-term drift due to ion trapping or material swelling [91,92]. In contrast, solution-gated FETs (SG-FETs) have a geometry that use an electrolyte as the gate dielectric, and ions modulate the surface potential at the semiconductor–electrolyte interface without penetrating the channel. In these devices, the channel between the source and drain is directly exposed to the analyte solution, and gating occurs through the electric double layer (EDL) that forms at the interface between the channel surface and the electrolyte (Figure 1g). A reference electrode is required to apply the gate voltage, which modulates the EDL capacitance for electrostatic control of the channel. Due to their large EDL capacitance, these devices work well with 2D materials and show ultrahigh sensitivity; they are therefore suitable for determining trace concentrations of heavy metals. The drawback of this device geometry is its susceptibility to contamination and drift as well as its sensitivity to ionic strength fluctuations of the solution (Debye screening) [93,94]. This interfacial gating enables fast, reversible responses and good stability, especially with materials like graphene or CNT networks, but the signal amplification is generally lower because modulation is confined to the surface rather than the bulk. Water-gated FETs (WG-FETs) represent a sub-type of SG-FETs in which a thin layer or droplet of water or electrolyte covers the channel and acts as the gate insulator (Figure 1h). Instead of a reference electrode, a metal electrode is placed in contact with the water layer (or positioned above it) as a gate electrode. This geometry allows for stable operation in aqueous environments and enables continuous monitoring of bulk solution properties, though it similarly faces challenges with interference from electrolyte composition and long-term stability.

Overall, to design a FET sensor for aqueous environments, factors such as ionic strength, fouling, and long-term stability dominate design choices. In electrolytes with realistic ionic strengths, the Debye screening length shrinks to ≈1 nm, which suppresses FET responses to charges located further from the channel; this is the core challenge for liquid-phase FET sensing. Practical routes include lowering ionic strength (when acceptable), using small receptors (aptamers) and porous/charge-excluding coatings (like ChemFETs), nano-confinement, or device formats such as the extended-gate FET (EG-FET) configuration. An EG-FET is a conventional MOSFET device with the gate contact electrically connected to an external sensing electrode, which may consist of glass, Ag/AgCl, or oxide materials, and can also be coated with an ion-selective membrane (Figure 1i). The sensing element is physically separated from the MOSFET, and the potential generated at the external electrode modulates the transistor. A key advantage of the EG-FET architecture is its ability to compensate for environment-induced signal drift. With the EG-FET geometry, the MOSFET is protected from corrosion, and the metal electrode can easily be functionalized or replaced with another electrode. Thus, this device is cost-effective, since it requires only a standard MOSFET and a replaceable electrode, and it offers robustness with the flexibility to easily exchange the sensing head. However, drawbacks include increased parasitic capacitance and higher noise levels due to additional wiring, and the design is not well suited for nanoscale integration [95].

All ion-sensing FET devices inherently require a gate electrode, which is implemented as a reference electrode in many geometries to provide a stable and well-defined electrochemical potential. Incorporating such a reference element brings both advantages and constraints. On the one hand, a stable reference electrode helps decouple the transistor from fluctuations in the sample matrix, improving baseline stability, reducing drift, and enabling more reproducible measurements in complex aqueous

environments. This stability is especially valuable when dealing with variable ionic strengths, biofouling, or long-term continuous monitoring, where uncontrolled potential shifts would otherwise dominate the signal [96]. On the other hand, integrating a reference electrode into a compact sensor platform introduces practical challenges. Maintaining a constant potential requires careful material choice, hydration control, and sometimes bulky internal electrolyte reservoirs, all of which complicate miniaturization and packaging. Additionally, adding a separate reference element increases wiring, parasitic capacitance, and mechanical complexity, making it harder to achieve robust, field-deployable devices with consistent performance [29,97].

Chemiresistive sensors, in contrast, use a simpler two-electrode geometry, commonly interdigitated microelectrodes bridged by a conductive sensing film composed of materials such as graphene, reduced graphene oxide, CNTs or conducting polymers (Figure 1j) [11,98-102]. Adsorption or complexation of ions alters the film's resistance, producing a measurable signal. Selectivity arises from the chemical modification of the sensing layer with specific functional groups or chelating agents [42]. These sensors offer low-cost fabrication, easy scalability, and compatibility with printed and microfluidic systems, although their performance can be affected by baseline drift, and cross-sensitivity to ionic strength [11]. Chemiresistors easily integrate with ISMs, as it was recently reported that membrane-coated devices can achieve low-microgram-per-liter detection of Pb^{2+} in water, hinting at practical continuous monitoring of priority metals [11,103,104].

Each method of detection and sensor geometry has distinct advantages and limitations. Membrane-coated sensors including SC-ISEs, ChemFETs, ECT, and ion-selective chemiresistive sensors are well-suited for long-term, continuous measurements of ion activity due to their selectivity and compact integration. ASV provides high sensitivity for trace metal ions, while amperometric and voltammetric sensors deliver rapid kinetic responses for electroactive analytes [22]. Ongoing advancements in material science and studies on nanostructured interfaces significantly improved the quality of these electronic sensors, which will be discussed in detail in the following sections.

Active layer materials for electrodes, FETs, and chemiresistors

For effective ion sensing in aqueous media, a channel material for a FET sensor must combine several key attributes. First, high interfacial sensitivity at low voltage, manifested as a large transconductance ($\mu \cdot C$) for thin channels and strong coupling through the EDL in electrolyte gating, is essential for detecting small changes in the ion-induced surface potential. Second, for accurate and reliable ion sensing, the transistor channel material must not chemically degrade or react with the aqueous environment, must minimize charge-trapping-related noise and hysteresis through clean and defect-controlled interfaces, and must maintain stable electronic properties over time so that any electrical signal change reflects only the analyte concentration, not material instability. Third, the material's surface must allow for functionalization, enabling integration with chelators and/or ion-selective membranes to create a selective binding layer for analyte detection. Finally, processability and scalability of the material are important considerations [105]. For practical ion-sensing platforms, materials must be compatible with mass-producible, reproducible, low-cost, and reliable fabrication techniques. The material choice is therefore influenced not only by performance metrics (sensitivity, limit of detection, selectivity, stability) but also by how easily, inexpensively, and reliably it can be produced, patterned, and integrated into devices at scale. In the case of chemiresistors, the channel should also offer a large accessible surface area to maximize adsorption-induced conductance change. In addition, it should be engineered to operate near the percolation threshold, where charge transport is dominated by a small number of critical junctions, thereby enabling high transduction gain from small adsorption events [106]. The active layer of an electrochemical electrode should provide high electrochemical activity with efficient ion and electron transport, ensuring fast charge/discharge kinetics. It must also maintain chemical stability and mechanical integrity during repeated cycling to deliver long-term performance [107].

Inorganic materials

Semiconducting metal oxides. Metal-oxide thin films (such as ZnO, SnO_2, IGZO, In_2O_3) are classified as classic inorganic semiconductors with a wide bandgap (3–4 eV). The surface of a semiconducting metal oxide is its most chemically active region that can have a significant impact on the electronic structure of the material. Because metal oxides combine metal cations and oxygen anions with partly ionic bonding, their surfaces behave very differently from covalent semiconductors like silicon. Surface atoms tend to rearrange, react, or adsorb species to reduce surface free energy, leading to non-ideal, defect-rich surfaces. These defects often cause the film to be n-type doped and form surface states inside the bandgap, affecting charge trapping, catalytic activity, and sensing behavior. Due to their structure, charge transfer in metal oxide semiconductor channels is strongly influenced by their defect chemistry, surface adsorbates, and polaronic transport behavior. Charges primarily transfer through defect-induced n-type conduction by a combination of band-like transport and polaron hopping. The charge transfer gets heavily modulated by surface adsorbate interac-

tions and grain boundary barriers. Metal oxides typically show conductivities of 10^{-6}–10^{2} S/m, mobilities of 0.1–50 $cm^2/V{\cdot}s$, and electron concentrations of 10^{16}–10^{19} cm^{-3}. These values shift dramatically with oxygen vacancies, doping, and microstructure. The specific surface area of sensing semiconducting metal oxides (SMOs) is in a range of 20–200 m^2/g depending on their degree of porosity and nanostructuring [108,109].

As an example of an SMO-based device, a WG-FET based on a SnO_2 thin-film channel was developed for the selective detection of Pb^{2+} and Cu^{2+} ions in water [110]. The device employed a clinoptilolite-filled, plasticized PVC membrane as an ion-selective layer, which generates a potential difference between the sample and reference pools (Figure 2). This potential modulates the threshold voltage (ΔV_{th}) of the SnO_2 transistor, with the shift following a Langmuir–Freundlich isotherm that reflects heterogeneous ion-binding behavior. The WG-FET exhibited a rapid response at low ion concentrations and signal saturation at higher levels, achieving detection limits of 0.9 nM for Pb^{2+} and 14 nM for Cu^{2+}, both well below the WHO regulatory limits [110]. Because metal-oxide thin films typically exhibit lower conductivity, carrier mobility, and surface area than 2D materials such as graphene or CNTs, integrating them with a highly conductive 2D component allows the hybrid structure to leverage the superior electronic and interfacial properties of the 2D material for effective online ion sensing in electrochemical and electronic devices. Arora et al. demonstrated that combining ZnO with graphene can result in a highly sensitive FET device for Pb^{2+} detection [111]. Integration of conductive graphene with semiconducting ZnO significantly reduces the ZnO bandgap (from ≈3.7 eV to ≈2.2 eV), thereby enhancing charge transfer and overall electrochemical activity. The homogeneous dispersion of nanoscale ZnO on graphene provides a large active surface area for Pb^{2+} adsorption and reduction, resulting in improved sensitivity. Cyclic voltammetry reveals that the redox current varies linearly with the square root of the scan rate, confirming a diffusion-controlled electrochemical process. Additionally, the graphene–ZnO nanocomposite lowers the reduction potential of Pb^{2+} compared to a bare glassy carbon electrode, facilitating electron transfer. Collectively, these effects, bandgap narrowing, increased surface area, and synergistic catalytic activity, make the graphene–ZnO nanocomposite a sensitive and selective film for detecting trace lead ions in aqueous environments [111].

Although metal oxides have good chemical stability and exhibit robust semiconducting behavior with high transconductance,

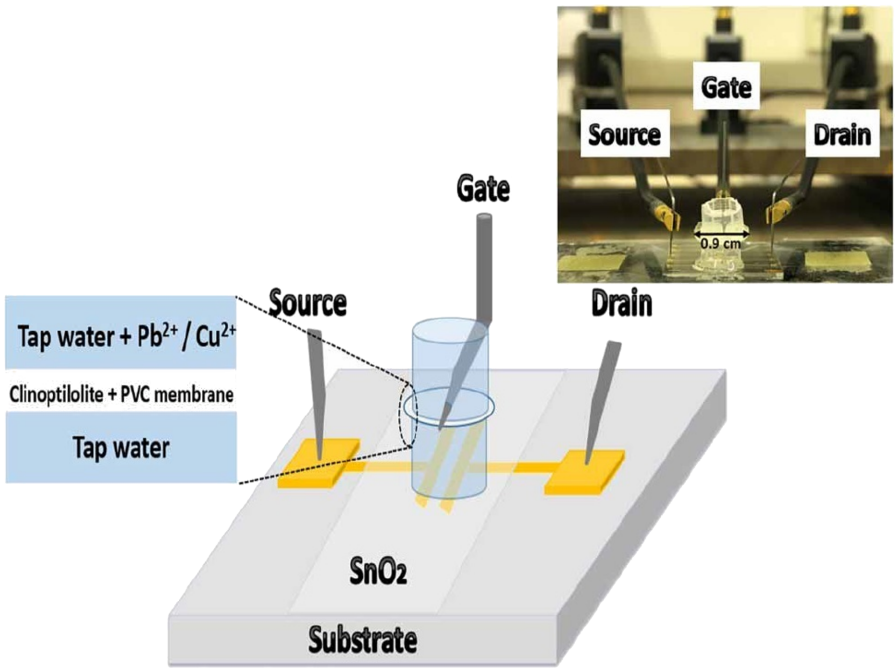


Figure 2: Design of a water-gated field effect transistor sensor. The inner "tap water" pool acts as a reference against the outer "sample" pool. Source and drain transistor contacts are contacted by tungsten needles mounted on Karl Suss probeheads. A third probehead is used to immerse another tungsten needle into the water in the sample pool to provide a gate contact. Inset: photograph of clinoptilolite-sensitised SnO_2 WG-FET sensor platform. Figure 2 was reproduced from [110] (© 2020 Z. Alqahtani et al., published by IWA Publishing, distributed under the terms of the Creative Commons Attribution 4.0 International License, https://creativecommons.org/licenses/by/4.0).

making them good candidates for gas and pH sensing [112,113], their high density of surface states makes sensing in aqueous environments challenging. A high density of surface states can cause charge scattering effects, which decrease the charge mobility while increasing contact resistance, noise, and hysteresis. The FET device can be designed in a way that mitigates these issues, but at the cost of increased complexity. Nonetheless, detection of trace concentrations of heavy-metal ions in real water has already been practically demonstrated by metal-oxide-based electrochemical methods in a much simpler way than the design and fabrication process needed for metal-oxide FET devices. ASV on inexpensive screen-printed electrodes routinely achieves sub-parts-per-billion LODs and has already been packaged for in situ and portable use. For instance, a cost-effective electrochemical sensor based on Fe_3O_4/MWCNTs/LSG composites functionalized with chitosan was fabricated for the simultaneous detection of Cd^{2+} and Pb^{2+} using ASV. The in situ bismuth film deposition enabled ultralow detection limits of 0.1 µg/L (Cd^{2+}) and 0.07 µg/L (Pb^{2+}) [114]. That is why the field of ion sensing by metal-oxide FETs has developed more slowly.

In terms of device fabrication, metal oxides often endure harsh aqueous conditions (acidic and alkaline) better than many organics, making them favorable for long-term deployment. They have well-established fabrication methods (thin films, sputtering, ALD, solution deposition) [115]. They also face some challenges in sensing; for instance, in high-ionic-strength aqueous media, the Debye screening length can be very short (<1 nm). Hence, ion-to-channel coupling often relies on an ion-selective membrane that will be in a ChemFET geometry or a remote gate with a EG-FET geometry rather than direct ion adsorption on the oxide. This complicates device architecture. Fabrication and processing may need high temperatures or vacuum deposition to achieve high-quality films, which can limit inexpensive, printed deployment [28].

Graphene. Single-layer graphene, few-layer graphene (FLG), and bulk graphene differ in structure and properties, which affect their sensing performance. Single layer graphene is extremely surface sensitive because every atom is at the surface. It has a low density of electronic states near its Dirac point; thus, even minor changes in surface charge can shift its Fermi level significantly, making it highly responsive to external stimuli. Molecules or ions with electric dipoles can therefore easily shift the Fermi level electrostatically. However, its predominantly basal-plane surface, limited density of electrochemically active edge sites, and susceptibility to chemical and mechanical degradation often lead to signal instability in liquid-phase sensing. In contrast, FLG, typically comprising two to five stacked graphene layers, provides improved structural robustness and reduced noise while retaining high electrical conductivity. The increased edge density and defect accessibility in FLG facilitate faster electron transfer kinetics and enhanced electrochemical activity, making it especially suitable for electrochemical sensing platforms. Bulk (multilayer) graphene, which approaches graphite-like behavior, offers excellent mechanical stability and ease of fabrication but suffers from reduced surface accessibility, interlayer charge screening, and slower charge-transfer processes, resulting in lower sensitivity. Thus, it can be concluded that FLG represents the optimal compromise between sensitivity, stability, and electrochemical performance for practical sensing applications [116]. FLG typically shows conductivities of 10^4–10^5 S/m, mobilities of 1,000–50,000 $cm^2/V{\cdot}s$, and a sheet carrier density of 10^{12}–10^{13} cm^{-2}. Its specific surface area ranges from 300 to 800 m^2/g. Graphene conducts via band-like transport of delocalized π-electrons, with extremely high mobility. Charge transfer from adsorbates or ions occurs by electron donation or withdrawal, shifting the Fermi level and modulating carrier density. Hopping transport only occurs if graphene is heavily defected (e.g., reduced graphene oxide, rGO) [117]. Graphene is a strong channel candidate for FET devices because its atomically thin, all-surface conduction enables very good coupling to the electric double layer under electrolyte gating, yielding large transconductance at low bias and high sensitivity to ion-induced interfacial potential changes. In practice, graphene (and rGO) integrates readily with ion-selective membranes, which localize the recognition event within the Debye length and translate ion activity into reproducible shifts in the Dirac point [118].

Chen et al. developed a rGO-based FET sensor for detection of nitrate ions in water. The device employs rGO nanosheets as the conductive channel, functionalized with benzyltriethylammonium chloride (TEBAC), whose quaternary ammonium groups exhibit strong electrostatic affinity for nitrate ions. The TEBAC molecules are immobilized on rGO via π–π interactions, forming a stable hybrid sensing layer. Upon exposure to nitrate, electrostatic binding between NO_3^- and the $-N^+(CH_2CH_3)_3$ sites induces electron transfer and redistribution within the rGO/TEBAC interface (since nitrate ions have a delocalized π bond due to the p_z orbitals from nitrogen and oxygen atoms, after adsorption onto the TEBAC probe, they interact with the electron cloud of the rGO nanosheets), leading to a modulation of carrier density and a measurable decrease in channel conductance (due to the fact that rGO material is p-doped). This transduction process enables the device to rapidly (2–7 s) achieve an ultralow limit of detection (4.9 µg/L NO_3^-) with excellent selectivity against competing anions (Cl^-, SO_4^{2-}, CO_3^{2-}). The sensor's performance, reusability through simple NaCl regeneration, and enzyme-free design underscore

its potential as a robust, low-cost platform for real-time nitrate monitoring in water [119].

Also, ultratrace nitrate detection was proposed with an interdigital graphene-FET integrated with a nitrate-sensitive membrane (Figure 3). The sensing mechanism relies on selective complexation of nitrate ions with ionophores within the ISM, which generates a membrane potential proportional to the nitrate concentration according to the Nernst relation. This potential modulates the graphene surface potential, shifting its Fermi level and producing a measurable Dirac point displacement ($\Delta V_{\mathrm{Dirac}}$) in the transfer characteristics. Optimization of the graphene channel geometry and ISM thickness enhances the device transconductance, amplifying its response to ionic potential changes. The resulting electrical signal, expressed as a linear Dirac point shift with logarithmic dependence on nitrate concentration, enables precise quantitative detection with a low limit of detection (0.041 ppt; 4.8×10^{-13} M), a wide linear range (0.1 ppt to 100 ppm), and Nernstian sensitivity (≈28 mV/decade), with excellent selectivity against common anions and validated performance in real water samples [17].

Graphene's processability as inks and large-area films also supports scalable arrays and simple chemiresistive formats, further underscoring its suitability for practical sensing application [11]. Despite graphene's advantages, it exhibits several intrinsic limitations that can hinder its effectiveness as a FET channel material. Its zero bandgap results in intrinsically low on/off current ratios, high off-state leakage, and excessive static power waste, preventing reliable digital switching performance. Efforts to induce a bandgap, such as graphene nanoribbons, bilayer gating, or strain engineering, inevitably degrade mobility and increase scattering. Device performance is further limited by strong sensitivity to substrate interactions (e.g., charge traps, phonon scattering, and impurities on SiO_2), which introduce noise and variability. High and inconsistent metal–graphene contact resistance, arising from Fermi-level pinning and the absence of a semiconducting gap, also hampers reproducible device operation. Moreover, fabrication processes

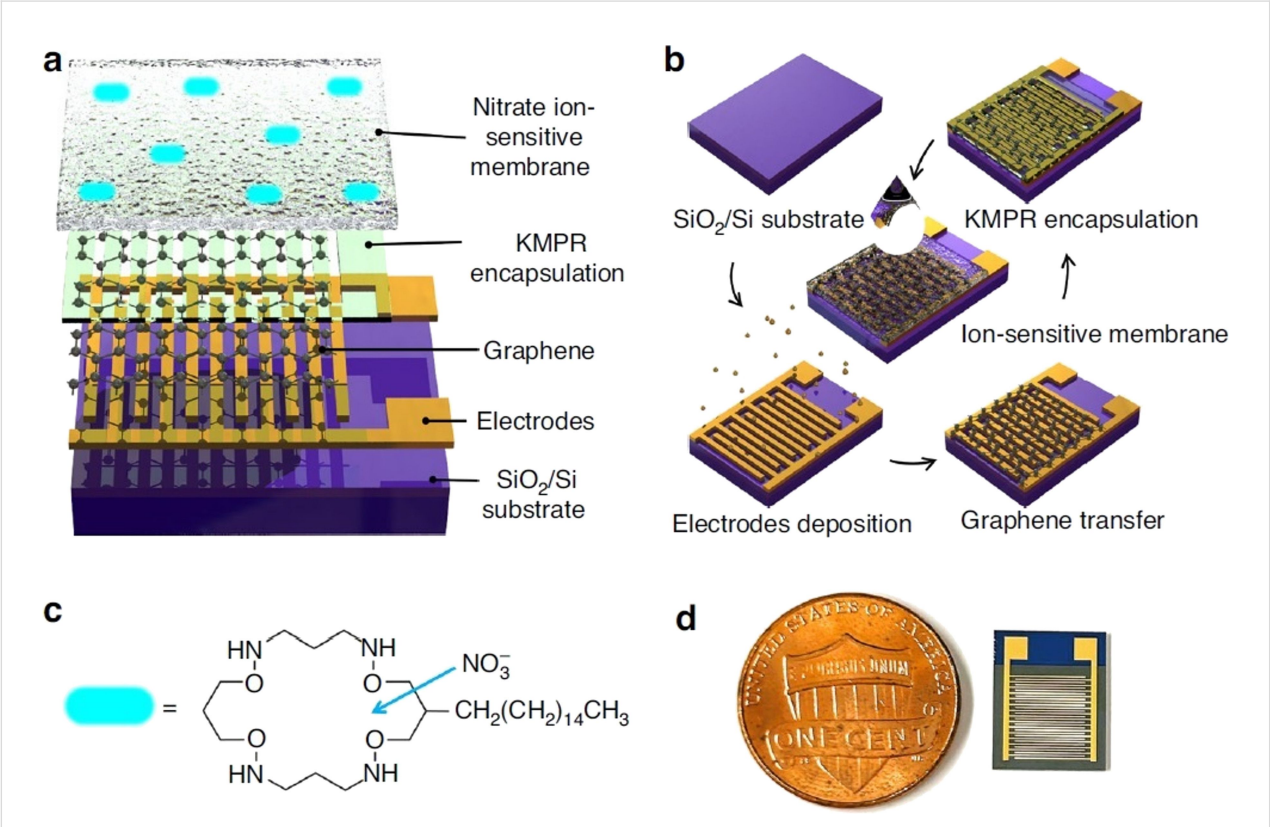


Figure 3: Structure and fabrication of graphene ion-sensitive field-effect transistors (ISFETs). (a) Schematic illustration of the structure of the devices. (b) Fabrication flow chart. Preparation of SiO_2 substrate. E-beam deposition of Cr/Au source-drain electrodes. CVD graphene transfer. Device encapsulation via KMPR negative photoresist. Device dicing and a nitrate ion sensitive membrane deposition. (c) Chemical structure of nitrate ionophore. (d) Optical image of an individual graphene ISFET beside of one cent coin. Figure 3 was reproduced from [17] (© 2024 Y. Xu et al., published by Springer Nature, distributed under the terms of the Creative Commons Attribution 4.0 International License, https://creativecommons.org/licenses/by/4.0).

often leave polymer residues and adsorbates that deteriorate electronic quality, and large-area CVD graphene suffers from structural non-uniformities, including grain boundaries, wrinkles, and non-uniform doping, that create substantial device-to-device variability [120]. Beyond these limitations, studies found how graphene's high mobility, chemical functionalizability and compatibility with extended-gate layouts help overcome screening and drift in complex electrolytes and make it suitable for electrical and electrochemical sensing [117,120,121].

Carbon nanotubes. Carbon nanotubes (CNTs) are one-dimensional nanostructures composed of seamless cylinders of sp^2-bonded carbon atoms formed by rolling up graphene sheets, with their material properties governed primarily by the number of walls, diameter, chirality, and defect structure. Single-walled carbon nanotubes (SWCNTs) consist of a single graphene cylinder with complete surface exposure and a highly anisotropic, chirality-dependent electronic structure with either metallic (zero bandgap) or semiconducting (a bandgap of 0.5–1.5 eV) character, resulting in favorable intrinsic electrical and mechanical properties but relatively low robustness. Double-walled carbon nanotubes (DWCNTs), comprising two concentric graphene shells held together by van der Waals interactions, exhibit a hierarchical architecture in which the outer wall dictates surface chemistry while the inner wall enhances mechanical integrity and stabilizes charge transport. Multi-walled carbon nanotubes (MWCNTs) are composed of multiple concentric shells or a scroll-like structure, display predominantly metallic behavior, and outstanding mechanical strength and chemical durability, though with reduced surface accessibility of inner walls. Across all CNT types, SWCNTs are ideal for ultrasensitive electrical detection, DWCNTs provide a balanced combination of performance and stability, and MWCNTs are particularly well-suited for robust, scalable electrochemical sensors and composite-based electrodes [122]. CNTs typically show conductivities of 10^4–10^6 S/m, mobilities of 10,000–100,000 $cm^2/V{\cdot}s$, and charge carrier densities of 10^{15}–10^{19} cm^{-3}. CNTs possess high specific surface area (SSA; generally in the range of 200–800 m^2/g) and can be functionalized with selective ionophores, membranes, or chelating ligands [20]. In CNTs, charges move inside individual CNTs via band conduction, then cross to another tube via tunneling/hopping, forming a percolation network. Modulation of the carrier density of CNTs can happen via direct charge transfer, dipole fields (electrostatic gating effect), or Schottky-barrier changes caused by interacting molecules or ions. CNTs are well suited as channel materials for sensing in aqueous environments because their high aspect ratio, one-dimensional structure, and excellent electrical properties yield strong coupling to surface and interfacial phenomena under electrolyte gating [123,124].

Melzer et al. reported the development of a membrane-coated CNT-based electrochemical charge-transfer device for detecting K^+, Ca^{2+}, and Cl^- in complex sample matrices with high ionic strength. Upon interaction of a membrane-coated CNT film (semiconducting SWCNT) with the ion of interest, the ion-activity-dependent electrochemical response of polymeric ion-selective membranes modulate the effective gate potential and produce threshold voltage (V_{th}) shifts in the FET transfer characteristics. Potassium sensing using a valinomycin-based ISM yielded a linear V_{th} shift of +39.3 mV per decade of K^+ activity from 10^{-1} to 10^{-7} M. A chloride-selective membrane incorporating tridodecylmethylammonium chloride produced a −51.5 mV/decade shift between 10^{-1} and 10^{-5} M, while calcium sensing using a diamide-based membrane achieved a +21.7 mV/decade response from 10^{-1} to 10^{-6} M with good selectivity over common interfering ions [125].

Although SWCNTs exhibit high intrinsic carrier mobility and electrostatic gate control, they face several challenges. A major challenge is the presence of mixed metallic and semiconducting CNTs in as-grown films, which may degrade device performance by lowering on/off ratios and causing leakage pathways that are difficult to eliminate at scale. Even for semiconducting SWCNTs, electronic properties are highly sensitive to chirality, diameter, and defects, leading to substantial device-to-device variability [126]. CNT networks also suffer from high contact resistance at metal–nanotube and tube–tube junctions, which limits current drive and introduces nonuniform conduction pathways [127,128]. Moreover, environmental sensitivity, particularly the adsorption of oxygen and other ambient contaminants, can lead to threshold-voltage instability and hysteresis, thereby complicating biasing conditions and degrading long-term reliability [129]. Despite these challenges, many CNT sensors for water-based analytes have been reported, emphasizing that CNT films can deliver good stability, low baseline drift and robust responses when properly engineered for aqueous operation [20,130,131].

Silicon nanowires. Silicon nanowires (SiNWs) consist of silicon confined to nanoscale diameters (10–100 nm) and elongated to form high-aspect-ratio one-dimensional structures. The bandgap of bulk silicon is 1.12 eV. Very thin SiNWs (<5–10 nm) have a larger bandgap due to quantum confinement (up to ≈2 eV) depending on their diameter. SiNWs behave similarly to doped bulk silicon, but surface depletion and quantum confinement decrease their conductivity (10^2–10^4 S/m) and mobility (50–1500 $cm^2/V{\cdot}s$). Charge transport in SiNWs is primarily band-like inside the crystalline core. Even though surface effects reduce conductivity and mobility, they dramatically enhance sensitivity since surface depletion means surface charge changes control the entire wire. Quantum confinement

results in strong current modulation by even small potential changes. This is why SiNWs are among the most sensitive FET-based chemical sensors. Their charge carrier density is 10^{15}–10^{18} cm^{-3} and their SSA falls in the range of 10–100 m^2/g, depending on diameter and aspect ratio. Work on silicon SiNW-FETs has shown that binding of charged ions at the solid–liquid interface leads to measurable shifts in threshold voltage or channel conductance, enabling label-free detection and rapid responses [132-134]. Charge transfer between SiNWs and analyte species occurs through electrostatic gating by intrinsic charges, direct electron donation/withdrawal by the analyte, and trap-mediated exchange at oxide surface states. The native and engineered oxide surfaces on silicon allow for precise functionalization (e.g., via silane chemistry and self-assembled monolayers) to install ion-selective membranes [135,136]. A study by Chen et al. demonstrates an integrated sensing platform based on SiNW-ChemFETs capable of detecting sodium ions. Selectivity toward Na^+ is achieved through a membrane deposited on the gate insulator, where the Na-ionophore III selectively complexes Na^+, generating a stable interfacial potential at the membrane–electrolyte boundary that modulates the SiNW channel and produces a potentiometric response. This ion-coupled gating mechanism enables the sensor to exhibit a near-Nernstian sensitivity of 57.9 ± 0.7 mV/decade across concentrations from 100 μM to 100 mM, with a detection limit of ≈60 μM, matching the performance of conventional ion-selective electrodes employing the same ionophore. Despite its strong intrinsic selectivity, the membrane suffers from competitive binding effects, particularly from K^+, yielding a selectivity coefficient of $10^{-1.2}$ for Na^+ over K^+. This interference effects become pronounced in complex matrices such as river water, though their influence diminishes at higher Na^+ activities. Thus, further membrane optimization is needed to mitigate molecular-ion partitioning and enhance performance in real-world environmental samples [137].

SiNWs offer good electrical stability and noise characteristics when properly passivated and have attracted significant interest as channel materials for FETs; however, several key limitations hinder their broad practical adoption. The high surface-to-volume ratio of SiNWs causes their electrical performance to be heavily dominated by surface states and interface traps, resulting in degraded carrier mobility and pronounced hysteresis in transfer characteristics [134,138,139]. Additionally, quantum confinement and stochastic dopant distributions in extremely thin SiNWs introduce variability in threshold voltages, making reproducibility difficult across large arrays [140]. Similar to other materials, when SiNW-based sensors are used in high-ionic-strength environments, Debye screening and drift of the reference electrode are possible, which further limit robustness and real-world applicability [141]. In terms of device fabrication, SiNW-FETs are a commercially proven, industrially scalable sensing technology, ideal for miniaturized, mass-produced, electronics-integrated ion sensors; however, achieving uniform nanowire diameter, high crystalline quality, low-resistance contacts, and conformal coating of the channel with a highly dielectric insulating material in the fabrication process still are of concern to researchers in this field [136,141].

Aluminium gallium nitride/gallium nitride heterostructures. An aluminium gallium nitride/gallium nitride (AlGaN/GaN) heterostructure is a layered semiconductor made by placing AlGaN (with a bandgap of 3.4–6.2 eV) on GaN (with a bandgap of 3.4 eV), creating a 2D electron gas (2DEG) at the interface due to the strong spontaneous and piezoelectric polarization fields inherent to the wurtzite crystal structure of group-III nitrides. When a thin AlGaN barrier is grown on GaN, the discontinuity in polarization charges creates an intense internal electric field that bends the GaN conduction band downward, forming a triangular quantum well at the heterojunction. As a result, charge transport in AlGaN/GaN devices is dominated by this 2DEG layer, which serves as the conductive channel in high-electron-mobility transistors (HEMTs) with minimal impurity scattering. 2DEG in AlGaN/GaN structures typically shows conductivities of 10^4–10^5 S/m, mobilities of 1000–2000 $cm^2/V{\cdot}s$, and electron densities of 10^{12}–10^{13} cm^{-2} in the 2DEG. The 2DEG's proximity to the surface (20–30 nm below the AlGaN barrier) also makes it very sensitive to surface charges, enabling strong field-effect modulation by adsorbates, ions, or electrochemical interactions. Charge transfer between analyte species and the channel occurs electrostatically; external charges or dipoles modulate the 2DEG density by changing the surface potential of AlGaN. Direct charge transfer is weak because GaN is chemically inert, but surface traps can capture or release charge, altering band bending and 2DEG conductivity [142]. Zhao et al. introduced a differential extended-gate (DEG) AlGaN/GaN HEMT device (a type of EG-FET geometry) for detection of Fe^{3+} ions in aqueous environments. GaN (measuring gate) is capped with a layer of gold, which serves as the surface for a self-assembled monolayer of 2-mercaptosuccinic acid. The thiol groups in 2-mercaptosuccinic acid form Au–S linkages with the gate surface, while the carboxyl groups selectively bind Fe^{3+} ions. Therefore, the surface charge modulates at the measuring gate and generates localized charge variations. These changes are capacitively coupled to the HEMT channel, altering the density of the 2DEG and producing a measurable shift in the output signal. The differential configuration, comprising a reference and a sensing gate, cancels common-mode noise from environmental fluctuations such as light or vibration, thereby enhancing detection precision. This device achieved a very low detection limit of 10 fM, a broad dynamic range (10 fM–100 mM),

and excellent linearity (R^2 = 0.9955), outperforming conventional AlGaN/GaN HEMT sensors and demonstrating strong potential for real-time monitoring of trace concentration of ions [95].

The 2DEG at the interface delivers high transconductance at low bias while remaining chemically and physically stable in aqueous electrolytes, resulting in low-noise AlGaN/GaN HEMT devices [143-146]. Selective detection of PO_4^{3-} using ion-imprinted polymers (IIPs), as well as quantification of NO_3^-, Hg^{2+}, Ca^{2+}, and Pb^{2+} ions via ISMs have also been demonstrated with AlGaN/GaN HEMT devices, illustrating the platform's compatibility with ion-selective layers for specificity [147-151]. The architecture also supports water-gated and extended-gate formats [95,152]. In terms of scalability of these transistors, GaN-on-Si or GaN-on-sapphire epitaxy allows for full wafer-scale growth using metalorganic chemical vapor deposition (MOCVD), compatible with power-electronics fabrication workflows. Batch processing enables thousands of devices per wafer. GaN HEMTs are already manufactured at scale for radio frequency and power electronics, meaning the industry infrastructure already exists. The wide bandgap and chemical stability also make them suitable for aqueous ion sensing directly in harsh environments without special lab-only handling. Meanwhile, performance and reliability of AlGaN/GaN transistors in sensing applications are hampered by several device-level challenges, including self-heating effects, current collapse, gate leakage, high electric field concentration, elevated ohmic contact resistance, and threshold voltage instability. Excessive channel heating and charge trapping can degrade sensitivity and stability, while gate leakage and high contact resistance reduce power efficiency and transduction accuracy. Moreover, threshold voltage drift and field-induced trapping compromise long-term reliability and reproducibility of sensor responses. To overcome these limitations, optimization of thermal management, suppression of trapping effects, and minimization of leakage and contact resistance are essential. Incorporating advanced structural strategies, such as field plates, passivation layers, and refined gate architectures, can further improve the stability, sensitivity, and overall performance of AlGaN/GaN-based sensors [142].

MXenes. MXenes (e.g., $Ti_3C_2T_x$) are metallic 2D transition-metal carbides/nitrides with abundant surface terminations (–O, –OH, –F, generated during the etching process using hydrochloric acid and lithium fluoride), which are represented by T_x with a fractional coverage of x. Their metal centers possess partially filled d orbitals with a high density of states at the Fermi level and strong M–C or M–N bonding, which leads to delocalized electronic states, high electrical conductivity (10^4–10^5 S/m), and small or zero bandgaps (0–0.3 eV). Electrons move freely within the 2D basal plane, similar to a disordered metal. MXenes are formed by wet-chemical etching. They carry functional groups on their surfaces, which cause electron scattering, local band bending, and modification of the effective mass of the charge carriers. This limits mobility (1–100 $cm^2/V{\cdot}s$) and prevents fully ballistic transport. In the films, interflake transport occurs via tunneling and hopping, which influences the conductivity of the film. Thus, thin flakes conduct better than thick, restacked films. In MXenes, ions (H^+, Li^+, Na^+, K^+, Ca^{2+}) can enter the interlayer space and change the charge distribution, resulting in mixed ionic–electronic transport. Few-layer MXenes (delaminated form) typically show a SSA of about 50–300 m^2/g, which can be modified by engineering the structure such as making it porous or pillared. Due to the metallic d-band contribution from the transition metal centers, MXenes exhibit very high charge carrier densities (10^{13}–10^{15} cm^{-2}) [153,154].

MXenes exchange charge with their environment via direct chemical electron transfer, electrostatic gating by ions and dipoles, redox reactions involving surface transition-metal sites, and ion-intercalation-induced modulation of the Fermi level. Their exposed metallic surfaces and tunable terminations make them very sensitive to charge-transfer processes. In practice, MXene channels have delivered selective heavy-metal detection in challenging matrices [155,156], for example, Hg^{2+} sensing in high-salinity water using $Ti_3C_2T_x$-based MOSFET devices. The sensor employs $Ti_3C_2T_x$ nanosheets as the conductive channel material deposited on interdigitated gold electrodes. The sensing mechanism is governed by the strong adsorption and subsequent reduction of Hg^{2+} to Hg^+ on the MXene surface, which perturbs the electronic structure. $Ti_3C_2T_x$ nanosheets are electron-rich, so when they donate electrons to mercury ions, the channel conductivity decreases, resulting a drop in current. This intrinsic adsorption–reduction process enables high sensitivity and selectivity toward Hg^{2+}, with negligible interference from competing metal ions (As^{5+}, Cd^{2+}, K^+, Pb^{2+}, Cu^{2+}, Ca^{2+}). Furthermore, the device maintains stable performance in 1 M NaCl, demonstrating robustness against interfering species [157].

MXenes also interface well with ion-selective layers [12], and MXene-based FETs can be fabricated via printing or solution-based methods [158]. A limitation to the application of these materials is their ease of oxidation in aqueous solutions, but recently proposed chemistry and storage strategies (defect passivation, polymer composites, controlled dispersions) address this issue and extend operational lifetimes [153,154]. Therefore, the high conductivity, hydrophilicity, tunable surface terminations, and processability of MXenes make them a suitable choice for sensing applications.

Transition metal dichalcogenides. Transition metal dichalcogenides (TMDCs) are a broad class of layered materials with the chemical formula MX_2, where M is a transition metal (e.g., Mo, W, Nb, V, Ti) and X is a chalcogen (S, Se, Te). In their bulk form, TMDCs consist of stacks of weakly bonded van der Waals layers, each only a few angstroms thick, allowing individual monolayers to be mechanically exfoliated or chemically isolated. Each monolayer comprises a plane of metal atoms sandwiched between two planes of chalcogen atoms, forming a trigonal prismatic or octahedral coordination environment. TMDCs show conductivities of 10^{-3}–10^{2} S/m, mobilities of 0.1–500 $cm^2/V{\cdot}s$, and SSAs in the range of 10–200 m^2/g (few-layer, exfoliated nanosheets) [159,160]. The electronic band structure of TMDCs is strongly thickness-dependent. In the bulk form, interlayer coupling leads to an indirect bandgap (1.0–1.3 eV), whereas removal of interlayer interactions and enhanced quantum confinement in the monolayer shift the band extrema to the same k-point, yielding a larger direct bandgap (1.6–2.1 eV). This well-defined, thickness-tunable bandgap allows for strong electrostatic gate control over carrier transport, which is essential for efficient transistor switching [161,162]. TMDCs conduct charge via band conduction in high-quality monolayers, trap-limited transport in most practical devices (made with CVD-grown TMDCs), and hopping/tunneling in defective or multilayer films (solution-processed TMDC nanosheets, printed electronics, and thick films). Transport is strongly influenced by defects, the dielectric environment, and contact interfaces [163,164].

TMDCs undergo strong chemical charge transfer with adsorbates, electrostatic coupling with external charges, and trap-mediated exchange at vacancies. Their atomic thickness makes their conductivity extremely sensitive to molecular doping, contact barriers, and ionic environments, enabling powerful sensing capabilities [165]. An example of a sensing application of TMDCs is an agent-free MoS_2-based FET sensor that was developed for real-time and in situ monitoring of silver ions in aqueous media. Agent-free means that MoS_2 acted as active layer and sensing layer without any additional recognition agents. In MoS_2, surface sulfur atoms interact with Ag^+ ions; Ag^+ acts as a Lewis acid, accepting lone-pair electrons from S atoms and inducing p-type doping. This adsorption decreases electron concentration in the MoS_2 channel, resulting in a positive threshold voltage shift, reduced carrier mobility, and lower the channel current. The sensor achieved an ultralow detection limit of 10^{-10} $mol{\cdot}L^{-1}$ and rapid response (≤5 min) with high operational stability [166].

Another study reports the development of solid-state chemiresistors based on MoS_2 nanosheets functionalized with L-cysteine (Cys) for real-time detection of cadmium ions (Cd^{2+}) in drinking water at ultralow concentrations (1–500 ppb) (Figure 4). The MoS_2-Cys films were fabricated via a simple one-pot synthesis involving thioglycolic acid carboxylation and amide coupling with L-cysteine, deposited onto porous poly(ether)sulfone membranes to enable continuous flow sensing. The sensing mechanism is based on selective adsorption of Cd^{2+} ions to the L-cysteine functional groups, followed by charge transfer that alters the electronic gap states and modulates MoS_2 conductivity. This interaction results in a substantial resistivity increase, up to 20× at 5 ppb Cd^{2+}, with high selectivity under neutral pH conditions. The devices exhibit rapid response (≈1 s), reusability, and operational simplicity without the need for external reagents or complex instrumentation [167].

From a practical perspective, 2D-TMDCs can be fabricated via scalable methods (CVD, ALD, mechanical exfoliation) and integrated into thin-film FET stacks, enabling compact, low-voltage sensors suitable for remote or continuous monitoring of water. They exhibit high mechanical flexibility, chemical stability, and atomically clean surfaces without dangling bonds, making them compatible with a wide variety of substrates, including flexible and transparent electronics. While some challenges remain (such as managing aqueous degradation or selecting optimal functionalization chemistry), the suite of morphological, electrical, and chemical features makes 2D-TMDCs a suitable material class for ion sensing [160].

Organic materials

Small organic molecules and conjugated polymers. Organic channel materials for organic FETs (OFETs) include conjugated small molecules (such as pentacene, rubrene), and conjugated polymers (such as poly(3-hexylthiophene) (P3HT)- and diketopyrrolopyrrole (DPP)-based polymers). Charge transport in organic semiconductors is fundamentally different from that inorganic materials. Charge transport in organic systems arises from localized electronic states, where carriers move through hopping or polaron mechanisms. Because these materials are held together by weak van der Waals forces, their π orbitals do not form extended bands, and transport is strongly affected by intermolecular arrangement, variations in local site energies, and electrolyte interactions in solution-gated OFET geometry. Charge transport occurs via thermally activated hopping between localized states, resulting in strong temperature dependence, low mobility, and high sensitivity to morphology and crystallinity. Charges in organic semiconductors also distort the surrounding molecular environment, forming polarons that hop between sites at rates governed by reorganization energy and π–π stacking, further limiting mobility and making transport highly sensitive to structural order [168-170].

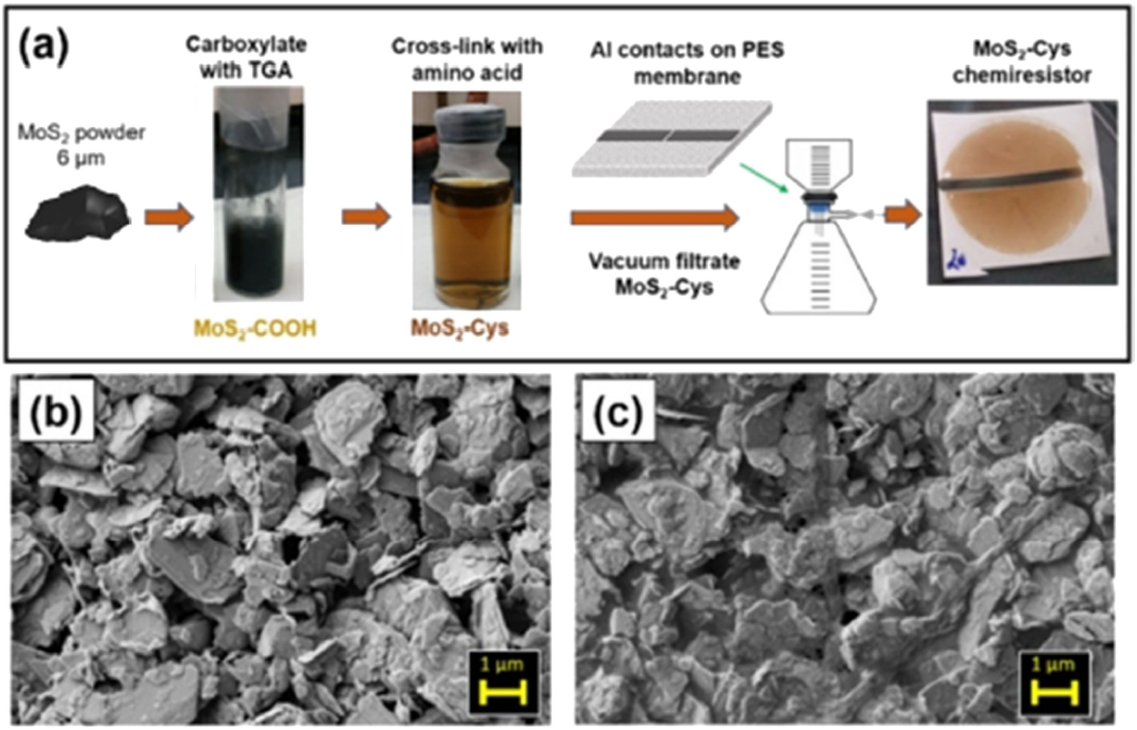


Figure 4: (a) MoS_2–Cys preparation using thioglycolic acid (TGA) to add carboxyl groups followed by amide cross-linking for Cys functionalization and fabrication of two-terminal chemiresistors. MoS_2–Cys thin films can be prepared by vacuum filtration and incorporated in these devices. 2 keV scanning electron microscopy (SEM) images of (b) MoS_2–COOH and (c) MoS_2–Cys (1:20 MoS_2/Cys mass ratio), showing Cys functionalization as a network of filaments on the surface of MoS_2 aggregates. Figure 4 was reprinted from [167], P. Bazylewski et al., "Solid-State Chemiresistors from Two-Dimensional MoS_2 Nanosheets Functionalized with L-Cysteine for In-Line Sensing of Part-Per-Billion Cd^{2+} Ions in Drinking Water", *ACS Omega*, Copyright © 2019 American Chemical Society, licensed under the Standard ACS Author Choice/Editors' Choice Usage Agreement, https://pubs.acs.org/page/policy/authorchoice_termsofuse.html. This content is not subject to CC BY 4.0.

Organic thin films are structurally heterogeneous, consisting of crystalline π–π stacked domains, amorphous regions, and grain boundaries. Charge transport therefore proceeds along percolation pathways through ordered domains and incomplete percolation leads to drastic drops in charge carrier mobility [168-170]. As highlighted by Lamport et al., the choice of the organic semiconductor strongly impacts charge carrier mobility, on/off ratio, and threshold voltage behavior [168]. In practice, small organic molecules and conjugated polymers used in ECT channels typically exhibit low conductivities (10^{-8}–10^{-3} S/m), moderate mobilities (10^{-3}–10 $cm^2/V{\cdot}s$), and charge carrier densities of 10^{13}–10^{18} cm^{-3}, reflecting their localized π electron structure and hopping-dominated transport. Their SSAs are relatively small (1–20 m^2/g), and their surface-to-volume ratios range from 10^5 to 10^6 m^{-1}, depending on film thickness and morphology. Upon environmental exposure, charge transfer can occur via electrostatic double-layer gating, electrochemical (Faradaic) charge transfer at higher gate voltages, or trap-mediated exchange [168-170]. For example, Schmoltner et al. presented a modular solution-gated OFET platform for selective, low-voltage ion sensing in aqueous environments. By directly interfacing a P3HT semiconductor with an electrolyte rather than a solid dielectric, the device enables potentiometric detection through a sodium-selective ISM that establishes a Nernstian membrane potential dependent on analyte ion activity. The sensor exhibits a linear, reversible response to Na^+ concentrations from 10^{-6} to 10^{-1} M with a sensitivity of ≈62 mV/decade and minimal cross-interference from K^+. The architecture supports straightforward ion exchange for multianalyte detection and demonstrates good operational stability with low drift [171].

Most small-molecule or polymeric organic semiconductors are chosen as the active layer in OFET-based sensors because their molecular structure can be tailored to interact with analytes, and because their fabrication is compatible with flexible substrates and low-cost manufacturing [170,172]. The key merits are ease of chemical modification (to attach recognition groups), compatibility with printable electronics, and sufficient electronic performance for transistors.

Organic mixed ionic–electronic conductors. Organic mixed ionic–electronic conductors (OMIECs) are conjugated polymers that enable both ionic and electronic transport, making

them ideal for aqueous environments and organic electrochemical transistors (OECTs). Unlike solution-gated OFETs, which rely on surface channels, OMIECs operate through volumetric conduction where ions and electrons move together. Electronic transport occurs via hopping, π–π percolation, and polaron drift, with mobilities of 10^{-3}–1 $cm^2/V·s$ and conductivities rising from 10^{-6}–10^{-2} S/m (undoped) to 1–100 S/m (doped) upon electrochemical oxidation. Ionic transport, slower but essential, involves ion diffusion through solvated sites and polymer free volume, with mobilities of 10^{-8}–10^{-6} $cm^2/V·s$. Ions act as dopants, dynamically modulating conductivity by activating or deactivating electronic states. Because ions permeate the entire film thickness, OMIECs exhibit high volumetric capacitance and strong signal amplification at low voltages. Charge transfer is governed by electrochemical doping, where ionic motion maintains electroneutrality and couples directly with electronic carriers, defining the key performance of OECTs [173]. OMIECs include poly(3,4-ethylenedioxythiophene) (PEDOT) derivatives, glycolated conjugated polymers, DPP-based polymers, redox-active polymers such as polyaniline (PANI), polypyrrole (PPy), and side-chain-engineered polythiophenes. These materials are intrinsically well-suited to aqueous sensing because of their hydrated matrices, which enable volumetric ion uptake and doping/de-doping, yielding large transconductance at low voltage in solution-gated formats. Their ability to swell in water allows for bulk channel participation [173,174].

Among them, poly(3,4-ethylenedioxythiophene) polystyrene sulfonate (PEDOT:PSS) is the most widely used in OECTs as the combination of PEDOT with the polyanion PSS provides solubility, mixed ionic–electronic conduction, and environmental stability. While PEDOT is intrinsically conductive, it is insoluble and requires the sulfonate groups of PSS to maintain its oxidized, p-doped state and to enable dispersion into water, yielding uniform, printable thin films. The resulting composite supports simultaneous electronic transport through PEDOT backbones and ionic transport through the hydrophilic PSS matrix, giving rise to high volumetric capacitance and strong ionic–electronic coupling essential for high-transconductance sensing. PSS also promotes a favorable film morphology by spacing PEDOT chains into a nanostructured network that improves flexibility, mechanical robustness, and tunable conductivity. Furthermore, the PEDOT:PSS ratio can be adjusted to modulate ion penetration, swelling, softness, and device performance. The hydrophilicity and biocompatibility imparted by PSS make PEDOT:PSS stable in aqueous and physiological environments, in contrast to the hydrophobic and unstable pristine PEDOT, thereby positioning it as an ideal material for electronic and aqueous sensing applications [173,175]. For instance, ion-selective OECTs that couple PEDOT:PSS channels to ISMs deliver selective K^+ and Na^+ sensing in real time and can be multiplexed or even made on paper substrates for scalable, in-line monitoring [176-178]. Materials innovations (such as porous and foam PEDOT:PSS, as well as tailored side-chain chemistries) further boost transconductance and speed for aqueous detection [179]. Beyond transistors, PANI and PPy offer robust, water-stable chemiresistive channels beneath ISMs; their redox-active backbones and affinity for metal-ion complexation have been leveraged for heavy-metal sensing in water [180]. Finally, OECTs can serve as on-site amplifiers for electrochemical ion sensors, improving sensitivity without complex external electronics, useful for embedded, online analysis in water networks [181].

Analyte detection in OECTs typically occurs through three mechanisms: (1) electrochemical reactions, where analytes oxidize or reduce the polymer; (2) ion uptake, which alters local ion concentration and doping levels; and (3) pH or ion-specific modulation, where species such as H^+, Na^+, K^+, or Ca^{2+} affect charge compensation and conductivity. Because ions penetrate the polymer bulk, analytes can strongly influence doping, giving OECTs exquisite sensitivity. In contrast, conventional organic semiconductors interact only at the film surface, leading to limited ion sensitivity, low transconductance, and the need for higher operating voltages. Their hydrophobic nature also reduces stability in aqueous environments, though they respond faster since they do not swell during measurement. Overall, OMIECs provide superior performance for continuous aqueous monitoring due to their bulk ion–electron coupling and stable operation in water [173,182-184].

Recognition elements

FETs, chemiresistors, and working electrodes in electrochemical setups are not inherently selective. The selectivity can be built into the film or a separate material layered atop the film. In this section we discuss the different strategies that can be applied to make the film selective to specific targets: Introducing defects to the film, doping the film with nanoparticles, functionalizing the surface of the film with organic molecules or polymers, synthesizing nanocomposites of two or more materials, using biomaterials as sensing element, or coating the film with ISMs are different ways to create the recognition element in electrical and electrochemical sensing devices for ion detection.

Engineered structural nanoscale defect-rich films

Engineered structural nanoscale defects, such as atomic vacancies, grain boundaries, adatoms, or substitution sites, can serve as highly effective sensing sites in electronic and electrochemical ion sensors. In two-dimensional materials, for example, the creation of S-vacancies in MoS_2 or point defects in graphene markedly enhance the chemical reactivity of the surface,

allowing water-dissolved ions to adsorb or bind more strongly, thereby modulating the channel conductance or surface potential [159,160,185]. These defect sites often induce localized states in the bandgap or trap states that strongly couple to ionic charge, improving sensitivity and lowering detection limits in ion monitoring. Moreover, defects may enable preferential binding of specific metal ions; thereby, they can be engineered to tune sensing selectivity [185,186]. However, care must be taken because such defects can also degrade carrier mobility and increase noise or drift (especially in water where fouling or oxidation may occur); thus, balancing defect introduction and channel integrity is critical.

Defects can be introduced to the thin film with several techniques including electron beam or ion irradiation, plasma, ozone or chemical treatments, substitutional doping and ion implantation. These methods enable precise control over defect types and distributions, allowing researchers to tailor the electronic, and optoelectronic properties of thin films for advanced applications [186]. For instance, a MoS_2-based electrochemical sensor was developed by creating nanoscale incisions and sulfur vacancies on MoS_2 films by swift heavy ion (SHI) irradiation. SHI irradiation produces molybdenum-rich edges and removes sulfur atoms from the basal planes of MoS_2, creating active sites for catalytic reactions to detect hydrogen ions (H^+) in water. The irradiated MoS_2 samples showed improved current densities and lower onset values for electrochemical reactions (i.e., lower LOD) [187]. Another study demonstrated that graphene's pH sensitivity can be tuned by controlling its defect density. Different levels of defects (such as vacancies, dopants, functional groups, and sp^3-hybridized regions) were introduced by sonication and chemical treatments. At high defect densities, the sensing response is dominated by the protonation and deprotonation of pH-sensitive functional groups (e.g., carboxy, hydroxy, and amino groups) on the graphene surface. These groups act as active sites for acid–base interactions, modulating graphene's conductivity. The sensitivity of the chemiresistive graphene-based pH sensor has been shown to increase with higher defect density [188]. In summary, engineered structural defects provide a route to tailor-made high-sensitivity sensing sites in both electrochemical and electrical sensor formats.

Nanoparticle-doped films

Incorporating nanoparticles as dopants into sensor channel materials offers a powerful strategy to enhance sensing capability by introducing high-activity sites and boosting signal transduction. When nanoparticles (NPs) such as Au, Ag, Pt are embedded within or on the surface of a channel material, they act as ion-capture and catalytic centers, improving the local binding affinity for target ions, facilitating faster kinetics of ion–electron coupling, increasing the density of active sites, and lowering baseline resistance [189,190]. As an example, in a study done by Zhou et al., Au NPs play a central role in enhancing the electronic and sensing performance of the rGO-based sensor through their distinct electronic characteristics and chemical functionality (Figure 5). The higher work function of Au NPs (5.1–5.47 eV) relative to rGO (4.4–4.65 eV) drives electron transfer from rGO to the Au NPs, thereby increasing the hole concentration within the rGO channel and improving its electrical conductivity. Although the incorporation of Au NPs introduces scattering sites that can locally hinder charge-carrier mobility, the dominant effect of charge transfer leads to an overall increase in current flow through the device. Beyond their electronic influence, Au NPs can serve as platform for further functionalization due to their strong affinity for thiolated molecules. The immobilization of glutathione (GSH) onto the Au NP surface enables selective coordination of Pb^{2+} ions, thereby significantly enhancing both the sensitivity and specificity of the sensing interface [191].

Therefore, nanoparticle doping enhances sensor performance by amplifying signals via high-surface-area nanostructures, enabling tailored selectivity through functionalized NP dopants. However, potential issues include NP agglomeration or leaching during extended aqueous exposure, baseline noise or drift due to complex NP–matrix interfaces, and added fabrication complexity or cost. Thus, critical design priorities involve stabilizing NPs, controlling their distribution and size for reproducible sensor responses, and ensuring long-term durability in real water matrices [29,192].

Molecularly functionalized films

Molecules such as ion-chelating ligands, self-assembled monolayers, or crown ethers functionalized onto the electrode or transistor channel surface can create discrete recognition sites and significantly enhance selectivity and sensitivity of ionic sensors [29,193,194]. Such molecular layers also serve to position the ionic binding event within the electrical double layer (EDL) zone adjacent to the transducer surface, maximizing coupling and signal transduction. Studies of EDL accumulation show how ion binding at functionalized interfacial sites amplifies charge modulation in solution-gated devices [195]. Moreover, surface functionalization can help mitigate non-specific adsorption and fouling in complex water matrices by introducing hydrophilic groups that serve an antifouling function. Indeed, hydrophilic groups bind water strongly and create a hydration shell. This hydrated layer minimizes hydrophobic interactions, reduces van der Waals attraction, and increases steric repulsion. Therefore, biofouling and nonspecific adsorption can be suppressed by surface functionalization [29].

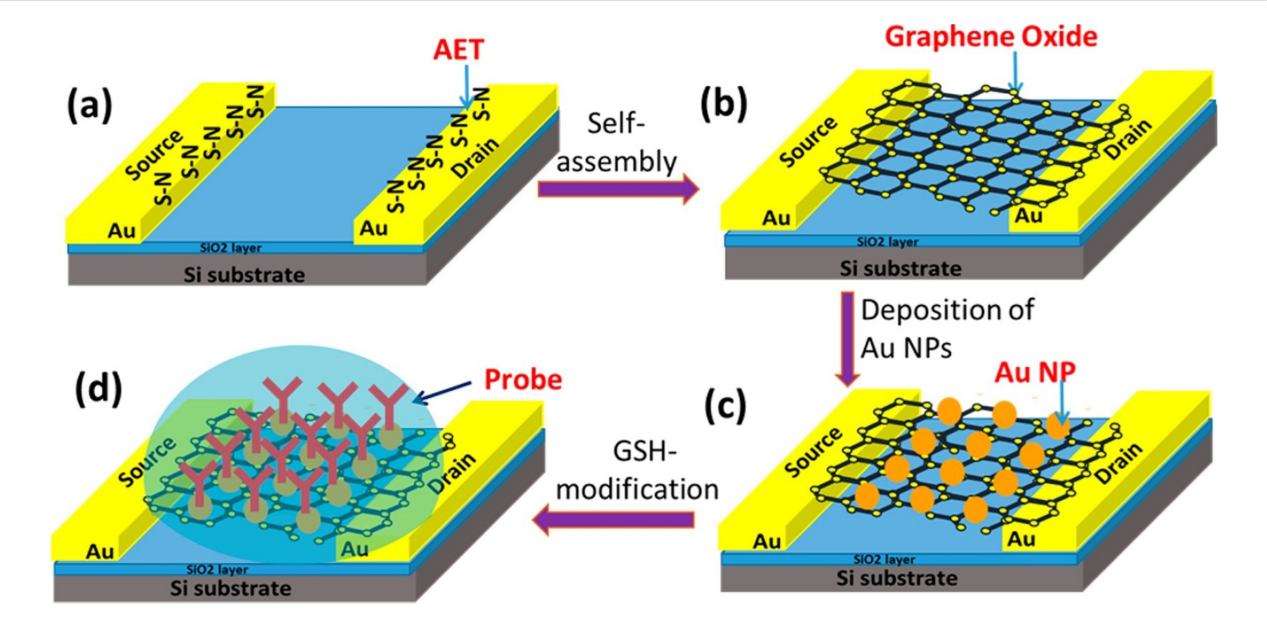


Figure 5: Schematic diagram of the rGO/GSH-Au NP hybrid sensor fabrication process. (a) A layer of AET coating on the bare interdigitated electrode surface. (b) Self-assembly of GO monolayer sheets on the AET-modified electrodes, which is followed by the thermal reduction of GO to rGO. (c) The assembly of Au NPs onto the rGO film. (d) GSH-modification of Au NPs on the rGO sheet surface to form specific recognition groups to detect Pb^{2+}. Figure 5 was reprinted with permission from [191]. Copyright 2014 American Chemical Society. This content is not subject to CC BY 4.0.

Molecules can be bound covalently or noncovalently onto the active layer. As an example of covalent functionalization, Kaur et al. fabricated an electrode by electro-copolymerizing PEDOT and 2-(anthracen-9-yl)benzo[*d*]thiazole (AA-BTZ) and then drop-casting Au NPs to create receptor sites for Hg^{2+} ions. The sulfur atoms in the benzothiazole moiety of AA-BTZ provide a soft base environment that complements the soft acid nature of Hg^{2+} ions, following the hard–soft acid–base (HSAB) principle. AuNPs further enhanced selectivity and sensitivity of the sensor due to their strong binding affinity with Hg^{2+} ions, resulting in a low detection limit of 0.60 nM [196].

Dalmieda et al. reported a chemiresistive Ag^+ sensor based on FLG that was noncovalently functionalized with bathocuproine via π–π stacking [99]. It is a noncovalent strategy that preserves the intrinsic electronic properties of graphene while introducing controlled n-doping through electron donation from the adsorbed molecules. The sensing mechanism is governed by the selective formation of a silver–bathocuproine complex upon exposure to Ag^+ ions, which alters the electronic structure of the ligand and creates electron-trapping sites at the graphene interface. This induces charge transfer from the FLG surface to the complex, increasing the hole density within the graphene film and producing a measurable decrease in resistance proportional to the Ag^+ concentration. This strategy of sensing is limited to ions that are willing to form planar complexes, such as Ag^+ and Cu^{2+}(/Cu^+) [197]. The chelation process is fully reversible since protonation of the bathocuproine imine groups under mildly acidic conditions (pH 3) disrupts complex formation and restores the baseline conductance, enabling sensor regeneration. Through this charge-transfer-driven modulation of film resistance, the platform achieves sensitive and selective Ag^+ detection across a range of 3 ppb to 1 ppm in aqueous media [99].

Polymer-functionalized films

Engineered porous materials such as metal–organic frameworks (MOFs), covalent organic frameworks (COFs), and IIPs can directly incorporate sensing sites for ion detection in water via electrochemical or electrical devices. These frameworks combine high surface area, tunable pore structures, and specific binding chemistries that enhance ion uptake and transduction.

Metal–organic frameworks. MOFs are crystalline materials with highly ordered pores and channels. This uniform network structure provides controlled pathways for electron and ion transport; so, ion diffusion pathways are predictable. Ions travel through well-defined pores rather than random spaces, which results in faster diffusion, reproducible sensor responses, and better signal stability. Also, pore size and chemistry of MOFs can be precisely tuned. They can be hydrophilic or hydrophobic pores with selective coordinative sites, specific electrostatic charges, specific pore diameters. Moreover, MOFs have large specific surface areas (1000–7000 m^2/g) with many active sites for adsorbing analytes or creating redox-active centers that are accessible, resulting in signal amplification and high sensi-

tivity. MOFs can also be further functionalized, and due to their large surface area, a higher loading of catalytic or recognition molecules is possible. Furthermore, many MOFs contain metal nodes that are not fully coordinated. These unsaturated metal sites act like Lewis acid sites and bind analytes, act as redox-active centers, or catalyze electrochemical reactions [198,199]. Selvaraj et al. reported a UiO-67–modified electrode for cadmium detection using differential pulse voltammetry. The highly mesoporous UiO-67 structure (998 m^2/g specific surface area, 0.70 cm^3/g specific pore volume) efficiently adsorbs and concentrates Cd^{2+} ions from solution. This accumulation enhances the interfacial electron transfer kinetics, evidenced by a marked decrease in redox peak separation compared with the bare electrode, enabling efficient electrooxidation of Cd^{2+}. The natural affinity of UiO-67 for cadmium ions, adsorption capability, electrostatic enrichment, and electrocatalytic activity allow UiO-67 to function as a sensitive (with a LOD of 1.43 nM/μA) and low-cost platform for trace-level Cd^{2+} monitoring in aqueous media [200].

Most MOFs are made of electrically insulating organic linkers and metal clusters that are not in direct electronic communication. As a result, typical MOFs have very low conductivities of around 10^{-10}–10^{-15} S/cm. Nevertheless, there have been efforts to specifically develop conductive MOFs, enabling their use in FET sensors. Shen et al. synthesized a conductive $Ni_3(HITP)_2$ membrane via a one-step hydrothermal process, subsequently functionalizing it with glutaraldehyde and single-stranded DNA probes and measuring Hg^{2+} selectively through thymine–Hg^{2+}–thymine coordination within the SG-FET configuration. The $Ni_3(HITP)_2$ membrane was structurally optimized by regulating the ammonia–water ratio to improve its carrier mobility and strengthen its transduction efficiency. This combination of conductive MOF architecture and specific nucleic-acid-based binding afforded a highly sensitive and selective sensor capable of detecting Hg^{2+} over a wide dynamic range from 10 pM to 100 nM [201]. Several challenges remain in the use of MOFs, such as their instability in aqueous environments. This is particularly true for carboxylate-based MOFs, which undergo hydrolysis because metal–ligand bonds such as Zn–O and Cu–O are not resistant to water or humidity. Another limitation is their poor adhesion to electrode surfaces, as MOFs are inherently crystalline powders with limited chemical affinity, covalent bonding, or mechanical compatibility with substrates. As a result, particles often detach during rinsing, cycling, or sonication. These drawbacks can be mitigated by designing MOF-based composites that enhance surface adhesion, water stability, and electrical conductivity [198,199].

Covalent organic frameworks. COFs likewise offer robust, crystalline, covalently bonded porous networks that permit fast mass transport of water and ions as well as functionalization of binding sites [202]. Unlike MOFs, COFs bind through organic donor groups, not metal clusters. Ion sensing in COFs operates through four main mechanisms: (1) coordination binding, where donor atoms in the framework form bonds or strong interactions with incoming ions, guided by HSAB principles and geometry matching; (2) π-interaction and charge transfer, in which ions interact with the extended π-conjugated planes, leading to electron redistribution, charge transfer, and changes in conductivity; (3) size-selective pore sieving, as the rigid, periodic pores discriminate ions based on size, shape, and diffusion pathways; and (4) electrostatic attraction or repulsion, where charged pores enhance selectivity by drawing in or excluding specific ions. COFs are suitable for sensing due to their fast ion diffusion through ordered pores and high density of accessible binding sites (a large specific surface area of 1000–3000 m^2/g). In contrast to the metal–ligand bonds in MOFs, COFs rely on organic covalent bonds, which can be highly water-stable if chosen appropriately. At the molecular level, COFs can be designed with selective chelators, redox-responsive groups, proton-binding moieties, and ion-exchange functionalities [202].

Hou et al. developed a flexible electrochemical sensor for ultratrace mercury detection that utilizes a COF-based AuNPs-modified carbon fiber cloth to achieve highly efficient signal transduction. The electrode was subsequently functionalized with methylene blue (MB) and rDNA to selectively interact with Hg^{2+} ions. In this scenario Hg^{2+} acts as a specific bivalent linker between thymidine bases on the rDNA probe, thus shifting the electroactivity of MB. The COF/Au/MB/rDNA probe architecture significantly enhances sensitivity through the high surface area and biocompatibility of the COF, efficient electron transfer pathways provided by Au NPs, and the MB signaling moiety. This synergistic design enables a broad linear detection range from 0.1 pM to 100 nM and a very low detection limit of 45.2 fM. The proposed sensor also demonstrates good stability (given the use of rDNA), reproducibility, and practical applicability, achieving high recovery rates in diverse real water samples, including tap, lake, drinking, and seawater [203]. In another study, Wang et al. developed a screen-printed COFDATA-TP-based electrochemical sensor for multiplex heavy-metal detection using the ASV method. The COFDATA-TP framework contains abundant carboxyl (–COOH) and secondary amino (–NH) functional groups, which serve as high-affinity binding sites, enabling efficient enrichment of Hg^{2+}, Cu^{2+}, Pb^{2+}, and Cd^{2+} from solution and directing them to the electrode interface. The π-conjugated backbone of COFDATA-TP enhances electrical conductivity, while its ordered porous architecture promotes mass transport and facilitates rapid ion diffusion, collectively improving signal strength and sensitivity.

The detection limits of the sensor to detect Hg^{2+}, Cu^{2+}, Pb^{2+}, and Cd^{2+} are calculated to be 2.80, 5.01, 1.83, and 2.91 nM, respectively [204]. Similar to MOFs, COFs also tend to suffer from low intrinsic conductivity. They are often electrically insulating unless they are doped, prepared as composites with carbon materials or made with fully π-conjugated linkers. Also, their stability depends on linkage chemistry, for example imine COFs may undergo hydrolysis but ketoenamine COFs are more stable [202]. They may also suffer from weak adhesion to surfaces of substrates. Overall, COFs represent a promising platform for ion sensing, though advances in conductivity, stability, and surface adhesion remain essential for their widespread application.

Ion-imprinted polymers. IIPs are synthesized to create "molecular memory" cavities that match a target ion in size and coordination environment, enabling highly selective recognition, even in complex water matrices, with demonstrated nanomolar detection limits [205,206]. IIPs are highly selective because binding pockets are pre-organized around divalent or monovalent ions, they can discriminate different geometries and coordination numbers (octahedral (e.g., Co^{2+}), tetrahedral (e.g., Zn^{2+}), linear (e.g., Ag^{+})). Moreover, they do donor-atom matching based on HSAB theory (soft S donors to Hg^{2+} and Ag^{+}, hard O donors to $Ca^{2+}$and Mg^{2+}). In addition, polymer cavities reject ions that are too large or ions with mismatched hydration radius or incorrect geometry due to their steric constraints. During sensing, ions migrate through the aqueous medium into the polymer's surface pores where electrostatic forces guide them toward donor atoms. Within these cavities, the ions coordinate with donor sites to form stable complexes. This interaction induces subtle conformational adjustments in the polymer, such as localized movements of chain segments or side groups, that help secure the ion within the binding pocket. As a result, the sensor generates a measurable transduction signal. The IIP-based sensing is fast (because cavities are preformed), highly selective (due to geometry and donor atom matching), and stable (chelation-like binding) [150].

As an example, Zhang et al. synthesized Ni(II)-imprinted polymers on a magnetic MWCNT substrate using a surface imprinting technique and selectively detected Ni^{2+} ions with a LOD of 0.27 µg/L. These imprinting cavities are tailored in size, geometry, and charge distribution to match Ni^{2+}, which enables selective adsorption. When an applied potential drives Ni^{2+} ions into the binding sites, they coordinate with functional monomer groups through electrostatic and ligand–metal interactions. Incorporation of Fe_3O_4@MWCNTs into the electrode matrix substantially enhances electron-transfer kinetics and increases the effective electroactive surface area approximately fourteen-fold compared with a bare electrode, yielding a markedly amplified electrochemical response [207].

Shamsabadi et al. developed a novel IIP–modified carbon paste electrode through a simple bulk polymerisation process, which was able to selectively measure Hg^{2+} ions with a LOD of 0.2 nM (Figure 6). The sensing mechanism proceeds through sequential preconcentration, reduction, and stripping steps. During the open-circuit preconcentration stage, Hg^{2+} ions in solution selectively bind to morpholine-4-carbodithioic acid phenyl ester (MCP) sites within the imprinted polymer matrix, forming Hg^{2+}–MCP complexes that accumulate at the elec-

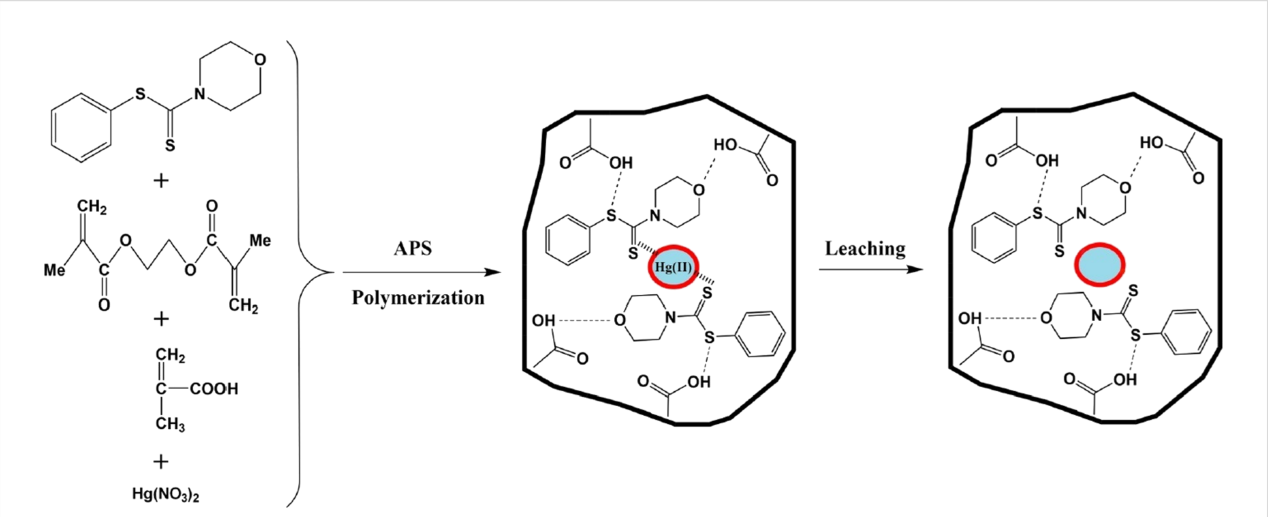


Figure 6: Schematic representation of the fabrication of Hg(II)-IIP. Figure 6 was reproduced from [205] (© 2024 E. Shamsabadi et al., published by Springer Nature, distributed under the terms of the Creative Commons Attribution-NonCommercial-NoDerivatives 4.0 International License, https://creativecommons.org/licenses/by-nc-nd/4.0/). This content is not subject to CC BY 4.0.

trode surface. Upon applying a potential of −0.5 V, the preconcentrated Hg^{2+} is electrochemically reduced to elemental mercury (Hg^0), regenerating the MCP ligand in the process. In the subsequent differential pulse anodic stripping voltammetry (DPASV) step, the deposited Hg^0 is reoxidized to Hg^{2+}, producing a well-defined anodic peak that serves as the quantitative analytical signal [205].

In summary, MOFs, COFs, and IIPs can act as pre-concentration and binding layers at the interface of a sensor such that ion binding causes modulation of surface potential, ionic flux, or channel conductivity. Despite their promise, several challenges persist: MOFs and COFs often face stability issues in aqueous environments, IIPs require careful management of fouling and regeneration, and seamless integration with electronic transducers must be achieved without introducing drift or baseline noise. Even so, their porous architectures, rapid response, and very high selectivity and sensitivity establish these materials as leading candidates for robust, real-time ion sensing in water.

Nanocomposite films

Engineered nanocomposites, hybrid materials composed of two or more nanoscale phases (e.g., carbon nanostructures + metal/metal-oxide nanoparticles or conjugated polymers) offer powerful advantages as ion sensing sites. By combining the high surface area of 2D materials and nanotubes (e.g., graphene, MXenes, CNTs) with functional modifiers (ionophore polymers, metal-oxide nanostructures), these composites can provide enhanced ion adsorption/binding, accelerated charge transfer, and stable aqueous operation [107,208]. When the density of active sites increases, the sensitivity of the sensor improves. Moreover, enhanced electron and ion transport pathways lead to faster kinetics, and the underlying conductive framework prevents agglomeration or leaching, which results in more stable devices [107]. Zhang et al. developed a one-step fabricated electrochemical sensor for highly selective Pb^{2+} detection using an integrated TCPP-MWCNTs@Fe_3O_4 nanocomposite probe, in which the sensing mechanism is governed by the selective chelation of lead ions by *meso*-tetra(4-carboxyphenyl)porphyrin (TCPP). The tetrapyrrolic cavity of TCPP provides electron-rich nitrogen coordination sites that selectively accommodate Pb^{2+}, forming a stable chelate that enables highly discriminative recognition over competing metal ions. Aminated MWCNTs serve as a conductive scaffold for covalent immobilization of TCPP through amidation, creating a high-surface-area interface that promotes Pb^{2+} adsorption while facilitating efficient electron transport during electrochemical transduction. The incorporation of Fe_3O_4 nanoparticles imparts magnetic responsiveness, allowing for rapid magnetic separation and direct assembly of the nanocomposite onto a magnetic glassy carbon electrode, thereby integrating pre-concentration, probe immobilization, and detection into a single streamlined step. Together, selective porphyrin–Pb^{2+} chelation, enhanced conductivity of the MWCNT network, and magnetic fixation of the sensing interface result in a stable, regenerable, and highly sensitive platform capable of detecting Pb^{2+} with a LOD of 0.067 ppt [209].

Sharma et al. reported a highly sensitive platform for real-time mercury ion detection based on an Ag nanowire–MoS_2 nanocomposite integrated onto the gate region of an AlGaN/GaN HEMT. The sensing mechanism arises from the interaction of Hg^{2+} ions with the MoS_2 surface within the nanocomposite, which modulates the gate potential and, consequently, the drain-to-source current (I_{DS}) of the HEMT. At low Hg^{2+} concentrations, strong chemisorption and the formation of Hg–S complexes dominate, increasing the gate potential and producing a corresponding rise in I_{DS}. As the concentration increases and MoS_2 binding sites become saturated, additional Hg^{2+} uptake occurs primarily through electrostatic attraction, leading to a reduction in surface potential and a subsequent decrease in I_{DS}. This dual-stage response enables highly discriminative electrical transduction. Combining AgNWs with MoS_2 results in a nanocomposite with superior electron transport properties and more adsorption sites, enabling the sensor to achieve a sensitivity of 1.604 mA/ppb and a very low detection limit of 20 ppt, which is the best reported for AlGaN/GaN HEMT-based sensors for Hg^{2+} detection [210]. Another group of researchers reported a 3D flower-like nickel oxide-decorated poly(diallyldimethylammonium chloride) (PDDA)-functionalized rGO nanocomposite (Figure 7). The NiO/PDDA-rGO electrochemical sensor detects nitrite through a diffusion-controlled catalytic oxidation process facilitated by the synergistic properties of the nanocomposite. Nitrite ions are first adsorbed onto the NiO/PDDA-rGO surface, forming a transient NiO/PDDA-rGO–NO_2^- complex through electrostatic interactions. This interfacial complex undergoes electron transfer, yielding nitrogen dioxide (NO_2), which subsequently disproportionates to generate additional nitrite (NO_2^-) and nitrate (NO_3^-). The newly formed nitrite is further electrooxidized to nitrate as the final product, producing the characteristic oxidation current used for quantitative detection. The high sensitivity of the sensor arises from the combination of flower-like NiO nanostructures that offer abundant catalytic sites and the PDDA-functionalized rGO matrix that enhances charge transport and adsorption, collectively enabling an operating range of 5 μM−8 mM and a detection limit of 0.98 μM [211]. Despite the benefits of nanocomposites, some new challenges arise such as achieving robust dispersion and a uniform interface between components (to avoid baseline drift or noise) or fabricating reproducible and scalable sensors, which require careful consideration in sensor development [208].

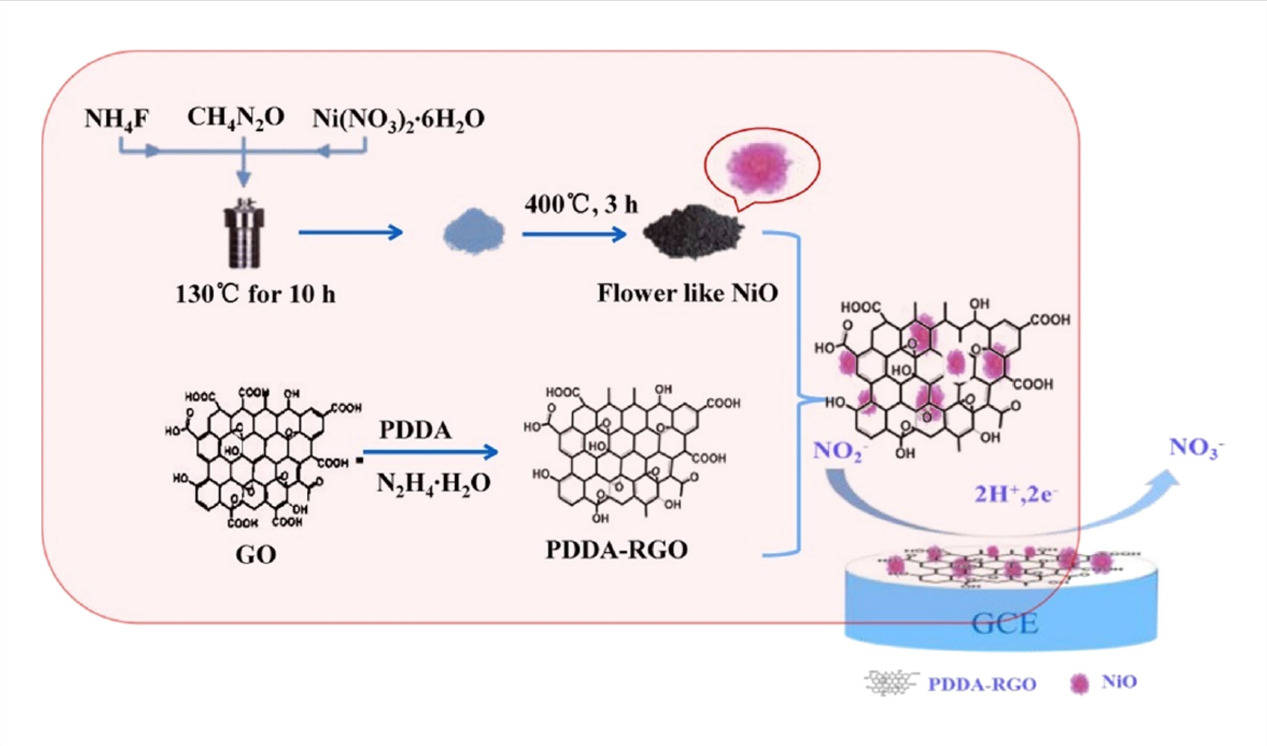


Figure 7: Scheme of the preparation route for the NiO/PDDA-RGO composite and its electrochemical application for nitrite detection. Figure 7 was reprinted with permission from [211]. Copyright 2022 American Chemical Society. This content is not subject to CC BY 4.0.

Biomolecule-functionalized films

Biomolecules such as enzymes, DNA, aptamers, antibodies, and DNAzymes can serve as precise recognition elements for sensing applications. Aptamers or single-strand nucleic acids selected via systematic ligand evolution by exponential enrichment can bind specific metal ions with high affinity and be integrated into electrical and electrochemical sensors [212,213]. DNAzymes (catalytic nucleic acids) can change their conformation or activity in response to specific ions, generating a measurable electrical signal when immobilized on an electrode [214]. Enzymes and antibodies provide complementary functionality. Enzymes can catalyze ion-related reactions (for instance, urease producing NH_4^+ from urea, leading to pH changes), while antibodies bind specifically to ion complexes (not free ions because free metal ions are very small and hard for antibodies to recognize) and enable high-selectivity immunosensors [215]. Zhang et al. designed an ultrasensitive electrochemical aptasensor for Pb^{2+} detection. $Ti_3C_2T_x$ as a substrate has outstanding metallic conductivity for efficient electron transfer, good biocompatibility, and a high surface area with abundant reactive surface sites to facilitate stable immobilization of biomolecular probes. When combined with polypyrrole and gold nanoparticles, $Ti_3C_2T_x$ also exhibits improved oxidative stability, resulting in a robust platform for constructing high-performance aptasensing interfaces. After preparation of the $Ti_3C_2T_x$/PPy/AuNPs nanocomposite, the capture probe immobilized on the electrode hybridizes with the lead-specific aptamer probe to form a duplex DNA structure that anchors MB as the electrochemical indicator. Upon exposure to Pb^{2+}, the aptamer undergoes a selective conformational switch from the double helix to a Pb^{2+}-stabilized G-quadruplex, triggering the release of MB from the electrode surface and producing a measurable decrease in current proportional to the Pb^{2+} concentration. Collectively, the Pb^{2+}-responsive G-quadruplex transition and the MXene-based conductive architecture enabled a highly sensitive measurement of Pb^{2+} ions in a range from 5×10^{-14} to 1×10^{-8} M with a low LOD of 1×10^{-14} M [216].

Nanozymes are synthetic nanomaterials that mimic the catalytic activity of natural enzymes. They offer relatively high stability, low cost, and tunable surface properties, enabling enzyme-like functions without the fragility of biological catalysts [217]. Wen et al. utilized cobalt oxyhydroxide (CoOOH) nanoflakes as a nanozyme to detect arsenate ions (As^{5+}) (Figure 8). The sensing mechanism relies on the strong electrostatic and surface-complexation interactions between As(V) and CoOOH, where the formation of As–O coordination complexes inhibits the intrinsic peroxidase-like activity of the nanozyme. This suppression reduces the catalytic oxidation of 2,2′-azinobis(3-ethylbenzothiazoline-6-sulfonic acid) (ABTS) to $ABTS_{ox}$, resulting in a measurable decrease in the electrochemical reduction current of $ABTS_{ox}$ during transduction. The degree of

signal inhibition correlates directly with As(V) concentration, enabling ultrasensitive detection with a limit of 56.1 ppt [218]. The advantages of biomaterials in ion sensing include excellent selectivity, potential for regeneration, compatibility with miniaturized electronics, and adaptability to real-time, in-line measurements in flowing water. However, challenges arise in terms of their long-term stability in complex water matrices (biofouling, denaturation, drift), and the need to interface them effectively with solid-state transducers (electrode functionalization, stable immobilization) to maintain signal accuracy. Proper integration of biomaterial recognition layers with electrical and electrochemical surfaces thus enables high-performance ion sensing platforms for water quality monitoring [215].

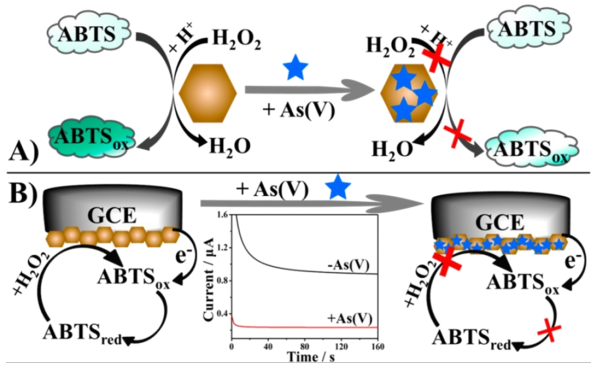


Figure 8: Schematic illustration of the dual-mode assay of arsenate based on CoOOH nanoflakes with peroxidase-like activity: (A) Illustration of the colorimetric method of CoOOH nanoflakes as probe for arsenate detection; (B) Illustration of the electrochemical strategy of CoOOH nanoflakes modified glassy carbon electrode for arsenate detection. Figure 8 was reprinted with permission from [218]. Copyright 2019 American Chemical Society. This content is not subject to CC BY 4.0.

Ion-selective membrane-coated films

Throughout the review, the prominent role of ISMs has been emphasized repeatedly. These membranes act as recognition layers, enabling the selective conversion of ion activity in the aqueous phase into measurable electrical signals. Typically, an ISM consists of a plasticized polymer matrix incorporating an appropriate ionophore, often supplemented with a lipophilic additive that enhances ionophore performance through electrostatic interactions, thereby improving ion selectivity. In ISEs, the membrane binds specifically to the target ion and generates a phase boundary potential, which is detected by a transducer. Within the field of SC-ISEs, extensive research has focused on optimizing ISM composition and refining membrane deposition techniques to create sensing platforms with high reproducibility and minimal signal drift [75,76,219]. A recent study by Yu et al. reported an all-solid-state potassium ISE. Potassium ions in solution are selectively complexed by the cyclododecapeptide (CP12) ionophore embedded in the K^+-selective carrier membrane, generating a transmembrane ion-activity gradient that produces a diffusion potential consistent with Nernstian behavior. This ionic potential is converted into a stable electronic signal by an underlying layer of egg-shell hollow carbon nanospheres, whose high capacitance facilitates rapid charge transfer while the hydrophobic carbon surface suppresses water-layer formation between the membrane and electrode substrate. Together, these features yield fast response kinetics, high sensitivity, and excellent potential stability, enabling reliable K^+ detection over a range of concentration from 5.0 μM to 10 mM even in complex sample matrices [220].

Although ISMs are fundamental components of potentiometric ISEs, they are also employed, albeit less frequently, in amperometric, voltammetric, and FET-based sensors to improve selectivity, facilitate ion preconcentration, minimize interference, and protect surfaces. When positioned over a transistor channel, as in ChemFET configurations, ISMs establish ionic gating or ion-specific accumulation layers that modulate the channel's surface potential. Unlike potentiometric ISEs, where the membrane generates a measurable phase boundary potential, detection in this geometry arises from changes in channel conductance governed by ion access to the semiconductor surface. Liu et al. developed an ISM-ISFET sensor for Cr^{6+}detection. Under mildly acidic conditions, Cr^{6+} exists primarily as $Cr_2O_7^{2-}$, which binds to quinaldine red ionophores in the membrane, triggering a proton-releasing reaction that alters the membrane-solution interfacial potential. This potential modulation directly affects the ISFET gate surface, producing a measurable change in drain current corresponding to Cr^{6+} concentration. To suppress background noise and eliminate signal drift from non-specific ions or pH fluctuations, a differential sensing architecture is used in which ISFET pixels coated with the ISM are compared against uncoated reference pixels, and the resulting differential current (ΔI_D) isolates the Cr^{6+}-specific response. A microfluidic control system further stabilizes the pH and ensures precise solution mixing, enhancing signal accuracy and the overall reliability of Cr^{6+} quantification in complex aqueous samples [221].

In potentiometric systems, ISM-coated electrodes form part of the electrochemical cell. In other sensing approaches, however, membranes may be less advantageous, as they can impede electron transfer, introduce diffusion barriers, or reduce catalytic efficiency. Moreover, incorporating membranes increases fabrication complexity. In many cases, selectivity can instead be achieved through direct surface modification strategies, such as self-assembled monolayers, chelating agents, polymers, or nanomaterials. Consequently, ISMs are most valuable when high selectivity is required, interfering ions are prevalent, ion

preconcentration is beneficial, or surface fouling must be mitigated. Nonetheless, their use presents challenges, including membrane drift, ion interference, fouling, and ionophore leaching in complex water matrices, that demand robust membrane formulations and carefully designed transducers. Choi et al. recently introduced a durable ISE platform in which ionophore-doped poly(decyl methacrylate) (PDMA) sensing membranes are covalently anchored to both inert polymeric supports and conductive carbon contacts, overcoming long-standing issues of membrane delamination, water-layer formation, and signal drift common in conventional ISEs (Figure 9). Using a two-step photo-induced graft polymerization method, a robust chemical bonding between the sensing membrane and electrode substrates was achieved, thereby stabilizing the interfacial structure essential for reliable potentiometric transduction. The resulting electrodes exhibited excellent performance metrics, including highly reproducible standard potentials (electrode-E_0 SD = 0.2 mV), minimal long-term drift (7 µV/h over 260 h), and full retention of sensing capability following harsh autoclave sterilization (121 °C, 2 atm). Furthermore, the devices maintained stable operation after six months of storage and exposure to elevated temperatures and organic solvents. Although demonstrated using pH-selective membranes, the approach is readily extendable to other target ions through appropriate ionophore incorporation, representing a significant advance toward robust, miniaturizable, and long-lived ISEs suitable for wearable, implantable, and industrial sensing environments [219].

Sensor arrays

Sensor arrays are groups of multiple sensors arranged to simultaneously measure different ions or improve sensitivity and selectivity. Instead of using one sensor that is perfectly selective for a single ion, an array of sensors can be used in which each sensor has a different binding chemistry and responds differently to each ion in the sample. By analyzing all responses together, the array can identify or quantify ions with higher specificity. There are two types of arrays which are developed, namely, arrays of single-analyte sensors and cross-reactive arrays (electronic tongue).

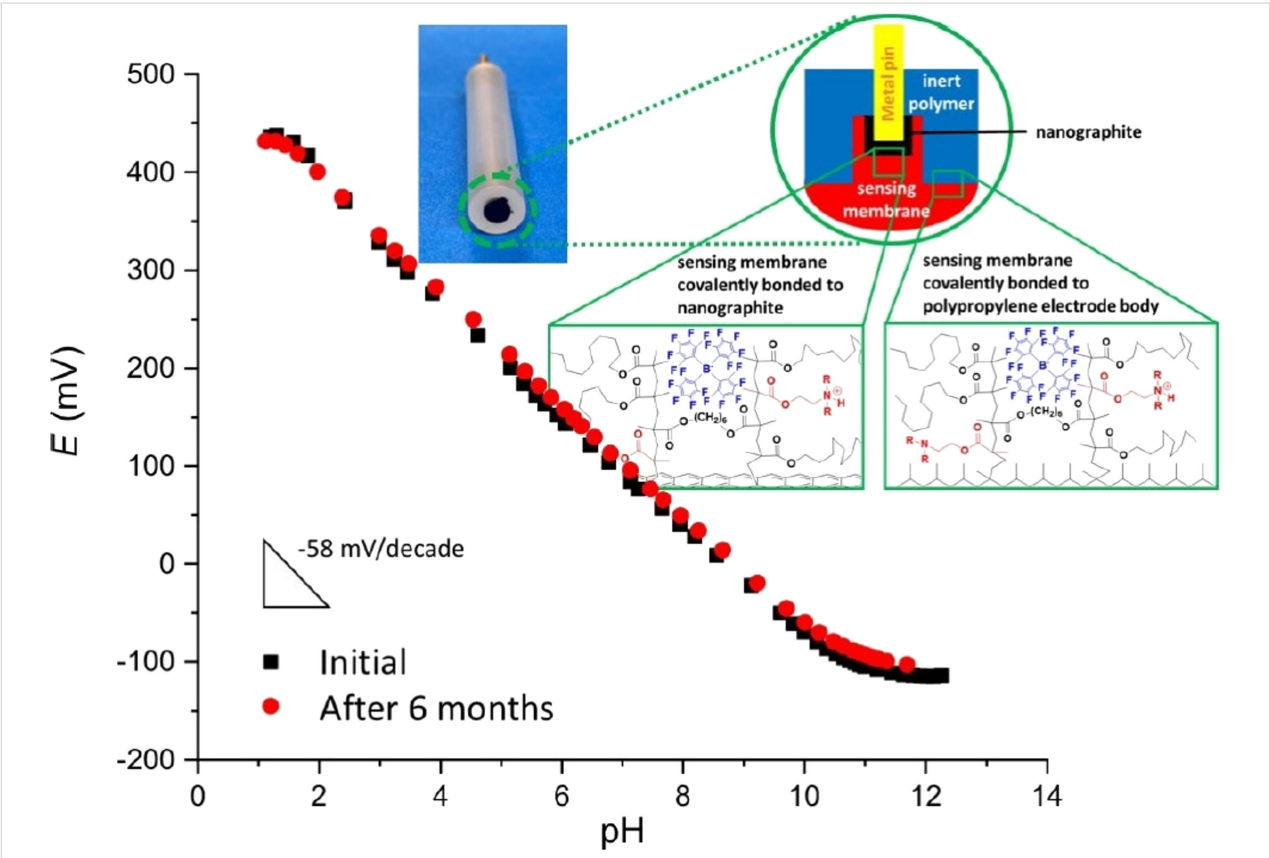


Figure 9: Initial EMF response (squares) and response after 6 months (circles) to pH for an ISE with a PDMA membrane (doped with ionophore and ionic sites) photografted onto a polypropylene-based electrode body and nanographite solid contact, relative to a free-flowing double-junction reference electrode. The pH was adjusted by the addition of 1.0 M HCl or 1.0 M NaOH to 10 mM sodium phosphate buffer solution (pH 7.1). The pH value shown on the *x*-axis was measured using a pH glass electrode. Figure 9 was reproduced from [219] (© 2023 K. R. Choi et al., *Angewandte Chemie, International Edition* published by Wiley-VCH GmbH, distributed under the terms of the Creative Commons Attribution-NonCommercial-NoDerivatives 4.0 International License, https://creativecommons.org/licenses/by-nc-nd/4.0/). This content is not subject to CC BY 4.0.

Arrays of single-analyte sensors

These types of sensor arrays consist of multiple sensing units, each engineered to detect a single ionic species. The outputs from these sensors can be directly interpreted without reliance on advanced chemometric methods. Such arrays are typically constructed using ion-selective membranes or molecular recognition components such as ionophores, crown ethers, or IIPs. They enable the simultaneous measurement of several ions, with each channel functioning independently and providing orthogonal chemical selectivity. These arrays deliver high accuracy and allow for straightforward quantification, minimizing the need for computational correction or pattern recognition. Their reliability makes them particularly valuable in contexts requiring precise ion determination, including blood electrolyte analysis and water quality monitoring [222,223].

Fakih et al. reported a graphene-based IS-FET array capable of real-time, high-resolution, and simultaneous detection of multiple cations (K^+, Na^+, NH_4^+) and anions (NO_3^-, SO_4^{2-}, HPO_4^{2-}, Cl^-) (Figure 10). The device was fabricated by growing a monolayer of graphene via CVD, which was then transferred onto a fused silica substrate. Source and drain contacts (Ti/Au) were deposited, after which the wafer was diced into individual chips, mounted on printed circuit boards, and encapsulated with epoxy to prevent direct contact with the electrolyte. ISMs tailored to specific ions were drop-cast onto the graphene surface to enable selective sensing. The array achieved a resolution of 2×10^{-3} log concentration units, with sensitivities ranging from 22.6 to 58.6 mV/decade. Detection limits were approximately 10^{-5} M for all analytes. Performance was validated in multi-ion solutions and in an aquarium envi-

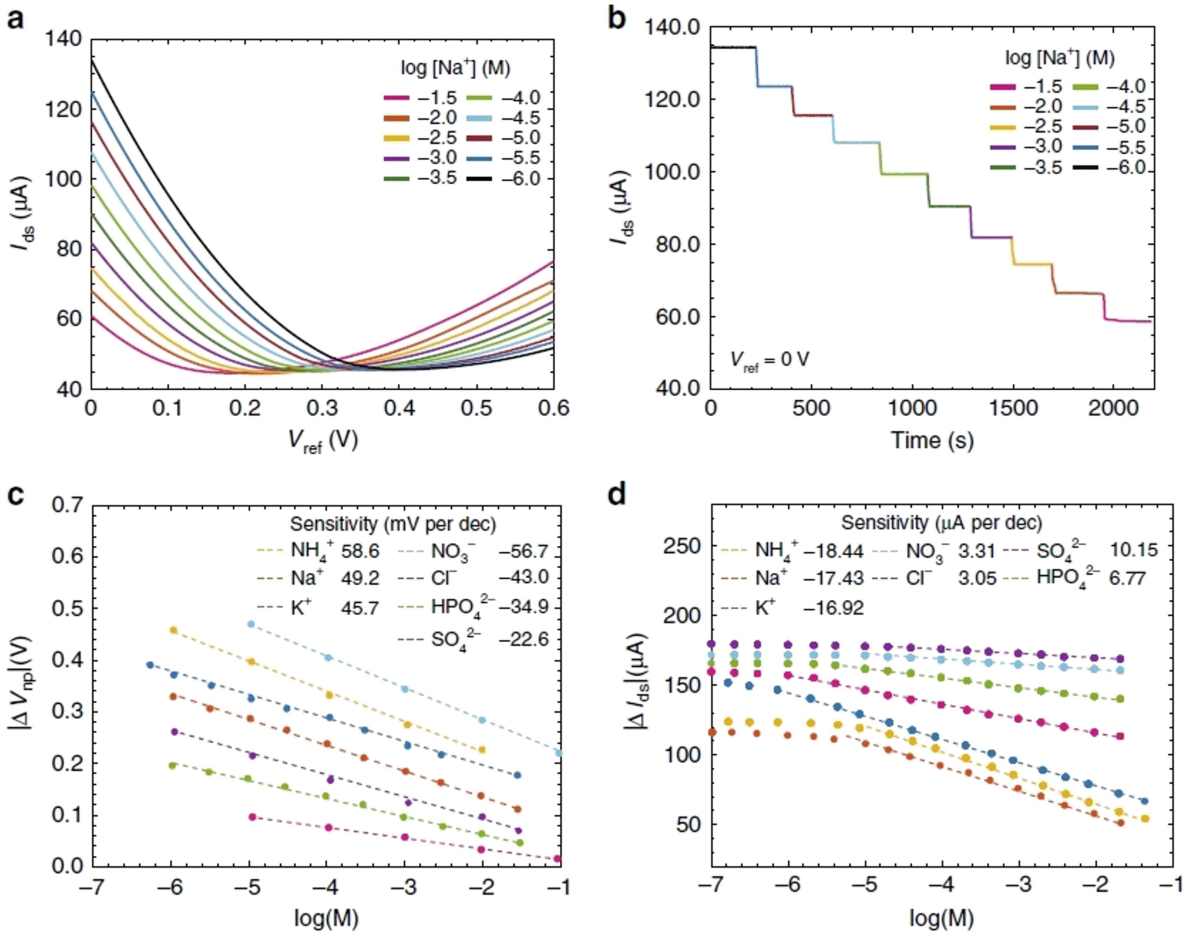


Figure 10: IS-FET sensitivities with respect to their target ions. a) The channel current, I_{ds}, of an Na^+ IS-FET versus V_{ref}, for different Na^+ molar concentrations. b) Continuous real-time measurement of I_{ds} for the same Na^+ IS-FET when increasing Na^+ molar concentrations by half decade steps while keeping V_{ref} = 0 V. c) The changes in V_{np} (neutrality point voltage, it is the gate voltage at which the channel has minimum conductance) for the different IS-FETs with respect to concentrations of their respective target ions, with a linear fit to extract their voltage sensitivities. d) The changes in I_{ds} for the different IS-FETs with respect to concentrations of their respective target ions, with a linear fit to extract their current sensitivities. Figure 10 was reproduced from [10] (© 2020 I. Fakih et al., published by Springer Nature, distributed under the terms of the Creative Commons Attribution 4.0 International License, https://creativecommons.org/licenses/by/4.0).

ronment over a three-week period. As expected, the IS-FETs exhibited some cross-sensitivity to non-target ions, necessitating calibration via the Nikolskii–Eisenman method, which compensates for interference by solving nonlinear equations to accurately determine ion concentrations in complex mixtures. Overall, this graphene IS-FET array combines high resolution, accuracy, and scalability for diverse real-world applications [10].

Cross-reactive arrays (electronic tongues)

In complex environments, selectivity is low, interfering ions distort readings, biofouling and drift affect single sensors, and multiple ions interact nonlinearly. An electronic tongue is a system consisting of a sensor array made of multiple partially selective sensors, a transduction system (such as potentiometric, voltammetric, FET, and chemiresistive sensors), and a pattern recognition engine (machine learning or statistical models). All the sensors in the array overlap in their responses, together creating a fingerprint for each ion. Selectivity then emerges from the pattern of responses, not from the individual sensors [222,224,225].

Machine learning algorithms can be employed to interpret how ions influence the response patterns of sensor arrays. The typical workflow begins with the collection of training data, where the array is exposed to known concentrations of ions. Each sensor generates a multidimensional signal (for example, a 12-sensor array yields a 12-channel response vector), which serves as the input for computational analysis. Machine learning methods include principal component analysis for dimensionality reduction, linear discriminant analysis for classification, support vector machines, random forests, neural networks, and regression approaches such as partial least squares or principal component regression. One of these methods is applied to extract discriminative patterns that differentiate individual ions. Through this process, the model learns a mapping between sensor response profiles and ion concentrations. During actual sensing, the array produces a new response pattern that the trained model can decode to predict which ions are present, their concentrations, and even resolve complex mixtures in heterogeneous matrices. Machine learning compensates for sensor drift, temperature variations, baseline offsets, overlapping sensitivity, and nonlinear sensor behavior. Machine learning models can update or self-calibrate. In other words, instead of requiring each sensor to behave perfectly, machine learning finds the statistically relevant features [224,225].

Margarit-Taulé et al. introduced an innovative strategy to mitigate common limitations of ISFET sensors in pH monitoring, including temporal drift, cross-sensitivity, and aging effects. Their approach integrates an array of ISFETs selective to H^+ ions as well as interfering ions (Na^+ and K^+) with machine learning models (Figure 11). A range of ML algorithms, linear regression, support vector regression, multilayer perceptron, and deep neural networks (DNNs), were evaluated using sensor data collected over 90 days from a drinking water treatment facility. Among these, DNNs delivered the highest predictive accuracy. Incorporating signals from ISFETs targeting inter-

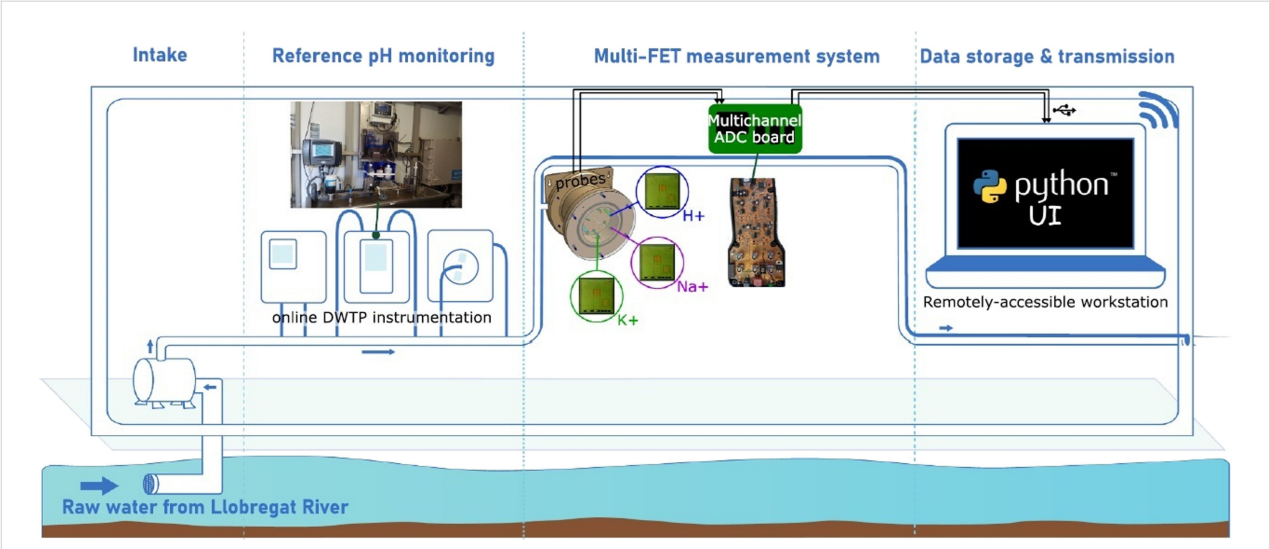


Figure 11: Experimental setup for continuously acquiring water quality data. The ISFET array was deployed in a custom probe connected to readout electronics fabricated in house at the Instituto de Microelectronica de Barcelona. A laptop received raw ISFET measurements via USB, for storage and wireless transmission. Figure 11 was reproduced from [226] (© 2021 J. M. Margarit-Taulé et al., published by Elsevier B.V., distributed under the terms of the Creative Commons Attribution-NonCommercial- NoDerivatives 4.0 International License, https://creativecommons.org/licenses/by-nc-nd/4.0/). This content is not subject to CC BY 4.0.

fering ions significantly enhanced both stability and precision, with DNNs achieving a 73% reduction in root-mean-square error compared to conventional two-point calibration. This work highlights the promise of DNN-based sensor fusion in improving the robustness and operational lifespan of FET sensors for real-world applications such as water quality assessment. Moreover, the methodology can be extended to other potentiometric sensors for analyte detection in complex environments [226].

Systematic evaluation of active materials for ion sensing in water

Table 3 provides a concise comparison of the electronic properties and specific surface areas of the active material classes reviewed in this work. Figure 12 complements this by summarizing each material category through representative structures or mesoscopic film morphologies, their key advantages and dominant challenges in aqueous media, the device geometries they are most compatible with, and their demonstrated sensing applications. Table 4 further evaluates the performance of sensors fabricated with these materials, including sensitivity, selectivity, water stability, response time, scalability, and fabrication cost. Overall, most active materials used for electrochemical and electronic ion detection are inorganic, owing to their intrinsically higher conductivity, charge mobility, and surface area relative to their organic counterparts (Table 3). As shown in Table 4, organic thin films generally exhibit lower sensitivity, selectivity, and long-term stability in water, despite their fast response time and low-cost fabrication, whereas OMIECs-based channels offer more practical performance for ion sensing. However, OMIECs in OECTs typically suffer from slower ion transport (leading to longer response times), potential issues with long-term chemical stability in harsh aqueous media, and often lower mobility compared to inorganic semiconductors. In contrast, inorganic channel materials deliver higher carrier mobilities, sharper gating behavior (higher on/off ratios), better chemical and thermal stability under aggressive conditions, and well-established microfabrication/integration through semiconductor processing. The trade-off for inorganic materials is often that ion-to-electronic coupling must rely on surface gating (rather than bulk volumetric coupling), which places constraints due to Debye screening in high-ionic-strength water; also, fabrication can be more complex and costlier when scaling to large-area or flexible platforms. In summary, organic channels offer excellent integration and low-voltage operation but face durability and speed challenges, while inorganic channels deliver high performance and robustness but may require more complex gating architectures and fabrication to function optimally in real-world aqueous ion sensing. Regarding stability, most inorganic semiconductors (except metal oxides and MXenes) maintain their properties in water while organic semiconductors, metal oxides and MXenes may gradually change due to hydration, oxidation, or ion intercalation, causing baseline drift. High-quality and well-passivated graphene, CNT, SiNW, MXene, TMDC FETs, and AlGaN/GaN HEMTs show low hysteresis, but amorphous metal oxides in IS-FET geometry, or conducting polymer channels in OECTs can show higher noise and hysteresis unless surface/interface engineering is

Table 3: Comparison of the electronic properties and specific surface area of classified materials.

Material	Bandgap (eV)	Electrical conductivity (S/m)	Charge mobility ($cm^2/(V·s)$)	Specific surface area (m^2/g)	Ref.
SMOs	3.0–4.0	10^{-6}–10^{2}	0.1–50	20–200 (nanostructured)	[229]
FLG	≈0 (semi-metal)	10^{4}–10^{5}	1000–50000 (high-quality)	300–800	[230]
SWCNTs	0.5–1.5	10^{4}–10^{6}	10000–100000	200–800	[20]
SiNWs	1.1–2.0 (bulk to strongly confined)	10^{2}–10^{4}	50–1500	10–100	[28]
AlGaN/GaN heterostructures	—	10^{4}–10^{5} (2DEG sheet conductivity)	1000–2000	—	[142]
MXenes	0–0.3	10^{4}–10^{5}	1–100	50–300	[154]
TMDCs	1.6–2.1	10^{-3}–10^{2}	0.1–500	10–200	[159]
organic semiconductors	1.5–3.0	10^{-8}–10^{-3}	10^{-3}–10	1–20	[170]
OMIECs	1.3–2.5	1–100 (doped)	10^{-3}–1	not typically reported	[173]
COFs	1.5–3.0	10^{-8}–1 (increases if doped)	0.1–10 (reported for some 2D COFs)	1000–3000	[202]
MOFs	2–5	10^{-12}–1 (increases if doped)	very low–few	1000–7000	[198]
IIPs	3–5	10^{-10}–10^{-6}	very low	10–200	[205]

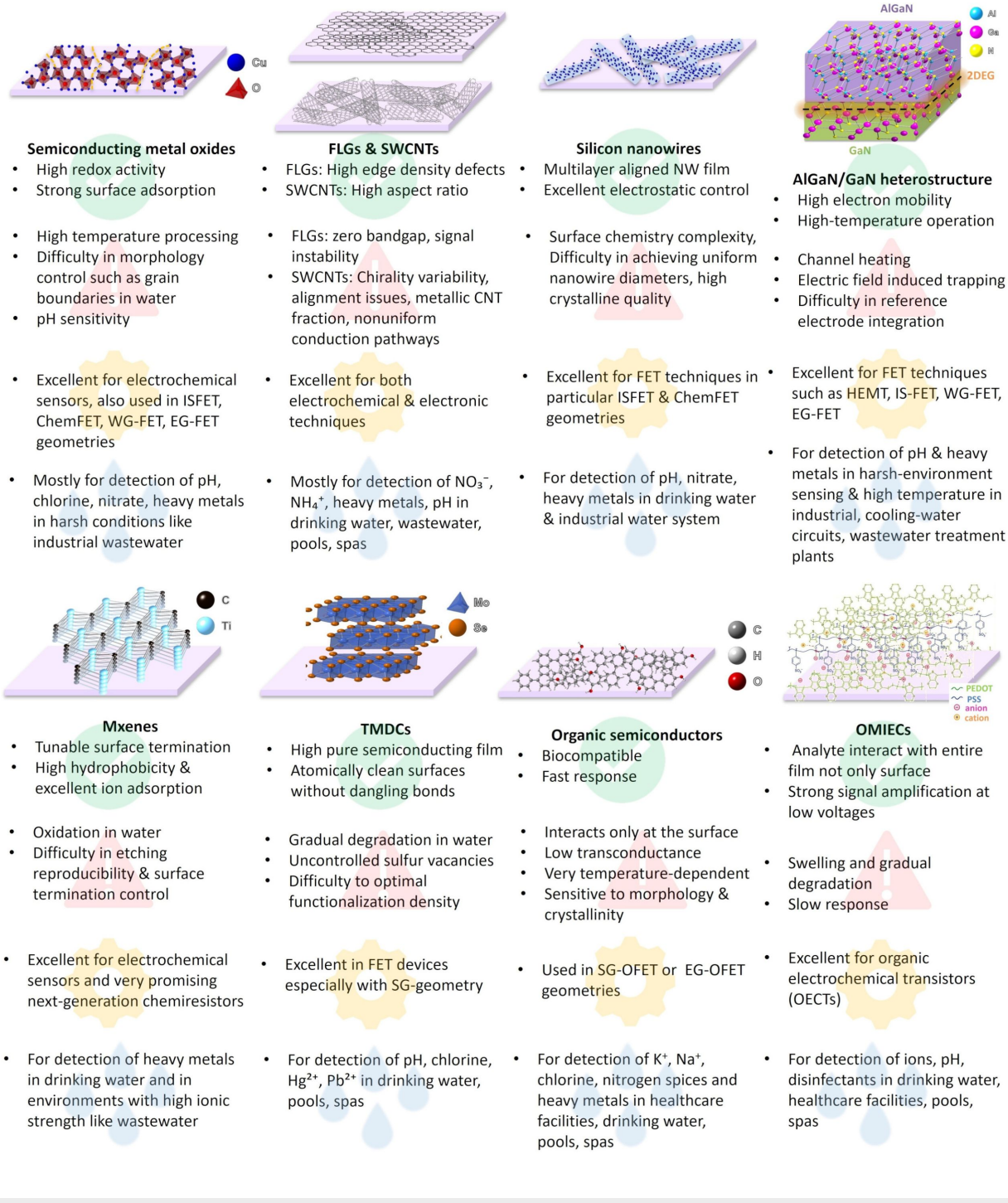


Figure 12: Summary of the properties of classified active-layer materials, highlighting their representative structures, key advantages, challenges specific to aqueous environments, compatible device types and geometries, and demonstrated applications in ion sensing. Images of material structures were generated using CrystalMaker®: a crystal and molecular structures program for Mac and Windows. CrystalMaker Software Ltd, Oxford, England (https://www.crystalmaker.com). This content is not subject to CC BY 4.0.

applied. Between all introduced channel materials, AlGaN/GaN heterostructures and SiNWs are the most electrically robust and stable channels under continuous gating [105,173,227]. In conclusion, the choice of an appropriate sensing material depends on the intended detection mechanism, the practical constraints of the fabrication process, and the specific require-

Table 4: Performance of classified materials for ion sensing in water, accompanied by an analysis of their device-fabrication considerations.

Material	Sensitivity	Selectivity	Water stability	Response time	Scalability	Fabrication cost	Ref.
SMOs	high	low (improves with surface ligands or composites)	high	moderate to fast	high	low (sol–gel, hydrothermal, screen-printing)	[229]
FLGs	high	low (improves with surface modification)	moderate (GO more hydrophilic, rGO more stable)	fast	high	moderate–high (CVD, transfer, functionalization)	[230]
SWCNTs	high	low (improves with surface modification)	high	fast	high	moderate (purification, dispersion, functionalization)	[20]
SiNWs	high	high with appropriate surface chemistry	high (native oxide stable in water)	fast	moderate to high (CMOS-compatible but cleanroom-intensive)	high (lithography, doping, passivation)	[28]
AlGaN/GaN	high	moderate to high with ISMs or receptors	high (chemically robust wide-bandgap surface)	fast	high (III–V wafer tech)	high (epitaxy, device processing)	[142]
MXenes	high	high	low (oxidation and structural degradation in water if not protected)	fast	high	moderate (etching, delamination, stabilization)	[154]
TMDCs	moderate to high	high if functionalized	moderate (surface oxidation/defects in aqueous media)	moderate to fast	moderate to high	moderate to high (CVD, exfoliation, printing)	[159]
organic thin films	moderate	moderate to high with specific ligands	low–moderate (swelling, fouling, degradation)	fast	high	low	[170]
OMIECs	high	moderate to high (depends on receptor design)	high if built on robust substrates and encapsulation	slow to moderate (often diffusion-limited through layers)	high	moderate (molecular design and device integration)	[173]
COFs	high	high	low to moderate (many COFs hydrolyze; some are water-stable)	moderate	moderate	moderate to high (synthesis and crystallinity control)	[202]
MOFs	high	high	low (many MOFs unstable in water; some water-stable variants exist	slow to moderate (diffusion into pores)	moderate	moderate	[198]
IIPs	high	high	high (cross-linked polymer networks stable in water)	moderate (binding and diffusion-limited)	high	low	[205]

ments of the target application. The advantages of both organic and inorganic materials can be combined by fabricating channels from hybrid materials for instance OMIEC–CNT composites. Using this strategy, mobility or electronic conduction via conductive fillers can be improved, ion uptake via polymer matrix can be enhanced, and the morphology can be tuned for balancing ion access vs. electronic conduction [173,228]. Devices can also be integrated with advanced materials such as

COFs, MOFs, and IIPs to simultaneously achieve high conductivity and high selectivity. Their intrinsic properties are summarized in Table 3, and their sensing performance is evaluated in Table 4. Notably, IIPs meet many criteria of an ideal ion sensor, that is, high sensitivity, strong selectivity, excellent water stability, scalability, cost-effectiveness, and reproducibility, highlighting their potential for practical deployment.

Operating continuously in aqueous environments poses distinctive challenges. Biofouling of membranes, FET gates, channel materials, and chemiresistive films can impede mass transport, change surface charge, or add parasitic potentials, resulting in drift, hysteresis, and sluggish responses. The use of antifouling polymer coatings or flow-through cells, or the application of self-cleaning strategies can mitigate fouling-induced degradation [16]. For instance, robust solid-contact ISEs designed with antifouling layers and advanced transduction have improved stability for chloride, nitrate, ammonium, and heavy-metal monitoring in natural waters and treatment streams [12,16]. Another issue is that variations in the supporting electrolyte can change the solution ionic strength, alter the analyte activity coefficient, and may introduce competing ionic species to the system that interact with the sensor. To mitigate these effects, matrix-matched calibration or algorithm-based compensation strategies are required such as potentially leveraging ISFET arrays and machine-learning models [8,10]. Moreover, variations in temperature and flow rate change both thermodynamics and kinetics, perturbing the ion transport and reference electrode stability. Using multiparameter sensing and algorithmic compensation can help to stabilize outputs [17]. Flow-through ISFET systems for automated ammonium monitoring and high-transconductance nitrate ISFETs further highlight progress toward deployments that couple microfabrication with rugged fluidic packaging [11,231]. Furthermore, the requirement for stable reference electrodes remains a critical challenge in continuous sensing platforms, particularly when miniaturized. In response, significant research is directed toward solid-state reference technologies and reference-free or self-calibrating sensing methodologies [7,13,15]. As an example, ion-selective-membrane-coated chemiresistive devices have achieved LODs around 1–2 μg/L for Pb^{2+} in water during continuous operation, indicating a viable path for low-cost monitoring of trace concentration of heavy metals [103]. In addition, many sensing materials suffer from significant contact-resistance issues at the terminals, and/or require proper passivation layers to remain stable. These factors demand careful materials selection and precise engineering strategies to ensure reliable device performance. Last, long-term drift from material aging, membrane leaching, or interfacial redox phenomena remains a major barrier, making self-diagnostics and autonomous recalibration highly valuable in multiweek monitoring [14,15,17].

Conclusion

This review highlights the diverse landscape of materials and strategies employed in solid-state ion sensing, emphasizing both their potential and limitations. As the field advances, it is increasingly clear that no single material system will dominate all sensing scenarios. Instead, progress will depend on smart choices of channel material, interfacial chemistry, and sensing architecture, which is dictated by the target analyte, operating environment, and required performance metrics such as sensitivity, selectivity, stability, and response time. Metal oxides, while not commonly used as FET channel materials due to their wide bandgap and abundance of surface states, remain valuable as redox-active components in nanocomposites that enhance electrochemical signal transduction. Their catalytic activity and chemical robustness make them particularly well suited for oxidizing or reducing analytes such as heavy-metal ions, reactive oxygen species, and disinfectants. Carbon-based materials such as graphene and carbon nanotubes and their functionalized derivatives offer high sensitivity owing to their high transconductance and strong surface-charge coupling. These materials are well suited for detecting low-concentration analytes such as trace metal ions or biologically relevant ions in buffered systems. However, future efforts must prioritize improved control over synthesis, surface chemistry, and device fabrication to overcome reproducibility challenges that currently limit large-scale deployment and commercialization. In contrast, silicon nanowires and AlGaN/GaN channels demonstrate excellent stability. For applications requiring long-term stability and minimal drift, such as continuous water quality monitoring or implantable and wearable biosensors, semiconductor platforms like silicon nanowires and AlGaN/GaN heterostructures are likely to remain dominant. Their inherent robustness, mature fabrication processes, and compatibility with existing electronics infrastructure make them particularly appealing for commercialization and field deployment although their device-fabrication workflows remain relatively complex and costly. MXenes provide high electrical conductivity and high surface activity, making them attractive for rapid and highly sensitive ion detection. However, they suffer from instability in aqueous environments due to surface terminations. Future research must focus on surface passivation strategies, compositional tuning, or hybridization with stabilizing matrices to unlock their full potential for real-world sensing applications. TMDCs stand out as a versatile class of semiconductors whose tunable bandgap and atomically thin structure, enable stable and sensitive electrical sensing platforms, most commonly implemented in SG-FET geometries.

Conventional organic FETs, based on small molecules or conjugated polymers, generally exhibit lower sensitivity compared to inorganic materials, which limits their use in ultratrace detec-

tion. However, they offer a number of advantages such as rapid response times, mechanical flexibility and biocompatibility, making them attractive for transient sensing, wearable platforms, and low-cost disposable devices. OMIECs attempt to overcome the weaker performance of conventional OFETs by incorporating volumetric electrochemical interactions, thereby significantly enhancing sensitivity. This improvement in sensitivity, however, comes at the expense of response speed, which highlights a broader challenge in OMIECs, that is, the need to decouple ion transport kinetics from electronic response. Future material design efforts should aim to optimize polymer morphology, ion mobility, and device architecture to achieve both high sensitivity and rapid temporal resolution. Looking ahead, application-specific material selection will become increasingly important. For example, environmental monitoring of pH, heavy metals, and nutrients benefits from stable inorganic channels (SiNWs, GaN) or robust carbon-based materials functionalized with chelating ligands. Biomedical sensing of electrolytes is well served by OMIECs, TMDCs, and CNT-based FETs functionalized with biomolecular receptors. Industrial process control, which often involves harsh chemical environments, may rely on metal-oxide nanocomposites or protected MXene-based architectures. Wearable and flexible sensing aligns naturally with organic semiconductors, and hybrid polymer–nanomaterial composites.

Beyond channel materials, surface engineering plays a critical role in optimizing sensor performance. The deliberate introduction of defects and nanoparticle dopants enhances ion diffusion, charge transfer, and signal amplification. At the same time, covalent or noncovalent functionalization with organic molecules can improve operational stability and selectivity. However, lack of tight control over interfacial structure and defects remains a major source of noise, hysteresis, and drift. A deeper mechanistic understanding of ion–interface interactions, supported by in situ characterization and modeling, will be essential to rationally designing stable and low-noise sensor interfaces. Nanocomposites offer an alternative to surface functionalization, with the potential to either mitigate or exacerbate interface issues depending on their phase distribution, percolation pathways, and interfacial compatibility. As such, future work should focus on predictive design rules that link nanocomposite structure to sensing performance.

Advanced porous materials including MOFs, COFs, and IIPs are expected to play an increasingly important role in achieving high selectivity. Their well-defined pore structures, large surface areas, tunable chemistry, and predictable sensing mechanisms make them particularly attractive for discriminating among chemically similar ions. Given their intrinsically low electrical conductivity, these materials are best deployed as functional layers or composite components integrated with conductive or semiconductive channels. Biomolecular recognition elements deliver excellent selectivity. However, their limited operational lifetime, susceptibility to denaturation, and high cost constrain their widespread adoption. Future directions may include the development of biomimetic or synthetic analogues that retain selectivity while improving robustness and shelf life. Ion-selective membranes remain one of the most effective strategies for achieving stable and selective ion sensing, particularly in long-term or fouling-prone environments. They are necessary when film protection and ion buffering are required such as in physiological matrices or wastewater monitoring. However, in applications where direct channel–analyte interactions are essential for sensitivity or response speed, membrane integration may be unnecessary or even detrimental. A more detailed understanding of when and how to deploy membranes will be critical for optimal sensor design.

At the system level, sensor arrays represent a powerful approach for multiplexed detection and signal amplification. Arrays of single-analyte sensors are powerful when absolute accuracy and direct readouts are required, such as in clinical diagnostics or regulatory water monitoring. Conversely, cross-reactive arrays are more flexible for complex mixtures where single-analyte selectivity is neither feasible nor necessary, though they rely on computational models such as machine learning, chemometric analysis, and pattern-recognition algorithms for interpretation. In summary, the future of solid-state ion sensing lies in the convergence of tailored material selection, sophisticated interface engineering, and intelligent system integration. Continued progress will require interdisciplinary collaboration across chemistry, material engineering, electrical engineering, and data science. By embracing application-specific design principles and leveraging the complementary strengths of diverse material classes, the field is well positioned to deliver robust, real-time, and scalable ion sensors capable of operating in complex aqueous environments.

Funding

The authors gratefully acknowledge funding provided by the Natural Sciences and Engineering Research Council of Canada (NSERC) via the Discovery Grant program (Grant No. RGPIN-2023-04927).

Author Contributions

Maryam Darestani-Farahani: conceptualization; visualization; writing – original draft; writing – review & editing. Peter Kruse: conceptualization; resources; supervision; writing – review & editing.

ORCID® iDs

Maryam Darestani-Farahani - https://orcid.org/0000-0002-8620-8747
Peter Kruse - https://orcid.org/0000-0003-4051-4375

Data Availability Statement

Data sharing is not applicable as no new data was generated or analyzed in this study.

References

1. Jaywant, S. A.; Arif, K. M. *Sensors* **2019,** *19,* 4781. doi:10.3390/s19214781
2. World Health Organization (WHO). *Guidelines for Drinking-Water Quality*; consolidated tables of guideline values available. 2022; https://www.who.int/publications/i/item/9789240045064 (accessed Oct 29, 2025).
3. U.S. Environmental Protection Agency (EPA). National Primary Drinking Water Regulations (overview page with MCLs). https://www.epa.gov/sdwa/drinking-water-regulations-and-contaminants (accessed Oct 29, 2025).
4. Umberg, M.; Allgeier, S. *Online Water Quality Monitoring in Distribution Systems*. 2018; https://www.epa.gov/sites/default/files/2018-05/documents/owqm-ds_guidance_042018.pdf.
5. *Directive (EU) 2020/2184 of the European Parliament and of the Council of 16 December 2020 on the Quality of Water Intended for Human Consumption (Recast)*. Vol. 435. 2020; https://eur-lex.europa.eu/legal-content/EN/TXT/?uri=CELEX%3A32020L2184.
6. Tatara, R.; Shibasaki, Y.; Igarashi, D.; Osada, H.; Aoki, K.; Miyamoto, Y.; Takayama, T.; Matsui, T.; Komaba, S. *Anal. Chem. (Washington, DC, U. S.)* **2025,** *97,* 4819–4823. doi:10.1021/acs.analchem.4c06470
7. Kim, Y.; Seo, M.; Baek, S. *Sens. Actuators Rep.* **2025,** *9,* 100258. doi:10.1016/j.snr.2024.100258
8. Goma, P.; Rana, A. K. *Silicon* **2024,** *16,* 1–14. doi:10.1007/s12633-023-02675-1
9. Maity, A.; Pu, H.; Sui, X.; Chang, J.; Bottum, K. J.; Jin, B.; Zhou, G.; Wang, Y.; Lu, G.; Chen, J. *Nat. Commun.* **2023,** *14,* 4184. doi:10.1038/s41467-023-39701-0
10. Fakih, I.; Durnan, O.; Mahvash, F.; Napal, I.; Centeno, A.; Zurutuza, A.; Yargeau, V.; Szkopek, T. *Nat. Commun.* **2020,** *11,* 3226. doi:10.1038/s41467-020-16979-y
11. McGarrity, M.; Zhao, F. *Sensors* **2023,** *23,* 9828. doi:10.3390/s23249828
12. Huang, Y.; Afolabi, M. A.; Gan, L.; Liu, S.; Chen, Y. *Environ. Sci. Technol.* **2024,** *58,* 1359–1368. doi:10.1021/acs.est.3c06235
13. Kuczak, J.; Górski, Ł. *Anal. Chim. Acta* **2025,** *1378,* 344473. doi:10.1016/j.aca.2025.344473
14. Abdollahzadeh, M.; Zhu, Y.; Bayatsarmadi, B.; Vepsäläinen, M.; Razmjou, A.; Murugappan, K.; Rodopoulos, T.; Asadnia, M. *Comput. Electron. Agric.* **2024,** *227,* 109455. doi:10.1016/j.compag.2024.109455
15. Zhou, Y.; Liang, R.; Qin, W. *Analyst* **2025,** *150,* 1103–1111. doi:10.1039/d4an01583e
16. Siangdee, N.; Supchocksoonthorn, P.; Suwanboriboon, J.; Meesiri, W.; Chauyrod, K.; Chaisriratanakul, W.; Bunjongpru, W.; Youngvises, N.; Paoprasert, P. *Electrochim. Acta* **2024,** *499,* 144721. doi:10.1016/j.electacta.2024.144721
17. Xu, Y.; Zhou, P.; Simon, T.; Cui, T. *Microsyst. Nanoeng.* **2024,** *10,* 137. doi:10.1038/s41378-024-00768-4
18. Polidori, G.; Tonello, S.; Serpelloni, M. *IEEE Sens. J.* **2024,** *24,* 7375–7394. doi:10.1109/jsen.2024.3354321
19. Hu, T.; Lai, Q.; Fan, W.; Zhang, Y.; Liu, Z. *Sensors* **2023,** *23,* 4125. doi:10.3390/s23084125
20. Cho, G.; Azzouzi, S.; Zucchi, G.; Lebental, B. *Sensors* **2022,** *22,* 218. doi:10.3390/s22010218
21. Elli, G.; Hamed, S.; Petrelli, M.; Ibba, P.; Ciocca, M.; Lugli, P.; Petti, L. *Sensors* **2022,** *22,* 4178. doi:10.3390/s22114178
22. Thakur, A.; Devi, P. *Crit. Rev. Anal. Chem.* **2024,** *54,* 193–218. doi:10.1080/10408347.2022.2070838
23. Mukherjee, S.; Bhattacharyya, S.; Ghosh, K.; Pal, S.; Halder, A.; Naseri, M.; Mohammadniaei, M.; Sarkar, S.; Ghosh, A.; Sun, Y.; Bhattacharyya, N. *Trends Food Sci. Technol.* **2021,** *109,* 674–689. doi:10.1016/j.tifs.2021.01.062
24. Saez, J.; Catalan-Carrio, R.; Owens, R. M.; Basabe-Desmonts, L.; Benito-Lopez, F. *Anal. Chim. Acta* **2021,** *1186,* 338392. doi:10.1016/j.aca.2021.338392
25. Yaroshenko, I.; Kirsanov, D.; Marjanovic, M.; Lieberzeit, P. A.; Korostynska, O.; Mason, A.; Frau, I.; Legin, A. *Sensors* **2020,** *20,* 3432. doi:10.3390/s20123432
26. Meyer, A. M.; Oliveri, E.; Kautenburger, R.; Hein, C.; Kickelbick, G.; Beck, H. P. *Environ. Sci.: Adv.* **2025,** *4,* 1238–1249. doi:10.1039/d5va00021a
27. Li, Y.; Liu, J.; Zhang, L.; Yang, Q.; Chen, W.; Wu, J.; Zhang, L.; Li, X.; Xu, K. *Langmuir* **2024,** *40,* 19187–19194. doi:10.1021/acs.langmuir.4c02342
28. Falina, S.; Syamsul, M.; Rhaffor, N. A.; Sal Hamid, S.; Mohamed Zain, K. A.; Abd Manaf, A.; Kawarada, H. *Biosensors* **2021,** *11,* 478. doi:10.3390/bios11120478
29. Kruse, P. *J. Phys. D: Appl. Phys.* **2018,** *51,* 203002. doi:10.1088/1361-6463/aabb93
30. Paramparambath, S.; Oflaz, K.; Geetha, M.; Ahmed, M. E. *Chem. Afr.* **2025,** *8,* 1115–1126. doi:10.1007/s42250-024-01177-w
31. Winkler, S.; Rieger, L.; Saracevic, E.; Pressl, A.; Gruber, G. *Water Sci. Technol.* **2004,** *50,* 105–114. doi:10.2166/wst.2004.0678
32. Fewtrell, L. *Environ. Health Perspect.* **2004,** *112,* 1371–1374. doi:10.1289/ehp.7216
33. Lal, K.; Jaywant, S. A.; Arif, K. M. *Sensors* **2023,** *23,* 7099. doi:10.3390/s23167099
34. Badger Meter. *S::can Messtechnik GmbH, Water Quality OnLine Drinking Water*. https://www.badgermeter.com/products/water-quality-monitoring/scan/ (accessed Nov 3, 2025).
35. *Directive (EU) 2024/3019 of the European Parliament and of the Council of 27 November 2024 concerning urban wastewater treatment*. https://eur-lex.europa.eu/eli/dir/2024/3019/oj/eng.
36. Higgins, P. *Ammonium-Based Aeration Control in Wastewater*. Xylem, 2014; https://www.xylem.com/siteassets/brand/wtw/resources/white-papers/white-paper-ammonium-based-aeration-control-in-wastewater-wtw.pdf (accessed Nov 4, 2025).

37. *Urban Wastewater Treatment, Updating EU Rules; EU Legislation in Progress*. 2024; https://www.europarl.europa.eu/RegData/etudes/BRIE/2023/739370/EPRS_BRI%282023%29739370_EN.pdf.
38. *Aquamonitrix: Real-time analyser for nitrate and nitrite measurements in fresh and effluent water*. https://www.aquamonitrix.com.
39. Rahimi, S.; Modin, O.; Mijakovic, I. *Biotechnol. Adv.* **2020,** *43,* 107570. doi:10.1016/j.biotechadv.2020.107570
40. Ryu, H.; Thompson, D.; Huang, Y.; Li, B.; Lei, Y. *Sens. Actuators Rep.* **2020,** *2,* 100022. doi:10.1016/j.snr.2020.100022
41. EU4Environment. *Water Resources and Environmental Data (ENI/2021/425-550)*. https://www.unece.org.
42. Dalmieda, J.; Kruse, P. *Sensors* **2019,** *19,* 5134. doi:10.3390/s19235134
43. Xeni, C.; Oliva, R.; Jahan, F.; Romaina, I.; Naser, A. M.; Rahman, M.; Fleming, L. E.; O Gribble, M.; Makris, K. C. *Environ. Res.: Health* **2023,** *1,* 035006. doi:10.1088/2752-5309/ace076
44. Christensen, M. L.; Keiding, K.; Nielsen, P. H.; Jørgensen, M. K. *Water Res.* **2015,** *82,* 14–24. doi:10.1016/j.watres.2015.04.019
45. Guo, L.; Xie, Y.; Sun, W.; Xu, Y.; Sun, Y. *Water* **2023,** *15,* 684. doi:10.3390/w15040684
46. Alotaibi, M.; Refaat, A.; Munshi, F.; El-Said, M. A.; El-Shafai, S. A. *Water* **2024,** *16,* 2629. doi:10.3390/w16182629
47. Sankaran, M. *The Impact of Salinity Levels on Industrial Systems & Equipment*. KETOS, 2025; https://ketos.co/the-impact-of-salinity-levels-on-industrial-systems-equipment (accessed Nov 4, 2025).
48. Yurtsever, A.; Calimlioglu, B.; Görür, M.; Çınar, Ö.; Sahinkaya, E. *Chem. Eng. J.* **2016,** *287,* 456–465. doi:10.1016/j.cej.2015.11.061
49. World Health Organization (WHO). *Chemical fact sheets: Bromate*. https://www.who.int/publications/m/item/chemical-fact-sheets--bromate (accessed Nov 5, 2025).
50. Hong, Y.; Lee, J.; Park, S.; Kim, J.; Jang, K.-J. *AgriEngineering* **2024,** *6,* 4786–4811. doi:10.3390/agriengineering6040274
51. Rho, H.; Lee, Y.-g.; Cho, J.; Woo, Y. C.; Chon, K. *Sci. Total Environ.* **2023,** *903,* 166127. doi:10.1016/j.scitotenv.2023.166127
52. Patel, V.; Selvaganapathy, P. R. *Sens. Actuators, B* **2021,** *349,* 130789. doi:10.1016/j.snb.2021.130789
53. Patel, V.; Kruse, P.; Selvaganapathy, P. R. *J. Electrochem. Soc.* **2022,** *169,* 077505. doi:10.1149/1945-7111/ac7c3b
54. Zhu, Z.; Zhou, H.; Zou, J.; Wang, J. *Water Cycle* **2023,** *4,* 95–103. doi:10.1016/j.watcyc.2023.05.001
55. Cui, Y.-W.; Zhang, H.-Y.; Ding, J.-R.; Peng, Y.-Z. *Sci. Rep.* **2016,** *6,* 24825. doi:10.1038/srep24825
56. Akinnawo, S. O. *Environ. Challenges* **2023,** *12,* 100733. doi:10.1016/j.envc.2023.100733
57. Mahmud, M. A. P.; Ejeian, F.; Azadi, S.; Myers, M.; Pejcic, B.; Abbassi, R.; Razmjou, A.; Asadnia, M. *Chemosphere* **2020,** *259,* 127492. doi:10.1016/j.chemosphere.2020.127492
58. Kardos, M. K.; Patziger, M.; Jolánkai, Z.; Clement, A. *Environ. Sci. Eur.* **2025,** *37,* 10. doi:10.1186/s12302-024-01040-2
59. *Environmental, Health, and Safety Guidelines: Wastewater and Ambient Water Quality*. 2007; https://www.ifc.org/en/insights-reports/general-environmental-health-and-safety-guidelines (accessed Nov 3, 2025).
60. Lee, J.; Shin, Y.; Ryu, H.; Boo, C.; Hong, S. *Water Res.* **2025,** *279,* 123410. doi:10.1016/j.watres.2025.123410
61. Sinharoy, A.; Chung, C. M. *Environ. Eng. Res.* **2024,** *29,* 240179. doi:10.4491/eer.2024.179
62. Liang, X.; Xu, Y.; Yin, L.; Wang, R.; Li, P.; Wang, J.; Liu, K. *Water* **2023,** *15,* 4135. doi:10.3390/w15234135
63. Özkaymak, G.; Şahan, A. N.; Yakamercan, E.; Çakmak, Y.; Uçar, D. *J. Chem. Technol. Biotechnol.* **2024,** *99,* 1921–1928. doi:10.1002/jctb.7699
64. Elmobarak, W. F.; Hameed, B. H.; Almomani, F.; Abdullah, A. Z. *Catalysts* **2021,** *11,* 782. doi:10.3390/catal11070782
65. Lee, C.-H.; Ho, H.-J.; Chen, W.-S.; Iizuka, A. *Adv. Sustainable Syst.* **2024,** *8,* 2300460. doi:10.1002/adsu.202300460
66. Jomova, K.; Alomar, S. Y.; Nepovimova, E.; Kuca, K.; Valko, M. *Arch. Toxicol.* **2025,** *99,* 153–209. doi:10.1007/s00204-024-03903-2
67. Hong, Y.-S.; Kim, Y.-M.; Lee, K.-E. *J. Prev. Med. Public Health* **2012,** *45,* 353–363. doi:10.3961/jpmph.2012.45.6.353
68. Yang, W.; Song, W.; Li, J.; Zhang, X. *Chemosphere* **2020,** *249,* 126134. doi:10.1016/j.chemosphere.2020.126134
69. Olejnik, D. *Sustainability* **2024,** *16,* 5198. doi:10.3390/su16125198
70. Colford, S.; Dhirani, A.-A. *Colloids Surf., A* **2025,** *723,* 137416. doi:10.1016/j.colsurfa.2025.137416
71. Balali-Mood, M.; Naseri, K.; Tahergorabi, Z.; Khazdair, M. R.; Sadeghi, M. *Front. Pharmacol.* **2021,** *12,* 643972. doi:10.3389/fphar.2021.643972
72. Saravanan, P.; Saravanan, V.; Rajeshkannan, R.; Arnica, G.; Rajasimman, M.; Baskar, G.; Pugazhendhi, A. *Environ. Res.* **2024,** *258,* 119440. doi:10.1016/j.envres.2024.119440
73. Babuji, P.; Thirumalaisamy, S.; Duraisamy, K.; Periyasamy, G. *Water* **2023,** *15,* 2532. doi:10.3390/w15142532
74. Rehman, K.; Fatima, F.; Waheed, I.; Akash, M. S. H. *J. Cell. Biochem.* **2018,** *119,* 157–184. doi:10.1002/jcb.26234
75. Gao, L.; Tian, Y.; Gao, W.; Xu, G. *Sensors* **2024,** *24,* 4289. doi:10.3390/s24134289
76. Wardak, C.; Pietrzak, K.; Morawska, K.; Grabarczyk, M. *Sensors* **2023,** *23,* 5839. doi:10.3390/s23135839
77. Criscuolo, F.; Hanitra, M. I. N.; Taurino, I.; Carrara, S.; De Micheli, G. *IEEE Sens. J.* **2021,** *21,* 22143–22154. doi:10.1109/jsen.2021.3099209
78. Cuartero, M.; Crespo, G. A. *Curr. Opin. Electrochem.* **2018,** *10,* 98–106. doi:10.1016/j.coelec.2018.04.004
79. Zdrachek, E.; Bakker, E. *Anal. Chem. (Washington, DC, U. S.)* **2021,** *93,* 72–102. doi:10.1021/acs.analchem.0c04249
80. Kanoun, O.; Müller, C.; Benchirouf, A.; Sanli, A.; Dinh, T. N.; Al-Hamry, A.; Bu, L.; Gerlach, C.; Bouhamed, A. *Sensors* **2014,** *14,* 10042–10071. doi:10.3390/s140610042
81. Revsbech, N. P.; Nielsen, M.; Fapyane, D. *Sensors* **2020,** *20,* 4326. doi:10.3390/s20154326
82. Wygant, B. R.; Lambert, T. N. *Front. Chem. (Lausanne, Switz.)* **2022,** *9,* 809535. doi:10.3389/fchem.2021.809535
83. Wang, J.; Lu, J.; Kirgöz, Ü. A.; Hocevar, S. B.; Ogorevc, B. *Anal. Chim. Acta* **2001,** *434,* 29–34. doi:10.1016/s0003-2670(01)00818-2
84. Pratiwi, N. H.; Azis, M. Y.; Setyorini, D. A.; Rahayu, R. S. *Anal. Bioanal. Electrochem.* **2022,** *14,* 331–347.
85. Jimenez-Jorquera, C.; Orozco, J.; Baldi, A. *Sensors* **2010,** *10,* 61–83. doi:10.3390/s100100061
86. Wang, Y.; Yang, M.; Wu, C. *Sensors* **2020,** *20,* 6921. doi:10.3390/s20236921
87. Parizi, K. B.; Xu, X.; Pal, A.; Hu, X.; Wong, H. S. P. *Sci. Rep.* **2017,** *7,* 41305. doi:10.1038/srep41305
88. Ayadi, N.; Lale, A.; Hajji, B.; Launay, J.; Temple-Boyer, P. *Sensors* **2024,** *24,* 8091. doi:10.3390/s24248091

89. Bresnahan, P. J.; Takeshita, Y.; Wirth, T.; Martz, T. R.; Cyronak, T.; Albright, R.; Wolfe, K.; Warren, J. K.; Mertz, K. *Limnol. Oceanogr.: Methods* **2021,** *19,* 132–144. doi:10.1002/lom3.10410
90. Joly, M.; Marlet, M.; Durieu, C.; Bene, C.; Launay, J.; Temple-Boyer, P. *Sens. Actuators, B* **2022,** *351,* 130949. doi:10.1016/j.snb.2021.130949
91. Dasca, A.; Blondeau, P.; Riu, J.; Andrade, F. J. *Talanta* **2025,** *282,* 126957. doi:10.1016/j.talanta.2024.126957
92. Meng, X.; Zou, T.; Chan, M. H. M.; Chan, D. T. M.; Tsang, A. C. O.; Leung, G. K. K.; Zhang, S.; Chan, P. K. L. *Adv. Sens. Res.* **2024,** *3,* 2300097. doi:10.1002/adsr.202300097
93. Kim, J.; Liu, Q.; Cui, T. *Org. Electron.* **2020,** *78,* 105551. doi:10.1016/j.orgel.2019.105551
94. Sonmez, B. G.; Ertop, O.; Mutlu, S. *Sci. Rep.* **2017,** *7,* 12190. doi:10.1038/s41598-017-12439-8
95. Zhao, L.; Liu, X.; Miao, B.; Gu, Z.; Wang, J.; Peng, H.; Zhang, J.; Zeng, B.; Li, J. *Anal. Methods* **2019,** *11,* 3981–3986. doi:10.1039/c9ay01019j
96. Hu, J.; Stein, A.; Bühlmann, P. *TrAC, Trends Anal. Chem.* **2016,** *76,* 102–114. doi:10.1016/j.trac.2015.11.004
97. Fennell, J. F., Jr.; Liu, S. F.; Azzarelli, J. M.; Weis, J. G.; Rochat, S.; Mirica, K. A.; Ravnsbæk, J. B.; Swager, T. M. *Angew. Chem., Int. Ed.* **2016,** *55,* 1266–1281. doi:10.1002/anie.201505308
98. Akbar, M. A.; Sharif, O.; Selvaganapathy, P. R.; Kruse, P. *ACS Appl. Eng. Mater.* **2023,** *1,* 3040–3052. doi:10.1021/acsaenm.3c00505
99. Dalmieda, J.; Zubiarrain-Laserna, A.; Ganepola, D.; Selvaganapathy, P. R.; Kruse, P. *Sens. Actuators, B* **2021,** *328,* 129023. doi:10.1016/j.snb.2020.129023
100. Akbar, M. A.; Selvaganapathy, P. R.; Kruse, P. *ACS ES&T Water* **2024,** *4,* 4041–4051. doi:10.1021/acsestwater.4c00341
101. Akbar, M. A.; Selvaganapathy, P. R.; Kruse, P. *J. Phys. Chem. C* **2025,** *129,* 14583–14592. doi:10.1021/acs.jpcc.5c03233
102. Zubiarrain-Laserna, A.; Angizi, S.; Akbar, M. A.; Divigalpitiya, R.; Selvaganapathy, P. R.; Kruse, P. *RSC Adv.* **2022,** *12,* 2485–2496. doi:10.1039/d1ra08264g
103. Darestani-Farahani, M.; Mendoza Montealegre, I.; Tavakkoli Gilavan, M.; Kirby, T.; Selvaganapathy, P. R.; Kruse, P. *Analyst* **2024,** *149,* 2915–2924. doi:10.1039/d4an00159a
104. Darestani-Farahani, M.; Ma, F.; Patel, V.; Selvaganapathy, P. R.; Kruse, P. *Analyst* **2023,** *148,* 5731–5744. doi:10.1039/d3an01267k
105. Ma, X.; Peng, R.; Mao, W.; Lin, Y.; Yu, H. *Electrochem. Sci. Adv.* **2023,** *3,* e2100163. doi:10.1002/elsa.202100163
106. Tang, R.; Shi, Y.; Hou, Z.; Wei, L. *Sensors* **2017,** *17,* 882. doi:10.3390/s17040882
107. Munonde, T. S.; Nomngongo, P. N. *Sensors* **2021,** *21,* 131. doi:10.3390/s21010131
108. Dutta, T.; Noushin, T.; Tabassum, S.; Mishra, S. K. *Sensors* **2023,** *23,* 6849. doi:10.3390/s23156849
109. Zappa, D.; Bertuna, A.; Comini, E.; Kaur, N.; Poli, N.; Sberveglieri, V.; Sberveglieri, G. *Beilstein J. Nanotechnol.* **2017,** *8,* 1205–1217. doi:10.3762/bjnano.8.122
110. Alqahtani, Z.; Alghamdi, N.; Grell, M. *J. Water Health* **2020,** *18,* 159–171. doi:10.2166/wh.2020.186
111. Arora, S.; Punith Kumar, M. K.; Srivastava, C. *Philos. Mag. Lett.* **2020,** *100,* 533–541. doi:10.1080/09500839.2020.1811416
112. Staerz, A.; Weimar, U.; Barsan, N. *Sens. Actuators, B* **2022,** *358,* 131531. doi:10.1016/j.snb.2022.131531
113. Sinha, S.; Pal, T. *Electrochem. Sci. Adv.* **2022,** *2,* e2100147. doi:10.1002/elsa.202100147
114. Xu, Z.; Fan, X.; Ma, Q.; Tang, B.; Lu, Z.; Zhang, J.; Mo, G.; Ye, J.; Ye, J. *Mater. Chem. Phys.* **2019,** *238,* 121877. doi:10.1016/j.matchemphys.2019.121877
115. Rim, Y. S. *J. Inf. Disp.* **2020,** *21,* 203–210. doi:10.1080/15980316.2020.1714762
116. Zubiarrain-Laserna, A.; Kruse, P. *J. Electrochem. Soc.* **2020,** *167,* 037539. doi:10.1149/1945-7111/ab67a5
117. Szunerits, S.; Rodrigues, T.; Bagale, R.; Happy, H.; Boukherroub, R.; Knoll, W. *Anal. Bioanal. Chem.* **2024,** *416,* 2137–2150. doi:10.1007/s00216-023-04760-1
118. Kesler, V.; Murmann, B.; Soh, H. T. *ACS Nano* **2020,** *14,* 16194–16201. doi:10.1021/acsnano.0c08622
119. Chen, X.; Pu, H.; Fu, Z.; Sui, X.; Chang, J.; Chen, J.; Mao, S. *Environ. Sci.: Nano* **2018,** *5,* 1990–1999. doi:10.1039/c8en00588e
120. Ono, T.; Okuda, S.; Ushiba, S.; Kanai, Y.; Matsumoto, K. *Materials* **2024,** *17,* 333. doi:10.3390/ma17020333
121. Angizi, S.; Hong, L.; Huang, X.; Selvaganapathy, P. R.; Kruse, P. *npj 2D Mater. Appl.* **2023,** *7,* 67. doi:10.1038/s41699-023-00431-y
122. Zaporotskova, I. V.; Boroznina, N. P.; Parkhomenko, Y. N.; Kozhitov, L. V. *Mod. Electron. Mater.* **2016,** *2,* 95–105. doi:10.1016/j.moem.2017.02.002
123. Shkodra, B.; Petrelli, M.; Costa Angeli, M. A.; Garoli, D.; Nakatsuka, N.; Lugli, P.; Petti, L. *Appl. Phys. Rev.* **2021,** *8,* 041325. doi:10.1063/5.0058591
124. Liu, Y.; Zhi, Z.; Liu, S.; Qian, J.; Huang, K.; Hua, Z. *ACS Omega* **2025,** *10,* 27462–27472. doi:10.1021/acsomega.5c03243
125. Melzer, K.; Münzer, A. M.; Jaworska, E.; Maksymiuk, K.; Michalska, A.; Scarpa, G. *Analyst* **2014,** *139,* 4947–4954. doi:10.1039/c4an00714j
126. Islam, A. E. *Electronics (Basel, Switz.)* **2013,** *2,* 332–367. doi:10.3390/electronics2040332
127. Franklin, A. D.; Farmer, D. B.; Haensch, W. *ACS Nano* **2014,** *8,* 7333–7339. doi:10.1021/nn5024363
128. Yoon, J.; Lim, M.; Choi, B.; Kim, D. M.; Kim, D. H.; Kim, S.; Choi, S.-J. *Sci. Rep.* **2017,** *7,* 5453. doi:10.1038/s41598-017-05653-x
129. Prakash, P.; Mohana Sundaram, K.; Anto Bennet, M. *Renewable Sustainable Energy Rev.* **2018,** *89,* 194–203. doi:10.1016/j.rser.2018.03.021
130. Deng, Y.; Liu, L.; Li, J.; Gao, L. *Biosensors* **2022,** *12,* 776. doi:10.3390/bios12100776
131. Kausar, A.; Ahmad, I. *e-Prime - Adv. Electr. Eng. Electron. Energy* **2024,** *7,* 100419. doi:10.1016/j.prime.2024.100419
132. Clément, N.; Nishiguchi, K.; Dufreche, J. F.; Guerin, D.; Fujiwara, A.; Vuillaume, D. *Appl. Phys. Lett.* **2011,** *98,* 014104. doi:10.1063/1.3535958
133. Vu, C.-A.; Hu, W.-P.; Yang, Y.-S.; Chan, H. W.-H.; Chen, W.-Y. *ACS Omega* **2019,** *4,* 14765–14771. doi:10.1021/acsomega.9b01264
134. Bhattacharjee, A.; Nguyen, T. C.; Pachauri, V.; Ingebrandt, S.; Vu, X. T. *Micromachines* **2021,** *12,* 39. doi:10.3390/mi12010039
135. Ahoulou, S.; Perret, E.; Nedelec, J.-M. *Nanomaterials* **2021,** *11,* 999. doi:10.3390/nano11040999
136. Chen, K.-I.; Li, B.-R.; Chen, Y.-T. *Nano Today* **2011,** *6,* 131–154. doi:10.1016/j.nantod.2011.02.001
137. Chen, X.; Hu, Q.; Chen, S.; Netzer, N. L.; Wang, Z.; Zhang, S.-L.; Zhang, Z. *Sens. Actuators, B* **2018,** *270,* 89–96. doi:10.1016/j.snb.2018.05.018

138. Prabha Rajeev, K.; Opoku, C.; Stolojan, V.; Constantinou, M.; Shkunov, M. *arXiv* **2015,** No. 1507.04719. doi:10.48550/arxiv.1507.04719
139. Gao, A.; Chen, S.; Wang, Y.; Li, T. *Sens. Mater.* **2018,** *30,* 1619–1628. doi:10.18494/sam.2018.1829
140. Noor, M. O.; Krull, U. J. *Anal. Chim. Acta* **2014,** *825,* 1–25. doi:10.1016/j.aca.2014.03.016
141. Li, H.; Li, D.; Chen, H.; Yue, X.; Fan, K.; Dong, L.; Wang, G. *Sensors* **2023,** *23,* 6808. doi:10.3390/s23156808
142. Haziq, M.; Falina, S.; Abd Manaf, A.; Kawarada, H.; Syamsul, M. *Micromachines* **2022,** *13,* 2133. doi:10.3390/mi13122133
143. Bhat, A. M.; Poonia, R.; Varghese, A.; Shafi, N.; Periasamy, C. *Micro Nanostruct.* **2023,** *176,* 207528. doi:10.1016/j.micrna.2023.207528
144. Ye, M.; Sun, J.; Zhan, T.; Sokolovskij, R.; Zhang, Y.; Wei, J.; Chen, S.; Liu, Z. *Appl. Sci.* **2024,** *14,* 6131. doi:10.3390/app14146131
145. Sandeep, V.; Pravin, J. C.; Kumar, S. A. *Microelectron. Reliab.* **2024,** *159,* 115445. doi:10.1016/j.microrel.2024.115445
146. Upadhyay, K. T.; Chattopadhyay, M. K. *Mater. Sci. Eng., B* **2021,** *263,* 114849. doi:10.1016/j.mseb.2020.114849
147. Jia, X.; Chen, D.; Bin, L.; Lu, H.; Zhang, R.; Zheng, Y. *Sci. Rep.* **2016,** *6,* 27728. doi:10.1038/srep27728
148. Myers, M.; Khir, F. L. M.; Podolska, A.; Umana-Membreno, G. A.; Nener, B.; Baker, M.; Parish, G. *Sens. Actuators, B* **2013,** *181,* 301–305. doi:10.1016/j.snb.2013.02.006
149. Asadnia, M.; Myers, M.; Akhavan, N. D.; O'Donnell, K.; Umana-Membreno, G. A.; Mishra, U. K.; Nener, B.; Baker, M.; Parish, G. *Anal. Chim. Acta* **2016,** *943,* 1–7. doi:10.1016/j.aca.2016.08.045
150. Asadnia, M.; Myers, M.; Umana-Membreno, G. A.; Sanders, T. M.; Mishra, U. K.; Nener, B. D.; Baker, M. V.; Parish, G. *Anal. Chim. Acta* **2017,** *987,* 105–110. doi:10.1016/j.aca.2017.07.066
151. Chen, Y.-T.; Sarangadharan, I.; Sukesan, R.; Hseih, C.-Y.; Lee, G.-Y.; Chyi, J.-I.; Wang, Y.-L. *Sci. Rep.* **2018,** *8,* 8300. doi:10.1038/s41598-018-26792-9
152. Abidin, M. S. Z.; Hashim, A. M.; Sharifabad, M. E.; Rahman, S. F. A.; Sadoh, T. *Sensors* **2011,** *11,* 3067–3077. doi:10.3390/s110303067
153. Cao, F.; Zhang, Y.; Wang, H.; Khan, K.; Tareen, A. K.; Qian, W.; Zhang, H.; Ågren, H. *Adv. Mater. (Weinheim, Ger.)* **2022,** *34,* 2107554. doi:10.1002/adma.202107554
154. Song, H.; Jiang, D.-e. *Nanoscale* **2023,** *15,* 16010–16015. doi:10.1039/d3nr02538a
155. Pei, Y.; Zhang, X.; Hui, Z.; Zhou, J.; Huang, X.; Sun, G.; Huang, W. *ACS Nano* **2021,** *15,* 3996–4017. doi:10.1021/acsnano.1c00248
156. Navitski, I.; Ramanaviciute, A.; Ramanavicius, S.; Pogorielov, M.; Ramanavicius, A. *Nanomaterials* **2024,** *14,* 447. doi:10.3390/nano14050447
157. Hao, S.; Liu, C.; Chen, X.; Zong, B.; Wei, X.; Li, Q.; Qin, H.; Mao, S. *J. Hazard. Mater.* **2021,** *418,* 126301. doi:10.1016/j.jhazmat.2021.126301
158. Siva, S.; Bodkhe, G. A.; Cong, C.; Hyun Kim, S.; Kim, M. *Chem. Eng. J.* **2024,** *479,* 147492. doi:10.1016/j.cej.2023.147492
159. Hassan, J. Z.; Raza, A.; Din Babar, Z. U.; Qumar, U.; Kaner, N. T.; Cassinese, A. *J. Mater. Chem. A* **2023,** *11,* 6016–6063. doi:10.1039/d2ta07653e
160. Lee, C. W.; Suh, J. M.; Jang, H. W. *Front. Chem. (Lausanne, Switz.)* **2019,** *7,* 708. doi:10.3389/fchem.2019.00708
161. Singh, A. K.; Kumar, P.; Late, D. J.; Kumar, A.; Patel, S.; Singh, J. *Appl. Mater. Today* **2018,** *13,* 242–270. doi:10.1016/j.apmt.2018.09.003
162. Samy, O.; Zeng, S.; Birowosuto, M. D.; El Moutaouakil, A. *Crystals* **2021,** *11,* 355. doi:10.3390/cryst11040355
163. Saha, D.; Selvaganapathy, P. R.; Kruse, P. *ACS Appl. Nano Mater.* **2020,** *3,* 10864–10877. doi:10.1021/acsanm.0c02135
164. Saha, D.; Angizi, S.; Darestani-Farahani, M.; Dalmieda, J.; Selvaganapathy, P. R.; Kruse, P. *Langmuir* **2022,** *38,* 3666–3675. doi:10.1021/acs.langmuir.1c03061
165. Saha, D.; Kruse, P. *J. Electrochem. Soc.* **2020,** *167,* 126517. doi:10.1149/1945-7111/abb34b
166. Kou, C.; Hu, H.; Tang, Y.; Luo, Y.; Han, C.; Bao, Y.; Guo, Z.; Niu, L. *Talanta* **2025,** *283,* 127141. doi:10.1016/j.talanta.2024.127141
167. Bazylewski, P.; Van Middelkoop, S.; Divigalpitiya, R.; Fanchini, G. *ACS Omega* **2020,** *5,* 643–649. doi:10.1021/acsomega.9b03246
168. Lamport, Z. A.; Haneef, H. F.; Anand, S.; Waldrip, M.; Jurchescu, O. D. *J. Appl. Phys.* **2018,** *124,* 071101. doi:10.1063/1.5042255
169. Wang, Z.; Huang, L.; Chi, L. *Front. Mater.* **2020,** *7,* 295. doi:10.3389/fmats.2020.00295
170. Amna, B.; Ozturk, T. *J. Mater. Chem. C* **2025,** *13,* 8354–8424. doi:10.1039/d4tc04265d
171. Schmoltner, K.; Kofler, J.; Klug, A.; List-Kratochvil, E. J. W. *Adv. Mater. (Weinheim, Ger.)* **2013,** *25,* 6895–6899. doi:10.1002/adma.201303281
172. Zhang, X.; Pu, Z.; Su, X.; Li, C.; Zheng, H.; Li, D. *Anal. Bioanal. Chem.* **2023,** *415,* 1607–1625. doi:10.1007/s00216-023-04553-6
173. Ohayon, D.; Druet, V.; Inal, S. *Chem. Soc. Rev.* **2023,** *52,* 1001–1023. doi:10.1039/d2cs00920j
174. Bai, L.; Elósegui, C. G.; Li, W.; Yu, P.; Fei, J.; Mao, L. *Front. Chem. (Lausanne, Switz.)* **2019,** *7,* 313. doi:10.3389/fchem.2019.00313
175. Song, J.; Li, L.; Wong, W.-Y.; Yan, F. *Acc. Mater. Res.* **2024,** *5,* 1036–1047. doi:10.1021/accountsmr.4c00124
176. Li, C.; Li, Z.; Nguyen, T. D. D.; Ingebrandt, S.; Vu, X. T. *Electrochim. Acta* **2024,** *507,* 145111. doi:10.1016/j.electacta.2024.145111
177. Dasca Beneito, A.; Andreo Acosta, A. A.; Sierra, A. F.; Blondeau, P.; Ballester, P.; Riu, J.; Andrade, F. J. *ACS Omega* **2025,** *10,* 36475–36480. doi:10.1021/acsomega.5c04973
178. Clua Estivill, M.; Ait Yazza, A.; Blondeau, P.; Andrade, F. J. *Sens. Actuators, B* **2024,** *401,* 135027. doi:10.1016/j.snb.2023.135027
179. He, S.; Xiang, S.; Wang, J.; Wang, K.; Yu, L.; Song, Y.; Zhu, C.; Gong, Z.; Zhang, Y.; Gao, K.; Kang, X.; Wang, T.; Yu, H.-D.; Lu, G. *J. Mater. Chem. C* **2023,** *11,* 9504–9513. doi:10.1039/d3tc01491f
180. Aljabali, A. A. A.; Alkaraki, A.; Gammoh, O.; Qnais, E.; Alqudah, A.; Mishra, V.; Mishra, Y.; El-Tanani, M. *RSC Adv.* **2025,** *15,* 27493–27523. doi:10.1039/d5ra04634c
181. Ji, X.; Lin, X.; Rivnay, J. *Nat. Commun.* **2023,** *14,* 1665. doi:10.1038/s41467-023-37402-2
182. Woeppel, A. B.; Schaefer, J.; Kim, H. J.; Boudouris, B. W.; Beaudoin, S. P. *ACS Appl. Polym. Mater.* **2022,** *4,* 6667–6674. doi:10.1021/acsapm.2c01030
183. Demuru, S.; Kim, J.; Kiselev, I.; Jeanneret-Grosjean, G. J.; Kunnel, B. P.; Liu, M.; Chen, X.; Saubade, M.; Lafaye, C.; Liu, S.-C.; Briand, D. *Biosens. Bioelectron.: X* **2025,** *26,* 100661. doi:10.1016/j.biosx.2025.100661
184. Hu, Z.; Hu, Y.; Huang, L.; Zhong, W.; Zhang, J.; Lei, D.; Chen, Y.; Ni, Y.; Liu, Y. *Biosensors* **2024,** *14,* 330. doi:10.3390/bios14070330

185. Schleberger, M.; Kotakoski, J. *Materials* **2018,** *11,* 1885. doi:10.3390/ma11101885
186. Jiang, J.; Xu, T.; Lu, J.; Sun, L.; Ni, Z. *Research (Beijing, China)* **2019,** *2019,* 4641739. doi:10.34133/2019/4641739
187. Madauß, L.; Zegkinoglou, I.; Vázquez Muiños, H.; Choi, Y.-W.; Kunze, S.; Zhao, M.-Q.; Naylor, C. H.; Ernst, P.; Pollmann, E.; Ochedowski, O.; Lebius, H.; Benyagoub, A.; Ban-d'Etat, B.; Johnson, A. T. C.; Djurabekova, F.; Roldan Cuenya, B.; Schleberger, M. *Nanoscale* **2018,** *10,* 22908–22916. doi:10.1039/c8nr04696d
188. Angizi, S.; Yu, E. Y. C.; Dalmieda, J.; Saha, D.; Selvaganapathy, P. R.; Kruse, P. *Langmuir* **2021,** *37,* 12163–12178. doi:10.1021/acs.langmuir.1c02088
189. Woeppel, K. M.; Zheng, X. S.; Schulte, Z. M.; Rosi, N. L.; Cui, X. T. *Adv. Healthcare Mater.* **2019,** *8,* 1900622. doi:10.1002/adhm.201900622
190. Zhang, P.; Cao, S.; Sui, N.; Xu, Y.; Zhou, T.; He, Y.; Zhang, T. *Chemosensors* **2022,** *10,* 364. doi:10.3390/chemosensors10090364
191. Zhou, G.; Chang, J.; Cui, S.; Pu, H.; Wen, Z.; Chen, J. *ACS Appl. Mater. Interfaces* **2014,** *6,* 19235–19241. doi:10.1021/am505275a
192. Darwish, M. A.; Abd-Elaziem, W.; Elsheikh, A.; Zayed, A. A. *Nanoscale Adv.* **2024,** *6,* 4015–4046. doi:10.1039/d4na00214h
193. Kyaw, H. H.; Boonruang, S.; Mohammed, W. S.; Dutta, J. *AIP Adv.* **2015,** *5,* 107226. doi:10.1063/1.4934934
194. Gezahegn, T. F.; Ambaye, A. D.; Mekoyete, T. M.; Malefane, M. E.; Oyedotun, K. O.; Mokrani, T. *Talanta Open* **2024,** *10,* 100354. doi:10.1016/j.talo.2024.100354
195. Mariani, S.; Strambini, L. M.; Barillaro, G. *ACS Sens.* **2018,** *3,* 595–605. doi:10.1021/acssensors.7b00650
196. Kaur, R.; Rana, S.; Kaur, R.; Jyoti; Kaur, N.; Singh, B. *Microchim. Acta* **2023,** *190,* 396. doi:10.1007/s00604-023-05972-z
197. Dalmieda, J.; Zubiarrain-Laserna, A.; Saha, D.; Selvaganapathy, P. R.; Kruse, P. *J. Phys. Chem. C* **2021,** *125,* 21112–21123. doi:10.1021/acs.jpcc.1c04509
198. Liu, G.-Z.; Liang, Z.-D.; Long, Z.-J.; Liu, J.-W.; Li, H.-Y.; Mo, Z.-W. *CrystEngComm* **2025,** *27,* 5087–5094. doi:10.1039/d5ce00412h
199. Shafqat, S. S.; Rizwan, M.; Batool, M.; Shafqat, S. R.; Mustafa, G.; Rasheed, T.; Zafar, M. N. *Chemosphere* **2023,** *318,* 137920. doi:10.1016/j.chemosphere.2023.137920
200. Selvaraj, B.; Priya G, L.; Balasubramanian, S. *RSC Adv.* **2024,** *14,* 35618–35627. doi:10.1039/d4ra06811d
201. Shen, S.; Tan, P.; Tang, Y.; Duan, G.; Luo, Y. *ACS Appl. Electron. Mater.* **2022,** *4,* 622–630. doi:10.1021/acsaelm.1c01009
202. Mohan, B.; Kumari, R.; Virender; Singh, G.; Singh, K.; Pombeiro, A. J. L.; Yang, X.; Ren, P. *Environ. Int.* **2023,** *175,* 107928. doi:10.1016/j.envint.2023.107928
203. Hou, C.; Liu, J.; Zhang, S.; Tian, C.; Yan, M. *Sens. Actuators, B* **2024,** *417,* 136221. doi:10.1016/j.snb.2024.136221
204. Wang, C.; Pei, L.; Chen, R.; Zhu, Y.; Su, J. *Ionics* **2022,** *28,* 4025–4033. doi:10.1007/s11581-022-04611-6
205. Shamsabadi, E.; Akhlaghi, H.; Baghayeri, M.; Motavalizadehkakhky, A. *Sci. Rep.* **2024,** *14,* 25052. doi:10.1038/s41598-024-77139-6
206. Zheng, X.; Khaoulani, S.; Ktari, N.; Lo, M.; Khalil, A. M.; Zerrouki, C.; Fourati, N.; Chehimi, M. M. *Sensors* **2021,** *21,* 4300. doi:10.3390/s21134300
207. Zhang, W.; Ye, S.; Diao, Y.; Deng, X.; Li, W.; He, H.; Liu, Q.; Hu, G. *Mater. Today Chem.* **2024,** *35,* 101863. doi:10.1016/j.mtchem.2023.101863
208. Kanoun, O.; Lazarević-Pašti, T.; Pašti, I.; Nasraoui, S.; Talbi, M.; Brahem, A.; Adiraju, A.; Sheremet, E.; Rodriguez, R. D.; Ben Ali, M.; Al-Hamry, A. *Sensors* **2021,** *21,* 4131. doi:10.3390/s21124131
209. Zhang, C.; Hao, T.; Lin, H.; Wang, Q.; Wu, Y.; Kang, K.; Ji, X.; Guo, Z. *Anal. Chim. Acta* **2020,** *1128,* 174–183. doi:10.1016/j.aca.2020.07.007
210. Sharma, N.; Nigam, A.; Lobanov, D.; Gupta, A.; Novikov, A.; Kumar, M. *IEEE Internet Things J.* **2022,** *9,* 14317–14324. doi:10.1109/jiot.2021.3071382
211. Yi, W.; Li, Z.; Dong, W.; Han, C.; Guo, Y.; Liu, M.; Dong, C. *ACS Appl. Nano Mater.* **2022,** *5,* 216–226. doi:10.1021/acsanm.1c02690
212. Guo, W.; Zhang, C.; Ma, T.; Liu, X.; Chen, Z.; Li, S.; Deng, Y. *J. Nanobiotechnol.* **2021,** *19,* 166. doi:10.1186/s12951-021-00914-4
213. Reynoso, E. C.; Sfragano, P. S.; González-Perea, M.; Palchetti, I.; Torres, E. *Chemosensors* **2024,** *12,* 59. doi:10.3390/chemosensors12040059
214. Khan, S.; Burciu, B.; Filipe, C. D. M.; Li, Y.; Dellinger, K.; Didar, T. F. *ACS Nano* **2021,** *15,* 13943–13969. doi:10.1021/acsnano.1c04327
215. Xiao, Y.; Du, Z.; Li, Y.; Cao, L.; Zhu, B.; Kitaguchi, T.; Huang, C. *Sensors* **2025,** *25,* 4945. doi:10.3390/s25164945
216. Zhang, Z.; Karimi-Maleh, H. *Chemosphere* **2023,** *324,* 138302. doi:10.1016/j.chemosphere.2023.138302
217. Unnikrishnan, B.; Lien, C.-W.; Chu, H.-W.; Huang, C.-C. *J. Hazard. Mater.* **2021,** *401,* 123397. doi:10.1016/j.jhazmat.2020.123397
218. Wen, S.-H.; Zhong, X.-L.; Wu, Y.-D.; Liang, R.-P.; Zhang, L.; Qiu, J.-D. *Anal. Chem. (Washington, DC, U. S.)* **2019,** *91,* 6487–6497. doi:10.1021/acs.analchem.8b05121
219. Choi, K. R.; Troudt, B. K.; Bühlmann, P. *Angew. Chem., Int. Ed.* **2023,** *62,* e202304674. doi:10.1002/anie.202304674
220. Yu, S.; Li, B.; Chen, P.; Lian, W.; Jiang, L.; Jin, Y.; Wu, L.; Xiao, Z.; Yu, D.; Cao, Z. *Microchem. J.* **2025,** *215,* 114287. doi:10.1016/j.microc.2025.114287
221. Liu, T.-Y.; Hsu, H.-Y.; Liu, H.-C.; Huang, N.-T. *Lab Chip* **2025,** *25,* 3559–3569. doi:10.1039/d4lc01099j
222. Zhai, J.; Duan, S.; Luo, B.; Jin, X.; Dong, H.; Wang, X. *Anal. Methods* **2024,** *16,* 8068–8079. doi:10.1039/d4ay01346h
223. Riedel, V.; Hinck, S.; Peiter, E.; Ruckelshausen, A. *Electronics (Basel, Switz.)* **2024,** *13,* 4958. doi:10.3390/electronics13244958
224. Tibaduiza, D.; Anaya, M.; Gómez, J.; Sarmiento, J.; Perez, M.; Lara, C.; Ruiz, J.; Osorio, N.; Rodriguez, K.; Hernandez, I.; Sanchez, C. *Biosensors* **2024,** *14,* 190. doi:10.3390/bios14040190
225. Podrażka, M.; Bączyńska, E.; Kundys, M.; Jeleń, P.; Witkowska Nery, E. *Biosensors* **2018,** *8,* 3. doi:10.3390/bios8010003
226. Margarit-Taulé, J. M.; Martín-Ezquerra, M.; Escudé-Pujol, R.; Jiménez-Jorquera, C.; Liu, S.-C. *Sens. Actuators, B* **2022,** *353,* 131123. doi:10.1016/j.snb.2021.131123
227. Sakata, T. *Commun. Chem.* **2024,** *7,* 35. doi:10.1038/s42004-024-01121-6
228. Zhang, S.; Massetti, M.; Ruoko, T.-P.; Tu, D.; Yang, C.-Y.; Liu, X.; Wu, Z.; Lee, Y.; Kroon, R.; Persson, P. O. Å.; Woo, H. Y.; Berggren, M.; Müller, C.; Fahlman, M.; Fabiano, S. *Adv. Funct. Mater.* **2022,** *32,* 2106447. doi:10.1002/adfm.202106447
229. Shirsat, M. D.; Hianik, T. *J. Compos. Sci.* **2023,** *7,* 473. doi:10.3390/jcs7110473

230. Sengupta, J.; Hussain, C. M. *Nanoscale* **2024,** *16,* 14195–14212. doi:10.1039/d4nr00956h
231. Gonski, S. F.; Luther, G. W., III; Kelley, A. L.; Martz, T. R.; Roberts, E. G.; Li, X.; Dong, B.; Watson, J. A.; Wirth, T. S.; Hussain, N.; Feris Serrano, R. J.; Hale, E.; Cai, W.-J. *Mar. Chem.* **2024,** *261,* 104373. doi:10.1016/j.marchem.2024.104373

License and Terms

This is an open access article licensed under the terms of the Beilstein-Institut Open Access License Agreement (https://www.beilstein-journals.org/bjnano/terms), which is identical to the Creative Commons Attribution 4.0 International License (https://creativecommons.org/licenses/by/4.0). The reuse of material under this license requires that the author(s), source and license are credited. Third-party material in this article could be subject to other licenses (typically indicated in the credit line), and in this case, users are required to obtain permission from the license holder to reuse the material.

The definitive version of this article is the electronic one which can be found at:
https://doi.org/10.3762/bjnano.17.66

BEILSTEIN JOURNAL OF NANOTECHNOLOGY

Molecular states and interfacial interactions at solid–liquid interfaces: advances and challenges in multimodal characterization

Shiou Yamada[‡1], Hinata Urano[‡1] and Koji Toma[*1,2]

Review

Open Access

Address:
[1]Graduate School of Engineering and Science, Shibaura Institute of Technology, 3-7-5 Toyosu, Koto-ku, Tokyo 135-8548, Japan and [2]College of Engineering, Shibaura Institute of Technology, 3-7-5 Toyosu, Koto-ku, Tokyo 135-8548, Japan

Email:
Koji Toma[*] - k-toma@shibaura-it.ac.jp

* Corresponding author ‡ Equal contributors

Keywords:
biointerfaces; molecular interactions; multimodal characterization; solid–liquid interfaces; spatiotemporal dynamics

Beilstein J. Nanotechnol. **2026,** *17,* 1223–1256.
https://doi.org/10.3762/bjnano.17.85

Received: 28 March 2026
Accepted: 19 August 2026
Published: 03 September 2026

This article is part of the thematic issue "Nanotechnology for cross-scale analysis: comprehensive evaluation of water environments".

Guest Editor: Y. Sasaki

© 2026 Yamada et al.; licensee Beilstein-Institut.
License and terms: see end of document.

Abstract

Solid–liquid interfaces govern key functions in biosensing, catalysis, energy conversion, drug delivery, and organic electronic devices because molecular adsorption, hydration, charge regulation, and structural reorganization occur within an ultrathin interfacial region. However, these phenomena are intrinsically multiscale and multidimensional, involving strongly coupled variables such as mass, interfacial potential, molecular orientation, viscoelasticity, and local nanoscale heterogeneity. As a result, no single measurement technique can fully describe interfacial states or their dynamics. This review summarizes recent advances in multimodal characterization strategies designed to overcome these limitations. We first outline the conceptual framework of molecular interactions at solid–liquid interfaces, focusing on electrostatic interactions, van der Waals forces, hydration structures, hydrophobic effects, specific adsorption, and protein conformational changes across wide temporal and spatial scales. We then compare the observation windows, defined here as the combined range of spatiotemporal resolution and accessible physical observables, and limitations of major stand-alone methods, including optical, electrochemical, acoustic, and scanning probe techniques. Building on this basis, we discuss the recent development of multimodal platforms that integrate optics with electrochemistry, optics with quartz crystal microbalance measurements, and local probes with optical or electrochemical readouts, highlighting how these combinations reveal correlations among dry and wet mass, charge state, molecular vibration, hydration, and local structure. Finally, we discuss remaining challenges, including causal ambiguity among coupled interfacial variables, the trade-off between spatial and temporal resolution, and the difficulty of quantitatively linking experimental data with theoretical models. Multimodal characterization is expected to provide a foundation for the rational design of next-generation biointerfaces, delivery systems, and organic devices.

Review

1 Introduction

Solid–liquid interfaces play a central role in a wide range of fields that underpin modern science and technology, including biosensors, catalysis, energy devices, and drug delivery systems. In the ultrathin region where an electrolyte solution contacts a solid surface, a unique molecular order forms that cannot be reduced to either the liquid phase or the solid phase alone, and this order essentially determines the function of the whole system. For example, in biosensors based on antigen–antibody reactions, orientation, density, and hydration state of surface-modifying molecules strongly affect signal sensitivity. In drug delivery using lipid nanoparticles, the dynamics of membrane fusion and cargo release at the solid–liquid interface determine carrier performance. In organic thin-film devices as well, charge accumulation and molecular conformational changes at the interface between the gate electrolyte and the semiconductor layer govern the field effect. In this way, a molecular-level understanding of solid–liquid interfaces provides a universal basis for the design of next-generation devices and materials.

The fundamental reason why molecular phenomena at solid–liquid interfaces are so complex is the diversity and interdependence of the interactions operating there. Electrostatic interactions, through the electrical double layer (EDL) formed cooperatively by surface charges and electrolyte ions, influence the orientation of adsorbed molecules and the ease of their desorption. van der Waals forces contribute to the early stages of adsorption as weak attractions among molecules and between molecules and substrates, while hydrophobic interactions promote the association of nonpolar sites by driving out water molecules. In addition, hydration structures, that is, multilayer shells of oriented water molecules formed near solid surfaces, not only create a dehydration energy barrier that must be overcome for direct molecular contact, but their structural changes themselves are also deeply involved in molecular orientation and function. These interactions do not vary independently; rather, they are modulated cooperatively as interlinked state variables. For example, changes in solution pH or salt concentration alter not only the interfacial charge density, but also the reorganization of hydration shells around adsorbed proteins, their conformational changes, and the viscoelastic properties of the entire adsorbed layer. A useful starting point for understanding solid–liquid interfaces is therefore to regard them not as a simple boundary, but as a nonlinear feedback system in which multiple physical quantities are strongly coupled.

Another essential feature of interfacial phenomena is their hierarchical time and length scales. Among the fastest processes, formation of the EDL and reorientation of water molecules proceed on timescales from picoseconds to microseconds [1,2], followed by the initial adsorption of molecules involving dehydration on timescales from nanoseconds to minutes [3,4]. Conformational relaxation and reorientation after adsorption have long time constants ranging from tens of minutes to hours [5,6], while collective membrane formation and phase transitions occur on timescales from seconds to hours [7,8]. In terms of length scale, the hydration shell formed by a single water molecule at a surface extends from angstroms to several nanometers, adsorption structures of proteins are on the nanometer scale, and heterogeneous distributions of reactive sites can extend to the micrometer scale. Integrating interfacial phenomena across such broad temporal and spatial scales is precisely where any single measurement method reaches its limits.

To determine the state of an interface accurately, it is necessary to evaluate multiple physical quantities dynamically, including mass and adsorption amount, charge state and interfacial potential, molecular vibrations and chemical structure, viscoelasticity and membrane structure, and local morphology and nanostructure. Traditionally, each of these has been studied by a dedicated stand-alone technique. Surface plasmon resonance (SPR) can measure adsorbed mass and binding kinetics with high sensitivity through refractive index changes near the interface, but it does not provide chemical structure information [9,10]. Quartz crystal microbalance with dissipation monitoring (QCM-D) can evaluate the “wet mass”, including hydration water, together with viscoelasticity, but it cannot directly detect molecular orientation or local charge [11,12]. Infrared (IR) spectroscopy and vibrational sum-frequency generation (VSFG) spectroscopy provide information on the vibrations and orientation of interfacial molecules, but in principle only as ensemble-averaged responses [13,14]. Scanning probe microscopy (SPM) provides local nanoscale morphological and mechanical information, but real-time dynamic measurements are limited [15-17]. Electrochemical methods can follow changes in interfacial charge and potential with high time resolution, but offer poor spatial information [18,19].

Each stand-alone method has its own intrinsic “observation window”. Here, we define this term as the combined range of spatiotemporal resolution and the specific physical observables accessible to each technique. Accordingly, any single method provides only one cross section of the multidimensional state space of an interface. For example, the question “How much of the adsorbed mass comes from hydration water?” becomes quantifiable only when SPR and QCM-D are combined to analyze the difference between dry mass and wet mass [12,20]. Likewise, the question “How does the adsorption orientation of

molecules at an electrode interface change dynamically with potential?" can be answered clearly only by integrating surface-enhanced Raman spectroscopy (SERS) with electrochemical measurements to track potential-dependent changes in specific vibrational modes [21,22]. Thus, the importance of multimodal characterization, that is, obtaining multiple physical quantities in a complementary manner from the same interface on the same time axis, follows directly from the intrinsically multidimensional nature of interfacial phenomena. Against this background, multimodal measurement systems that integrate methods based on different physical principles on the same interface have developed rapidly in recent years. The essential significance of multimodal integration is not simply that it increases the number of measurable quantities. Rather, it redefines interfacial phenomena, which were previously summarized only as single mass changes or current responses, in terms of the correlation structure among multiple physical quantities, thereby providing a clue to uncovering their underlying causal relationships.

This review systematically organizes recent progress in multimodal characterization of solid–liquid interfaces and discusses both the technical achievements and the remaining conceptual challenges. Section 2 outlines the conceptual framework for molecular states and interactions at solid–liquid interfaces and presents an overall picture of the physical quantities that should be measured. Section 3 surveys the principles and inherent limitations of existing stand-alone methods. Section 4 explains the major multimodal architectures in different categories, namely, optics combined with electrochemistry/acoustics and local probes integrated with optics/electrochemistry, and presents their spatiotemporal observation windows and representative applications. Section 5 then summarizes the essential limitations faced by current measurement technologies and discusses prospects for overcoming them.

2 Conceptual framework for molecular states and interactions at solid–liquid interfaces

2.1 Major intermolecular interactions at solid–liquid interfaces

2.1.1 Electrostatic interactions. Electrostatic interactions are forces that arise through space from the net charges or dipole moments carried by particles and molecules. They include charge–charge repulsion as well as charge–dipole and dipole–dipole interactions, which act over relatively short distances and can be attractive [23]. During molecular approach and binding, these forces dominate the early stage before the first hydration shells of the two partners come into contact, functioning either as the driving force for binding (attraction) or as an energy barrier (repulsion) [24]. In electrolyte solutions, counterions gather to neutralize the surface charge at the interface, forming an EDL composed of a Stern layer, where the finite size of ions causes steric exclusion, and an outer diffuse layer, where ions are distributed nonuniformly in space [25]. As a result, an interfacial potential distribution is established that decays from the charged interface into the solution. Owing to this screening by the EDL, the effective range over which surface charge exerts influence is limited (Figure 1), and this characteristic screening distance is defined as the Debye length [26]. When the ionic strength of the solution increases, screening by

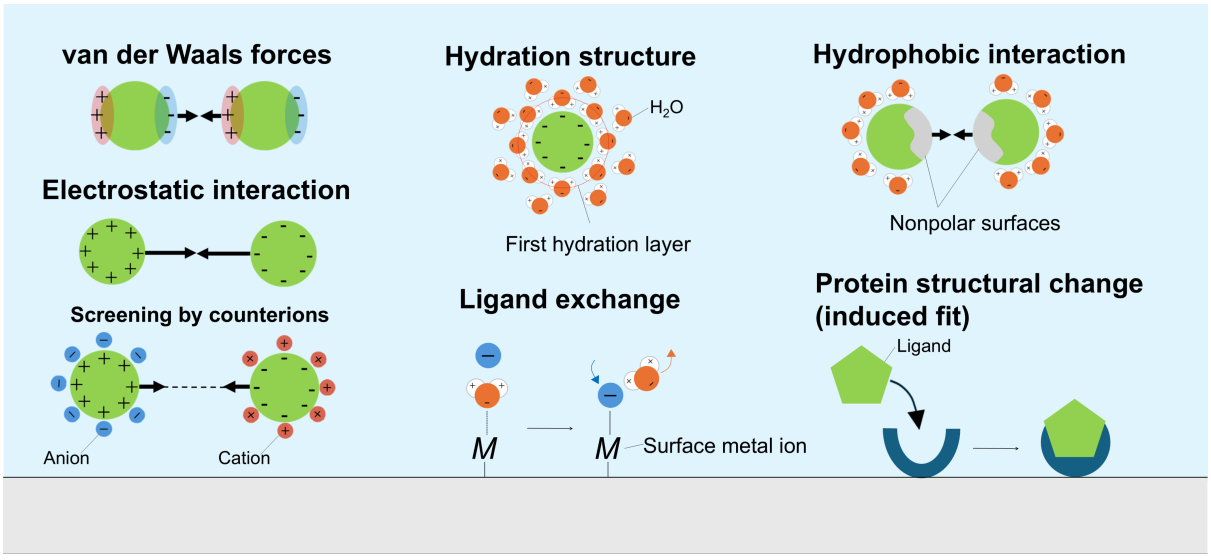


Figure 1: Summary schematic of intermolecular and interfacial interactions at solid–liquid interfaces.

counterions becomes stronger and the Debye length becomes shorter, thereby changing both the range and the strength of electrostatic interactions [24]. In this way, electrostatic interactions determine the final balance between attraction and repulsion that governs whether binding can occur before shorter-range interactions come into play [24,26].

2.1.2 Van der Waals forces. Van der Waals forces are electromagnetic interactions that act between all atoms and molecules, and they consist of Keesom, Debye, and London dispersion forces (Figure 1). For a single pair of molecules, the interaction energy decays with the sixth power of distance. However, when macroscopic bodies are involved at solid–liquid interfaces, spatial integration changes the distance dependence. It decays with the third power of distance for a single molecule interacting with an infinite flat plate and is inversely proportional to distance in the near-contact region between spherical particles [27]. These theories of distance dependence, however, are based on the ideal assumption of perfectly smooth surfaces. At real solid–liquid interfaces, microscopic surface roughness alters the interaction. Indeed, studies using atomic force microscopy to measure forces between extremely smooth hafnium oxide surfaces have shown that the strong van der Waals attraction predicted to dominate at close separation is not observed. This was attributed to the fact that physical contact between microscopic asperities on the two surfaces generates a new repulsive force that cancels the attractive dispersion force [28].

2.1.3 Hydration structure and hydrogen-bond network. Water molecules are polar because of the electronegativity difference between oxygen and hydrogen, and each molecule has two proton-accepting and two proton-donating sites. As a result, water molecules in the solid form a continuous tetrahedral hydrogen-bond network with an average coordination number slightly above four. At solid–liquid interfaces, however, this network is modified through interactions with charged surfaces, producing hydration structures in which orientation and mobility of water are constrained [29] (Figure 1). This hydration shell around a molecular surface forms a dense first hydration layer that is more compact than bulk water [24], and the ordering of these water molecules decays exponentially from the surface into the bulk [29]. Because this dense first hydration layer exists, direct molecular contact requires a dehydration process in which water molecules are stripped away from the interface. Dehydration from hydrophilic or charged surfaces is thermodynamically highly unfavorable, so this compact hydration layer acts as a strong energy barrier to contact. In contrast, dehydration from hydrophobic surfaces is energetically favorable and contributes as an attractive force that brings molecules together, namely hydrophobic interaction [24].

2.1.4 Hydrophobic interactions and ion specificity (Hofmeister series). Hydrophobic interaction refers to the attractive phenomenon in which hydrophobic surfaces associate with each other to reduce their contact area with water, thereby minimizing the large energetic penalty that arises when water molecules cannot form hydrogen bonds around exposed nonpolar surfaces [30] (Figure 1). This attraction is now known to have a nanoscale decay length [30,31]. Tabor and co-workers directly measured the force between liquid droplets after excluding all known surface forces and demonstrated that the force itself has an extremely short decay length of about 0.3 nm, close to the correlation length of water molecules [30]. This microscopic attraction drives hydrophobic collapse and macroscopic aggregation. Whether such processes proceed, however, is strongly influenced by ions from the Hofmeister series. Zhang examined the effect of the Hofmeister series on the lower critical solution temperature (LCST) of the thermoresponsive polymer poly(*N*-isopropylacrylamide) and showed that kosmotropic ions strongly promote aggregation, lowering the LCST, through enhanced water polarization and increased interfacial tension. By contrast, chaotropic ions both increase interfacial tension and bind directly to the polymer; this direct binding causes a salting-in effect that partially offsets the salting-out effect arising from interfacial tension, thereby suppressing the decrease in LCST and slowing aggregation [32].

2.1.5 Ligand exchange. Specific adsorption of molecules and anions at solid–liquid interfaces can be described as a surface complexation reaction analogous to complex formation in homogeneous solution. Its main mechanism is ligand exchange, in which water molecules or hydroxy groups coordinated to surface functional groups, such as surface metal ions on metal oxides, silanol groups on silica, or carboxyl groups in natural organic matter, are replaced by ligands in solution, such as anions [33] (Figure 1). Adsorbed states are broadly divided into strong inner-sphere complexes, in which the adsorbate binds directly to the surface functional group, and outer-sphere complexes, in which water molecules remain between them. In particular, for inner-sphere complex formation, intrinsic chemical affinity, such as Lewis acid–base interactions, acts as the dominant driving force, beyond purely electrostatic factors [29,33].

2.1.6 Protein structural changes. Protein conformational changes are observed prominently in specific molecular recognition [34-36] and in adsorption onto nonbiological solid surfaces [37,38]. For structural changes associated with molecular recognition, two main models are commonly discussed, namely, induced fit and conformational selection. In induced fit, a flexible binding site is deformed by the approach of the ligand so that the two become complementary (Figure 1). In conformational selection, the ligand binds to the most suitable state

among multiple dynamic conformations already populated by the protein, shifting the overall equilibrium toward the bound state [39]. Maus and co-workers used single-molecule Förster resonance energy transfer to analyze the binding mechanisms of competitive inhibitors to two structurally very similar enzymes, the NS2B-NS3 proteases of Zika virus and dengue virus. They showed that the Zika protease follows an induced-fit mechanism, whereas the dengue protease follows conformational selection [35]. Distinct structural changes also occur during adsorption onto solid surfaces. For example, Roach and co-workers used quartz crystal microbalance (QCM) and grazing-angle Fourier transform infrared spectroscopy to measure mass changes and secondary-structure changes during serum–protein adsorption on hydrophobic and hydrophilic model surfaces, demonstrating a clear correlation between adsorption-induced loss of α-helical structure and surface affinity [37].

2.2 Time scales and length scales

2.2.1 Structural relaxation of the electrical double layer (picoseconds to microseconds). Structural relaxation of the EDL is the dynamic process by which an interface responds to a sudden environmental change, such as in electric field or temperature, and moves toward a new thermodynamic equilibrium over a spatial range from the angstrom-scale specific adsorption region to the diffuse layer several nanometers thick. Reported timescales span from picoseconds to microseconds (Figure 2) [1,2]. Yamakata and co-workers irradiated a CO-covered platinum electrode with a pulsed laser to thermally desorb CO and tracked the resulting relaxation of the EDL. They showed that adsorption of water molecules onto the newly exposed sites and their collective rearrangement required several tens of microseconds to relax into a new double-layer structure, and that the relaxation time became longer as the initial electrode potential decreased (about 20 μs at 0.4 V and about 70 μs at −0.3 V) [1]. In contrast, Greco and co-workers applied an ultrafast temperature-jump method using an infrared laser to the spontaneously formed EDL at the air–electrolyte solution interface, thereby isolating the intrinsic relaxation process of the double layer without interference from electrode materials. They demonstrated that structural relaxation of the EDL takes 20–200 ps depending on concentration and temperature and argued that this provides a benchmark for the response speed of solid-electrode devices [2].

2.2.2 Protein structural relaxation (minutes to hours). Protein structural relaxation at a solid–liquid interface is the process by which, after initial adsorption, a molecule changes its own conformation and orientation so as to maximize interactions with the surface and minimize the free energy of the system, thereby stabilizing it [37]. Model studies of proteins

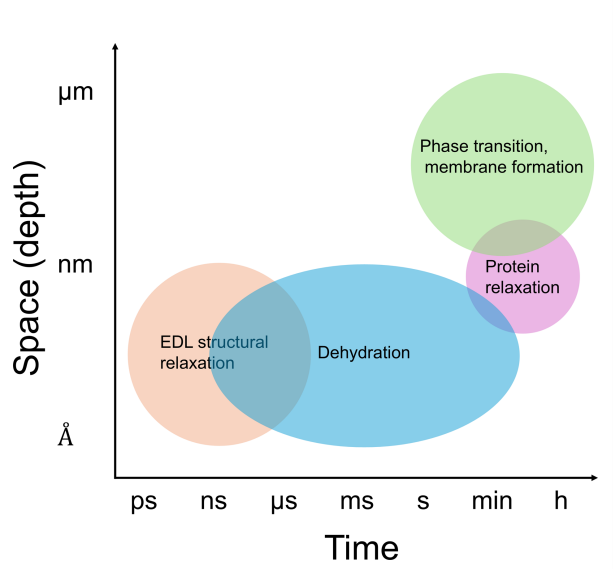


Figure 2: Spatiotemporal mapping of molecular and interfacial processes at solid–liquid interfaces.

have reported that, for single molecules on the nanometer scale, the molecular footprint can expand over tens to hundreds of square nanometers on very slow timescales of tens of minutes to hours (Figure 2) [5,6]. Wertz and co-workers used total internal reflection fluorescence microscopy (TIRFM) to measure the amount of model proteins (albumin and fibrinogen) adsorbed on uncharged hydrophilic and hydrophobic surfaces; from these data, they calculated the time-dependent increase in the area occupied per molecule (the footprint). They found that the footprint of adsorbed molecules continued to increase at a nearly constant rate for at least the first 15–20 min, and that the relaxation process began to converge only after about 2 h. The rate and final extent of expansion depended strongly on surface hydrophobicity. Specifically, the increase was modest on hydrophilic surfaces, whereas on hydrophobic surfaces it was much larger, accompanied by unfolding of the internal structure, and the footprint expanded to three to five times its initial size [6].

2.2.3 Collective phase transitions and membrane formation (seconds to hours). Collective phase transitions and membrane formation at solid–liquid interfaces refer to processes in which molecules that are initially adsorbed in a random manner self-organize through intermolecular and molecule–surface interactions into thermodynamically stable ordered structures. Spatially, these processes range from local molecular arrangements and domain formation on the nanometer scale to macroscopic regions extending over several hundred micrometers, while temporally they span from seconds to hours depending on the system and concentration (Figure 2) [7,8,40,41]. Gobbi and

co-workers used a graphene field-effect transistor (FET) to electrically track in real time the self-assembly dynamics of photoresponsive molecules at a solid–liquid interface. They showed that the rate of self-assembly of metastable merocyanine molecules generated by light irradiation depended strongly on molecular concentration near the interface, and that at a sufficiently high concentration (4 mM), membrane formation over a macroscopic area of 100 μm × 100 μm was completed rapidly on a timescale of seconds (time constant of 6 s) [40]. Son and co-workers also used scanning tunneling microscopy (STM) and X-ray photoelectron spectroscopy to observe the formation of self-assembled monolayers (SAMs) of amide-containing alkanethiols on Au(111). They visualized a transition from a structurally disordered liquid-like phase at the early stage of adsorption (1 min), to a mixed state after 10 min containing both ordered row structures (the α phase) and densely packed structures (the β phase), and finally to a uniform dense β phase after 1 h. They argued that this local structural transition is driven not only by increased sulfur chemisorption but also by rearrangement of the molecular backbone to maximize lateral intermolecular interactions [7].

2.2.4 Dehydration during molecular approach to and adsorption at an interface (nanoseconds to minutes). Molecules and ions in solution are thermodynamically stabilized by hydration shells, but in adsorption and related interactions, this hydration layer itself acts as a steric barrier that prevents direct contact. Therefore, for molecules and solid surfaces to approach each other and make direct contact, the hydration shell must be disrupted through a dehydration process [3]. Spatially, this dehydration is an interfacial process occurring over a highly localized region from angstroms to about 1 nm, and reported timescales range from nanoseconds to minutes (Figure 2) [3,4,42]. Camacho and co-workers used Brownian dynamics simulations to analyze binding between proteins for which long-range electrostatic attraction is weak. They found that within the dehydration layer, the average dehydration force is repulsive, limiting the lifetime of nonspecific collision complexes to about 4 ns. This suggests that under conditions without strong electrostatic steering, the search process involving molecular contact and dehydration takes place within a very short nanosecond time window [42]. By contrast, adsorption onto a solid–liquid interface under an external driving force can require much longer times. Yamakata and co-workers combined an electrochemical system with surface-enhanced infrared absorption spectroscopy (SEIRAS) to follow the approach of cations with hydrophobic hydration shells to a CO-covered platinum electrode. They showed that the rate of hydration-shell breakdown depends on the applied driving force (potential) and that even under strong driving conditions, the breakdown of the hydration shell required about 185 ms [3]. Maitra and co-workers further monitored the approach and adsorption of multivalent ions to probe molecules on a gold electrode by IR spectroscopy, demonstrating a delayed process that required about 11 min for dehydration in aqueous solution, and arguing that dehydration itself can become the rate-limiting step in adsorption [4].

2.3 Physical quantities that should be measured

2.3.1 Mass. Mass is a fundamental physical quantity for evaluating adsorption and desorption at solid–liquid interfaces. Real-time tracking of its temporal changes enables the evaluation of the kinetics and binding affinity of intermolecular interactions [43]. Furthermore, measuring mass changes in response to varied surface properties or solution conditions confirms whether molecular adsorption occurs under specific conditions, providing a key indicator for identifying the driving forces behind interfacial interactions [44,45].

2.3.2 Charge state and interfacial potential. Charge states and interfacial potentials are physical quantities that reflect the electrostatic environment at solid–liquid interfaces. Capturing these variables allows for the evaluation of a series of physicochemical processes that alter this electrostatic environment, such as the adsorption of target molecules and ions, as well as the conformational changes of probe molecules [46-48].

2.3.3 Molecular vibrations. The intrinsic vibrational states of molecules serve as chemical fingerprints for molecular identification. Analyzing these vibrational states therefore enables the characterization of chemical species, molecular structures, and hydrogen-bonding networks at solid–liquid interfaces [49,50].

2.3.4 Viscoelasticity. The viscoelasticity of the adsorbed layer formed at a solid–liquid interface is a physical quantity that characterizes the mechanical flexibility and hydration state of the molecular layer. In practical measurements, it serves as an indicator for evaluating the structural changes of adsorbed proteins or the growth processes of polymer layers [51,52].

2.3.5 Local structure (nanometer scale). Local structure is a physical parameter that reflects the spatial heterogeneity of solid–liquid interfaces, details that are often obscured in macroscopic, averaged measurements. Capturing this local structure makes it possible to extract features such as island-like clusters, fibril networks, and localized defects within adsorbed layers that might otherwise be perceived as uniform films [53-56].

These considerations clarify which physical quantities must be tracked to describe solid–liquid interfacial states in a meaningful way. The following section therefore reviews the major stand-alone measurement methods, focusing on what each technique can reveal and where its intrinsic limitations remain.

3 Existing stand-alone measurement methods

3.1 Optical Methods

3.1.1 Surface plasmon resonance spectroscopy. Surface plasmon resonance (SPR) spectroscopy is a measurement method based on the resonant excitation of surface plasmons, which are collective oscillations of free electrons, when polarized light is incident on the interface between a metal (mainly gold or silver) and a dielectric medium (solution) (Figure 3a). The evanescent field generated at the metal surface is localized within about a few hundred nanometers of the interface and decays exponentially, making the method highly sensitive to local refractive-index changes near solid–liquid interfaces [10]. Using this high sensitivity, SPR can track changes in interfacial mass in a label-free and real-time manner and can therefore evaluate the binding dynamics of target molecules [9,57]. For example, Sarcina and co-workers used shifts in the SPR angle together with the de Feijter equation to calculate the surface

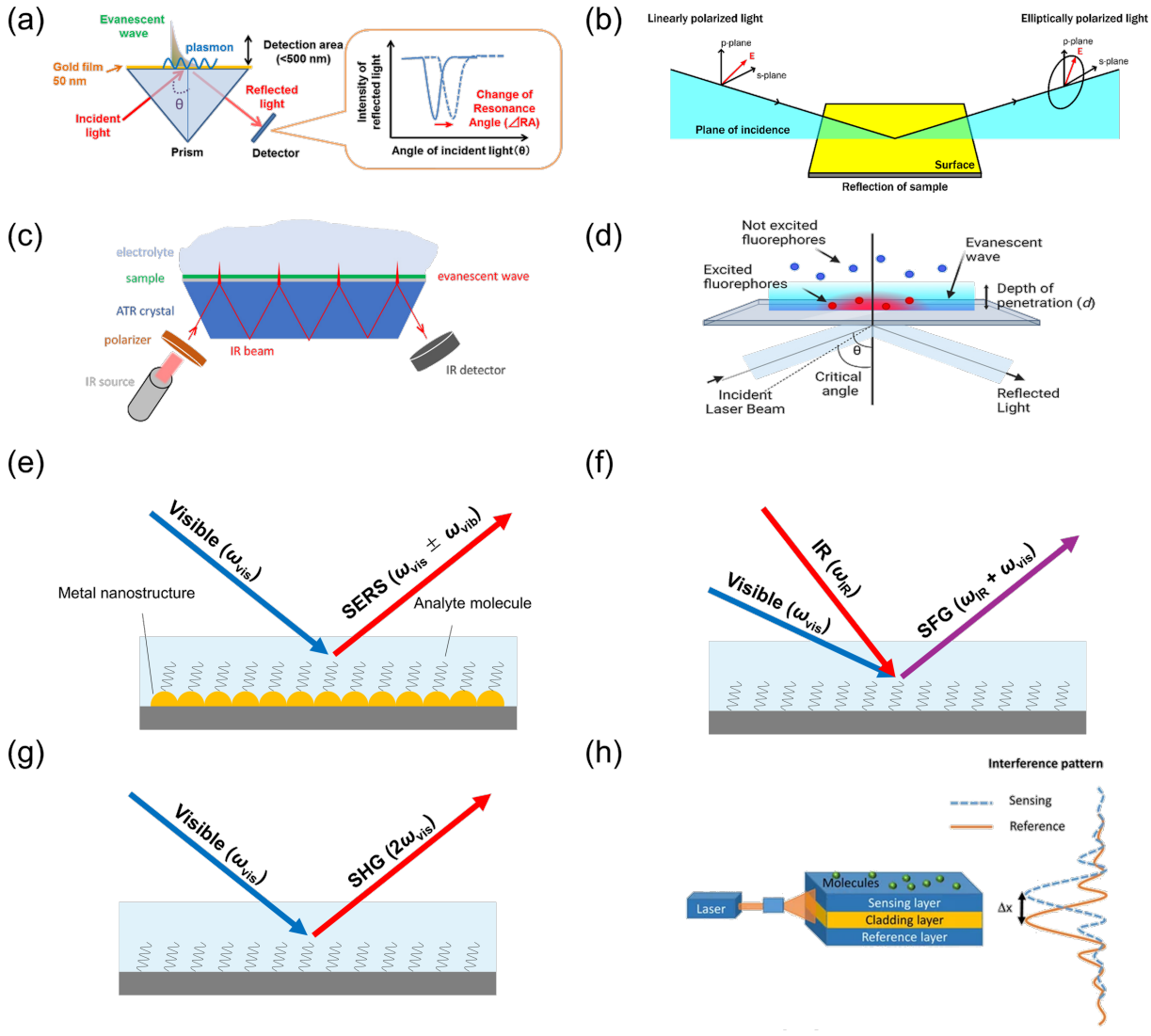


Figure 3: Schematic illustrations of measurement principles for optical methods. (a) SPR spectroscopy. Figure 3a was reproduced from [79] ("Surface Plasmon Resonance for Cell-Based Clinical Diagnosis", © 2014 Y. Yanase et al., published by MDPI, distributed under the terms of the Creative Commons Attribution 3.0 Unported License, https://creativecommons.org/licenses/by/3.0/). (b) Ellipsometry. Figure 3b was reproduced from [80] (© 2022 I. Plikusiene et al., published by MDPI, distributed under the terms of the Creative Commons Attribution 4.0 International License, https://creativecommons.org/licenses/by/4.0/). (c) ATR-IR spectroscopy. Figure 3c was reproduced from [81] (© 2021 A. Bieberle-Hütter et al., published by IOP Publishing, distributed under the terms of the Creative Commons Attribution 4.0 International License, https://creativecommons.org/licenses/by/4.0/). (d) TIRFM. Figure 3d was adapted from [82] (© 2023 L. Colson et al., published by MDPI, distributed under the terms of the Creative Commons Attribution 4.0 International License, https://creativecommons.org/licenses/by/4.0/). (e) SERS. (f) VSFG spectroscopy. (g) SHG spectroscopy. (h) DPI. Figure 3h was adapted from [76] with permission. Copyright 2014 American Chemical Society. This content is not subject to CC BY 4.0.

coverage (mass per unit area) and evaluate the antibody modification process on SAMs on gold surfaces. They demonstrated that the antibody concentration required could be reduced to one tenth of the conventional level without loss of analytical performance, thereby optimizing the surface-modification protocol for biosensors [57].

3.1.2 Ellipsometry. Ellipsometry is a non-destructive method for evaluating thin-film thickness and optical constants by analyzing the change in polarization that occurs when obliquely incident linearly polarized light is reflected from a sample surface. Specifically, it measures the change in polarization upon reflection, which is described by the amplitude ratio (Ψ) and phase difference (Δ) between the p- and s-polarized components of the reflected light [58] (Figure 3b). By fitting an appropriate optical model to the experimental data, the thickness and refractive index of the target layer can be derived [59,60]. This method can therefore be used to evaluate the mass and binding dynamics of adsorbed molecules. Mora and co-workers used spectroscopic ellipsometry to study the adsorption of an enzyme, D-amino acid oxidase, on carbon nanotubes. By performing dynamic adsorption experiments while varying pH and protein concentration, they calculated the surface mass and the initial adsorption rate, showing that the adsorption process was governed by a combination of hydrophobic and electrostatic interactions. Furthermore, by comparing the optical film thickness derived from ellipsometry with enzyme activity measured separately by biochemical assay, they reported that differences in pH during adsorption caused changes in enzyme orientation and conformation, which in turn produced differences in catalytic activity [59].

3.1.3 Infrared spectroscopy. Infrared (IR) spectroscopy is a method that uses the resonant absorption of specific infrared light associated with molecular vibrations (Figure 3c). The resulting infrared absorption spectrum directly reflects the vibrational states of molecules and is highly sensitive to their local chemical structures [13]. This makes the method useful not only for identifying chemical species at interfaces, but also for evaluating secondary-structure changes, orientation, and intermolecular interactions of adsorbed molecules [37,61,62]. Roach and co-workers used attenuated total reflection infrared (ATR-IR) spectroscopy to evaluate the adsorption of bovine serum albumin (BSA) and fibrinogen on silica nanoparticles of various sizes. By deconvoluting the amide-I band arising from peptide bonds, they quantified how surface hydrophilicity or hydrophobicity and nanoscale surface curvature affect the relative amounts of α-helical and other structural components in the proteins. They also evaluated differences in molecular orientation from the intensity ratio of the amide-I and amide-II bands, and the strength of hydrogen bonding between neighboring adsorbed proteins from specific component peaks [62].

3.1.4 Total internal reflection fluorescence microscopy. Total internal reflection fluorescence microscopy (TIRFM) is an imaging method that uses the evanescent field generated when an incident light undergoes total internal reflection at a solid–liquid interface. This field selectively excites fluorescent molecules within a few hundred nanometers layer on the solution side of the interface, and the resulting weak emission is captured with a highly sensitive camera [63] (Figure 3d). From the fluorescence intensity and two-dimensional coordinates of bright spots recorded by the camera, the method can evaluate the number of adsorbed molecules, single-molecule adsorption and desorption kinetics, and microfluidic dynamics near the interface [63-65]. Lyu and co-workers used TIRFM to evaluate the desorption kinetics of BSA from amine-modified glass surfaces. Through microscopic observation at the single-molecule level, they found that the desorption pattern of BSA changed clearly around 400 s after adsorption, revealing a complex aging process in which the initial weakly bound state gradually converted into a long-lived strongly bound state [63].

3.1.5 Raman spectroscopy. Raman spectroscopy is a method that uses inelastic scattering generated when monochromatic light interacts with molecules, and evaluates molecular vibrational energy levels from the energy difference between the incident and scattered light (the Raman shift). For solid–liquid interface measurements, SERS, which combines electromagnetic enhancement due to localized surface plasmon resonance (LSPR) in metallic nanostructures with chemical enhancement arising from charge transfer between molecules and the substrate, is widely used [66] (Figure 3e). The Raman spectrum directly reflects the vibrational states of specific chemical bonds and is therefore sensitive to local chemical structure. As a result, this method can be used not only to identify target molecules but also to evaluate structural changes, orientation, and intermolecular interactions [67-69]. Brulé and co-workers used dynamic SERS and principal component analysis to evaluate conformational changes of single BSA molecules adsorbed on gold nanoparticles. By analyzing time-dependent fluctuations in Raman bands arising from hydrophobic amino acid residues such as tryptophan and tyrosine, they identified the dynamics by which BSA changes from a naturally folded state under physisorption to an unfolded chemisorbed state in which internal amino acids become exposed through hydrophobic interaction with the surface [67].

3.1.6 Vibrational sum frequency generation spectroscopy. Vibrational sum frequency generation (VSFG) spectroscopy is a nonlinear optical method in which visible and tunable infrared

light are simultaneously irradiated onto an interface, and the emitted sum-frequency light is detected. Because signal generation is forbidden in centrosymmetric bulk liquids and amorphous media, only the signal from the symmetry-broken solid–liquid interface can be extracted without being buried in bulk noise [70] (Figure 3f). The resulting SFG spectrum (nonlinear susceptibility) directly reflects the vibrational states of interfacial molecules and is extremely sensitive to their microscopic local chemical structures. Accordingly, by analyzing vibrational spectra associated with specific functional groups at the interface, the method can evaluate not only chemical identity and hydrogen-bond networks but also changes in molecular structure and orientation, including absolute orientation [14,71,72]. Tian and co-workers used phase-sensitive VSFG spectroscopy to evaluate the hydrogen-bond network of water molecules at the interface between water and hydrophobic octadecyltrichlorosilane. By directly measuring the imaginary part of the interfacial vibrational spectrum while changing the pH of the bulk solution, they determined the absolute orientation of water molecules and demonstrated that hydroxide ions are specifically adsorbed at the interface even in nearly neutral pure water. They further clarified the dynamics by which the negative surface charge generated by these ions reorganizes the orientation of the hydrogen-bond network of interfacial water [71].

3.1.7 Second harmonic generation (SHG) spectroscopy. Second harmonic generation (SHG) spectroscopy is a nonlinear optical method in which light at twice the frequency of an incident single-wavelength beam is generated and detected at an interface (Figure 3g). As in SFG, the signal is generated only at interfaces where inversion symmetry is broken, giving SHG high interfacial selectivity [73]. The SHG signal directly reflects the electronic state of the interface and is highly sensitive to the interfacial electrostatic field. By tracking changes in SHG signal, macroscopic charging behavior associated with pH changes and acid–base equilibrium processes of interfacial molecules can be evaluated quantitatively [74,75]. Konek and co-workers studied the acid–base equilibrium of surface molecules at a carboxylic acid-modified silica/water interface. By analyzing titration curves of the field-induced SHG signal obtained while varying pH, they identified two deprotonation processes associated with different hydrogen-bonding states and quantified the acid dissociation constants for each [74].

3.1.8 Dual-polarization interferometry. Dual-polarization interferometry (DPI) is an optical technique that tracks nanoscale structural changes perpendicular to the solid–liquid interface in real time. It achieves this by independently measuring the phase shifts of transverse electric and transverse magnetic propagation modes, which are alternately introduced to the surface of a slab optical waveguide, as they respond to molecular adsorption and conformational changes at the interface (Figure 3h) [76]. The measured phase-shift data are converted into the thickness and refractive index of the adsorbed layer using an electromagnetic analytical model. This allows for the evaluation of the surface mass density and film density of the adsorbed molecules themselves, excluding the effects of hydration, as well as structural changes associated with protein adsorption and denaturation [77,78]. Zheng and co-workers exploited the ultrasensitive phase detection capability of DPI to evaluate the interaction between complement protein C1q, which is involved in the progression of Alzheimer's disease, and the pathogenic molecule amyloid β42 (Aβ42). Specifically, they simultaneously and continuously tracked changes in mass, thickness, and density during the binding processes of C1q with different aggregation states of Aβ42. Their results revealed that Aβ42 monomers exhibit a particularly high affinity for C1q compared to other aggregated forms. Furthermore, during the binding of Aβ42 monomers, they observed a rapid initial adsorption followed by a gradual structural reorganization that formed a denser layer [78].

3.2 Electrochemical Methods

3.2.1 Electrochemical impedance spectroscopy. Electrochemical impedance spectroscopy (EIS) is a method for evaluating the electrical properties of an interface by applying a small sinusoidal potential perturbation over a wide frequency range to an electrochemical system at steady state and measuring the impedance from the response current [83] (Figure 4a). In EIS, equivalent circuit parameters can be extracted by fitting the impedance response to an equivalent circuit model [83,84]. Magar and co-workers reported a point-of-care method for quantifying trace calcium ions in human saliva using a SAM-modified gold electrode. By analyzing EIS data acquired in the absence of a redox probe with a Randles equivalent circuit, they captured the increase in calcium concentration as a decrease in charge-transfer resistance and an increase in EDL capacitance. They further interpreted this response theoretically as a structural change in the EDL caused by specific ion adsorption, and finally derived the target concentration from the magnitude of the resistance decrease [84].

3.2.2 Field-effect transistor. A field-effect transistor (FET) converts changes in charge state and potential within the EDL at a solid–liquid interface directly into electrical signals, such as changes in semiconductor-channel conductance, through electrostatic interactions [85] (Figure 4b). This method can detect changes in interfacial charge state and potential caused by adsorption and desorption of target molecules or by charge rearrangement accompanying structural changes [18,86,87]. Nakatsuka and co-workers modified the surface of an ultrathin

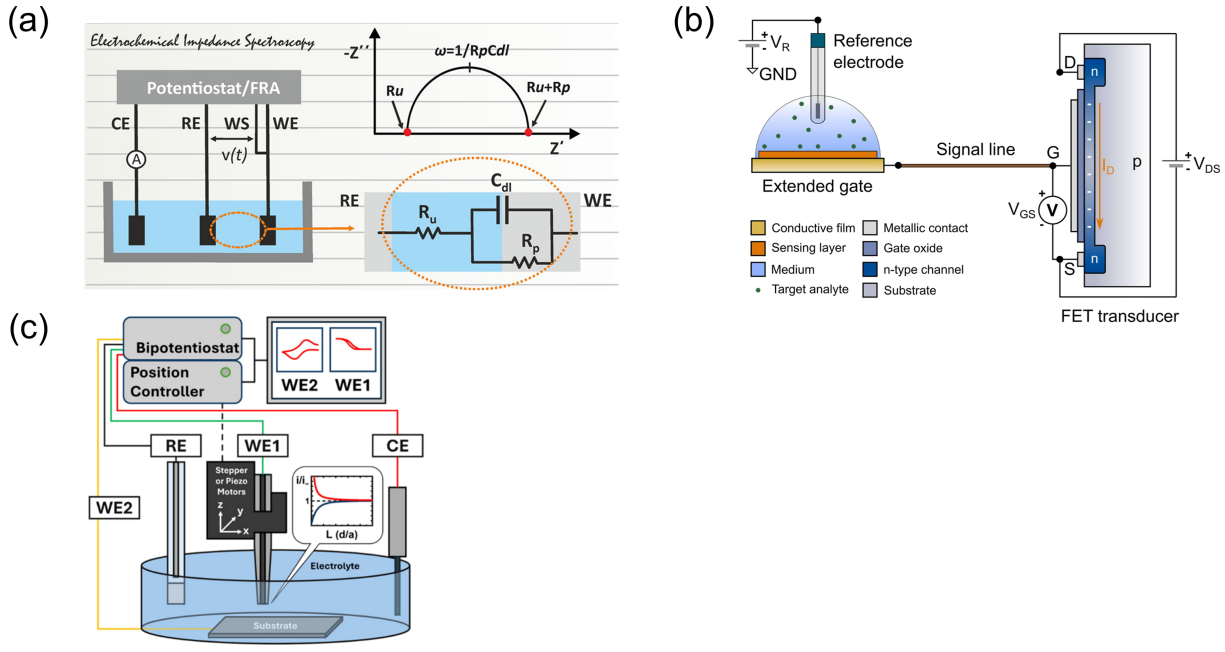


Figure 4: Schematic illustrations of measurement principles for electrochemical methods. (a) EIS. Figure 4a was reproduced from [83] (© 2023 A. Ch. Lazanas et al., published by American Chemical Society, distributed under the terms of the Creative Commons Attribution-NonCommercial-NoDerivatives 4.0 International License, http://creativecommons.org/licenses/by-nc-nd/4.0/). This content is not subject to CC BY 4.0. (b) ExG-FET. Figure 4b was reproduced from [90] (© 2023 Ž. Janićijević et al., published by Elsevier, distributed under the terms of the Creative Commons Attribution 4.0 International License, https://creativecommons.org/licenses/by/4.0/). (c) SECM. Figure 4c was adapted from [91] with permission. Copyright 2025 American Chemical Society. This content is not subject to CC BY 4.0.

indium oxide FET with DNA aptamers that undergo adaptive structural changes upon target binding and achieved highly sensitive detection of small molecules under physiological conditions [18].

3.2.3 Scanning electrochemical microscopy. Scanning electrochemical microscopy (SECM) is a method in which a small probe (an ultramicroelectrode, UME) is scanned in solution close to the sample surface, and the Faradaic current associated with redox reactions between the probe and the substrate is measured [88] (Figure 4c). The resulting current response is influenced by local electrochemical properties at the sample surface, such as enzymatic activity and electronic conductivity, as well as by the surface charge state. Analysis of this current response therefore allows one to evaluate local electron-transfer processes and electrostatic interactions at the interface, while also mapping the spatial distribution of electrochemical properties [41,89]. Boldt and co-workers used SECM to measure local electron-transfer processes on a carboxyl-terminated SAM on a gold electrode. They showed that changes in the protonation and deprotonation state of the SAM surface with solution pH generate electrostatic interactions (Coulomb forces) with redox mediators carrying different charges, thereby modulating the electron-transfer rate at the interface [41].

3.3 Mechanical response

3.3.1 Quartz crystal microbalance with dissipation monitoring. QCM-D is a label-free acoustic method that simultaneously measures the change in resonance frequency of a piezoelectric quartz crystal resonator and the energy dissipation of its vibration, thereby evaluating changes in surface mass, including hydration water, and the viscoelasticity of the system [11] (Figure 5a). From these measurements of hydrated mass and viscoelasticity, one can evaluate the binding dynamics, hydration state, and structural changes of molecules at interfaces [12,51,92]. For example, Lubarsky and co-workers used QCM-D to follow the hydration and dehydration process of a human serum albumin film adsorbed on a hydrophilic surface. Under dry conditions the adsorbed film showed low energy dissipation and behaved rigidly, whereas increasing ambient humidity promoted hydration, increased energy dissipation, and plastically transformed the film into a highly hydrated, flexible viscoelastic body. By applying the Voigt–Voinova model to the data, they further quantified the shear modulus and viscosity of the film, demonstrating that as the protein film absorbed water and gained mass through hydration, the entire adsorbed layer dynamically changed into a more elastic and flexible structure [92].

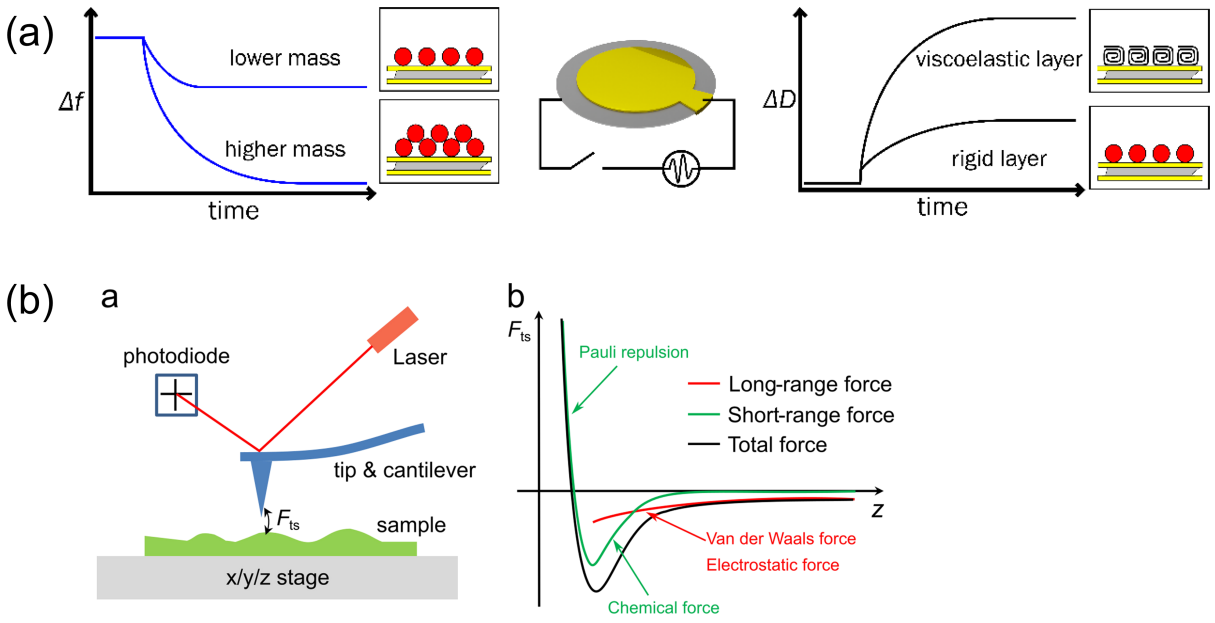


Figure 5: Schematic illustrations of measurement principles for mechanical methods. (a) QCM-D. Figure 5a was reproduced from [80] (© 2022 I. Plikusiene et al., published by MDPI, distributed under the terms of the Creative Commons Attribution 4.0 International License, https://creativecommons.org/licenses/by/4.0/). (b) AFM-based force spectroscopy. Figure 5b was reproduced from [15] (© 2021 J. Peng et al., published by Elsevier, distributed under the terms of the Creative Commons Attribution-NonCommercial-NoDerivatives 4.0 International License, https://creativecommons.org/licenses/by-nc-nd/4.0/). This content is not subject to CC BY 4.0.

3.3.2 Atomic force microscopy-based force spectroscopy. Atomic force microscopy (AFM)-based force spectroscopy is a method in which a probe located at the tip of a flexible cantilever is moved only in the direction normal to the sample surface, and the attractive and repulsive forces between the probe and the surface are measured with piconewton sensitivity [11] (Figure 5b). By analyzing the force curves obtained during approach, indentation, and retraction, this method can quantitatively examine local mechanical properties (such as elastic modulus) and interaction forces at solid–liquid interfaces [93,94]. Andriotis and co-workers applied AFM nanoindentation in aqueous solution to collagen fibrils glycated by ribose treatment. By analyzing the unloading portion of the force curve with a continuum-mechanics model, they calculated the local elastic modulus (indentation modulus) of the sample. They showed on the nanoscale that the glycated collagen fibrils exhibited enhanced swelling due to hydration (water adsorption), and that the resulting decrease in molecular packing density significantly lowered the local elastic modulus compared with untreated collagen fibrils [94].

3.4 Scanning probe microscopy

3.4.1 Atomic force microscopy. AFM is a method that scans the sample surface while using feedback control based on the minute forces acting between the probe and the sample, thereby producing high-resolution images of local three-dimensional topography [11] (Figure 6a). On this basis, the method can evaluate local three-dimensional structures and their dynamic changes [95,96]. Nishide and co-workers used high-speed AFM, which greatly increases scanning speed, to visualize in real time the condensation of DNA mediated by protamine. They captured the dynamic process in which the addition of protamine first caused DNA to form local coil-like structures and then to fold stepwise into rod-like intermediates, leading them to propose a condensation model that culminates in dense toroidal structures. By tracking the response of the structure while increasing salt concentration, for example with NaCl, they also observed that the formed toroidal condensates and related structures disassembled in a stepwise and reversible manner, demonstrating that these dynamic structural changes are driven by electrostatic intermolecular interactions [95].

3.4.2 Frequency-modulation AFM and three-dimensional AFM. Frequency-modulation AFM (FM-AFM) is a method that evaluates local structures at solid–liquid interfaces by detecting the resonant frequency shift of a cantilever caused by the minute interaction forces acting between the probe and the sample in a liquid environment. Three-dimensional AFM (3D-AFM), which extends this technique to three-dimensional scanning, acquires the 3D spatial distribution of the resonant frequency shift and the interaction forces at the interface by scanning the *XY* plane while simultaneously rapidly modulating the probe in the *Z* direction [97] (Figure 6b). Based on these principles, both methods go beyond determining solid surface topog-

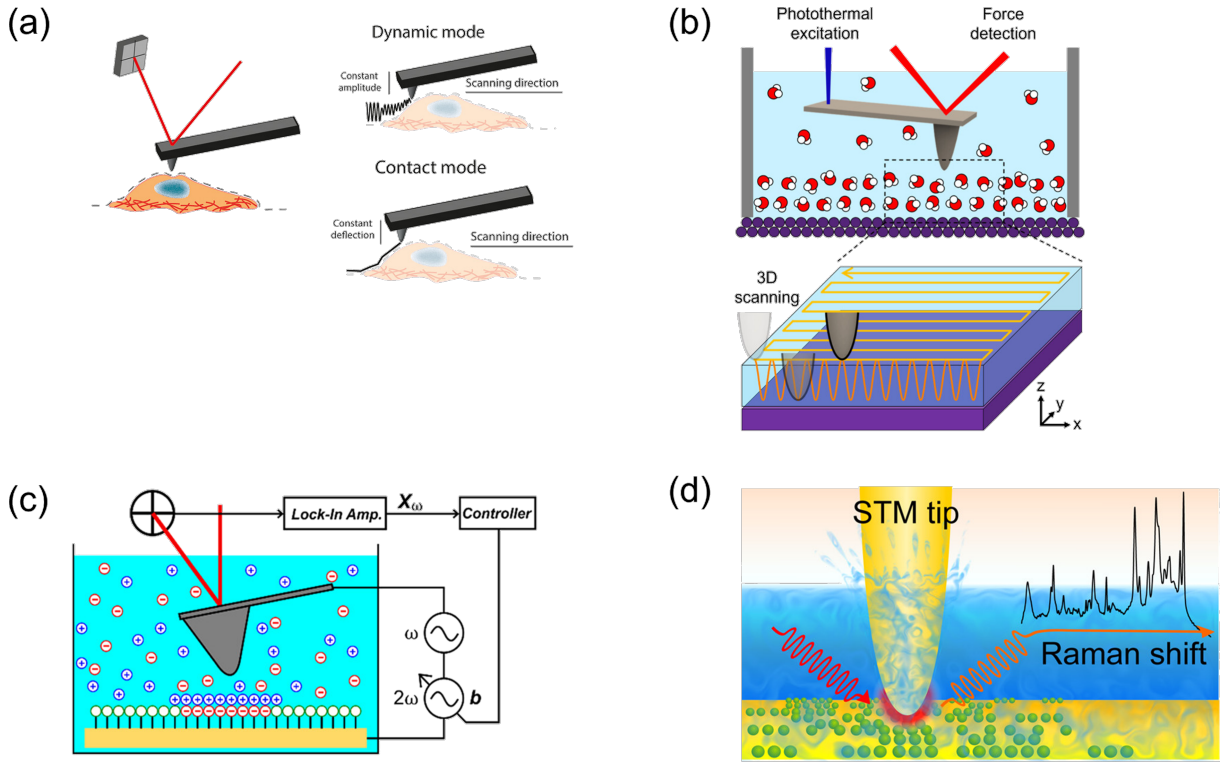


Figure 6: Schematic illustrations of measurement principles for SPM methods. (a) AFM. Figure 6a was adapted from [106] with permission. Copyright 2020 American Chemical Society. This content is not subject to CC BY 4.0. (b) 3D-AFM. Figure 6b was adapted from [107] with permission. Copyright 2025 American Chemical Society. This content is not subject to CC BY 4.0. (c) AC-KPFM. Figure 6c was adapted from [101] (© 2022 T. Hackl et al., published by American Chemical Society, distributed under the terms of the Creative Commons Attribution 4.0 International License, https://creativecommons.org/licenses/by/4.0/). (d) TERS. Figure 6d was reprinted from [108], N. M. Sabanés et al., "Versatile Side-Illumination Geometry for Tip-Enhanced Raman Spectroscopy at Solid/Liquid Interfaces", Analytical Chemistry, © 2016 American Chemical Society, distributed under the ACS AuthorChoice/Editors' Choice via Creative Commons CC-BY Usage Agreement, https://pubs.acs.org/page/policy/authorchoice_ccby_termsofuse.html. This content is not subject to CC BY 4.0.

raphy; they can evaluate hydration structures at the interface, the average conformation of lipid bilayer headgroups, and the molecular arrangement of SAMs with high spatial resolution [98-100]. Araki and co-workers used FM-AFM to observe the surface and hydration structures of a bioinert mixed-charged SAM (MC-SAM) in liquid at the molecular scale. They discovered that the molecules constituting the film form a highly ordered rectangular lattice array. Furthermore, they revealed the presence of a mechanically highly stable hydration layer near the MC-SAM surface, demonstrating that this robust hydration shell functions as a physical barrier preventing the adsorption of proteins and cells, thereby serving as the origin of its bioinert properties [100].

3.4.3 Kelvin probe force microscopy. Kelvin probe force microscopy (KPFM) is a method that detects the electrostatic force or its gradient acting between a conductive probe and a sample surface and determines the contact potential difference from the compensating voltage [16] (Figure 6c). Using this principle, the method can map the local surface-potential distribution at interfaces with high spatial resolution [101,102]. Hackl and co-workers used AC-KPFM, which employs a high-frequency AC voltage, to evaluate micropatterned SAMs in aqueous solution. They mapped the local surface-potential distributions of regions modified with amino and carboxyl groups to mimic biomolecules such as proteins. By changing solution pH, they controlled the ionization state of these functional groups and successfully measured the accompanying changes in charge state reversibly. Furthermore, from the polarity inversion and distance dependence of the measured local potential distribution, they inferred that counterions adsorb to the surface charge and form a Stern layer in aqueous solution, thereby revealing the spatial screening effect of the EDL that is characteristic of solid–liquid interfaces [101].

3.4.4 Tip-enhanced Raman spectroscopy. Tip-enhanced Raman spectroscopy (TERS) is a method that uses the intense electromagnetic near field enhanced by LSPR excited at the tip of a metallic SPM probe to obtain vibrational spectra of molecules with nanoscale spatial resolution [17] (Figure 6d). By

analyzing these spectra, the method can evaluate local chemical composition, spatial heterogeneity, chemical reaction processes, and structural changes and orientation [103-105]. El-Khoury carried out liquid-phase TERS measurements at a solid–liquid interface using gold nanoplates modified with 4-mercaptobenzonitrile (MBN) in water. By mapping the Raman scattering signal from the molecules, he visualized the heterogeneous molecular coverage with an extremely high spatial resolution of below 3 nm. He also captured in situ the local reaction process in which plasmon-induced hydrolysis of MBN generated 4-mercaptobenzoic acid, showing that water is involved not merely as a medium but also as a reactant [105].

3.5 Neutron and X-ray-based interfacial analysis

3.5.1 Neutron reflectometry. Neutron reflectometry (NR) is a technique for evaluating the nanoscale structure of stratified interfaces based on the reflectivity profile of a neutron beam reflected at the interface (Figure 7). A major advantage of this method is its ability to identify specific components at the interface using contrast variation through isotopic substitution [109]. By deriving the scattering length density profile from the measured reflectivity profile, it is possible to evaluate the surface mass density at the interface, the hydration state directly reflecting the spatial distribution of specific components, molecular orientational changes, and even heterogeneous multilayer structures in the thickness direction [110,111]. Pan and co-workers analyzed the self-assembled structure of polypeptoid brushes at the SiO_2–water interface using in situ NR. By carefully examining the volume fraction profiles obtained through contrast variation with deuterium substitution, they identified a two-tier heterogeneous structure consisting of a dense inner layer containing adhesive units tightly bound to the solid surface, and a highly hydrated, low-density outer layer. They demonstrated that this unique hydration structure contributes to the suppression of protein denaturation and provides excellent antifouling effects [110].

3.5.2 X-ray reflectometry and X-ray absorption spectroscopy. Similar to NR, X-ray reflectometry (XRR) is a technique capable of evaluating the nanoscale structure of stratified interfaces from the reflectivity profile of X-rays reflected at the interface. It has the advantage of more easily yielding high-resolution results than NR due to the overwhelming brilliance of synchrotron X-rays [112]. Based on this high resolution, an electron density profile (EDP) representing the spatial distribution of electrons in the material is derived from the measured reflectivity profile. This allows for the evaluation of surface mass density, the hydration state of adsorbed molecular layers, molecular orientation, and multilayer structures in the thickness direction [113,114]. In contrast, X-ray absorption spectroscopy (XAS) is a technique that evaluates the bonding states of molecules present near the substrate interface, such as those in the electric double layer, by analyzing the microscopic electronic components contained in surface-sensitive secondary electrons emitted upon X-ray irradiation. It also has the advantage of selectively extracting the bonding states of molecules by tuning the irradiation energy to specific electron orbitals. By leveraging these characteristics, it is possible to directly evaluate the microscopic bonding states of molecules in response to applied voltages [115]. Thus, while XRR evaluates the electron density distribution and the structure in the thickness direction of the layer formed at the interface, XAS can selectively evaluate the bonding states of molecules present near the interface. Therefore, both are X-ray measurement techniques capable of analyzing solid–liquid interfaces from different perspectives. Richter and co-workers evaluated the adsorption structure and formation process of proteins at the SiO_2–water interface using in situ XRR. By applying the average mass-to-electron-density ratio of amino acids, they calculated the net adsorbed mass at the interface from the EDP. This approach allowed them to capture the adsorption structure not merely as a static density distribution, but as a dynamic process of increasing adsorbed mass over time. Furthermore, with a spatial resolution superior to that of neutron reflectometry, they demonstrated that proteins adsorb in a highly hydrated, native state and form a dynamically heterogeneous structure in which the density distribution evolves over time to maximize interfacial interactions [114].

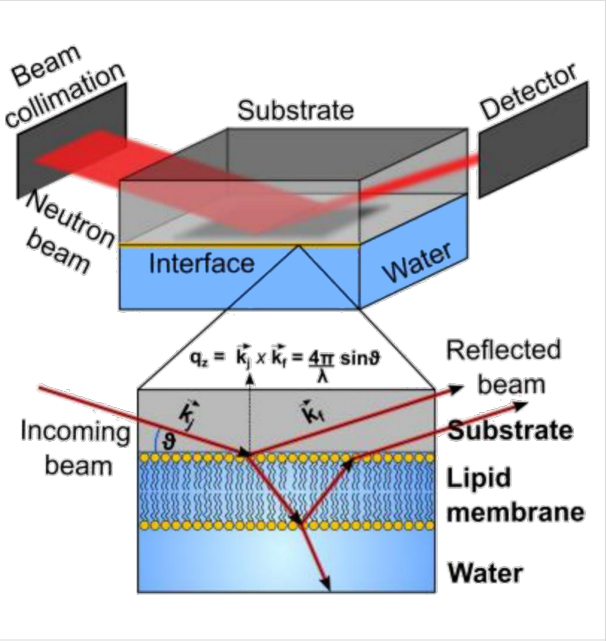


Figure 7: Schematic illustration of the measurement principle for NR. Figure 7 was adapted from [116] (© 2024 L. Caselli et al., published by Elsevier B.V., distributed under the terms of the Creative Commons Attribution 4.0 International License, https://creativecommons.org/licenses/by/4.0/).

As discussed above, each stand-alone method provides access to only a limited part of the interfacial state because its observation window is restricted by its physical principle. Consequently, no single technique can fully capture the coupled changes in mass, charge, molecular structure, hydration, and local morphology that govern solid–liquid interfacial phenomena. To facilitate a direct comparison, Figure 8 illustrates the spatiotemporal mapping of these stand-alone methods, highlighting their standard temporal and depth-direction spatial resolutions. Additionally, Table 1 summarizes their key characteristics, including the observable physical quantities and their inherent limitations discussed in Sections 3.1–3.4. Based on this comparison, the subsequent sections discuss how multimodal measurement platforms integrate complementary methods to overcome these limitations and provide a more comprehensive view of interfacial dynamics.

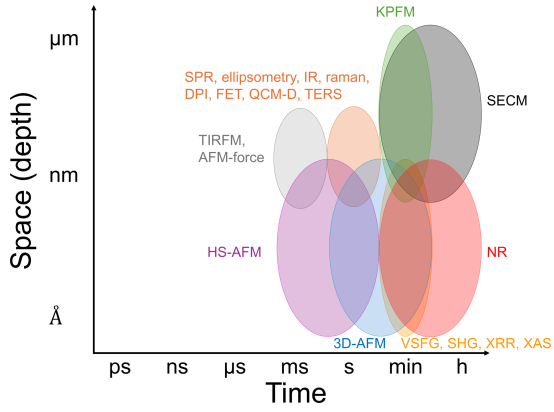


Figure 8: Spatiotemporal mapping that organizes the depth-direction spatial resolution and standard temporal resolution of stand-alone methods.

Table 1: Summary of stand-alone techniques for the characterization of solid–liquid interfaces.

Classification	Technique	Target physical quantity	Target interfacial phenomena	Ref.
optical	SPR	mass	binding kinetics	[9,57]
	Ellipsometry	mass	binding kinetics	[59,60]
	IR	molecular vibration	structural changes, orientation, Intermolecular interactions	[37,61,62]
	TIRFM	number of adsorbed molecules	single-molecule binding kinetics, microfluidic dynamics	[63-65]
	Raman/SERS	molecular vibration	structural changes, orientation, Intermolecular interactions	[67-69]
	VSFG	molecular vibration	structural changes, orientation, hydrogen-bonding network	[14,71,72]
	SHG	charge state, interfacial potential	charging behavior, acid-base equilibrium process	[74,75]
	DPI	mass	structural changes	[77,78]
electrochemical	EIS	charge state, interfacial potential	structural changes in the EDL	[84]
	FET	charge state, interfacial potential	binding kinetics, charge rearrangement	[18,86,87]
	SECM	electrochemical properties, local charge state	local electron transfer processes, electrostatic interactions	[41,89]
mechanical	QCM-D	hydrated mass, viscoelasticity	binding kinetics, hydration state, structural changes	[12,51,92]
	AFM-force	local mechanical properties, interaction forces	hydration state, structural changes	[93,94]
SPM	AFM	local structure	structural changes	[95,96]
	FM-AFM/3D-AFM	interaction forces, local structure	hydration structure	[98-100]
	KPFM	local interfacial potential	charging behavior, screening effect of the EDL	[101]
	TERS	local molecular vibration	structural changes, orientation, chemical reaction processes	[103-105]
neutrons and X-ray	NR	density profiles	hydration state, orientation, multilayered structure	[110,111]
	XRR	density profiles	hydration state, orientation, multilayered structure	[113,114]
	XAS	local bonding states	structural changes, orientation, hydrogen-bonding network	[115]

4 Advances in multimodal characterization techniques

4.1 Integration of optical methods with electrochemistry (EC)

4.1.1 SPR–EC systems. SPR–EC systems combine interfacial electrochemical readouts with local refractive-index responses from the same interface, thereby enabling direct comparison between charge-transfer processes and concomitant changes in adsorbed mass or effective film thickness [117-124]. The Kretschmann geometry, in which the metal film on the base of a prism serves as the working electrode, has been the standard optical configuration [118-120,122-124]. More recently, voltage-modulated normal-incidence SPR based on gold nanohole arrays that do not require a prism has also been developed to facilitate device miniaturization and integration with microfluidic channels [117,121].

Hatami and co-workers developed a hybrid sensor that integrates an extended-gate organic thin-film transistor (ExG-OTFT) with SPR and improved system stability by spatially separating the sensing surface from the transistor body. From simultaneous measurements during the formation of polyelectrolyte multilayers, they showed that SPR captures local refractive-index changes associated with mass adsorption, whereas the ExG-OTFT captures the collective distribution of charge carriers over the whole interface, thereby demonstrating the complementary nature of the information obtained [117] (Figure 9). Zhao and co-workers also constructed a device for the simultaneous measurement of cellular exocytosis by combining an UME with SPR, and used K^+ stimulation to trigger exocytosis in PC12 cells cultured on a gold thin film. The carbon nanopipette electrode detected small current spikes from dopamine released from single cells, while SPR simultaneously recorded macroscopic refractive-index changes caused by fusion of vesicles with the cell membrane, revealing a clear positive correlation between the SPR signal and the frequency of exocytotic events [118].

Technical limitations nevertheless remain. When a gold thin film serves as the working electrode, potential-dependent changes in surface electron density can introduce background shifts in the SPR response, which may obscure the redox-related signal of the target molecules [122]. In addition, the two channels do not necessarily probe the same spatial domain: In ExG-OTFT–SPR systems, the electrical signal reflects charge redistribution over the entire electrode, whereas SPR monitors local refractive-index changes only within the illuminated region. Consequently, delayed molecular transport within the flow cell can generate an apparent time lag between the two signals [117]. In more complex systems such as cellular exocytosis, the SPR response may also include contributions from cell-membrane deformation and bulk refractive-index changes, complicating rigorous quantification of released molecules [118,120].

Taken together, these examples show that the main advantage of SPR–EC systems is the ability to relate charge-transfer events to changes in adsorbed mass, effective film thickness, or interfacial refractive index, rather than measuring each response independently. However, this correlation can be complicated by potential-induced optical background shifts, differences in the effective sensing areas of the two channels, mass-transport delays within flow cells, and non-specific refractive-index contributions in complex biological samples. Therefore, future SPR–EC platforms should define the spatial, temporal, and physicochemical relationship between optical and electrochemical responses more rigorously, while improving the sensitivity of each measurement channel.

4.1.2 SERS–EC systems. SERS–EC systems, which integrate electrochemical measurements with surface-enhanced Raman scattering, are analytical platforms that enable real-time analysis of complex reaction dynamics at the molecular level by simultaneously measuring electrochemical responses at an interface and molecular vibrational signals reflecting the chemical structure and orientation of adsorbed molecules at the same interface [21,22,125-127]. The standard optical configuration employs roughened metal surfaces as the working electrode [21,22,125], but more recently shell-isolated nanoparticle-enhanced Raman spectroscopy, in which plasmonic nanoparticles are coated with an ultrathin inert silica shell, has also attracted attention [126,127]. Collectively, these approaches enable dynamic control of adsorbate orientation through potential modulation and highly sensitive operando measurements of biomacromolecules such as DNA and other complex organic molecules.

As a specific example, Wicaksono and co-workers used a CV-SERS device based on electrodeposited gold nanostructures on a screen-printed carbon electrode to simultaneously track the electrochemical oxidation of malachite green (MG) and changes in its adsorbate orientation. Analysis of the intensity ratio of specific peaks showed that under positive potentials MG forms dimers and adsorbs strongly in a tilted upright configuration through its aromatic rings [22]. Tran and co-workers further developed an SERS–EC method in which the surface potential was dynamically modulated during measurements of DNA oligonucleotides, thereby expanding the information that could be extracted from potential-dependent reorientation. By pulling different bases into the hotspot at different potentials and combining the resulting spectra from multiple conformations into a “superprofile”, together with machine learning, they

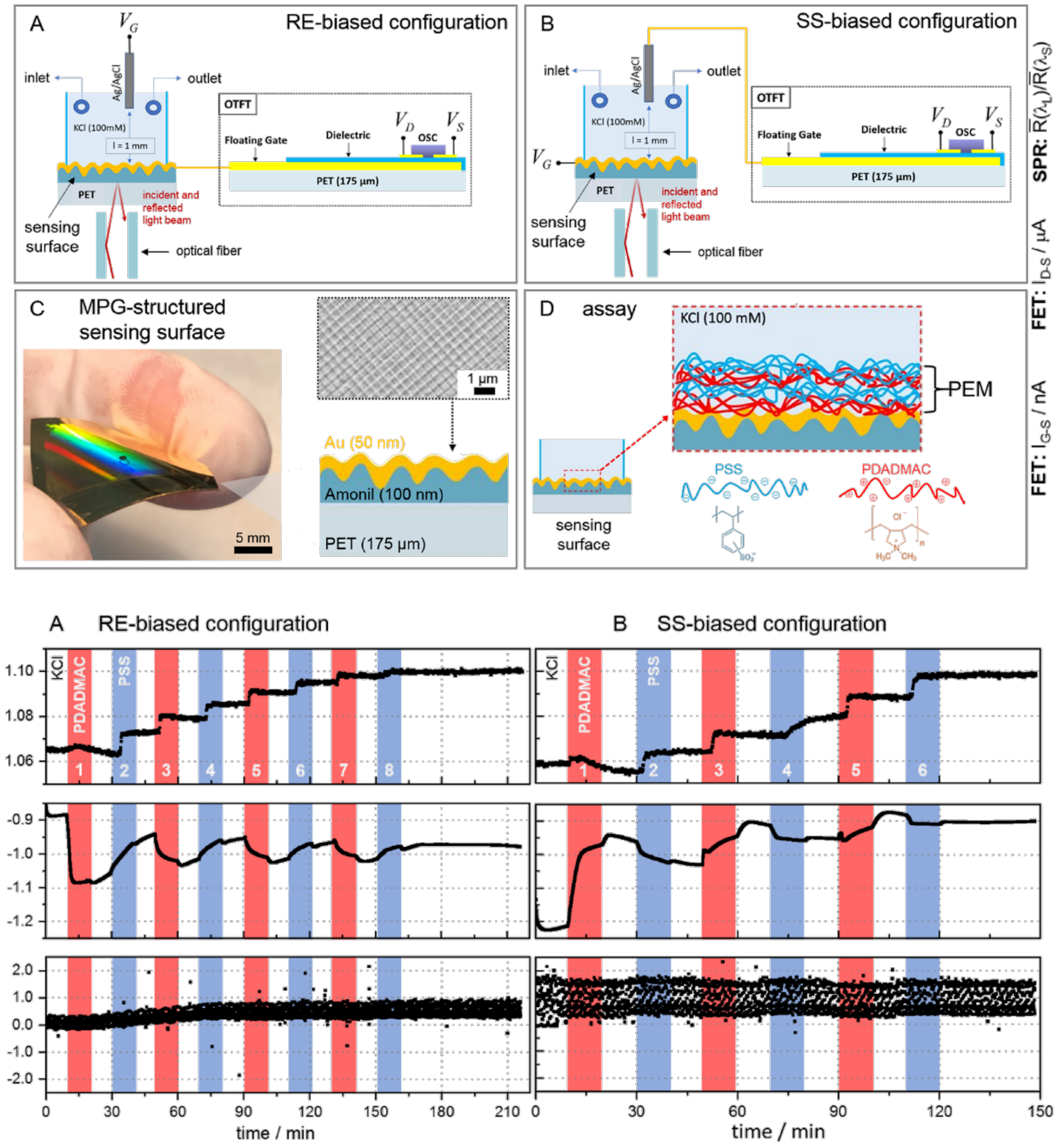


Figure 9: Representative multimodal measurement platforms integrating electrochemical control with optical measurements, together with representative outputs: SPR–EC platform used for polyelectrolyte sensing. Figure 9 was reproduced from [117] (© 2025 D. Hatami et al., published by Springer Nature, distributed under the terms of the Creative Commons Attribution-NonCommercial-NoDerivatives 4.0 International License, https://creativecommons.org/licenses/by-nc-nd/4.0/). This content is not subject to CC BY 4.0.

identified DNA base composition, strand length, and primary sequence with high accuracy [21].

Several technical limitations are also characteristic of SERS–EC systems. Potential modulation can alter the electronic environment at the metal surface and induce Raman peak shifts through the electrochemical Stark effect, so spectral changes must be interpreted with caution [125]. Under harsh electrochemical or catalytic conditions, electrode reconstruction or nanoparticle reshaping can further change hotspot distributions and destabi-

lize signal intensity [128]. In addition, for large molecules such as DNA, the surface selection rule preferentially enhances signals from segments located close to the substrate, so the measured spectra may represent only part of the molecular structure [125].

These studies demonstrate that SERS–EC is particularly useful for linking electrochemical potential control with molecular-level vibrational responses at plasmonic electrode interfaces, which cannot be obtained from current–potential measurements alone. At the same time, the main issue in SERS–EC systems is not only signal enhancement, but also the reliable assignment of potential-dependent spectral changes. Because SERS spectra can be influenced by adsorbate orientation, local electric fields, hotspot geometry, and surface-selection effects, apparent spectral changes do not always correspond directly to chemical transformation at the interface. Future SERS–EC studies should therefore combine stable plasmonic electrode designs with analytical strategies that distinguish true molecular changes from field-, orientation-, and geometry-dependent spectral variations.

4.1.3 IR–EC systems. IR–EC systems, which integrate electrochemical measurements with IR spectroscopy, are analytical platforms that enable molecular-level analysis of complex reaction dynamics by correlating electrochemical responses at an interface with molecular vibrational signals that reflect the chemical structure, hydrogen-bond network, and orientation of adsorbed molecules [128-130]. Methods tailored to the target system have been developed, including SEIRAS, which uses plasmonic field enhancement [129], polarization-modulation infrared reflection absorption spectroscopy (PM-IRRAS), which suppresses bulk-water absorption by polarization modulation [130], and polarized ATR methods that use orthogonal polarizations (p and s) to analyze molecular orientation with high precision [128]. As a result, applications have expanded broadly across organic and biological systems, from the basic behavior of monolayers to tracking antimicrobial mechanisms using model cell membranes and evaluating liposome-based drug-delivery systems.

This capability to evaluate and control interfacial molecular orientation using potential as a trigger has also been used to elucidate the behavior of complex biomolecular systems such as amino-acid residues and cell membranes. Pudžaitis and co-workers focused on the histidine side chain, which plays an important role in protein structure and function, and prepared an imidazole-terminated SAM on a gold electrode for SEIRAS analysis. By following the low-wavenumber shift of the imidazole =C–H stretching modes (3115 and 3150 cm^{-1}) when the potential was changed toward more negative potentials (from 0.3 to −0.5 V), they demonstrated at the molecular level that negative electrode polarization reversibly weakens hydrogen bonding of imidazole at the organic layer/water interface [129]. Extending this concept to a more complex membrane model, Su and co-workers constructed on a gold electrode a model lipid bilayer mimicking the outer membrane of Gram-negative bacteria (Lipid A and 1,2-dimyristoyl-*sn*-glycero-3-phosphoethanolamine) and tracked its interaction with the antibiotic polymyxin by operando PM-IRRAS. Analysis of specific peaks quantitatively revealed the process by which, under an applied membrane potential, polymyxin competes with Mg^{2+} to bind to polar headgroups, increases the tilt angle of lipid acyl chains, changes the orientation of C=O bonds, and thereby disrupts the membrane structure [130].

IR–EC systems also face several common interpretational challenges. In metal-enhanced configurations, potential-induced peak shifts may reflect either genuine changes in the local chemical environment, such as hydrogen-bond reorganization, or electric-field-induced Stark effects, and these contributions are not always easy to distinguish. Harsh potential cycling may also damage or delaminate the metal thin film used for signal enhancement [129]. In aqueous measurements using PM-IRRAS and related methods, variations in optical geometry, such as the thickness of the water gap, can strongly affect signal intensity, making rigorous normalization essential for quantitative comparison [130]. Furthermore, in complex biomimetic membranes or drug–membrane systems, absorption bands from different components often overlap, which complicates spectral assignment and quantitative interpretation [128,130].

The reviewed IR–EC studies show that coupling infrared spectroscopy with electrochemical control makes it possible to follow potential-dependent changes in interfacial molecular structure, hydrogen-bonding states, and molecular orientation that cannot be resolved from electrochemical responses alone. In particular, these systems provide vibrational evidence for how adsorbed species, hydrogen-bonding networks, and membrane components reorganize under applied potentials, thereby extending electrochemical analysis from charge-transfer behavior to molecular-level structural interpretation. However, the main interpretational difficulty in IR–EC systems arises from the fact that vibrational bands are strongly affected by hydrated and compositionally complex interfacial environments. Changes in hydrogen-bonding networks, electric-field effects, optical geometry, and overlapping absorption bands can produce similar spectral variations, making it difficult to assign a given IR response to a single molecular process [113-115]. Future IR–EC studies should therefore combine carefully controlled optical and electrochemical configurations with isotope labeling, spectral deconvolution, and computational support to distinguish genuine interfacial molecular rearrangements from hydration-,

field-, geometry-, and composition-dependent spectral variations.

4.1.4 VSFG–EC systems. VSFG–EC systems enable real-time, molecular-level analysis of complex reaction dynamics by simultaneously measuring electrochemical responses and nonlinear optical signals at the same interface, where the latter reflect the local orientation, chemical structure, and interfacial electric field of adsorbed molecules [131-134]. Applications of this system have expanded from high-precision mapping of local interfacial electric-field profiles using the vibrational Stark effect [132-134] to real-time tracking of trace reaction intermediates and their orientation in energy-conversion reactions [131].

This ability to evaluate molecular orientation and local electric fields at interfaces has also been applied to the clarification of the adsorption structures and interfacial environments of complex organic molecules. Liu and co-workers used broadband SFG with a polycrystalline copper electrode to simultaneously track the C–H stretching vibrations and dynamic structural changes of ethoxy groups, which are organic reaction intermediates in CO_2 reduction. Analysis of specific peaks demonstrated that the ethoxy group adopts two distinct adsorption structures, namely, a standing orientation, in which the ethyl group points away from the electrode, and a lying orientation, in which the methyl group lies very close to the surface [131]. Ge and co-workers further constructed SAMs of aromatic diisocyanide molecules with different chain lengths on gold electrodes and combined SFG-based measurements of the interfacial electric field with MD simulation. They quantified that short molecules form tightly packed layers, whereas longer and more flexible molecules leave intermolecular gaps that allow water and electrolyte ions to penetrate into the organic film (percolation), thereby changing the effective thickness of the EDL [133].

VSFG–EC systems have their own technical limitations as well. On metal electrodes, nonresonant background signals can interfere with resonant vibrational features, and phase changes associated with surface reconstruction may even invert the spectral line shape, making purely chemical interpretation difficult [131]. Under Faradaic conditions, the local interfacial electric field does not always scale linearly with the applied voltage; instead, “leaky capacitor” behavior may produce a mismatch between the applied potential and the actual molecular polarization [132]. In realistic catalytic environments, additional complications arise from solvent and ion penetration into the interfacial film and from hydrogen-bonding interactions with probe molecules, both of which can perturb vibrational frequencies and electric-field estimates [132,133].

By resolving nonlinear vibrational responses under electrochemical control, VSFG–EC studies have shown that potential-dependent changes in interfacial molecular orientation, ordering, and local electric fields can be analyzed beyond electrochemical responses alone. However, in contrast to linear vibrational spectroscopies, VSFG–EC measurements require particular care in separating genuine chemical dynamics from electrostatic and optical contributions in nonlinear interfacial spectra. Because VSFG responses are sensitive not only to molecular structure and orientation, but also to local electric fields, nonresonant background interference, and phase changes associated with metal-surface reconstruction, potential-dependent spectral variations do not necessarily map directly onto chemical transformations [117-120]. Future VSFG–EC studies should therefore combine controlled electrochemical measurements with phase-sensitive line-shape analysis and computational modeling to distinguish genuine interfacial molecular dynamics from electric-field- and optics-dependent spectral variations.

4.1.5 Time-resolved spectroscopy–EC systems. Systems that integrate electrochemistry with time-resolved spectroscopy provide a platform for tracking ultrafast charge transfer and short-lived intermediates at interfaces. Methodologically, they can be broadly divided into ultrafast spectroscopy triggered by photoexcitation and operando measurements triggered by potential perturbation [135-139]. The former includes pump–probe methods and two-dimensional electronic spectroscopy (2DES) and two-dimensional infrared spectroscopy using ultrashort pulsed lasers [135,137,139], which follow ultrafast responses immediately after excitation under potentiostatic control. The latter includes methods such as rapid-scan ATR-SEIRAS [136], which can follow transient responses after a potential step on a timescale of tens of milliseconds. These approaches have made it possible to elucidate highly diverse interfacial dynamics, including heterogeneous structural dynamics of molecules at electrode interfaces, molecular reorientation immediately after a potential step, and real-time tracking of electrochemical grafting on carbon electrodes [127,128,130].

These advanced time-resolved multimodal measurements have proven powerful for elucidating biohybrid photoelectrodes based on photosynthetic proteins and the charge-transfer dynamics of organic monolayers. Nawrocki, López-Ortiz, and their co-workers carried out simultaneous time-resolved spectroscopy and photocurrent measurements in systems where photosynthetic protein complexes (reaction center–light-harvesting 1 (RC-LH1) and photosystem I–light-harvesting complex I (PSI-LHCI)) were immobilized on electrodes. This enabled quantitative identification of bottlenecks in electron transfer that inhibit photoinduced charge separation and of energy-loss pathways caused by short-circuiting to the elec-

trode. By further extending this approach to photoelectrochemical two-dimensional electronic spectroscopy, they selectively extracted exciton dynamics that truly contribute to charge separation from the complicated spectra of densely packed pigments [137,139] (Figure 10a). As a simpler interfacial system involving organic molecules, Unni and co-workers constructed a SAM of the stable 2,2,6,6-tetramethylpiperidine-1-oxyl (TEMPO) radical on a gold island film and used time-resolved ATR-SEIRAS. By following the spectra with a high time resolution of 40 ms, they dynamically captured the reversible conformational change (chair inversion) of the piperidinyl ring accompanying the redox process of TEMPO and demonstrated at the molecular level that this conformational change contributes to asymmetric electron-transfer kinetics [136].

Time-resolved spectroscopy–EC systems also face several method-specific challenges. In ultrafast measurements, intense pulsed-laser irradiation can damage both samples and electrode surfaces, making careful control of excitation intensity essential [135]. In two-dimensional spectroscopy of multichromophoric systems, exciton–exciton annihilation and contamination by linear signals (incoherent mixing) can complicate the extraction of genuine energy-transfer and coherence dynamics [139]. In infrared-pulse-based measurements, additional background contributions may arise from free-carrier excitation in semiconductor substrates [135]. Moreover, because electrochemical current reflects a macroscopic response whereas optical readouts often probe a local region, spatiotemporal mismatches can arise between the two channels [136]. In some photoelectrochemical systems, comparison of spectroscopic and electrochemical responses has even enabled short-circuit losses to be quantified [137].

By combining time-resolved spectroscopy with electrochemical measurements, these systems have made it possible to relate transient photoinduced molecular events to subsequent charge separation, transfer, and extraction processes that cannot be resolved from steady-state electrochemical responses alone. For time-resolved spectroscopy–EC systems, the main difficulty lies in determining how transient molecular events captured optically are translated into measurable electrochemical outputs. Ultrafast or local spectroscopic signals do not necessarily represent charge carriers that are ultimately extracted as current, because optical artifacts, kinetic heterogeneity, and device-dependent losses can decouple the spectroscopic response from the electrochemical output [121-125]. Future platforms should therefore be designed to connect transient optical signatures more directly with electrochemical charge-extraction pathways through precise synchronization, optimized excitation conditions, and cell or substrate architectures that minimize such decoupling.

4.1.6 Nanoconfinement-assisted optical–electrochemical systems. As an example of a signal-amplified optical–electrochemical platform, plasmonic electrochemical microscopy (PEM) modified with a mesoporous silica film (MSF) uses electrostatic nanoconfinement within surface pores to locally enrich oxidized species and thereby enhance the optical signal [140]. This makes it possible to compensate for the limited sensitivity of conventional PEM and to visualize low-concentration species in microscopic regions in real time under operando conditions.

Using an Au–MSF electrode, Groysman and co-workers demonstrated a highly sensitive plasmonic imaging–electrochemistry platform in which nanoconfinement amplified the local concentration of electroactive species. With 1,1′-ferrocenedimethanol (FC) as a model analyte, confinement of oxidized FC^+ within the pores improved the detection limit up to 37-fold and the sensitivity 23-fold relative to standard PEM. The system also enabled visualization of dopamine oxidation following local delivery from a micropipette, illustrating its potential for real-time imaging of neurotransmitter release [140] (Figure 10b). This method nevertheless has several practical limitations. Nonuniform deposition of the MSF can generate spatial fluctuations in the PEM signal, and conversion of the optical response into absolute current or concentration remains difficult. In addition, differences between the concentration at the source and that at the confined surface complicate rigorous quantitative interpretation [140].

Although nanoconfinement provides a powerful strategy for amplifying optical–EC signals, this example also emphasizes that improved optical sensitivity must be accompanied by careful quantitative correlation with electrochemical processes. This requirement is common to the optical–EC systems reviewed in this section, in which electrochemical control is linked with optical information on interfacial mass transport, molecular orientation, bonding states, local electric fields, and transient reaction intermediates. Future optical–EC platforms should therefore be designed to correlate optical and electrochemical responses through controlled device architectures, appropriate calibration, synchronized measurements, and physically informed analysis.

4.2 Integration of optical methods with QCM-D

4.2.1 SPR–QCM-D systems. SPR–QCM-D systems integrate QCM-D with SPR-based techniques and serve as powerful analytical platforms that combine two different physical principles, acoustic waves and electromagnetic waves, to measure complex dynamics at the same interface in real time [12,20,141-147]. Their configurations range from approaches that evaluate the same model interface in parallel with independent instruments [12,20,141,144-147] to approaches that integrate both

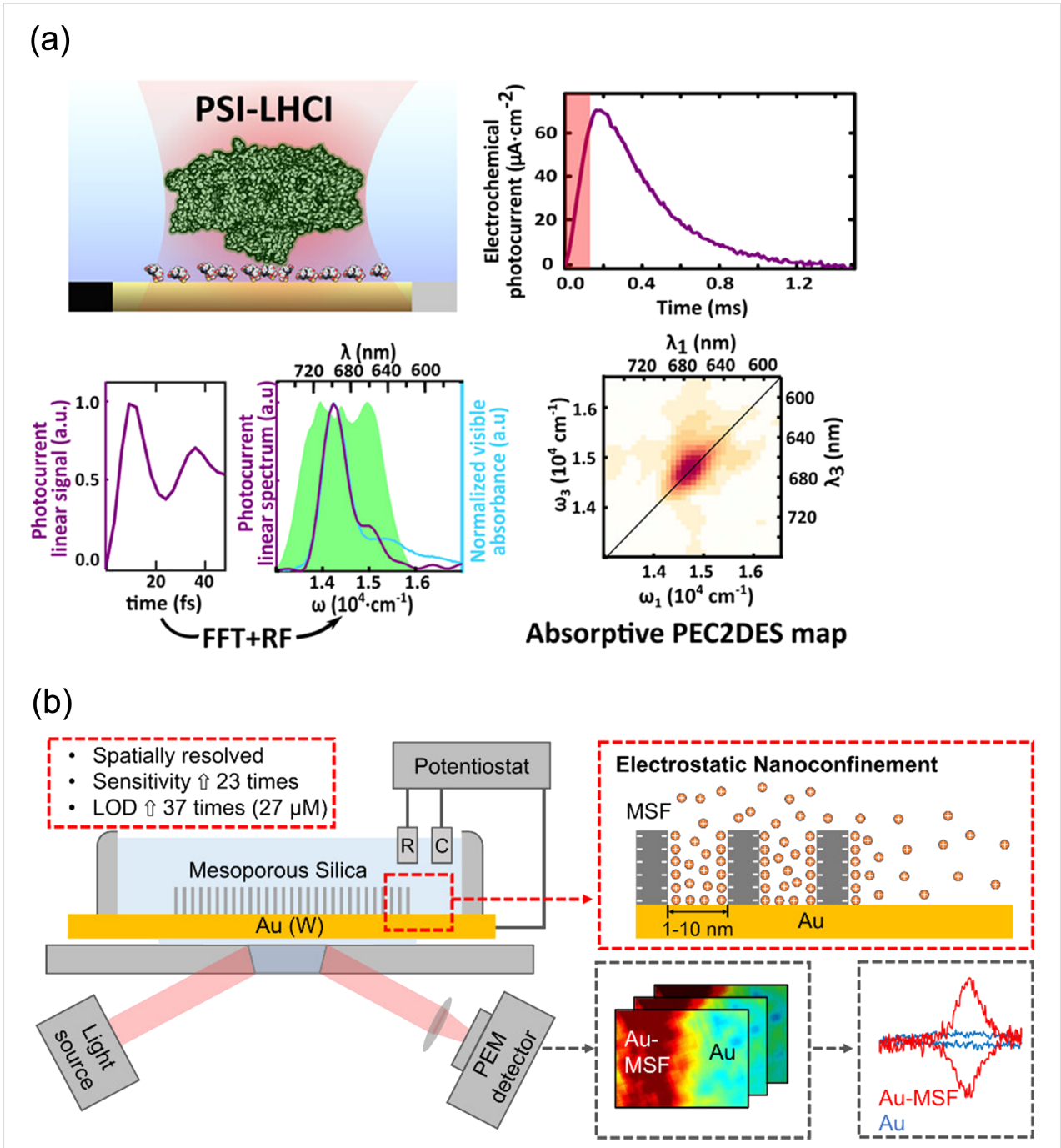


Figure 10: Representative multimodal measurement platforms integrating electrochemical control with optical measurements, together with representative outputs: (a) EC–2DES platform used for functional analysis of photosystem I. Figure 10a was reproduced from [139] (© 2024 M. López-Ortiz et al., published by American Chemical Society, distributed under the terms of the Creative Commons Attribution-NonCommercial-NoDerivatives 4.0 International License, https://creativecommons.org/licenses/by-nc-nd/4.0/). This content is not subject to CC BY 4.0. (b) MSF-modified PEM platform used for dopamine visualization. Figure 10b was reproduced from [140] (© 2025 S. Groysman et al., published by American Chemical Society, distributed under the terms of the Creative Commons Attribution-NonCommercial-NoDerivatives 4.0 International License, https://creativecommons.org/licenses/by-nc-nd/4.0/). This content is not subject to CC BY 4.0.

probes on a single sensor substrate, such as a quartz chip patterned with metallic nanostructures, and perform truly simultaneous in situ measurements in the same flow cell [142,143]. The greatest advantage of this method is that the hydration ratio of the adsorbed layer can be estimated from the difference between the "wet mass", including solvent, measured by QCM-D and the optically estimated "dry mass" or thickness obtained by SPR/LSPR, thereby providing important information on biolog-

ical interfaces that cannot be obtained by either technique alone [12,20,147].

Asai and co-workers constructed a LSPR–QCM-D sensor based on an anodic aluminum oxide nanohole array and evaluated the process from adsorption of giant liposomes (diameter about 220 nm) to local membrane deformation and disruption induced by exposure to the surfactant Triton X-100. Correlation analysis of resonance-frequency change, resonance resistance change, and LSPR resonance-wavelength shift revealed the interfacial response after liposome adsorption into a series of stepwise processes, that is, membrane deformation, swelling due to micelle interaction, membrane rupture accompanied by leakage of the internal solution, and finally lipid-bilayer formation [143]. Komorek and co-workers used analysis of the difference between the wet mass obtained by QCM-D and the dry mass obtained by SPR to show that the orientation of lysozyme adsorbed on a gold surface shifts from a side-on configuration to an end-on configuration as surface coverage increases. They also showed that the hydration ratio of this adsorbed layer changes with pH from about 70% at pH 4.0 to about 30% at pH 11.0 [20]. Yoon and co-workers further analyzed lysozyme adsorption in water–ethanol mixed solvents and showed that ethanol concentration non-monotonically affects densification of the adsorbed layer and the amount of hydration through changes in protein structural flexibility. In approximately 30% ethanol, pronounced densification of the adsorbed layer and dehydration were observed [147].

At the same time, significant technical limitations remain. Arrizabalaga and co-workers quantitatively demonstrated that in highly concentrated salt solutions, sensor signals are strongly governed by changes in the viscosity, density, and refractive index of the bulk liquid, making it difficult to separate these bulk effects from the true adsorption signal [146]. They also noted that as a basic limitation of the method, QCM-D essentially lacks an internal reference channel, so the reliability of the data becomes severely limited in systems where solution properties change substantially [146]. In addition, as noted in the analyses of several studies, choosing the wrong model, for example, between the Voigt and Sauerbrey models, and overlooking local heterogeneity because of macroscopic spatial averaging can also become general sources of error [12,144,146].

In SPR–QCM-D systems, comparison of the optical "dry" mass with the acoustic "wet" mass makes it possible to interpret their discrepancy not merely as an analytical limitation, but as a key source of information on hydration, viscoelasticity, molecular orientation, and interfacial heterogeneity [12,20,129,133]. However, extracting this information requires careful separation of true interfacial adsorption and restructuring from bulk-liquid effects, model-dependent QCM-D analysis, optical assumptions, and spatial averaging over heterogeneous interfaces [12,130,132]. Future platforms should therefore emphasize controlled solution conditions and coupled optical–acoustic modeling to quantitatively resolve hydration and viscoelastic contributions to interfacial processes.

4.2.2 SERS–QCM-D systems. SERS–QCM-D systems integrating QCM with SERS provide an analytical platform that acquires, in a complementary manner from the same interface, macroscopic changes in mass and viscoelasticity together with microscopic molecular vibrational spectra and chemical information [148-151]. The greatest strength of this approach lies in combining the quantitative adsorption-mass information from QCM with the molecular "chemical fingerprint" provided by SERS, thereby enabling simultaneous access to information that is in principle unattainable by either technique alone. Instrumentally, these systems can be divided into two principal configurations, namely, fully in situ simultaneous measurements, in which plasmonically active nanostructures are formed directly on the QCM electrode and measured under laser irradiation [148-150], and tandem measurements, in which the electrode is transferred to a Raman microscope after QCM measurements, often using SERS nanotags [151].

Lequeux and co-workers used a dual sensor patterned with a gold nanocylinder array to simultaneously evaluate the binding of DNA aptamers and the small-molecule antibiotic streptomycin by QCM-D and SERS. QCM-D quantified the dissociation constant (K_D = 23 nM) and binding stoichiometry, while SERS captured in situ local structural changes, with specific bases within the aptamer (adenine and guanine) showing Raman-band shifts and decreased intensity upon target recognition [150]. Bartolini and co-workers further used a sensor electrode coated with silver nanodendrites by electrodeposition to quantify FKBP12 binding by QCM with a limit of detection of 0.2 pM, while simultaneously detecting receptor conformational changes by SERS, such as reduced vibrational freedom of amide and aromatic-ring modes [148] (Figure 11a). Armero and co-workers captured prostate-specific antigen with an aptamer, quantified the mass by QCM-D, and then introduced three lectin-modified SERS nanotags to multiplex cancer-specific glycan patterns such as fucosylation and sialylation on a single platform [151]. Hou and co-workers used metal-organic frameworks-composite nanofibers to separate and simultaneously quantify chemically similar mixed gases (toluene and benzaldehyde), which cannot be discriminated by QCM alone, over the range of 0–100 ppm by integrating molecule-specific SERS peaks (777 and 820 cm^{-1}) with a mathematical algorithm [149].

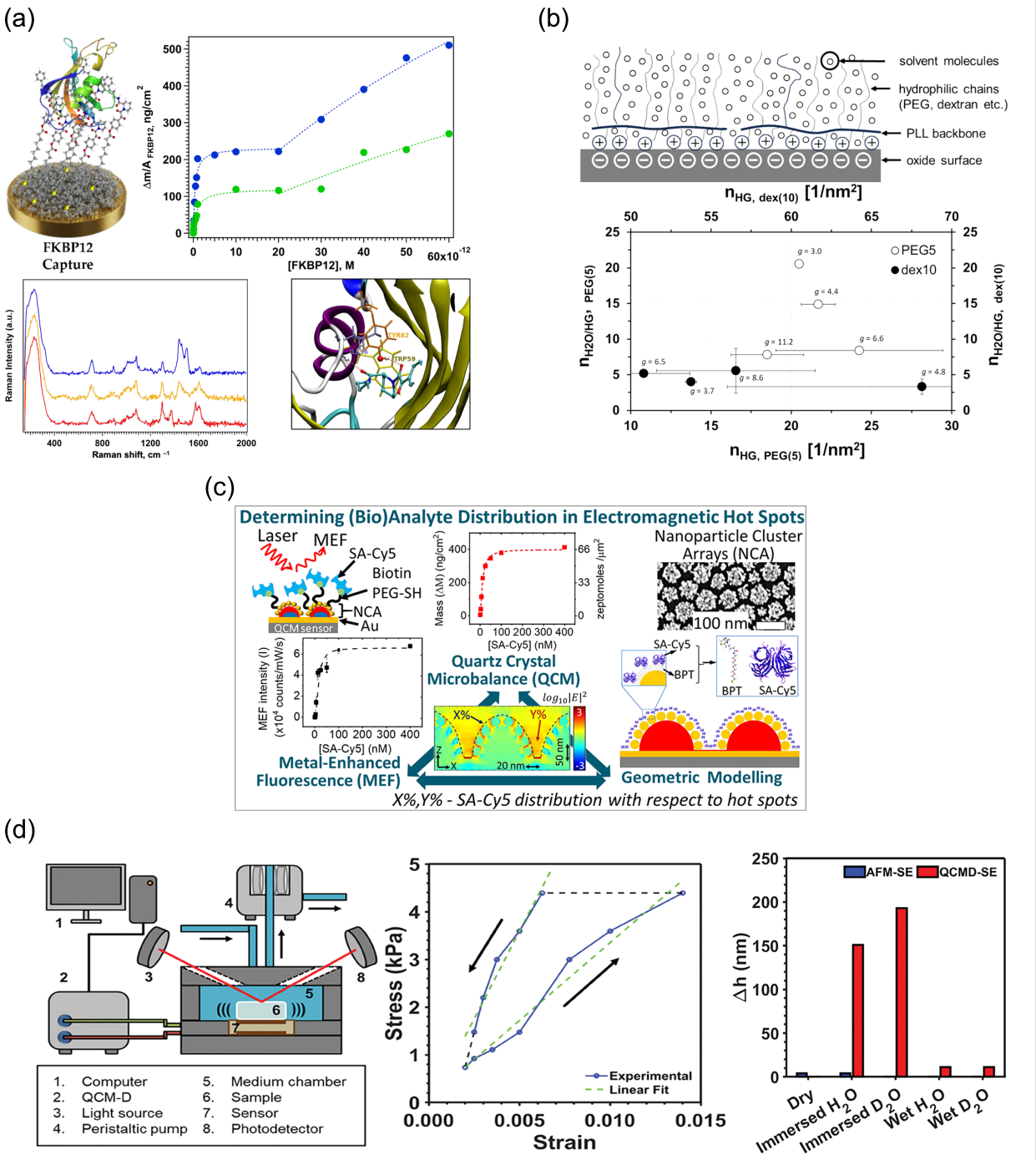


Figure 11: Representative multimodal solid–liquid interface measurement platforms that integrate optical probes with QCM measurements, together with representative outputs. (a) QCM–SERS platform used for FKBP12 detection. Figure 11a was adapted from [148] (© 2025 C. Bartolini et al., published by MDPI, distributed under the terms of the Creative Commons Attribution 4.0 International License, https://creativecommons.org/licenses/by/4.0/). (b) OWLS–QCM platform used for quantifying hydration of polymer brushes. Figure 11b was adapted from [152] (© 2024 C. Perrino et al., published by American Chemical Society, distributed under the terms of the Creative Commons Attribution 4.0 International License, https://creativecommons.org/licenses/by/4.0/). (c) MEF–QCM platform used for analysis of SA–Cy5 molecular distribution. Figure 11c was reproduced from [153] (© 2021 R. Rastogi et al., published by American Chemical Society, distributed under the terms of the Creative Commons Attribution-NonCommercial-NoDerivatives 4.0 International License, https://creativecommons.org/licenses/by-nc-nd/4.0/). This content is not subject to CC BY 4.0. (d) SE–QCM platform used for evaluating the physical properties of ultrathin hydrogels. Figure 11d was adapted from [154] (© 2024 J. Sans et al., published by Wiley-VCH GmbH, distributed under the terms of the Creative Commons Attribution 4.0 International License, https://creativecommons.org/licenses/by/4.0/).

At the same time, as pointed out in the background sections of these studies, SERS signals alone have serious limitations in quantitation [148,149]. The studies themselves note that nonuniform electromagnetic enhancement at hotspots and variation in molecular orientation constrain quantitative interpretation of SERS signals. Each work addressed this limitation in a different way. Hou and co-workers corrected signal fluctuations using a differential algorithm based on normalized intensities and then combined the results with total mass data from QCM [149], whereas Bartolini and co-workers ensured quantitation using a ratiometric internal standard approach (I_{1571}/I_{1438}) [148]. In complex environments, nonspecific adsorption (fouling) can also interfere directly with SERS signals, and, as shown by Armero and co-workers, robust aptamer immobilization strategies such as biotin–streptavidin coupling are indispensable [151].

These limitations indicate that the main value of SERS–QCM-D systems lies in assigning QCM-D-derived adsorption and viscoelastic changes to specific molecular fingerprints, rather than treating them as nonspecific interfacial responses. However, this requires not only quantitative correction of SERS signals, but also careful chemical interpretation of the mass and viscoelastic changes measured by QCM-D. Because QCM-D responses alone cannot identify which molecular species, binding events, or structural rearrangements are responsible for adsorption and mechanical changes, future SERS–QCM-D platforms should emphasize mass-normalized and time-correlated SERS analysis to improve the chemical assignment of QCM-D responses.

4.2.3 Other optical–QCM-D systems. In addition to plasmonic methods typified by SPR and SERS, a variety of optical measurements integrated with QCM have been proposed, including ellipsometry, waveguide-mode spectroscopy, and fluorescence enhancement. These methods combine optical and mass responses to obtain interfacial information. In this section, representative examples such as spectroscopic ellipsometry (SE)–QCM, optical waveguide lightmode spectroscopy (OWLS)–QCM, and metal-enhanced fluorescence (MEF)–QCM are briefly reviewed [152-154].

Perrino and co-workers operated QCM-D and OWLS as parallel but non-coincident measurements on equivalent substrates to compare the adsorption behavior of poly(L-lysine)-*graft*-poly(ethylene glycol) (PLL-*g*-PEG) and poly(L-lysine)-*graft*-dextran (PLL-*g*-dex) on oxide surfaces. By quantifying the hydration amount per unit area (Ψ) from the difference between the dry mass obtained by OWLS and the wet mass obtained by QCM-D, they found that Ψ increased with increasing grafting density for both systems; the increase was much larger for PEG, reflecting the greater structural rigidity of dextran. The authors further showed that PEG contains two to three strongly bound water molecules per ethylene glycol unit, forming cage-like structures that contribute to PEG's excellent antifouling and lubricating properties [152] (Figure 11b).

Rastogi and co-workers used a diblock copolymer template to self-assemble and pattern a gold nanoparticle cluster array on a QCM electrode and then carried out fully in situ simultaneous measurements of QCM and MEF through a microfluidic cell with a sapphire window. By correlating the surface mass density of fluorescently labeled streptavidin (SA-Cy5) obtained by QCM with the enhanced fluorescence intensity from MEF and combining the result with geometric modeling, they quantitatively demonstrated that about 83% of the SA-Cy5 were distributed in the matrix regions between the clusters, where they benefited from electromagnetic enhancement. They also showed that MEF could detect an extremely small amount of SA-Cy5, about 2 zmol, even though the measurement spot was less than one hundred-millionth of the QCM sensing area [153] (Figure 11c).

Sans and co-workers studied ultrathin hydrogel films prepared by plasma polymerization and performed fully simultaneous measurements of QCM-D and SE in a dedicated combined cell. From the difference in thickness measured by the two methods, they successfully separated water hydrated within the film from water trapped at the interface. By deforming the gel with the dynamic pressure of a peristaltic pump and combining the viscoelastic parameters obtained from QCM-D with the SE response and fluid-dynamics simulations, they obtained stress–strain curves for nanoscale thin films and calculated the Young's modulus and Poisson's ratio (about 0.43). The method was further applied to fatigue testing, temperature changes, and exposure to different solvents, and was established as a comprehensive characterization protocol for ultrathin hydrogels [154] (Figure 11d).

The examples reviewed in this section highlight that the role of optical integration with QCM-based measurements is not simply to add a second readout, but to clarify the physical origin of mass and viscoelastic responses at hydrated and mechanically complex interfaces. QCM-based measurements are highly sensitive to coupled mass and mechanical changes, whereas optical readouts provide complementary information on dry mass, optical thickness, fluorescence distribution, molecular fingerprints, and spatial organization. By comparing these responses, optical–acoustic platforms can help distinguish adsorption, hydration, conformational rearrangement, lateral heterogeneity, and changes in film mechanics. Future platforms should therefore place greater emphasis on controlled mea-

surement geometries, appropriate calibration, and coupled optical–acoustic analysis so that multimodal responses can be translated into physically meaningful information on interfacial hydration, organization, and nanoscale mechanics.

4.3 Integration of optical methods with SPM

4.3.1 TERS–SPM systems. TERS–SPM systems link local morphological information with molecular vibrational information on the same interface, enabling nanoscale analysis of molecular chemical state, local composition, orientation, and adsorption mode [108,155-160]. Their major advantage is that they can directly visualize interfacial structures and phase-separation behavior in microscopic regions that are difficult to capture with conventional spatially averaged spectroscopy. In recent years, their application has expanded to diverse systems, including electrode interfaces [155,156] and biological membranes [158,159].

As a specific example, Mrđenović and co-workers analyzed the membrane of human pancreatic cancer cells by bottom-illumination TERS–AFM. By combining a silver-coated probe, PeakForce tapping mode, and an extremely low-power laser (160–220 μW), they minimized damage to the biological sample and visualized chemically heterogeneous structures on the membrane surface without labeling and with a spatial resolution of about 2.5 nm. As a result, they revealed spatial separation of nanodomains rich in phenylalanine, histidine, and phosphatidylcholine, as well as colocalization of cholesterol and proteins [158]. Fiocco and co-workers further applied top-illumination TERS–EC-STM to the reduction process of a (4-nitrobenzyl)mercaptan (4-NBM) monolayer in alkaline aqueous solution. By combining a partially insulated gold tip, an extremely low-power laser, and bipotentiostat control, and synchronizing a potential sweep of 50 $mV \cdot s^{-1}$ with rapid acquisition of Raman spectra every 0.6–1.0 s, they tracked in real time the decrease in the nitro-group band intensity and the appearance of the azo-bond band at 1452 cm^{-1}, thereby demonstrating the dimerization reaction pathway [156].

In practice, however, the key challenge for TERS–SPM measurements in liquid or under operando conditions is how to avoid physical perturbation by tip contact and the occurrence of side reactions caused by laser irradiation [156,157]. Accordingly, each study adopted concrete measurement strategies suited to the target system. For example, in the cell-membrane analysis mentioned above, ex situ analysis after chemical fixation and drying was chosen in order to preserve the interfacial state by avoiding physical perturbation from the probe, with priority given to achieving the highest spatial resolution [158]. In this case, the strategy is better described as correlative sequential analysis on identical substrates rather than strictly simultaneous multimodal acquisition. Its validity depends on preserving the interfacial state through chemical fixation and on ensuring that the spectroscopic and microscopic measurements probe the same substrate region under reproducible conditions. In electrochemical operando measurements, photoinduced reactions can overlap with the intrinsic electrochemical process, but in the 4-NBM monolayer system this was suppressed successfully by combining an extremely low-power laser (about 160 μW) with constant raster scanning of the tip, allowing for reliable dynamic measurements [156].

The main value of TERS–SPM systems lies in correlating nanoscale morphology with local molecular vibrational fingerprints at the same interface, enabling analysis of chemical states, molecular orientation, adsorption modes, and nanodomain heterogeneity beyond spatially averaged spectroscopy. However, the measurement process itself can perturb the interfacial state through tip-induced disturbance, laser-induced damage or side reactions, instability under liquid or operando conditions, and structural changes during ex-situ fixation or drying. Future platforms should therefore emphasize low-power laser operation, controlled tip–sample interaction, suitable measurement protocols, and rigorous spatial registration between microscopic and spectroscopic information.

4.3.2 SPR–AFM systems. SPR–AFM systems combine the local topographical and force information of AFM with the effective film thickness and molecular binding kinetics of adsorbed layers obtained from plasmon resonance, thereby targeting interfacial phenomena in which macroscopic binding behavior and microscopic structural changes are intertwined [161-165].

Mei and co-workers combined LSPR with AFM in liquid to analyze the interaction of amyloid-β (Aβ) with artificial lipid membranes designed to mimic different stages of Alzheimer's disease progression, as well as the protective effect of melatonin. LSPR quantified that the Aβ adsorption layer was thickest in the early disease model and that addition of 400 μM melatonin reduced the adsorption amount by about 40%, while AFM imaging in liquid visually confirmed that this macroscopic adsorption behavior originated from physical defects in the lipid membrane (pore formation) and growth of Aβ clusters [164] (Figure 12). Komorek and co-workers also evaluated BSA adsorption on gold surfaces by multiparametric SPR and AFM, and visualized pH-dependent changes in BSA molecular shape, such as elongated forms at pH 4.0 and triangular forms at pH 6.0, using contact-mode AFM with a tip radius of 20 nm. By integrating these microscopic shape data with the macroscopic molecular orientations, such as flat-on configurations, calculated from the adsorption mass measured by multiparametric

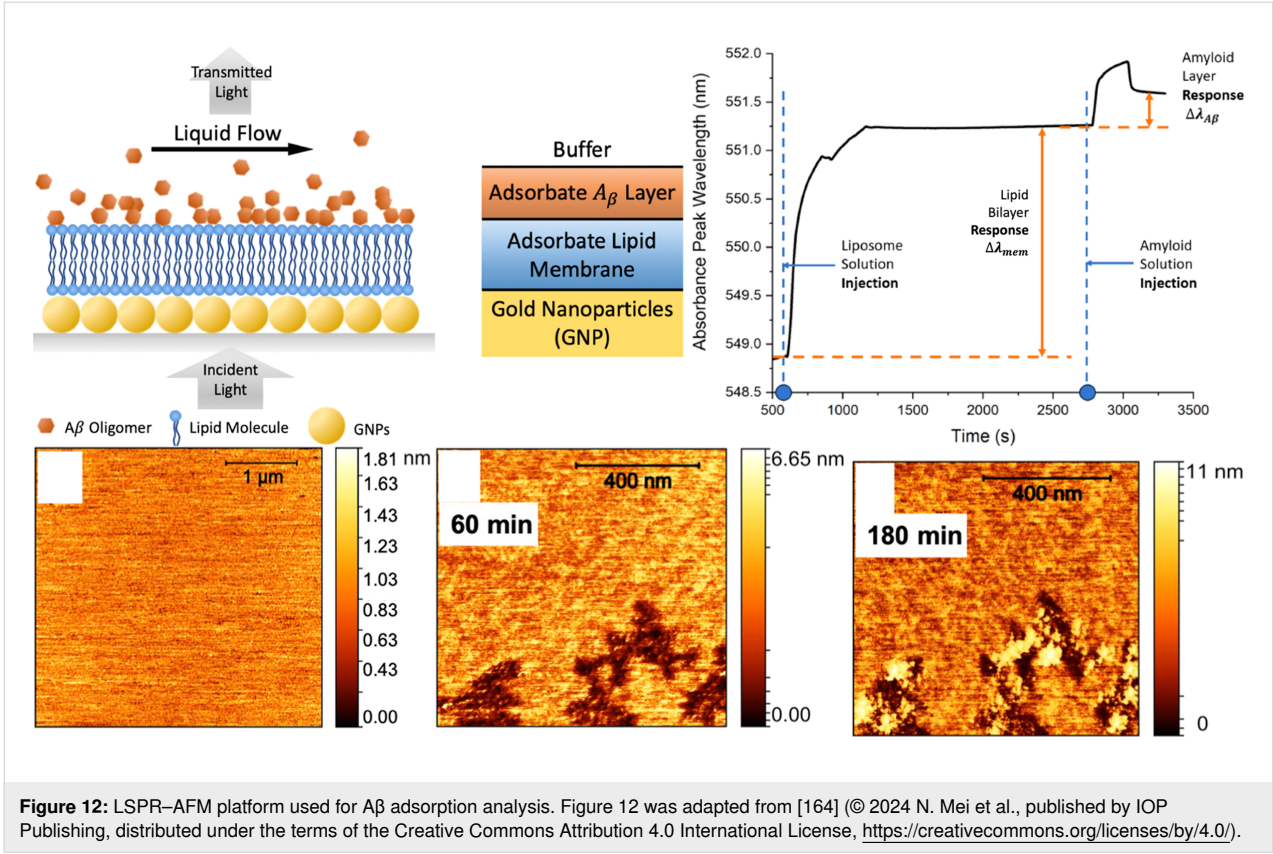


Figure 12: LSPR–AFM platform used for Aβ adsorption analysis. Figure 12 was adapted from [164] (© 2024 N. Mei et al., published by IOP Publishing, distributed under the terms of the Creative Commons Attribution 4.0 International License, https://creativecommons.org/licenses/by/4.0/).

SPR together with a random sequential adsorption model, they demonstrated from both perspectives the structural changes of BSA upon adsorption [161].

However, integrating these macroscopic optical responses with microscopic morphological observations requires careful attention to differences in spatial scale and to constraints associated with moving between measurement environments [164,165]. For example, in systems involving heterogeneous protein aggregates such as Aβ, the LSPR signal reflects the average refractive-index change over the entire sensor surface, forcing model-dependent interpretation as a spatially averaged "uniform effective film thickness". For soft biological samples such as extracellular vesicles, it is often difficult to perform fully synchronized and stable measurements in liquid. In such cases, SPR imaging (SPRi) is conducted first, after which the sample is chemically fixed and transferred for AFM observation in air [165]. During this process, however, dehydration and deformation caused by the physical pressure of the probe are unavoidable.

SPR–AFM systems are particularly useful for testing whether averaged plasmonic responses arise from specific nanoscale morphological changes at the interface. In heterogeneous biological layers, changes in effective film thickness, refractive index, adsorption mass, or binding kinetics measured by SPR/LSPR/SPRi may originate from localized defects, aggregates, molecular-shape changes, or surface deformation that cannot be resolved by the optical response alone. A key requirement for future SPR–AFM platforms is therefore to preserve the native hydrated interface while matching optical and AFM observations as closely as possible in space and time, thereby reducing model-dependent interpretation and artifacts from fixation, drying, air exposure, or tip-induced deformation.

4.3.3 Local chemical-state and morphological analysis using IR and AFM. IR–AFM multimodal measurements complement the local topographic and nanomechanical information from AFM with molecular vibrational spectra obtained by IR spectroscopy based on photothermal expansion or near-field optical scattering [166-168]. Their major advantage is that they overcome the diffraction limit of conventional bulk IR spectroscopy and allow for direct label-free identification of the chemical state and secondary structure of single protein aggregates and cell-membrane domains on the nanoscale.

Wang and co-workers developed liquid-phase peak force infrared microscopy (LiPFIR), which integrates total internal reflection (TIR) illumination with PeakForce tapping mode. By synchronizing irradiation of a wavelength-tunable pulsed laser

from below through a germanium prism only to the instant when the probe briefly contacts the sample, they eliminated lateral shear forces. This control enabled imaging with about 10 nm spatial resolution while avoiding physical damage to extremely soft biological samples such as swollen yeast cell walls and BSA fibrils; the authors also succeeded in mapping in situ the extent and local distribution of the copper-catalyzed azide–alkyne cycloaddition, a prototypical click reaction, on polymer surfaces in aqueous solution [167].

In practice, however, liquid-phase infrared measurements face major challenges in signal-to-noise ratio because of strong infrared absorption by water and the lowered Q-factor of the cantilever caused by fluid resistance [166,167]. Accordingly, each study has adopted concrete strategies suited to the target system to reduce these effects. For example, a method has been demonstrated in which live cells are measured through an ultrathin SiC/SiN membrane to physically exclude the influence of water, although local membrane-deformation artifacts caused by indentation of the probe still remain [168]. The TIR illumination mentioned above is also an effective strategy because it confines the influence of water to the near-field region, although it is subject to the physical constraint of the evanescent-field penetration depth [167]. Furthermore, in protein systems such as peptide aggregates, the solvent has been replaced with D_2O so that the key amide-I band can be separated from the water absorption band and secondary structure can be identified [166].

The main value of IR–AFM multimodal measurements lies in correlating nanoscale topographic and nanomechanical information with local vibrational spectra, chemical states, and protein secondary structures. However, in liquid-phase measurements, optical absorption by water, cantilever damping, probe-induced deformation, and deviations from native conditions can compromise sensitivity or perturb the interfacial state. Across these optical–SPM systems, correlating local optical or spectroscopic information with nanoscale morphological and mechanical information requires not only spatial registration, but also careful consideration of how the measurement process itself affects the interfacial state. Future platforms should therefore be designed to acquire local chemical, structural, and mechanical information under native or operando conditions while preserving the native interfacial state as much as possible.

4.4 Other integrated multimodal measurements: AFM–QCM-D systems

Although measurement architectures integrating AFM and QCM do not fall directly into the three major integrated categories discussed in Sections 4.1–4.3, they provide an example of other multimodal measurements in which adsorption mass and viscoelasticity at a solid–liquid interface obtained by QCM are linked with surface topography and coverage obtained by AFM, thereby enabling analysis of the relationship between interfacial coverage and wetting or fluid response [169]. In particular, they are used to analyze how polymer-adsorption dynamics at the molecular level affect drainage and rupture of hydrated thin films during bubble approach and the dynamic formation of a three-phase contact line.

This complementarity was demonstrated concretely in the study by Pawliszak and co-workers. They evaluated adsorption of guar gum (GG) on hydrophobic graphite by QCM-D and AFM and showed that GG forms a concentration-dependent interconnected network with nanometer-scale thickness, changing the surface coverage from 7% to about 60%. By combining these measurements with single-bubble collision experiments recorded using a high-speed camera, nanoscale surface states were directly correlated with macroscopic fluid behavior. They found that even incomplete surface coverage altered the hydrodynamic boundary condition at the solid–liquid interface from slip to partial-slip or no-slip. This change prolonged the thin-film drainage time by up to an order of magnitude, modified the bounce amplitude, and markedly reduced the receding contact angle. At concentrations of 25 $mg \cdot L^{-1}$ or higher, bubble attachment was completely suppressed [169] (Figure 13).

At the same time, this method has its own technical constraints. A spatial-averaging gap can arise between the local nanoscale structures observed by AFM (1–2 μm) and the macroscopic wettability sensed by actual bubbles (diameter 400–1000 μm). In addition, estimation of adsorption mass and film thickness may depend on the assumptions of the Voigt viscoelastic model. Differences in conditions between static environments (AFM and bubble experiments) and continuous-flow environments (QCM-D) can also lead to mismatches in adsorption amount and arrival time, and these factors remain important considerations in quantitative interpretation [169].

To address the multidimensional nature of solid–liquid interfaces, researchers have strategically combined different transduction principles to bridge the gaps in observable physical quantities. A comprehensive summary of representative multimodal characterization studies discussed throughout this section is provided in Table 2. This table highlights how the integration of disparate techniques, such as the coupling of mechanical, electrochemical, and optical probes, enables the simultaneous or sequential quantification of mass, charge, and molecular conformation. These synergetic approaches provide a far more holistic view of interfacial molecular states than any single-mode measurement, as evidenced by the specific research examples listed.

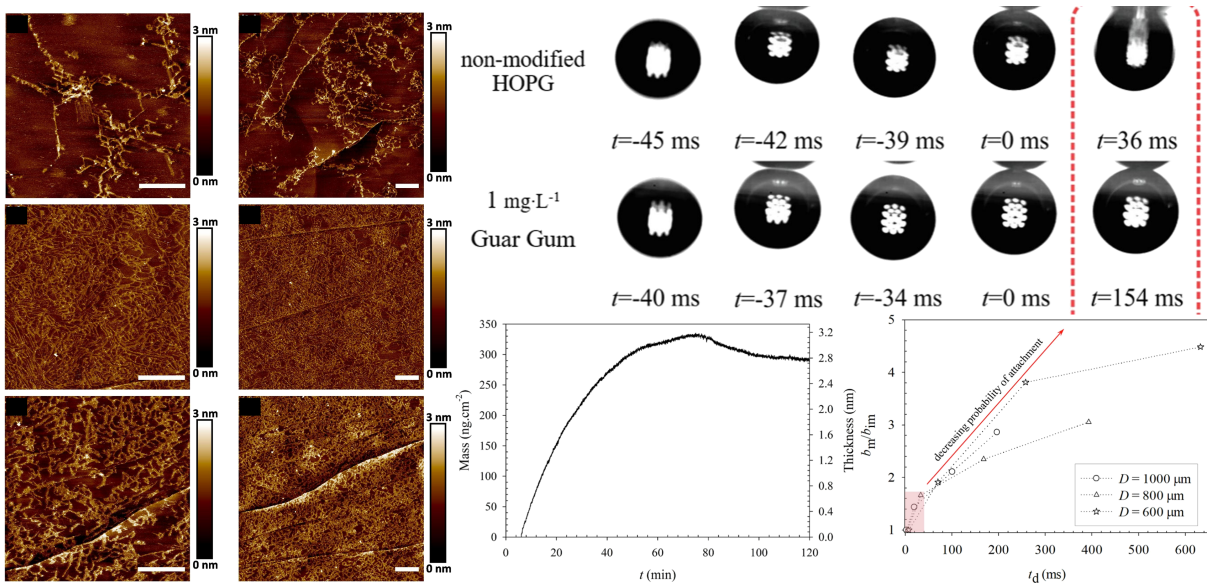


Figure 13: AFM–QCM-D platform used for evaluation of polymer adsorption. Figure 13 was adapted from [169] (© 2024 P. Pawliszak et al., published by Elsevier, distributed under the terms of the Creative Commons Attribution 4.0 International License, https://creativecommons.org/licenses/by/4.0/).

Table 2: Representative multimodal measurement platforms at solid–liquid interfaces, together with their target physical quantities, target interfacial phenomena, spatial scales, and temporal scales.

Technique	Target physical quantities	Target interfacial phenomena	Spatial scale	Temporal scale	Ref
SPR–EC	local mass, charge	interfacial dynamics associated with adsorption, reaction, recognition, and secretion	interface: angstroms to nanometers; probing depth: tens to hundreds of nanometers; observation area: square micrometers to square millimeters, ensemble-averaged	milliseconds to seconds	[117-124]
SERS–EC	charge, molecular vibrations, orientation	intermediate transformation, molecular reorientation, phase transition, and hydration change	interface: angstroms to nanometers; observation area: square micrometers, ensemble-averaged	seconds to minutes	[21,22,125-127]
IR–EC	molecular vibrations, orientation, intermolecular interactions	hydration structure changes, biomembrane structural change (drug interaction)	interface: angstroms to nanometers; observation area: square millimeters to square centimeters, ensemble-averaged	seconds to minutes	[128-130]
VSFG–EC	local electric field/surface charge, molecular vibrations, orientation	intermediate dynamics, local electric-field response, and monolayer change	interface: angstroms to a few nanometers; observation area: square micrometers, ensemble-averaged	seconds to minutes	[131-134]
EC–time-resolved spectroscopy (ultrafast optical trigger)	photocurrent, molecular vibrations, nonlinear polarization	exciton energy transfer, charge transfer/separation, and structural relaxation	interface: angstroms to nanometers; observation area: square micrometers to square millimeters, ensemble-averaged	femtoseconds to milliseconds (partly seconds)	[135,137,139]
EC–time-resolved spectroscopy (operando potential trigger)	molecular vibrations, local electric field, faradaic charge	molecular structural changes, intermediate transformation, and electrografting	interface: angstroms to nanometers; observation area: square micrometers to square millimeters, ensemble-averaged	sub-second to tens of seconds	[136,138]

Table 2: Representative multimodal measurement platforms at solid–liquid interfaces, together with their target physical quantities, target interfacial phenomena, spatial scales, and temporal scales. (continued)

PEM	local charge/current, concentration	ion enrichment, molecular adsorption/desorption, release dynamics, and thin-film formation	pores/electrical double layer: 1–10 nm; single particles: tens to hundreds of nanometers; observation area: tens to hundreds of micrometers	milliseconds to seconds	[140]
SPR–QCM	mass (dry/wet), film thickness, viscoelasticity	specific/non-specific molecular adsorption and structural change	observation area: square millimeters to square centimeters, ensemble-averaged; probing depth: tens to hundreds of nanometers	a few seconds to tens of seconds	[12,20,141-147]
SERS–QCM	mass, molecular vibrations, viscoelasticity	specific molecular adsorption and structural change	observation area: square micrometers (local) to square centimeters (ensemble-averaged); probing depth: tens to hundreds of nanometers	a few seconds to tens of seconds	[148-151]
OWLS–QCM	mass (dry/wet), surface grafting density	hydration and conformational change of surface-bound polymers	observation area: square millimeters to square centimeters, ensemble-averaged; probing depth: hundreds of nanometers	several minutes	[152]
MEF–QCM	mass (surface concentration), adsorption sites (spatial distribution)	specific molecular adsorption	observation area: 1.5 μm^2 (local) to 1.4 cm^2 (ensemble-averaged); probing depth: tens to hundreds of nanometers	a few seconds to tens of seconds	[153]
SE–QCM	mass, optical film thickness (swelling ratio), viscoelasticity (Poisson's ratio)	hydration, swelling, and mechanical response of ultrathin hydrogels	observation area: square millimeters to square centimeters, ensemble-averaged; probing depth: hundreds of nanometers (limit: 1 μm)	seconds to minutes	[154]
TERS–SPM	local morphology, mechanical response, molecular vibrations	nanoscale structural heterogeneity of molecular layers	lateral resolution: a few to tens of nanometers; probing depth: a few to 20 nanometers; mapping area: square micrometer scale	point: a few seconds; line: tens of seconds; map: ≤10 min	[108,155-160]
SPR–AFM	mass, local morphology, mechanical response	dynamics of interfacial molecular adsorption and morphological transformation	lateral resolution: ≤10 nm; probing depth: 20–250 nm; mapping area: square micrometer scale	SPR: real-time; map: measurement-time-dependent	[161-165]
IR–AFM	local morphology, mechanical response, molecular vibrations	dynamics of local interfacial chemistry and structural transformation	lateral resolution: ≤20 nm; probing depth: a few nanometers to several micrometers (measurement-principle-dependent); mapping area: square micrometer scale	point: several to tens of minutes; map: measurement-condition-dependent	[166-168]
AFM–QCM	mass/viscoelasticity, local structure	adsorption coverage and bubble collision/attachment response	lateral resolution: ≤2 nm; probing depth: 1–3 nm; observation area: square micrometer scale	milliseconds to seconds	[169]

5 Future perspectives

As discussed in Section 4, multimodal approaches that combine optics with electrochemistry, quartz crystal microbalance measurements, or scanning probe microscopy have provided a common framework for understanding solid–liquid interfaces through correlations among multiple physical quantities. Despite these important advances, current measurement technologies still face three fundamental limitations. In the

following, we discuss each of these limitations and outline possible strategies to overcome them.

5.1 Toward higher-order multimodal integration of interfacial state variables

Most current multimodal measurements are still limited to the integration of only two classes of physical quantities. This "two-quantity integration" has greatly deepened our understanding, but the reality of solid–liquid interfaces is more complex. Physical quantities such as charge, hydration, molecular orientation, and viscoelasticity do not change independently; they are modulated simultaneously as interlinked and non-separable state variables. For example, during protein adsorption at a solid–liquid interface, the increase in adsorbed mass (acoustic response), reorganization of the hydration layer (observed as the difference from the optical response), conformational change (vibrational spectroscopy), and change in viscoelasticity of the adsorbed layer (QCM dissipation) proceed simultaneously. At present, however, there is no technique that can extract all four quantities completely simultaneously and independently from the same probe volume.

A first direction for solving this problem is full integration of SERS, QCM-D, and electrochemistry on a single sensor chip. In recent years, integrated sensors have begun to be developed in which plasmonic nanostructures are formed directly on QCM chips, allowing for seamless realization of mass/viscoelastic measurements and Raman scattering on the same chip [148-150]. If this development is extended to a triple multimodal measurement that acquires vibrational spectroscopy, mechanical response, and electrochemical response simultaneously, it will, for the first time, become possible to capture on the same spatiotemporal scale the correlation among changes in the chemical state of adsorbed molecules, charge rearrangement at the interface, and the viscoelastic changes of the membrane induced by them. A second direction is the development of multiphysical probes that integrate TERS with electrochemical current measurements [156]. By acquiring nanoscale chemical state, mechanical response, and charge transfer in the same local space, this approach could answer simultaneously the three questions of where, what, and how things change. As a third direction, mathematical approaches that probabilistically separate independent components from averaged responses in which multiple physical quantities are superposed, by combining statistical deconvolution with machine learning, are also promising. However, since soft-modeling approaches such as multivariate curve resolution inherently suffer from rotational and intensity ambiguities, mathematical decomposition alone cannot uniquely recover true independent components. Therefore, introducing strict physical constraints or integrating independent measurements is indispensable to appropriately bound the solution. If realized, under these rigorous conditions, these approaches would provide the first true experimental breakthrough against the fundamental difficulty of the "non-separability" of state variables at solid–liquid interfaces.

5.2 Bridging multimodal experiments and theoretical models

The data obtained from multimodal measurements are large and multidimensional, and their interpretation requires close coupling not only with experimental analysis but also with computational chemistry. At present, DFT calculations and MD simulations mainly play supporting roles, such as assigning vibrational bands and estimating interfacial electric fields [128,129,133,134,157]. However, a fundamental gap still remains between experiment and computation. This gap is not merely numerical. For example, QCM-D measures "wet mass", which includes hydration water, whereas SPR reflects "dry mass", corresponding mainly to the molecular framework. More broadly, experiments probe open, fluctuating systems and yield ensemble-averaged responses, whereas most computational models rely on closed systems with periodic boundary conditions and often describe molecular-scale trajectories under idealized conditions.

5.3 Application-oriented design principles for biointerfaces, organic devices, and soft materials

If the technical advances outlined above are realized, multimodal solid–liquid interface characterization will provide new design principles for biointerfaces, delivery systems, soft materials, and organic devices. In biosensing and liquid biopsy, treating the adsorption of proteins and extracellular vesicles (EVs) as multidimensional interfacial information, including molecular orientation, hydration, viscoelasticity, and binding mass, will provide a basis for next-generation sensor platforms capable of discriminating molecular structure, functional state, and aggregation state beyond the capability of conventional mass-detection-based sensors. Early examples can already be seen in SPR–QCM-D measurements targeting tetraspanins (CD9, CD63, and CD81) in EVs derived from lung cancer cells [145] and in LSPR–AFM measurements that elucidated the membrane-disruption mechanism of amyloid-β [164]. If absolute concentrations can be quantified under complex reaction conditions and short-lived intermediates can be tracked, such approaches could substantially improve the sensitivity and specificity of biomarker detection and support the development of point-of-care diagnostics.

In drug delivery, membrane science, and biomaterials, multimodal platforms capable of quantitatively tracking liposome and lipid nanoparticle fusion with cell membranes, together with cargo-release dynamics, through correlated mass, optical,

and electrochemical signals will directly support the rational design of delivery carriers. Likewise, quantifying the relationships among surface hydration, viscoelasticity, and nonspecific protein adsorption will accelerate the development of biocompatible materials and antifouling coatings through the rational design of hydration networks. Beyond these biorelated systems, similar multimodal strategies may also transform the analysis of organic thin-film devices, including organic field-effect transistors and organic electroluminescent devices, by revealing how potential-dependent conformational changes in organic molecular layers are coupled to charge-transport properties. Solid–liquid interface science is thus evolving from the study of local boundary phenomena into an integrated discipline that provides molecular-level design principles for biointerfaces, soft materials, and organic devices.

Conclusion

Multimodal characterization has fundamentally shifted the description of solid–liquid interfaces from a uniform, averaged picture toward one based on locally heterogeneous and dynamically correlated structures. By revealing that interfacial phenomena are inherently coupled, multistep processes, these integrated methods have proven essential for capturing the complex realities of interfacial systems. However, moving forward, the true impact of this field will depend on addressing several unresolved challenges. First, the relevant interfacial state variables are physically coupled and not easily separable, making it difficult to infer causal relationships among charge, structure, and hydration from experimental data alone. Second, nanoscale spatial resolution and ultrafast temporal resolution remain difficult to achieve simultaneously, and no current method can fully reveal both where interfacial reactions occur and how they evolve in real time. Third, quantitative integration between experiment and theory is still limited by fundamental differences in physical definitions and boundary conditions, including the distinction between the hydration-inclusive wet mass measured by QCM-D and the dry mass detected by SPR, as well as the mismatch between open experimental systems and closed computational models.

To address these challenges, three future directions appear particularly important. The first is the realization of true simultaneous acquisition of multiple physical quantities through deeper multimodal integration, for example by combining SERS, QCM-D, and EC on a single platform or by developing multiphysical TERS probes. The second is to overcome the current trade-off in spatiotemporal resolution through pulse-laser-synchronized TERS and super-resolution tracking approaches. The third is to establish a framework for quantitative integration of experiment and theory through inverse modeling combined with molecular dynamics simulations and deep learning. Progress along these directions should accelerate the emergence of a new measurement paradigm capable of linking temporal and spatial scales while simultaneously capturing multiple interfacial observables in real time.

We hope that the conceptual framework and design principles summarized in this review will support further advances in molecular science at solid–liquid interfaces and contribute to the rational design of biosensing platforms, delivery systems, biocompatible materials, and organic devices.

Funding

This work was supported by the Japan Society for the Promotion of Science (JSPS) KAKENHI Grant Number JP23H03864.

Declaration of Generative AI and AI-Assisted Technologies

AI-based tools (ChatGPT, OpenAI; Gemini, Google) were used for language editing and for suggestions on manuscript organization. The authors reviewed and validated all content and took full responsibility for the manuscript. No AI tools were used for data generation, analysis, or image creation/editing.

Author Contributions

Shiou Yamada: data curation; resources; validation; writing – original draft; writing – review & editing. Hinata Urano: data curation; resources; validation; visualization; writing – original draft; writing – review & editing. Koji Toma: conceptualization; funding acquisition; project administration; writing – original draft; writing – review & editing.

ORCID® iDs

Koji Toma - https://orcid.org/0000-0002-1683-1496

Data Availability Statement

Data sharing is not applicable as no new data was generated or analyzed in this work.

References

1. Yamakata, A.; Osawa, M. *J. Phys. Chem. C* **2008,** *112,* 11427–11432. doi:10.1021/jp8018149
2. Greco, A.; Imoto, S.; Backus, E. H. G.; Nagata, Y.; Hunger, J.; Bonn, M. *Science* **2025,** *388,* 405–410. doi:10.1126/science.adu5781
3. Yamakata, A.; Soeta, E.; Ishiyama, T.; Osawa, M.; Morita, A. *J. Am. Chem. Soc.* **2013,** *135,* 15033–15039. doi:10.1021/ja408326d
4. Maitra, A.; Pennathur, A. K.; Chiang, P.-H.; Dawlaty, J. M. *ACS Appl. Energy Mater.* **2024,** *7,* 5528–5536. doi:10.1021/acsaem.4c01012
5. Wertz, C. F.; Santore, M. M. *Langmuir* **2002,** *18,* 706–715. doi:10.1021/la011075z
6. Wertz, C. F.; Santore, M. M. *Langmuir* **2001,** *17,* 3006–3016. doi:10.1021/la0017781

7. Son, Y. J.; Han, J. W.; Kang, H.; Seong, S.; Han, S.; Maeda, S.; Chikami, S.; Hayashi, T.; Hara, M.; Noh, J. *Int. J. Mol. Sci.* **2023,** *24,* 3241. doi:10.3390/ijms24043241
8. Reimhult, E.; Larsson, C.; Kasemo, B.; Höök, F. *Anal. Chem. (Washington, DC, U. S.)* **2004,** *76,* 7211–7220. doi:10.1021/ac0492970
9. Chang, A. L.; McKeague, M.; Liang, J. C.; Smolke, C. D. *Anal. Chem. (Washington, DC, U. S.)* **2014,** *86,* 3273–3278. doi:10.1021/ac5001527
10. Butt, M. A. *Biosensors* **2025,** *15,* 35. doi:10.3390/bios15010035
11. Bonet, N. F.; Cava, D. G.; Vélez, M. *Front. Mol. Biosci.* **2022,** *9,* 935376. doi:10.3389/fmolb.2022.935376
12. Komorek, P.; Martin, E.; Jachimska, B. *Int. J. Mol. Sci.* **2021,** *22,* 1322. doi:10.3390/ijms22031322
13. Glassford, S. E.; Byrne, B.; Kazarian, S. G. *Biochim. Biophys. Acta, Proteins Proteomics* **2013,** *1834,* 2849–2858. doi:10.1016/j.bbapap.2013.07.015
14. Guo, W.; Lu, T.; Crisci, R.; Nagao, S.; Wei, T.; Chen, Z. *Chem. Sci.* **2023,** *14,* 2999–3009. doi:10.1039/d2sc06958j
15. Peng, J.; Guo, J.; Ma, R.; Jiang, Y. *Surf. Sci. Rep.* **2022,** *77,* 100549. doi:10.1016/j.surfrep.2021.100549
16. Rahimi, E.; PalaciosCorella, M.; Mol, A.; Pané, S.; Puigmartí-Luis, J. *Adv. Mater. (Weinheim, Ger.)* **2025,** e10671. doi:10.1002/adma.202510671
17. Kumar, N.; Zheng, L.-Q.; Pollard, A. J.; Wain, A. J.; Zenobi, R. *Chem. Rev.* **2026,** *126,* 2653–2677. doi:10.1021/acs.chemrev.5c00707
18. Nakatsuka, N.; Yang, K.-A.; Abendroth, J. M.; Cheung, K. M.; Xu, X.; Yang, H.; Zhao, C.; Zhu, B.; Rim, Y. S.; Yang, Y.; Weiss, P. S.; Stojanović, M. N.; Andrews, A. M. *Science* **2018,** *362,* 319–324. doi:10.1126/science.aao6750
19. Lim, K.; Fenk, B.; Popovic, J.; Maier, J. *ACS Appl. Mater. Interfaces* **2021,** *13,* 51767–51774. doi:10.1021/acsami.1c15607
20. Komorek, P.; Wałek, M.; Jachimska, B. *Bioelectrochemistry* **2020,** *135,* 107582. doi:10.1016/j.bioelechem.2020.107582
21. Tran, C. T.; Nguyen, L. B. T.; Tan, E. X.; Preiser, P. R.; Phang, I. Y.; Ling, X. Y. *J. Am. Chem. Soc.* **2026,** *148,* 12321–12332. doi:10.1021/jacs.6c02165
22. Wicaksono, W. P.; Dang, H.; Lee, S.; Choo, J. *Appl. Surf. Sci.* **2024,** *649,* 159163. doi:10.1016/j.apsusc.2023.159163
23. Singh, S. N.; Yadav, S.; Shire, S. J.; Kalonia, D. S. *Pharm. Res.* **2014,** *31,* 2549–2558. doi:10.1007/s11095-014-1352-0
24. Laue, T. M.; Shire, S. J. *J. Pharm. Sci.* **2020,** *109,* 154–160. doi:10.1016/j.xphs.2019.10.045
25. Wu, J. *Chem. Rev.* **2022,** *122,* 10821–10859. doi:10.1021/acs.chemrev.2c00097
26. Adamczyk, Z. *Adv. Colloid Interface Sci.* **2003,** *100–102,* 267–347. doi:10.1016/s0001-8686(02)00062-3
27. Agmo Hernández, V. *ChemTexts* **2023,** *9,* 10. doi:10.1007/s40828-023-00182-9
28. Eom, N.; Parsons, D. F.; Craig, V. S. J. *J. Phys. Chem. B* **2017,** *121,* 6442–6453. doi:10.1021/acs.jpcb.7b03131
29. Grasso, D.; Subramaniam, K.; Butkus, M.; Strevett, K.; Bergendahl, J. *Rev. Environ. Sci. Technol.* **2002,** *1,* 17–38. doi:10.1023/a:1015146710500
30. Tabor, R. F.; Wu, C.; Grieser, F.; Dagastine, R. R.; Chan, D. Y. C. *J. Phys. Chem. Lett.* **2013,** *4,* 3872–3877. doi:10.1021/jz402068k
31. Kanth, J. M. P.; Vemparala, S.; Anishetty, R. *Phys. Rev. E* **2010,** *81,* 021201. doi:10.1103/physreve.81.021201
32. Zhang, Y.; Furyk, S.; Bergbreiter, D. E.; Cremer, P. S. *J. Am. Chem. Soc.* **2005,** *127,* 14505–14510. doi:10.1021/ja0546424
33. Blesa, M. A.; Weisz, A. D.; Morando, P. J.; Salfity, J. A.; Magaz, G. E.; Regazzoni, A. E. *Coord. Chem. Rev.* **2000,** *196,* 31–63. doi:10.1016/s0010-8545(99)00005-3
34. Reddish, M. J.; Vaughn, M. B.; Fu, R.; Dyer, R. B. *Biochemistry* **2016,** *55,* 1485–1493. doi:10.1021/acs.biochem.5b01364
35. Maus, H.; Hinze, G.; Hammerschmidt, S. J.; Schirmeister, T.; Basché, T. *ChemistryEurope* **2023,** *1,* e202300060. doi:10.1002/ceur.202300060
36. Dogan, J.; Schmidt, T.; Mu, X.; Engström, Å.; Jemth, P. *J. Biol. Chem.* **2012,** *287,* 34316–34324. doi:10.1074/jbc.m112.399436
37. Roach, P.; Farrar, D.; Perry, C. C. *J. Am. Chem. Soc.* **2005,** *127,* 8168–8173. doi:10.1021/ja042898o
38. Larsericsdotter, H.; Oscarsson, S.; Buijs, J. *J. Colloid Interface Sci.* **2004,** *276,* 261–268. doi:10.1016/j.jcis.2004.03.056
39. Du, X.; Li, Y.; Xia, Y.-L.; Ai, S.-M.; Liang, J.; Sang, P.; Ji, X.-L.; Liu, S.-Q. *Int. J. Mol. Sci.* **2016,** *17,* 144. doi:10.3390/ijms17020144
40. Gobbi, M.; Galanti, A.; Stoeckel, M.-A.; Zyska, B.; Bonacchi, S.; Hecht, S.; Samorì, P. *Nat. Commun.* **2020,** *11,* 4731. doi:10.1038/s41467-020-18604-4
41. Boldt, F.-M.; Baltes, N.; Borgwarth, K.; Heinze, J. *Surf. Sci.* **2005,** *597,* 51–64. doi:10.1016/j.susc.2004.04.062
42. Camacho, C. J.; Kimura, S. R.; DeLisi, C.; Vajda, S. *Biophys. J.* **2000,** *78,* 1094–1105. doi:10.1016/s0006-3495(00)76668-9
43. Khalid-Salako, F.; Kurt, H.; Yüce, M. *ACS Omega* **2026,** *11,* 1396–1409. doi:10.1021/acsomega.5c08871
44. Davantès, A.; Nigen, M.; Sanchez, C.; Renard, D. *Colloids Interfaces* **2023,** *7,* 26. doi:10.3390/colloids7020026
45. Arteta, M. Y.; Berti, D.; Montis, C.; Campbell, R. A.; Eriksson, C.; Clifton, L. A.; Skoda, M. W. A.; Soltwedel, O.; Koutsioubas, A.; Baglioni, P.; Nylander, T. *Soft Matter* **2015,** *11,* 1973–1990. doi:10.1039/c4sm02712d
46. Kurkina, T.; Vlandas, A.; Ahmad, A.; Kern, K.; Balasubramanian, K. *Angew. Chem., Int. Ed.* **2011,** *50,* 3710–3714. doi:10.1002/anie.201006806
47. Sivakumarasamy, R.; Hartkamp, R.; Siboulet, B.; Dufrêche, J.-F.; Nishiguchi, K.; Fujiwara, A.; Clément, N. *Nat. Mater.* **2018,** *17,* 464–470. doi:10.1038/s41563-017-0016-y
48. Pham, C. D.; Nguyen, T. T. H.; Zhang, J.; Jamali, S.; Nguyen, N.-T.; Nguyen, T.-K. *ACS Appl. Nano Mater.* **2026,** *9,* 4469–4481. doi:10.1021/acsanm.6c00645
49. Dhopatkar, N.; Defante, A. P.; Dhinojwala, A. *Sci. Adv.* **2016,** *2,* e1600763. doi:10.1126/sciadv.1600763
50. Wu, G.; Fang, J.; Shrawankar, K.; Guo, W.; Nagao, S.; Chen, X.; Wu, Y.; Wei, T.; Chen, Z. *Anal. Chem. (Washington, DC, U. S.)* **2026,** *98,* 7676–7684. doi:10.1021/acs.analchem.5c07876
51. Dunér, G.; Thormann, E.; Dėdinaitė, A. *J. Colloid Interface Sci.* **2013,** *408,* 229–234. doi:10.1016/j.jcis.2013.07.008
52. Jordan, J. L.; Fernandez, E. J. *Biotechnol. Bioeng.* **2008,** *101,* 837–842. doi:10.1002/bit.21977
53. Doudevski, I.; Schwartz, D. K. *J. Am. Chem. Soc.* **2001,** *123,* 6867–6872. doi:10.1021/ja0042783
54. Dziubak, D.; Strzelak, K.; Sek, S. *Membranes* **2020,** *11,* 11. doi:10.3390/membranes11010011
55. Kujawa, P.; Moraille, P.; Sanchez, J.; Badia, A.; Winnik, F. M. *J. Am. Chem. Soc.* **2005,** *127,* 9224–9234. doi:10.1021/ja044385n
56. Gurdak, E.; Dupont-Gillain, C. C.; Booth, J.; Roberts, C. J.; Rouxhet, P. G. *Langmuir* **2005,** *21,* 10684–10692. doi:10.1021/la051227g

57. Sarcina, L.; Torsi, L.; Picca, R. A.; Manoli, K.; Macchia, E. *Sensors* **2020,** *20,* 3678. doi:10.3390/s20133678
58. Politano, G. G.; Versace, C. *Spectrosc. J.* **2023,** *1,* 163–181. doi:10.3390/spectroscj1030014
59. Mora, M. F.; Giacomelli, C. E.; Garcia, C. D. *Anal. Chem. (Washington, DC, U. S.)* **2009,** *81,* 1016–1022. doi:10.1021/ac802068n
60. Höök, F.; Vörös, J.; Rodahl, M.; Kurrat, R.; Böni, P.; Ramsden, J. J.; Textor, M.; Spencer, N. D.; Tengvall, P.; Gold, J.; Kasemo, B. *Colloids Surf., B* **2002,** *24,* 155–170. doi:10.1016/s0927-7765(01)00236-3
61. Häbich, A.; Qiao, G. G.; Ducker, W. *Langmuir* **2010,** *26,* 13944–13953. doi:10.1021/la101641r
62. Roach, P.; Farrar, D.; Perry, C. C. *J. Am. Chem. Soc.* **2006,** *128,* 3939–3945. doi:10.1021/ja056278e
63. Lyu, K.; Chen, H.; Gao, J.; Jin, J.; Shi, H.; Schwartz, D. K.; Wang, D. *Biomacromolecules* **2022,** *23,* 4709–4717. doi:10.1021/acs.biomac.2c00917
64. Pandey, S.; Gautam, D.; Chen, J. *J. Phys. Chem. B* **2024,** *128,* 7254–7262. doi:10.1021/acs.jpcb.4c03359
65. Bouzigues, C. I.; Tabeling, P.; Bocquet, L. *Phys. Rev. Lett.* **2008,** *101,* 114503. doi:10.1103/physrevlett.101.114503
66. Wang, T.; Jiang, Y.; Feng, H.; Liu, L.; Deng, Q.; Liu, D.; Wang, C. *Catalysts* **2025,** *15,* 1131. doi:10.3390/catal15121131
67. Brulé, T.; Bouhelier, A.; Dereux, A.; Finot, E. *ACS Sens.* **2016,** *1,* 676–680. doi:10.1021/acssensors.6b00097
68. Niu, T.; Yuan, Y.; Yao, J.; Lu, F.; Gu, R. *Sci. China: Chem.* **2011,** *54,* 200–204. doi:10.1007/s11426-010-4184-8
69. Liu, C.; Lei, F.; Gong, M.; Zhou, X.; Zhao, X.; Li, Z.; Zhang, C.; Man, B.; Yu, J. *Energy Environ. Mater.* **2024,** *7,* e12517. doi:10.1002/eem2.12517
70. Miranda, P. B.; Shen, Y. R. *J. Phys. Chem. B* **1999,** *103,* 3292–3307. doi:10.1021/jp9843757
71. Tian, C. S.; Shen, Y. R. *Proc. Natl. Acad. Sci. U. S. A.* **2009,** *106,* 15148–15153. doi:10.1073/pnas.0901480106
72. Rehl, B.; Li, Z.; Gibbs, J. M. *Langmuir* **2018,** *34,* 4445–4454. doi:10.1021/acs.langmuir.7b04289
73. Eisenthal, K. B. *Chem. Rev.* **1996,** *96,* 1343–1360. doi:10.1021/cr9502211
74. Konek, C. T.; Musorrafiti, M. J.; Al-Abadleh, H. A.; Bertin, P. A.; Nguyen, S. T.; Geiger, F. M. *J. Am. Chem. Soc.* **2004,** *126,* 11754–11755. doi:10.1021/ja0474300
75. Fitts, J. P.; Shang, X.; Flynn, G. W.; Heinz, T. F.; Eisenthal, K. B. *J. Phys. Chem. B* **2005,** *109,* 7981–7986. doi:10.1021/jp040297d
76. Escorihuela, J.; González-Martínez, M. Á.; López-Paz, J. L.; Puchades, R.; Maquieira, Á.; Gimenez-Romero, D. *Chem. Rev.* **2015,** *115,* 265–294. doi:10.1021/cr5002063
77. Cross, G. H.; Reeves, A. A.; Brand, S.; Popplewell, J. F.; Peel, L. L.; Swann, M. J.; Freeman, N. J. *Biosens. Bioelectron.* **2003,** *19,* 383–390. doi:10.1016/s0956-5663(03)00203-3
78. Zheng, Y.; Ma, L.; Wang, Y.; Huang, J.; Ye, J.; Yang, X. *Anal. Chem. (Washington, DC, U. S.)* **2025,** *97,* 14675–14683. doi:10.1021/acs.analchem.5c02188
79. Yanase, Y.; Hiragun, T.; Ishii, K.; Kawaguchi, T.; Yanase, T.; Kawai, M.; Sakamoto, K.; Hide, M. *Sensors* **2014,** *14,* 4948–4959. doi:10.3390/s140304948
80. Plikusiene, I.; Maciulis, V.; Ramanavicius, A.; Ramanaviciene, A. *Polymers (Basel, Switz.)* **2022,** *14,* 1056. doi:10.3390/polym14051056
81. Bieberle-Hütter, A.; Bronneberg, A. C.; George, K.; van de Sanden, M. C. M. *J. Phys. D: Appl. Phys.* **2021,** *54,* 133001. doi:10.1088/1361-6463/abd435
82. Colson, L.; Kwon, Y.; Nam, S.; Bhandari, A.; Maya, N. M.; Lu, Y.; Cho, Y. *Sensors* **2023,** *23,* 7691. doi:10.3390/s23187691
83. Lazanas, A. C.; Prodromidis, M. I. *ACS Meas. Sci. Au* **2023,** *3,* 162–193. doi:10.1021/acsmeasuresciau.2c00070
84. Magar, H. S.; Abbas, M. N.; Ali, M. B.; Ahmed, M. A. *J. Solid State Electrochem.* **2020,** *24,* 723–737. doi:10.1007/s10008-020-04500-w
85. Syu, Y.-C.; Hsu, W.-E.; Lin, C.-T. *ECS J. Solid State Sci. Technol.* **2018,** *7,* Q3196–Q3207. doi:10.1149/2.0291807jss
86. Minamiki, T.; Minami, T.; Kurita, R.; Niwa, O.; Wakida, S.-i.; Fukuda, K.; Kumaki, D.; Tokito, S. *Appl. Phys. Lett.* **2014,** *104,* 243703. doi:10.1063/1.4883739
87. Wang, S.-L.; Hsieh, C.-Y.; Wu, C.-R.; Chen, J.-C.; Wang, Y.-L. *Biomicrofluidics* **2021,** *15,* 024110. doi:10.1063/5.0042977
88. Zhang, X.; Han, C.; Xu, W. *Chem. Biomed. Imaging* **2023,** *1,* 205–219. doi:10.1021/cbmi.2c00008
89. Roberts, W. S.; Davis, F.; Collyer, S. D.; Higson, S. P. J. *Analyst* **2011,** *136,* 5287. doi:10.1039/c1an15589j
90. Janićijević, Ž.; Nguyen-Le, T.-A.; Baraban, L. *Next Nanotechnol.* **2023,** *3-4,* 100025. doi:10.1016/j.nxnano.2023.100025
91. Putnam, S. T.; Santiago-Carboney, A.; Qian, P.; Rodríguez-López, J. *Anal. Chem. (Washington, DC, U. S.)* **2025,** *97,* 8147–8181. doi:10.1021/acs.analchem.4c06996
92. Lubarsky, G. V.; Davidson, M. R.; Bradley, R. H. *Biosens. Bioelectron.* **2007,** *22,* 1275–1281. doi:10.1016/j.bios.2006.05.024
93. Drew, M. E.; Chworos, A.; Oroudjev, E.; Hansma, H.; Yamakoshi, Y. *Langmuir* **2010,** *26,* 7117–7125. doi:10.1021/la904151h
94. Andriotis, O. G.; Elsayad, K.; Smart, D. E.; Nalbach, M.; Davies, D. E.; Thurner, P. J. *Biomed. Opt. Express* **2019,** *10,* 1841. doi:10.1364/boe.10.001841
95. Nishide, G.; Lim, K.; Kobayashi, A.; Qiu, Y.; Hazawa, M.; Ando, T.; Okada, Y.; Wong, R. W. *Nucleic Acids Res.* **2025,** *53,* gkaf152. doi:10.1093/nar/gkaf152
96. Ruan, Y.; Kao, K.; Lefebvre, S.; Marchesi, A.; Corringer, P.-J.; Hite, R. K.; Scheuring, S. *Proc. Natl. Acad. Sci. U. S. A.* **2018,** *115,* 10333–10338. doi:10.1073/pnas.1805621115
97. Fukuma, T.; Garcia, R. *ACS Nano* **2018,** *12,* 11785–11797. doi:10.1021/acsnano.8b07216
98. Asakawa, H.; Yoshioka, S.; Nishimura, K.-i.; Fukuma, T. *ACS Nano* **2012,** *6,* 9013–9020. doi:10.1021/nn303229j
99. Fukuma, T.; Ueda, Y.; Yoshioka, S.; Asakawa, H. *Phys. Rev. Lett.* **2010,** *104,* 016101. doi:10.1103/physrevlett.104.016101
100. Araki, Y.; Sekine, T.; Chang, R.; Hayashi, T.; Onishi, H. *RSC Adv.* **2018,** *8,* 24660–24664. doi:10.1039/c8ra03569e
101. Hackl, T.; Schitter, G.; Mesquida, P. *ACS Nano* **2022,** *16,* 17982–17990. doi:10.1021/acsnano.2c07121
102. Hackl, T.; Poik, M.; Schitter, G. *IEEE Trans. Instrum. Meas.* **2023,** *72,* 1–8. doi:10.1109/tim.2022.3230477
103. Zheng, L.-Q.; Servalli, M.; Schlüter, A. D.; Zenobi, R. *Chem. Sci.* **2019,** *10,* 9673–9678. doi:10.1039/c9sc03296g
104. Kurouski, D.; Deckert-Gaudig, T.; Deckert, V.; Lednev, I. K. *J. Am. Chem. Soc.* **2012,** *134,* 13323–13329. doi:10.1021/ja303263y
105. El-Khoury, P. Z. *J. Am. Chem. Soc.* **2023,** *145,* 6639–6642. doi:10.1021/jacs.3c01626

106. Müller, D. J.; Dumitru, A. C.; Lo Giudice, C.; Gaub, H. E.; Hinterdorfer, P.; Hummer, G.; De Yoreo, J. J.; Dufrêne, Y. F.; Alsteens, D. *Chem. Rev.* **2021,** *121,* 11701–11725. doi:10.1021/acs.chemrev.0c00617
107. Ai, Q.; Bonagiri, L. K. S.; Farokh Payam, A.; Aluru, N. R.; Zhang, Y. *J. Phys. Chem. C* **2025,** *129,* 5273–5286. doi:10.1021/acs.jpcc.5c00088
108. Martín Sabanés, N.; Driessen, L. M. A.; Domke, K. F. *Anal. Chem. (Washington, DC, U. S.)* **2016,** *88,* 7108–7114. doi:10.1021/acs.analchem.6b01080
109. Cousin, F.; Fadda, G. *EPJ Web Conf.* **2020,** *236,* 04001. doi:10.1051/epjconf/202023604001
110. Pan, F.; Aaron Lau, K. H.; Messersmith, P. B.; Lu, J. R.; Zhao, X. *Langmuir* **2020,** *36,* 12309–12318. doi:10.1021/acs.langmuir.0c02247
111. Li, Z.; Saurabh, S.; Hollowell, P.; Kalonia, C. K.; Waigh, T. A.; Li, P.; Webster, J. R. P.; Seddon, J. M.; Bresme, F.; Lu, J. R. *ACS Appl. Mater. Interfaces* **2024,** *16,* 70231–70241. doi:10.1021/acsami.4c14407
112. Skoda, M. W. A. *Curr. Opin. Colloid Interface Sci.* **2019,** *42,* 41–54. doi:10.1016/j.cocis.2019.03.003
113. Khassanov, A.; Steinrück, H.-G.; Schmaltz, T.; Magerl, A.; Halik, M. *Acc. Chem. Res.* **2015,** *48,* 1901–1908. doi:10.1021/acs.accounts.5b00022
114. Richter, A. G.; Kuzmenko, I. *Langmuir* **2013,** *29,* 5167–5180. doi:10.1021/la3049532
115. Velasco-Velez, J.-J.; Wu, C. H.; Pascal, T. A.; Wan, L. F.; Guo, J.; Prendergast, D.; Salmeron, M. *Science* **2014,** *346,* 831–834. doi:10.1126/science.1259437
116. Caselli, L.; Nylander, T.; Malmsten, M. *Adv. Colloid Interface Sci.* **2024,** *325,* 103120. doi:10.1016/j.cis.2024.103120
117. Hatami, D.; Hasler, R.; Spanu, A.; Dostalek, J.; Kleber, C.; Knoll, W.; Bonfiglio, A. *Sci. Rep.* **2025,** *15,* 15244. doi:10.1038/s41598-025-99656-8
118. Zhao, R.; Yan, B.; Li, D.; Guo, Z.; Huang, Y.; Wang, D.; Yao, X. *Anal. Chem. (Washington, DC, U. S.)* **2024,** *96,* 10228–10236. doi:10.1021/acs.analchem.4c00680
119. Thakur, B.; Anbalagan, A. C.; Koyande, P.; Sawant, S. N. *Sci. Rep.* **2025,** *15,* 16902. doi:10.1038/s41598-025-99351-8
120. Yan, B.; Han, X.; Zhao, R.; Guo, Z.; Li, D.; Yan, Y.; Wang, D.; Yao, X. *Anal. Chem. (Washington, DC, U. S.)* **2025,** *97,* 23858–23867. doi:10.1021/acs.analchem.5c03150
121. Ma, S.-C.; Gupta, R.; Ondevilla, N. A. P.; Barman, K.; Lee, L.-Y.; Chang, H.-C.; Huang, J.-J. *Biomed. Opt. Express* **2023,** *14,* 182. doi:10.1364/boe.478164
122. Jungnickel, R.; Balasubramanian, K. *Adv. Sens. Res.* **2024,** *3,* 2400028. doi:10.1002/adsr.202400028
123. Fritz, P. A.; Bera, B.; van den Berg, J.; Visser, I.; Kleijn, J. M.; Boom, R. M.; Schroën, C. G. P. H. *Langmuir* **2021,** *37,* 6549–6555. doi:10.1021/acs.langmuir.1c00828
124. Gibson, J. S.; Mendes, P. M. *ChemPhysChem* **2021,** *22,* 684–692. doi:10.1002/cphc.202000988
125. Zhan, C.; Dattila, F.; Rettenmaier, C.; Bergmann, A.; Kühl, S.; García-Muelas, R.; López, N.; Cuenya, B. R. *ACS Catal.* **2021,** *11,* 7694–7701. doi:10.1021/acscatal.1c01478
126. Wu, J.; Zhou, R.; Radjenovic, P. M.; Liu, S.; Wu, D.; Li, J.; Mao, B.; Yan, J. *Electrochim. Acta* **2021,** *390,* 138859. doi:10.1016/j.electacta.2021.138859
127. Zhu, C.; Fan, C.; Cortés, E.; Xie, W. *J. Mater. Chem. A* **2021,** *9,* 20024–20031. doi:10.1039/d1ta04218a
128. Alvarez-Malmagro, J.; Ruano, L.; Cuartero-González, M.; Nogueira, J. J.; Prieto-Dapena, F. *J. Phys. Chem. B* **2025,** *129,* 4715–4727. doi:10.1021/acs.jpcb.5c00523
129. Pudžaitis, V.; Talaikis, M.; Sadzevičienė, R.; Labanauskas, L.; Niaura, G. *Materials* **2022,** *15,* 7221. doi:10.3390/ma15207221
130. Su, Z.; Chen, A.; Lipkowski, J. *Langmuir* **2024,** *40,* 8248–8259. doi:10.1021/acs.langmuir.4c00480
131. Liu, X.; Ma, Y.; Song, Q.; Huang, H.; He, Y.; Sun, S.; Wang, Z. *J. Phys. Chem. C* **2023,** *127,* 23675–23686. doi:10.1021/acs.jpcc.3c06086
132. Patrow, J. G.; Sorenson, S. A.; Dawlaty, J. M. *J. Phys. Chem. C* **2017,** *121,* 11585–11592. doi:10.1021/acs.jpcc.7b03134
133. Ge, A.; Videla, P. E.; Lee, G. L.; Rudshteyn, B.; Song, J.; Kubiak, C. P.; Batista, V. S.; Lian, T. *J. Phys. Chem. C* **2017,** *121,* 18674–18682. doi:10.1021/acs.jpcc.7b05563
134. Bhattacharyya, D.; Videla, P. E.; Palasz, J. M.; Tangen, I.; Meng, J.; Kubiak, C. P.; Batista, V. S.; Lian, T. *J. Am. Chem. Soc.* **2022,** *144,* 14330–14338. doi:10.1021/jacs.2c05563
135. Bodine, M.; Rozyyev, V.; Elam, J. W.; Tokmakoff, A.; Lewis, N. H. C. *J. Phys. Chem. C* **2023,** *127,* 23199–23211. doi:10.1021/acs.jpcc.3c05445
136. Unni, B.; Burgess, I. J. *Electrochim. Acta* **2021,** *381,* 138263. doi:10.1016/j.electacta.2021.138263
137. Nawrocki, W. J.; Jones, M. R.; Frese, R. N.; Croce, R.; Friebe, V. M. *Joule* **2023,** *7,* 529–544. doi:10.1016/j.joule.2023.02.015
138. Siddiqui, A.-R.; N'Diaye, J.; Martin, K.; Baby, A.; Dawlaty, J.; Augustyn, V.; Rodríguez-López, J. *Anal. Chem. (Washington, DC, U. S.)* **2024,** *96,* 2435–2444. doi:10.1021/acs.analchem.3c04407
139. López-Ortiz, M.; Bolzonello, L.; Bruschi, M.; Fresch, E.; Collini, E.; Hu, C.; Croce, R.; van Hulst, N. F.; Gorostiza, P. *ACS Appl. Mater. Interfaces* **2024,** *16,* 43451–43461. doi:10.1021/acsami.4c03652
140. Groysman, S.; Chen, Y.; Garcia, A.; Martinez, C.; Diego-Perez, K.; Benavides, M.; Chen, Y.; Wan, Z.; Wang, S.; Liu, R.; Wang, D.; Liu, C.; Wang, Y. *ACS Electrochem.* **2025,** *1,* 974–986. doi:10.1021/acselectrochem.4c00227
141. Fernandes, E.; Costa, R. R.; Machado, R.; Reis, R. L.; Pashkuleva, I.; Lúcio, M. *Small Sci.* **2024,** *4,* 2300271. doi:10.1002/smsc.202300271
142. Spagnolo, S.; Sontakke, K.; Dubbert, L.; Urban, M.; Lednicky, T.; Csaki, A.; Wondraczek, K.; Fritzsche, W.; Hianik, T. *Biosensors* **2025,** *15,* 652. doi:10.3390/bios15100652
143. Asai, N.; Matsumoto, N.; Yamashita, I.; Shimizu, T.; Shingubara, S.; Ito, T. *Sens. Bio-Sens. Res.* **2021,** *32,* 100415. doi:10.1016/j.sbsr.2021.100415
144. Wang, P.; Liu, T.; Liu, Y.; Tian, J.; Zhang, X.; Guo, J.; Jin, Y.; Xiao, H.; Song, J. *Sens. Actuators, B* **2021,** *329,* 129114. doi:10.1016/j.snb.2020.129114
145. Kowalczyk, A.; Gajda-Walczak, A.; Ruzycka-Ayoush, M.; Targonska, A.; Mosieniak, G.; Glogowski, M.; Szumera-Cieckiewicz, A.; Prochorec-Sobieszek, M.; Bamburowicz-Klimkowska, M.; Nowicka, A. M.; Grudzinski, I. P. *Anal. Chem. (Washington, DC, U. S.)* **2023,** *95,* 9520–9530. doi:10.1021/acs.analchem.3c00772
146. Arrizabalaga, J.; Rafaniello, I.; Schäfer, T. *J. Membr. Sci.* **2025,** *713,* 123348. doi:10.1016/j.memsci.2024.123348
147. Yoon, B. K.; Ma, G. J.; Park, H.; Ferhan, A. R.; Cho, N.-J.; Jackman, J. A. *Int. J. Biol. Macromol.* **2021,** *182,* 1906–1914. doi:10.1016/j.ijbiomac.2021.05.113

148. Bartolini, C.; Tozzetti, M.; Gellini, C.; Ricci, M.; Menichetti, S.; Procacci, P.; Caminati, G. *Nanomaterials* **2025,** *15,* 1230. doi:10.3390/nano15161230
149. Hou, L.; Xu, X.; Tian, F.; Xu, Y. *Talanta* **2025,** *286,* 127509. doi:10.1016/j.talanta.2024.127509
150. Lequeux, M.; Salmain, M.; Krafft, J.-M.; Dostalek, J.; Vallée, A.; Loiseau, A.; Knoll, W.; Lamy de la Chapelle, M.; Boujday, S. *Sens. Actuators, B* **2025,** *442,* 138154. doi:10.1016/j.snb.2025.138154
151. Armero, L.; Plou, J.; Valera, P. S.; Serna, S.; García, I.; Liz-Marzán, L. M. *ACS Sens.* **2024,** *9,* 4811–4821. doi:10.1021/acssensors.4c01252
152. Perrino, C.; Lee, S.; Spencer, N. D. *Langmuir* **2024,** *40,* 14130–14140. doi:10.1021/acs.langmuir.4c01582
153. Rastogi, R.; Beggiato, M.; Dogbe Foli, E. A.; Vincent, R.; Dupont-Gillain, C.; Adam, P.-M.; Krishnamoorthy, S. *J. Phys. Chem. C* **2021,** *125,* 9866–9874. doi:10.1021/acs.jpcc.1c00793
154. Sans, J.; Azevedo Gonçalves, I.; Quintana, R. *Small* **2024,** *20,* 2312041. doi:10.1002/smll.202312041
155. Dinda, S.; Trivedi, S.; Roy, A.; Pammer, F. D.; Fichtner, M. *Adv. Energy Mater.* **2023,** *13,* 2302176. doi:10.1002/aenm.202302176
156. Fiocco, A.; Pavlic, A. A.; Kanoufi, F.; Maisonhaute, E.; Noël, J.-M.; Lucas, I. T. *Anal. Chem. (Washington, DC, U. S.)* **2024,** *96,* 2791–2798. doi:10.1021/acs.analchem.3c02601
157. Bartolomeo, G. L.; Zhang, Y.; Kumar, N.; Zenobi, R. *Anal. Chem. (Washington, DC, U. S.)* **2021,** *93,* 15358–15364. doi:10.1021/acs.analchem.1c03004
158. Mrđenović, D.; Ge, W.; Kumar, N.; Zenobi, R. *Angew. Chem., Int. Ed.* **2022,** *61,* e202210288. doi:10.1002/anie.202210288
159. Pandey, Y.; Kumar, N.; Goubert, G.; Zenobi, R. *Angew. Chem., Int. Ed.* **2021,** *60,* 19041–19046. doi:10.1002/anie.202106128
160. Proniewicz, E.; Olszewski, T. K. *J. Med. Chem.* **2022,** *65,* 4387–4400. doi:10.1021/acs.jmedchem.2c00031
161. Komorek, P.; Rakowski, K.; Szota, M.; Lekka, M.; Jachimska, B. *bioRxiv* **2023,** 567678. doi:10.1101/2023.11.18.567678
162. Makou, E.; Bailey, R. G.; Johnston, H.; Parkin, J. D.; Hulme, A. N.; Hähner, G.; Barlow, P. N. *J. Biol. Chem.* **2019,** *294,* 20148–20163. doi:10.1074/jbc.ra119.010913
163. Szczepanczyk, M.; Gonzalez-Martinez, J. F.; Ruzgas, T.; Björklund, S. *J. Colloid Interface Sci.* **2026,** *703,* 139139. doi:10.1016/j.jcis.2025.139139
164. Mei, N.; Liang, J.; McRae, D. M.; Leonenko, Z. *Nanotechnology* **2024,** *35,* 305101. doi:10.1088/1361-6528/ad403b
165. Raizada, G.; Guillouzouic, J.; Rouleau, A.; Lesniewska, E.; Le Ferrec, E.; Elie-Caille, C.; Boireau, W. *Biosensors* **2025,** *15,* 103. doi:10.3390/bios15020103
166. Ramer, G.; Ruggeri, F. S.; Levin, A.; Knowles, T. P. J.; Centrone, A. *ACS Nano* **2018,** *12,* 6612–6619. doi:10.1021/acsnano.8b01425
167. Wang, H.; González-Fialkowski, J. M.; Li, W.; Xie, Q.; Yu, Y.; Xu, X. G. *Anal. Chem. (Washington, DC, U. S.)* **2021,** *93,* 3567–3575. doi:10.1021/acs.analchem.0c05075
168. Veber, A.; Spedalieri, C.; Kneipp, J. *Small* **2025,** *21,* e07097. doi:10.1002/smll.202507097
169. Pawliszak, P.; Beheshti, A.; Møller, A.; Blencowe, A.; Beattie, D. A.; Krasowska, M. *J. Colloid Interface Sci.* **2024,** *667,* 393–402. doi:10.1016/j.jcis.2024.04.073

License and Terms

This is an open access article licensed under the terms of the Beilstein-Institut Open Access License Agreement (https://www.beilstein-journals.org/bjnano/terms), which is identical to the Creative Commons Attribution 4.0 International License (https://creativecommons.org/licenses/by/4.0). The reuse of material under this license requires that the author(s), source and license are credited. Third-party material in this article could be subject to other licenses (typically indicated in the credit line), and in this case, users are required to obtain permission from the license holder to reuse the material.

The definitive version of this article is the electronic one which can be found at:
https://doi.org/10.3762/bjnano.17.85

BEILSTEIN JOURNAL OF NANOTECHNOLOGY

Design of a yeast-based bio-interface on an optical fiber SPR platform toward drug adsorption monitoring

Natsumi Kitaya[1], Daisuke Yamanaka[*2], Kenji Morita[1], Ryota Naito[1], Hinako Suhara[1], Kento Suzuki[2], Hizuru Nakajima[3], Yukiko Moriiwa[1], Kazuhiro Morioka[1], Akio Yanagida[1] and Atsushi Shoji[*1]

Full Research Paper

Open Access

Address:
[1]Laboratory for Bioanalytical Chemistry, School of Pharmacy, Tokyo University of Pharmacy and Life Sciences, Hachioji, Tokyo 192-0392, Japan, [2]Laboratory for Immunopharmacology of Microbial Products, School of Pharmacy, Tokyo University of Pharmacy and Life Sciences, Hachioji, Tokyo 192-0392, Japan and [3]Department of Applied Chemistry for Environment, Graduate School of Urban Environmental Sciences, Tokyo Metropolitan University, 1-1 Minami-osawa, Hachioji, Tokyo, 192-0397, Japan

Email:
Daisuke Yamanaka[*] - ymnkd@toyaku.ac.jp; Atsushi Shoji[*] - ashoji@toyaku.ac.jp

* Corresponding author

Keywords:
bio-interface; biosorption; optical fiber surface plasmon resonance; yeast

Beilstein J. Nanotechnol. **2026,** *17,* 1290–1301.
https://doi.org/10.3762/bjnano.17.89

Received: 21 April 2026
Accepted: 13 August 2026
Published: 22 September 2026

This article is part of the thematic issue "Nanotechnology for cross-scale analysis: comprehensive evaluation of water environments".

Guest Editors: Y. Sasaki and T. Minami

© 2026 Kitaya et al.; licensee Beilstein-Institut.
License and terms: see end of document.

Abstract

Yeast biomass, *Saccharomyces cerevisiae*, has been widely studied for removing heavy metals and organic pollutants, including pharmaceuticals. However, conventional batch methods provide limited insight into time-resolved adsorption and interfacial molecular interactions. We developed an optical fiber-based surface plasmon resonance (SPR) sensor incorporating a yeast-derived bio-interface. A film formation monitoring method based on transmitted light absorbance during electroless Ni plating enabled reproducible fabrication of gold nanofilms. Yeast cells were uniformly immobilized via a spray-based method to construct the bio-interface. Using this sensor, real-time adsorption of pharmaceuticals onto yeast cells was evaluated: Doxorubicin showed a concentration-dependent SPR response, whereas ampicillin showed no significant change in SPR response. The optical fiber configuration allows for direct immersion into environmental waters for in situ measurements, providing a platform for dynamic analysis of microorganism–pollutant interactions and advancing water treatment and environmental monitoring technologies.

Introduction

Yeast, particularly *Saccharomyces cerevisiae*, is characterized by a cell wall rich in polysaccharides such as β-glucans and mannans, as well as proteins [1-3]. Because these cell wall components contain a variety of functional groups, they can interact with diverse chemical substances and exhibit adsorption properties on the cell surface. For example, studies on antibiotics and

aromatic organic compounds have reported that adsorption onto the yeast cell surface follows either the Langmuir adsorption isotherm or the Freundlich adsorption isotherm [4-6]. Further, quantitative structure–activity relationship analysis suggests that hydrophobic interactions, dispersion forces, and electrostatic interactions play important roles in adsorption onto the yeast surface.

Adsorption of metal ions by yeast has also been reported, and functional groups present in the cell wall, such as carboxyl, hydroxy, amino, and phosphate groups, are known to form electrostatic interactions and coordination bonds with metal ions. Indeed, the binding of divalent metal ions such as Pb^{2+}, Zn^{2+}, and Ni^{2+} to the yeast cell surface has been documented [7-9]. These adsorption behaviors are strongly influenced by solution conditions, particularly pH; in the pH range of 4–6, relatively high adsorption capacities are observed due to changes in the dissociation states of cell wall functional groups and the speciation of metal ions. Such diverse adsorption properties suggest a wide range of potential applications, including their use as drug carriers [10,11] and as adsorbent materials for pollutants as biosorption materials [12,13]. In environmental applications, the use of yeast biomass has been investigated for the removal of heavy metals from electroplating and mining wastewater [12,14,15], as well as organic pollutants such as dyes in textile effluents [16,17], and the development of yeast-based water purification technologies has been actively pursued.

Despite these advances, conventional methods for adsorption analysis have primarily relied on batch adsorption experiments [5], in which changes in solute concentration are evaluated using absorbance measurements or chromatographic analyses, and adsorption capacities are calculated under equilibrium conditions. Consequently, these approaches provide limited information on the time-resolved dynamics of adsorption and do not allow for direct observation of interfacial molecular interactions at the yeast surface. As a result, the dynamic adsorption behavior of drug molecules and pollutants on yeast has not been sufficiently elucidated. This limitation hampers a deeper understanding of adsorption kinetics and restricts the rational design of yeast-based materials for applications such as drug delivery and environmental remediation. To address these challenges, analytical platforms capable of directly monitoring adsorption processes at the bio-interface in real time are required. However, such approaches remain limited, particularly for systems involving complex biological surfaces such as yeast cells.

In this study, we developed an optical fiber-based surface plasmon resonance (SPR) sensor incorporating a yeast-derived bio-interface, enabling real-time and in situ monitoring of adsorption processes. In the fabrication of the SPR sensor, electroless Ni plating was performed while light from an LED was introduced into the optical fiber. The transmitted light intensity was measured using a spectrometer connected to the opposite end; by converting the obtained intensity into absorbance, we demonstrated that thin-film formation could be achieved while monitoring changes in film thickness in real time. The usefulness of this film thickness monitoring approach has been demonstrated in optical fiber SPR sensors incorporating Ag nanofilms [18]. This fabrication strategy improved the reproducibility and success rate of sensor preparation compared with conventional reflectance-based methods using bifurcated fibers [19]. After forming a gold nanofilm via Au displacement plating, yeast cells were successfully and uniformly immobilized on the gold surface by spraying a yeast suspension using an airbrush.

By integrating a yeast-based interface with an optical fiber SPR platform, the proposed system enables real-time monitoring of adsorption processes at biologically relevant interfaces, providing a useful tool for investigating molecular interactions at biological interfaces. Furthermore, the proposed platform has the potential to enable comprehensive evaluation of interactions between complex environmental samples and microbial cell surfaces. This approach provides a foundation for understanding such biological interfacial interactions.

Results and Discussion

Monitoring of film thickness during electroless Ni plating by absorbance measurement

We have previously reported that the progress of the electroless plating reaction at the tip of an optical fiber can be monitored by reflectance measurements [19]. However, the reflected light intensity exhibited poor reproducibility, with signal fluctuations observed between measurements (Supporting Information File 1, Figure S1). This variability is likely due to differences in the cutting angle and surface roughness of the fiber tip, which affect the efficiency of reflected light collection. In this study, we investigated the use of absorbance, calculated from transmitted light intensity, to monitor the progress of the electroless Ni plating reaction. As the reaction proceeded, the reflected light intensity decreased (Figure 1a). The time course of absorbance showed a gradual increase with reaction time, corresponding to an increase in the thickness of the Ni thin film formed at the fiber tip (Figure 1b). These results indicate that the progress of the electroless Ni plating reaction can be monitored in real time by absorbance measurements. To evaluate the relationship between absorbance and the thickness of the deposited Ni thin film, a portion of the optical fiber surface was etched with dilute nitric acid to create a step, and the step height

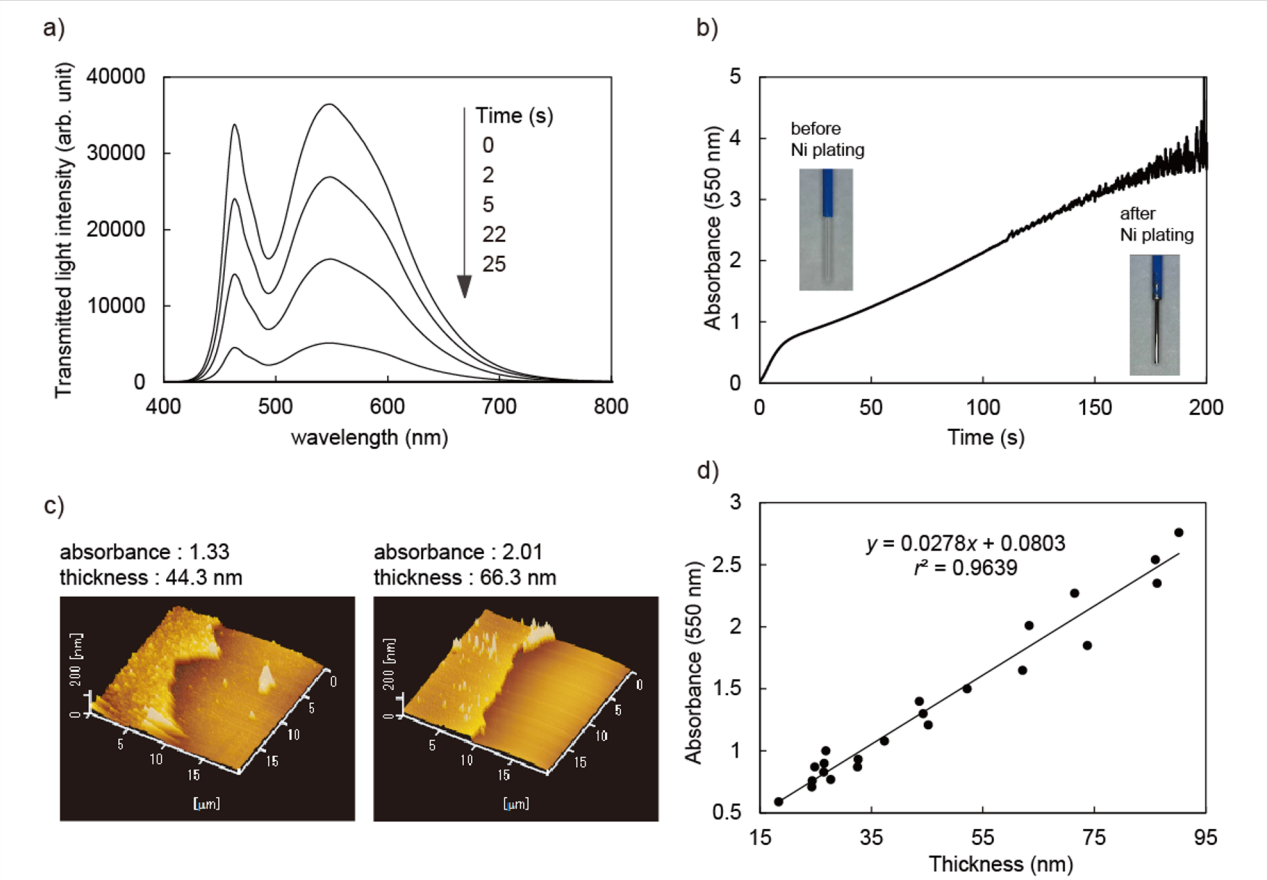


Figure 1: Formation of a gold thin film on an optical fiber core via electroless Ni plating. (a) Dependence of the transmitted light intensity through the fiber on the electroless plating reaction time. (b) Change in absorbance as a function of Ni deposition time. (c) Observation of Ni thin film thickness by AFM. (d) Correlation between absorbance and Ni film thickness.

was measured by atomic force microscopy (AFM) (Figure 1c). The results showed that higher absorbance values corresponded to larger step heights, indicating an increase in Ni film thickness. To further examine this relationship, absorbance was plotted against Ni film thickness, revealing a strong linear correlation, as shown in Figure 1d ($y = 0.0278x + 0.0803$, $r^2 = 0.9639$). This finding demonstrates that absorbance measurements can be used to monitor the thickness of Ni thin films formed during electroless plating. To form a gold thin film suitable for SPR measurements, Ni/Au displacement plating was subsequently performed. In this process, Ni was dissolved while Au was simultaneously deposited and grew on the fiber surface. Because Au has a larger atomic radius than Ni, the thickness of the resulting Au/Ni film formed by displacement plating may differ from that of the initial Ni thin film. Therefore, the relationship between the Ni film thickness before displacement and the Au/Ni film thickness after displacement was examined. As shown in Figure 2, a strong linear correlation was obtained between the two ($y = 93.817x - 29.607$, $r^2 = 0.9994$). In general, a gold thin film with a thickness of approximately 50 nm is considered optimal for SPR measurements. Based on this relationship, it was found that allowing the electroless Ni plating reaction to proceed until the absorbance reaches approximately 0.85 enabled the formation of a gold thin film with a thickness suitable for SPR sensing.

Performance evaluation of the SPR platform fabricated by absorbance-based thickness monitoring

To evaluate the performance of the optical fiber SPR sensor fabricated using absorbance-based thickness monitoring, SPR spectra were measured using aqueous sucrose solutions. As the sucrose concentration increased, the resonance wavelength of the SPR spectrum exhibited a shift toward longer wavelengths (red shift) (Figure 3a). This behavior is attributed to an increase in the refractive index of the solution with increasing sucrose concentration, which alters the SPR resonance condition. A linear relationship was observed between the resonance wavelength and sucrose concentration, with $y = 2.484x + 1.068$, $r^2 = 0.997$ (Figure 3b). The fabricated SPR sensor showed a good linear response over a refractive index range of 1.333–1.357, with a sensitivity of 1710 nm/RIU. The perfor-

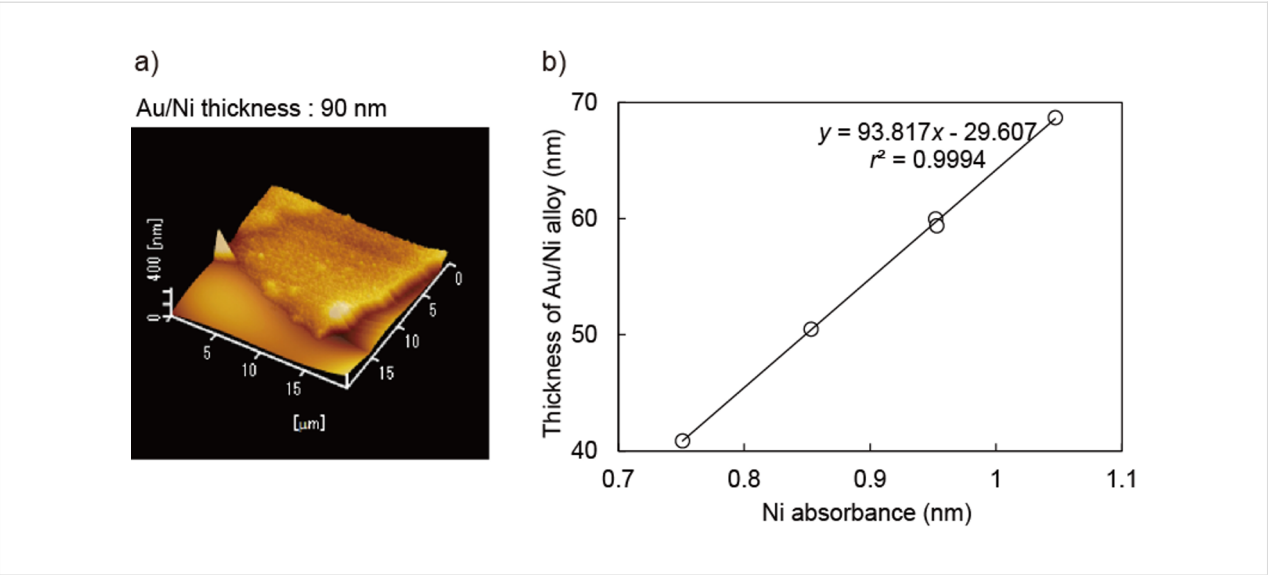


Figure 2: Formation of a gold thin film via electroless plating. (a) Thickness of the gold thin film observed by AFM. (b) Thickness of gold and Ni alloy thin films obtained by electroless gold plating, plotted as a function of absorbance during the electroless Ni plating reaction.

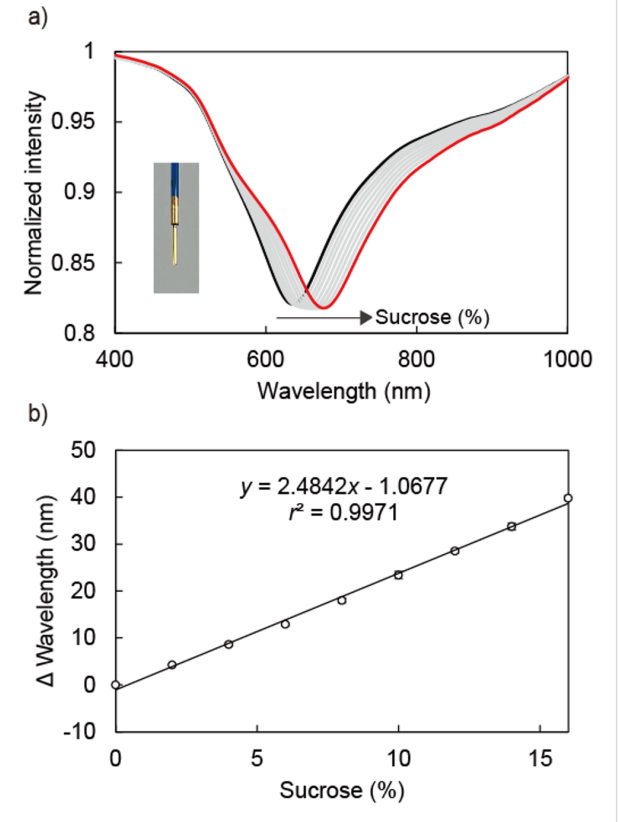


Figure 3: Performance evaluation of the optical fiber surface SPR sensor. (a) Dependence of the SPR spectrum on sucrose concentration; the inset shows the optical fiber SPR sensor. (b) Shift in SPR resonance wavelength as a function of sucrose concentration, calculated with the resonance wavelength obtained in water defined as 0 nm. Error bars represent the standard deviation (n = 3).

mance of the fabricated SPR sensor was compared with that of previously reported optical fiber SPR sensors fabricated by other methods. Optical fiber SPR sensors fabricated by sputtering have been reported to exhibit a linear range of 1.3342–1.3762 and a sensitivity of 1959 nm/RIU [20]. In contrast, sensors fabricated by vacuum evaporation exhibit a linear range of 1.333–1.3469 and a sensitivity of 1557 nm/RIU [21]. Compared with these reports, the optical fiber SPR sensor fabricated in this study using absorbance-based thickness monitoring demonstrates a comparable linear range and sensitivity to those of sensors prepared by conventional thin-film deposition methods, indicating that the present approach provides performance on par with established fabrication techniques.

Yeast immobilization on a gold nanofilm

The method for immobilizing yeast cells on the optical fiber SPR sensor interface was investigated. A strategy was adopted in which proteins were physically adsorbed onto the gold nanointerface, and yeast cells were subsequently immobilized via chemical linkage through amino groups. Bovine serum albumin (BSA) and lysozyme were considered as candidate proteins. BSA is known to bind various pharmaceutical compounds through hydrophobic pockets corresponding to two major drug-binding sites (Sudlow sites I and II) [22]. Therefore, interactions between pharmaceuticals and BSA could interfere with the evaluation of adsorption behavior onto yeast. In contrast, lysozyme has been reported to bind several compounds more weakly than BSA [23-25]. Based on these considerations, lysozyme was selected for immobilization on the gold nanointerface in this study. After physically adsorbing lysozyme onto the gold nanointerface, the surface was acti-

vated by introducing glutaraldehyde, followed by immersion in a yeast suspension. However, because yeast cells gradually sediment over time, sufficient contact between the cells and the sensor interface could not be maintained, resulting in inefficient immobilization onto the gold nanointerface. To address this issue, a spray-based immobilization method using an airbrush was investigated. In this approach, fine droplets gradually shrink as the solvent evaporates at room temperature, leading to concentration of yeast cells within the droplets (Figure 4a). As a result, yeast cells become concentrated on the gold nanointerface and are immobilized via the aldehyde groups of glutaraldehyde immobilized on the lysozyme-coated surface (Figure 4b). Upon yeast immobilization, the SPR signal increased by approximately 8 nm (Figure 4c). Furthermore, the stability of the immobilized yeast layer was evaluated by immersing the optical fiber SPR sensor with the yeast bio-interface vertically in water. The results showed that the yeast cells remained on the interface over a measurement period of 2 h, with no significant decrease in the SPR signal (Figure 4c). These findings demonstrate that the proposed spray immobilization method enables stable immobilization of yeast cells on the optical fiber SPR sensor interface.

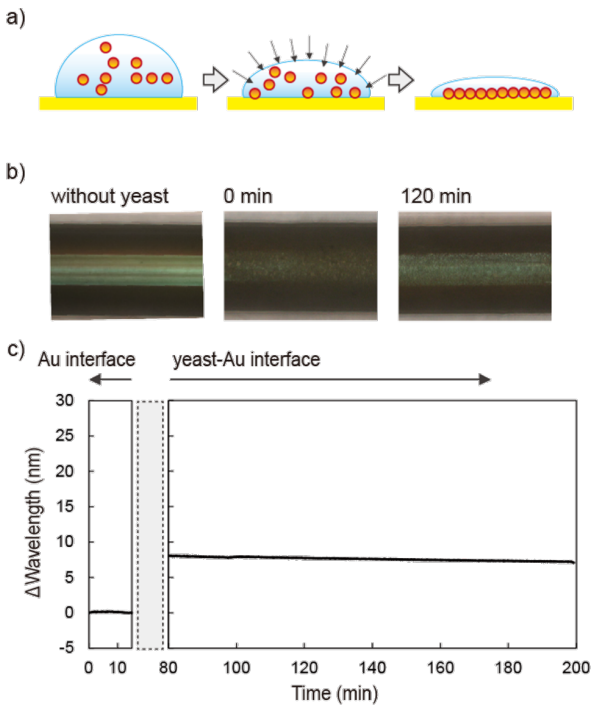


Figure 4: Immobilization of yeast on the gold surface of an optical fiber SPR sensor pre-adsorbed with lysozyme. (a) Schematic illustration of the immobilization method. Arrows indicate the decrease in water content due to evaporation, and circles represent yeast cells. (b) Process of yeast immobilization onto the lysozyme-functionalized fiber surface. (c) Change in SPR resonance wavelength before and after yeast immobilization. The gray square indicates the spraying step of fine droplets of yeast suspension using an airbrush; the resonance wavelength was not recorded during this process.

Interaction between the compound and the yeast cells surface

Knowledge regarding pharmaceutical adsorption by yeast remains limited, and a systematic understanding of the adsorption mechanisms, selectivity, and their relationships with molecular structure has not yet been fully established. Consequently, design guidelines for yeast-based materials as adsorbents for contaminant removal remain to be further developed. Yeast cell walls are composed of multiple biopolymers, including chitin, β-glucans, and mannoproteins, which together form a structurally and chemically complex three-dimensional architecture. Therefore, interactions between drug molecules and the cell wall cannot be attributed to a single component. In this context, this study does not aim to deconvolute the contributions of individual components but instead focuses on establishing a yeast-based interfacial sensing platform, for which chitin, a structurally stable component, was employed.

To screen for compounds that directly bind to the yeast cell wall, heat-killed yeast cells were prepared and mixed with an antibiotic-focused compound library (80 compounds). In this study, we focused on chitin, which is water-insoluble and stably present in the fungal cell wall, and performed non-wash chitin detection based on the split-luciferase complementation (SLC) assay using a chitin-specific binding protein. In this assay, inhibition rates were calculated based on changes in luciferase signals following compound treatment and visualized using a color scale (Figure 5a). Compounds shown in blue exhibit reduced luciferase signals, which may reflect decreased accessibility of cell surface chitin or masking of chitin-binding sites. In this context, these compounds may interact with cell wall chitin, thereby reducing its detectability in the assay. In contrast, compounds shown in red indicate increased signals, suggesting enhanced exposure or detectability of cell surface chitin.

In our compound library, compound no. 3, doxorubicin hydrochloride, reduced the surface chitin-derived signal by more than 20% (Figure 5a). In contrast, for example, compound no. 63, ampicillin trihydrate, which did not strongly suppress the chitin signal, was considered to have low affinity for the yeast cell wall and was used as a negative control in subsequent experiments. To verify that the results observed in the SLC assay were not due to inhibitory substances derived from yeast cells that could potentially affect luciferase activity, yeast cells were incubated with various concentrations of doxorubicin. The cells were then washed three times to remove unbound compounds and potential interfering substances, after which the assay was performed. As a result, even after thorough washing, the chitin signal was significantly and dose-dependently reduced with increasing concentrations of doxorubicin (Figure 5b). In contrast, no change in the chitin signal was observed even at increasing

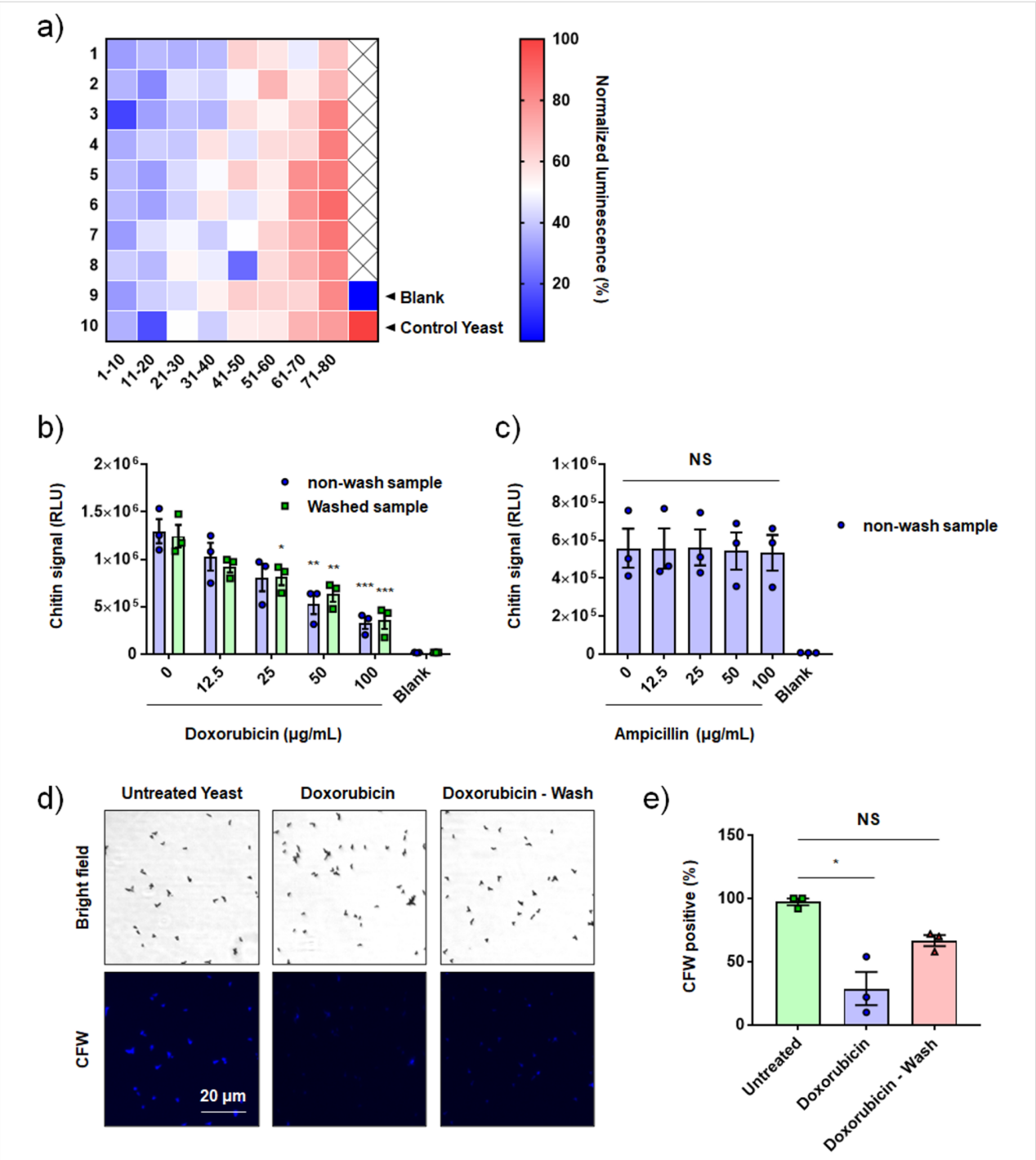


Figure 5: Screening of compounds that interact with cell wall chitin. (a) Cell surface chitin signals from compounds treated HKSc. The luciferase activity of control yeasts normalized to the luminescence of cell-free blank wells was set to 100%, with increased samples shown in red and decreased samples shown in blue. (b, c) Chitin signals from HKSc treated with (b) doxorubicin or (c) ampicillin (0–100 µg/mL, final). Blank indicates wells without yeast. Histograms show mean relative surface chitin ± SEM (n = 3). *p < 0.05, **p < 0.01, ***p < 0.001: significant difference vs control yeast (One-way ANOVA with Bonferroni's multiple test). (d) Microscopy images of total chitin stained with CFW in doxorubicin-treated yeast cells. (e) CFW-positive rate in doxorubicin-treated cells. Histograms show mean CFW-positive rate ± SEM (n = 3). *p < 0.05: significant difference vs untreated yeast (One-way ANOVA with Dunn's multiple test).

concentrations of ampicillin (Figure 5c). These results suggest that cell surface chitin may be masked by doxorubicin. To further validate this, live yeast cells were treated with doxorubicin, and total cell wall chitin was stained using a low-molecular-weight chitin-binding dye, Calcofluor white (CFW). Quantification of CFW-positive cells revealed a significant decrease

following doxorubicin treatment, while washing the treated cells increased the number of positive cells (Figure 5d,e). This result supports an interaction between doxorubicin and cell wall chitin.

Real-time monitoring of pharmaceutical adsorption on the yeast bio-interface

From the screening results, doxorubicin, which showed pronounced adsorption onto yeast, and ampicillin, which exhibited negligible adsorption, were selected as model compounds, and their adsorption behavior was evaluated by SPR measurements. Importantly, doxorubicin can enter the environment through hospital effluents and wastewater treatment processes. It is known that conventional wastewater treatment does not completely remove such compounds [26]. Doxorubicin, along with other anticancer agents, has been increasingly discussed in relation to emerging environmental contaminants due to concerns regarding persistence and potential toxicity to aquatic organisms [27].

The optical fiber SPR sensor with the yeast bio-interface was immersed in ultrapure water, followed by stepwise addition of a doxorubicin solution. Upon addition of doxorubicin, the SPR signal increased immediately (Figure 6a). Furthermore, with in-

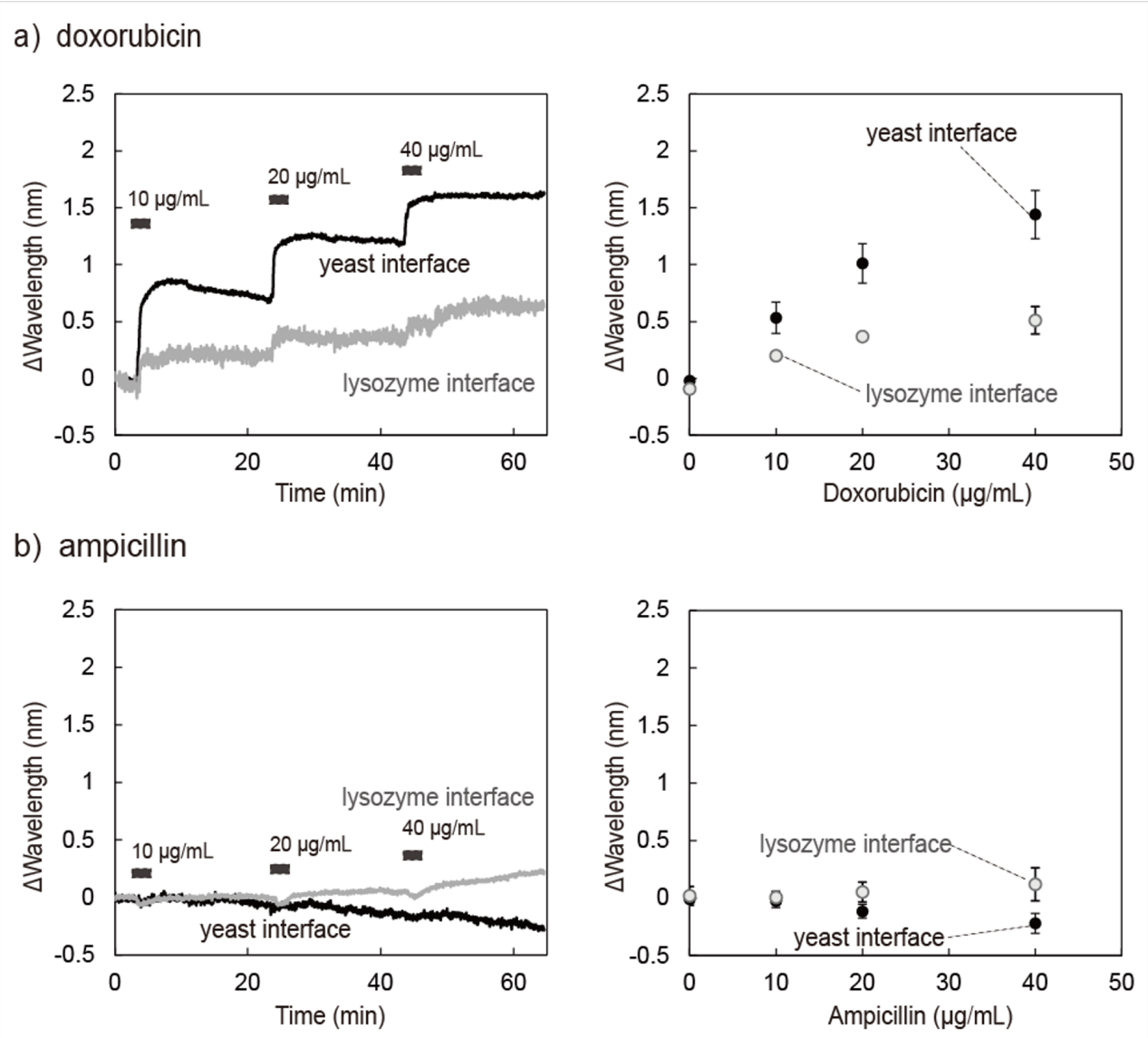


Figure 6: Responses of the optical fiber SPR sensor with a yeast-immobilized interface to (a) doxorubicin and (b) ampicillin. The left panels show sensorgrams representing changes in SPR resonance wavelength upon analyte addition; the black line corresponds to the yeast-immobilized optical fiber SPR sensor, while the gray line represents the lysozyme-functionalized optical fiber SPR sensor. Black squares indicate the time points of yeast suspension addition, and the concentrations shown correspond to the final concentrations after addition. The right panels show the dependence of the resonance wavelength shift on pharmaceuticals concentration. Error bars represent the standard deviation (n = 3).

creasing doxorubicin concentration, the SPR signal measured 20 min after addition, corresponding to the equilibrium value, also increased (Figure 6b). These results indicate that doxorubicin adsorbs onto the yeast surface in a concentration-dependent manner. In contrast, no significant increase in the SPR signal was observed for the lysozyme interface without immobilized yeast. Doxorubicin is composed of an anthracycline-based aromatic polycyclic structure and a sugar moiety containing an amino group. These structural features may enable multiple interactions with the yeast cell wall. For example, the aromatic polycyclic structure might facilitate hydrophobic interactions with hydrophobic regions of the cell wall, while the amino group may become protonated under near-neutral pH conditions, potentially enabling electrostatic interactions with negatively charged sites on the yeast surface. In addition, the aromatic rings may form π–π interactions with aromatic residues in cell wall proteins. The cooperative contribution of these interactions may be responsible for the relatively strong adsorption of doxorubicin onto the yeast surface. However, the proposed interaction mechanism remains speculative and is not directly supported by experimental evidence in this study. In contrast, when ampicillin was added, no significant increase in the SPR signal, as observed for doxorubicin, was detected (Figure 6c,d). This result indicates that ampicillin exhibits little adsorption onto the yeast surface, consistent with the screening results obtained using the chemiluminescence probe. Ampicillin is a relatively small molecule with a β-lactam structure and contains both carboxyl and amino groups; however, it is overall highly hydrophilic. Moreover, because ampicillin lacks an extended hydrophobic surface such as an aromatic polycyclic structure, it is expected to be less likely to form hydrophobic interactions with the cell wall. In addition, under near-neutral pH conditions, ampicillin predominantly exists as a zwitterion or partially negatively charged species, which may weaken electrostatic interactions with negatively charged sites on the yeast surface. These findings demonstrate that the yeast bio-interface-type optical fiber SPR sensor enables real-time evaluation of the adsorption behavior of pharmaceuticals onto yeast.

Conclusion

In this study, we established a method for monitoring film thickness during the electroless Ni plating process in the fabrication of an optical fiber SPR sensor by measuring the absorbance of transmitted light. A strong linear relationship was obtained between absorbance and the thickness of the Ni thin film, demonstrating that absorbance measurements enable reproducible formation of gold thin films suitable for SPR sensing. The optical fiber SPR sensor fabricated using this method exhibited sensitivity and a linear response range comparable to those of sensors prepared by conventional sputtering and vacuum evaporation methods when evaluated using sucrose solutions. These results indicate that a high-performance SPR sensor can be constructed through a simple plating process. Further, a spray-based immobilization method was proposed for yeast fixation onto the gold nanointerface, enabling the construction of a yeast bio-interface-type optical fiber SPR sensor. Using this sensor, the adsorption behavior of pharmaceuticals onto yeast was successfully monitored in real time. In particular, a concentration-dependent increase in the SPR signal was observed for doxorubicin, whereas no significant signal change was detected for ampicillin. These findings suggest that the interactions between yeast cell walls and pharmaceutical molecules depend on molecular structure and charge state.

In the future, the proposed method is expected to be applicable to in situ measurements in environmental waters, such as rivers and lakes. In natural aquatic environments, a wide variety of chemical constituents coexist and interact competitively with the yeast cell wall. Because faithfully reproducing such complex interfacial interactions under laboratory conditions is challenging, the proposed method has the potential to enable the direct evaluation of adsorption behavior in real environmental waters. Furthermore, the selectivity of the platform can be tailored by changing the immobilized microorganism. Different microorganisms possess distinct cell wall architectures and surface properties, resulting in different interaction profiles with chemical substances, potentially enabling the evaluation of a broader range of molecule–cell wall interactions. The proposed platform is expected to serve as a biological screening tool for evaluating the overall interactions between complex environmental samples and microorganism surfaces.

Experimental

Chemicals and materials

Unless otherwise specified, all reagents used in this study were of analytical grade. Dilute nitric acid, sulfuric acid, ethanol, glycine, acetone, silica gel, 0.1 M hydrochloric acid, sucrose, sodium dihydrogen phosphate, and disodium hydrogen phosphate were purchased from Kanto Chemical Co., Inc. (Tokyo, Japan). Hydrogen peroxide, Ni(II) sulfate hexahydrate, trisodium citrate dihydrate, 3-aminopropyltrimethoxysilane (APS), anhydrous toluene, palladium(II) chloride, sodium borohydride, 10% glutaraldehyde solution, ampicillin, Dulbecco's phosphate-buffered saline (D-PBS) without calcium and magnesium, dimethyl sulfoxide (DMSO), and Tween 20 were purchased from FUJIFILM Wako Pure Chemical Corporation (Osaka, Japan). Bovine serum albumin (BSA), Calcofluor white (CFW), and sodium hypophosphite were obtained from Sigma-Aldrich (St. Louis, MO, USA). Sodium dodecyl sulfate (SDS), lysozyme from chicken egg, and doxorubicin hydrochloride were purchased from Tokyo Chemical Industry Co., Ltd. (Tokyo, Japan). PlusOne Tris was purchased from Amersham

Biosciences. An antimicrobial compound library consisting of 80 compounds dissolved in DMSO at a stock concentration of 10 mM (Supporting Information File 1, Table S1) was purchased from Selleck Chemicals (Houston, TX, USA). The gold plating solution used for nickel-to-gold displacement plating was kindly provided by HIKIFUNE Co., Ltd. All water used in all experiments was purified using a PURELAB Flex 3 system (Veolia Jenets K.K., Tokyo, Japan).

Real-time monitoring system for Ni thin-film formation

A system for real-time monitoring of the thickness of Ni nanofilms formed by electroless plating is shown in Figure 1a. The system consists of a power LED (OSW4XNE3C1E, Opto-Supply Ltd., Hong Kong, China), a custom-built power supply for the LED, a bare fiber adapter (BFA-KIT, Ocean Insight, FL, USA), an optical fiber cable (M28L01, Thorlabs Inc., NJ, USA), and a spectrometer (USB4000, USB4E03214, Ocean Insight, FL, USA). In addition, a microheater, a power supply for heating, a relay, and a temperature controller were used to heat the Ni plating solution. Light emitted from the power LED was directed onto the end face of the fiber core, and the transmitted light emitted from the opposite end was guided through the optical fiber cable and detected by the spectrometer. The transmitted light intensity was measured at intervals of 0.1 s, and the monitoring wavelength was set at 550 nm. The transmitted light intensity was converted into absorbance using dedicated software, Optical Fiber SPR Monitor, Version 1.0.3.0 (Kyusyu Keisokki Co., Ltd., Fukuoka, Japan). The absorbance ($-\log I_t/I_0$) was calculated from the ratio of the transmitted light intensity at time t (I_t) to that at the start of the Ni plating reaction (I_0).

Amination of optical fiber surface

An optical fiber with a core diameter of 400 μm (FT400EMT, Thorlabs Inc., NJ, USA) was cut to a length of approximately 130 mm, and both end faces were polished to a smooth finish using a fiber polishing machine (Radian TrigLTTM, KRELL-TECH, NJ, USA). A section of the jacket approximately 5 mm in length was removed from one end using a fiber buffer stripper (T21S31, Thorlabs Inc., NJ, USA), and the cladding was subsequently removed with acetone-soaked cotton to expose the fiber core. The exposed fiber core was immersed in a piranha solution prepared by mixing hydrogen peroxide and sulfuric acid at a volume ratio of 1:3, followed by thorough rinsing with ultrapure water. The cleaned fiber was then dried for more than 1 h in a constant-temperature oven set at 120 °C (OFW-300V-R, AS ONE, Osaka, Japan). To introduce amino groups onto the fiber core surface, the exposed core was immersed in a 1.0% (v/v) solution of 3-aminopropyltrimethoxysilane (APS) prepared in toluene, and incubated at 40 °C with stirring at 100 rpm. After 1 h, the fiber was removed from the APS solution and dried at room temperature.

Monitoring of absorbance changes during electroless Ni plating

A Ni plating solution was prepared with ultrapure water containing 110 mM Ni(II) sulfate hexahydrate, 93 mM sodium hypophosphite, 270 mM glycine, 93 mM trisodium citrate dihydrate, and 0.5% (v/v) SDS. One milliliter of this solution was placed in a glass vial and heated to 85 °C using a coil connected to a heating unit (Figure 7). The exposed fiber core was first immersed in a 0.5% (w/v) Pd solution prepared in 0.1 M hydrochloric acid for 3 min at room temperature to adsorb Pd^{2+} ions, followed by immersion in a 0.1% (w/v) sodium borohydride solution prepared in ethanol for 3 min. Subsequently, the optical fiber was immersed in the Ni plating solution maintained at 85 °C to initiate plating. The absorbance was calculated from the transmitted light intensity immediately after immersion (I_0) and at a given time t (I_t), and the change in absorbance was monitored in real time. Electroless Ni plating was continued until the absorbance reached a value of 0.85.

Monitoring of the thickness of gold nanofilms formed by electroless Ni/Au plating

A volume of 1.0 mL of Au plating solution was transferred into a glass vial and heated to 84 °C. An optical fiber coated with a Ni film was immersed in the heated gold plating solution, and the Ni thin film was replaced with a gold thin film via a galvanic displacement reaction based on the difference in ionization tendency. The thickness of the Au layer depends on that of the underlying Ni thin film; therefore, electroless Ni/Au plating was conducted for 2 min, with an additional 25 s of reaction applied if necessary.

Thickness measurement of metal thin films formed by electroless plating

The thickness of the Ni film formed on the optical fiber core surface by electroless plating was evaluated by step-height measurement using an atomic force microscope (AFM5100N, Hitachi High-Technologies Co., Ltd., Tokyo, Japan). For the measurement, a portion of the Ni thin film on the optical fiber surface was chemically dissolved and removed using a dilute nitric acid solution to expose the underlying glass substrate. Subsequently, an area including both the Ni film surface and the exposed glass surface was scanned by AFM in tapping mode, and the height difference between the Ni surface and the glass surface was determined as the step height. The height profile was obtained by line profile analysis of the acquired AFM images, and the average height difference between the Ni film surface and the glass substrate surface was defined as the film thickness. Measurements were performed at multiple locations,

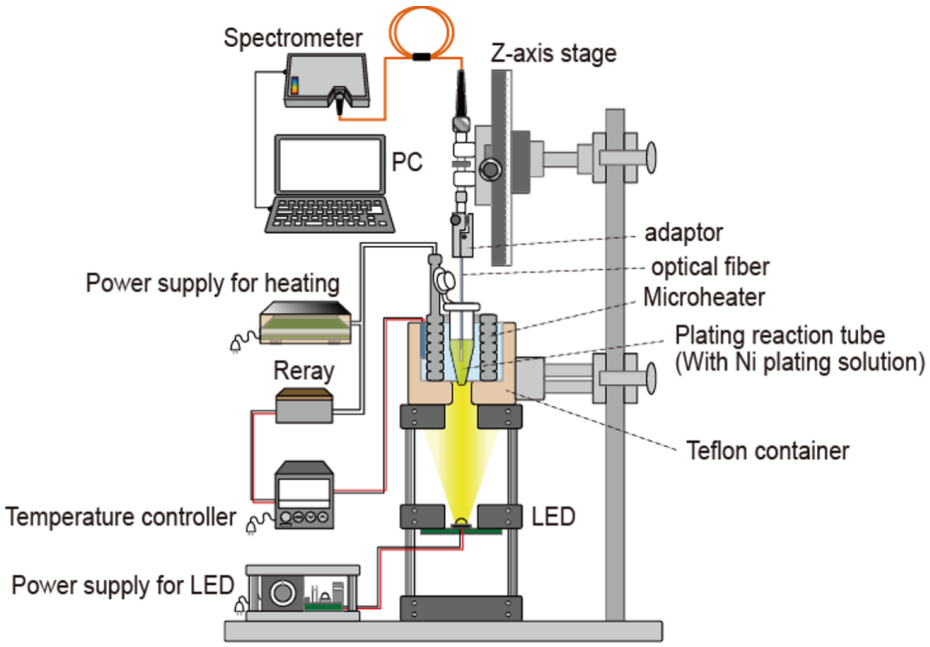


Figure 7: Schematic illustrations of the experimental setups. Monitoring system for the electroless Ni plating reaction.

and the average of the obtained values was reported as the thickness of the Ni film.

Evaluation of the fabricated sensor using sucrose measurements

The performance of the fabricated sensor was evaluated using the optical fiber SPR measurement system [18]. The system consists of a halogen lamp (KBEX-151B, Nissei Electric Co., Shizuoka, Japan), a bifurcated optical fiber (Thorlabs), and a spectrometer, to which the fabricated optical fiber SPR sensor was connected for measurements. Light emitted from the halogen lamp was guided to the sensor through the bifurcated fiber, and the light reflected from the sensor was detected by the spectrometer via the same fiber. The reflected light intensity obtained from the sensor immersed in the sample solution was normalized by the reflected light intensity measured in air to obtain the SPR spectrum. The performance of the fabricated sensor was evaluated using aqueous sucrose solutions with concentrations up to 16% (w/v). The minimum of the obtained SPR spectrum was defined as the SPR wavelength, and the shift in SPR wavelength (ΔSPR wavelength) with changing sucrose concentration was defined as the SPR signal. Furthermore, the sensor response was evaluated by plotting the SPR signal as a function of sucrose concentration.

Yeast and culture

Brewer's yeast, *Saccharomyces cerevisiae* strain NBRC 10217, was purchased from NITE biological resource center (NBRC, Chiba, Japan). Yeast cells maintained on potato dextrose (PD) agar were suspended in D-PBS and inoculated into a 50 mL conical tube containing 15 mL of PD medium and incubated for 24 h at 30 °C with shaking (200 rpm, BR-23FP Bioshaker, TAITEC Co., Saitama, Japan). The cells were then washed with water, and an aliquot was heat-treated at 90 °C for 10 min to obtain heat-killed yeast cells (HKSc).

Yeast cell wall analysis

HKSc suspended in water (1×10^8 yeast cells/mL) was mixed with antimicrobial compound library (100 μM, final), newly purchased compounds in water, or control (1 v/v % DMSO or water), incubated for 30 min at 30 °C and heat-treated at 90 °C for 10 min. To assess dose-dependent responses, samples were also prepared in which cells were washed with water after drug treatment to remove free compound. Cell surface-exposed chitin amount was evaluated using a split-luciferase complementation (SLC) assay, as described previously [28]. In brief, yeast suspension (1×10^8 yeast cells/mL) was mixed in equal volume of chitin-specific protein probes (SmBiT- or LgBiT-fused hChit1-E140Q, 100 nM each) in assay buffer (PBS containing 1% BSA and 0.05% Tween 20). Reaction mixture was incubated in a 384-well white microplates (Greiner Bio-one, Frickenhausen, Germany) with shaking (400 rpm). After 30 min, luciferase substrate (Furimazine, Promega, WI, USA) was added to each well and reconstituted NanoLuc activity based on surface chitin amount was measured using a microplate reader (GloMax Discover Microplate Reader, Promega).

Fluorescence microscopy images

Live yeast cells suspension in water (2×10^6 yeast cells/mL) was mixed with doxorubicin hydrochloride (dissolved in water, 10 μg/mL, final), incubated for 1 h at 30 °C, followed by either no washing or three washes with pure water. For the total chitin staining, yeast cells were treated with 10 μg/mL of CFW solution and observed using a microscope equipped with DAPI filter (EVOS M5000 Imaging System, Thermo Fisher Scientific, MA, USA). Fifty yeast cells were randomly selected from bright-field images, and the proportion of CFW-positive cells was determined in the corresponding fluorescence images of the same field.

Statistical analysis

All statistical analyses were performed using GraphPad Prism 7.0 (GraphPad Software, CA, USA). Based on the results of the normality test, significant differences were analyzed by one-way ANOVA followed by multiple comparisons using Dunn's test or Bonferroni's test.

Fabrication of a yeast bio-interface-type optical fiber SPR sensor

To form a protein layer on the surface of the optical fiber SPR sensor, the fiber was first immersed in 10 mM phosphate buffer (PB, pH 7.4), and stabilization of the SPR signal was confirmed. Subsequently, a lysozyme solution at 200 μg/mL prepared in 10 mM PB (pH 7.4) was added to the PBS to achieve a final concentration of 10 μg/mL. The sensor was incubated in the solution until the SPR wavelength shift before and after lysozyme addition reached approximately 3 nm. Afterward, the sensor was immersed in a 1% glutaraldehyde (GA) solution (50 mM PB, pH 7.4) for 1 h to introduce aldehyde groups onto the surface. A yeast suspension with a cell concentration of 1.5×10^5 yeast cells/mL was sprayed onto the GA-treated optical fiber SPR sensor surface using an airbrush, handpiece, connected to an oil-free air compressor (PROFIX NITRO-COMP V1, GSI Creos, Japan), generating fine droplets. After spraying, the sensor was left to stand for 1 h to allow immobilization of the yeast cells, followed by washing with water to remove non-immobilized cells. The sensor then underwent a blocking treatment by immersion in 10 mM Tris buffer (pH 7.4) for 20 min. Finally, the sensor was left to stand in 85 μL of water for 10 min to stabilize the sensor interface.

Real-time measurement of pharmaceutical adsorption onto yeast

The yeast bio-interface-type optical fiber SPR sensor was immersed in 85 μL of water, and after stabilization of the SPR signal, 5 μL aliquots of doxorubicin or ampicillin solutions prepared in water were sequentially added to achieve final concentrations of 10, 20, and 40 μg/mL. The SPR signal after the addition of the pharmaceuticals was recorded in real time.

Supporting Information

Supporting Information File 1

Additional figure and table.
[https://www.beilstein-journals.org/bjnano/content/supplementary/2190-4286-17-89-S1.pdf]

Funding

This study was supported by Grants-in-Aid for Scientific Research (KAKENHI 23K27411 and 23H03865) from the Japan Society for the Promotion of Science (JSPS), and by the JST SPRING program (Grant Number JPMJSP2134).

Author Contributions

Natsumi Kitaya: formal analysis; methodology; writing – review & editing. Daisuke Yamanaka: conceptualization; data curation; funding acquisition; methodology; writing – review & editing. Kenji Morita: formal analysis. Ryota Naito: formal analysis. Hinako Suhara: formal analysis. Kento Suzuki: formal analysis. Hizuru Nakajima: investigation. Yukiko Moriiwa: investigation. Kazuhiro Morioka: visualization. Akio Yanagida: visualization. Atsushi Shoji: conceptualization; data curation; project administration; supervision; writing – original draft; writing – review & editing.

ORCID® iDs

Hizuru Nakajima - https://orcid.org/0009-0000-3480-6537
Yukiko Moriiwa - https://orcid.org/0000-0002-4069-2780
Akio Yanagida - https://orcid.org/0000-0002-2783-7033

Data Availability Statement

Data generated and analyzed during this study is available from the corresponding author upon reasonable request.

References

1. Lesage, G.; Bussey, H. *Microbiol. Mol. Biol. Rev.* **2006,** *70,* 317–343. doi:10.1128/mmbr.00038-05
2. Klis, F. M.; Boorsma, A.; De Groot, P. W. J. *Yeast* **2006,** *23,* 185–202. doi:10.1002/yea.1349
3. Orlean, P. *Genetics* **2012,** *192,* 775–818. doi:10.1534/genetics.112.144485
4. Staroń, P.; Chwastowski, J. *Appl. Sci.* **2024,** *14,* 655. doi:10.3390/app14020655
5. Mun, S.-B.; Cho, B.-G.; Jin, S.-R.; Lim, C.-R.; Yun, Y.-S.; Cho, C.-W. *J. Environ. Manage.* **2023,** *334,* 117507. doi:10.1016/j.jenvman.2023.117507

6. de Lima Schlösser, L. M.; Simões, C. T.; Sarturi, J. A.; da Silva, C. R.; Laber, I. F.; Franco, D. S. P.; Mallmann, C. A. *Mycotoxin Res.* **2024,** *40,* 111–121. doi:10.1007/s12550-023-00508-z
7. do Nascimento, J. M.; de Oliveira, J. D.; Rizzo, A. C. L.; Leite, S. G. F. *Biotechnol. Rep.* **2019,** *21,* e00315. doi:10.1016/j.btre.2019.e00315
8. Chen, C.; Wang, J.-L. *Biomed. Environ. Sci.* **2007,** *20,* 478–482.
9. Zhang, Y.; Fan, C.; Meng, Q.; Diao, Z.; Dong, L.; Peng, X.; Ma, S.; Zhou, Q. *Bull. Environ. Contam. Toxicol.* **2009,** *83,* 708–712. doi:10.1007/s00128-009-9847-9
10. Tan, Y.; Chen, L.; Li, K.; Lou, B.; Liu, Y.; Liu, Z. *J. Controlled Release* **2022,** *346,* 358–379. doi:10.1016/j.jconrel.2022.04.032
11. Dou, F.; Lu, Y.; Nitin, N. *Int. J. Pharm.* **2021,** *609,* 121123. doi:10.1016/j.ijpharm.2021.121123
12. Sagar Jena, P.; Pradhan, A.; Prakash Nanda, S.; Kishore Dash, A.; Naik, B. *Mater. Today: Proc.* **2022,** *67,* 1140–1146. doi:10.1016/j.matpr.2022.07.306
13. Ojima, Y.; Kosako, S.; Kihara, M.; Miyoshi, N.; Igarashi, K.; Azuma, M. *Sci. Rep.* **2019,** *9,* 225. doi:10.1038/s41598-018-36306-2
14. Wang, J.; Chen, C. *Biotechnol. Adv.* **2006,** *24,* 427–451. doi:10.1016/j.biotechadv.2006.03.001
15. Bayhan, Y. K.; Keskinler, B.; Çakici, A.; Levent, M.; Akay, G. *Water Res.* **2001,** *35,* 2191–2200. doi:10.1016/s0043-1354(00)00499-1
16. Aeini, K.; Zoghi, A.; Khosravi-Darani, K. *Curr. Microbiol.* **2025,** *82,* 368. doi:10.1007/s00284-025-04343-6
17. Rusu, L.; Grigoraş, C.-G.; Suceveanu, E. M.; Simion, A.-I.; Dediu Botezatu, A. V.; Istrate, B.; Doroftei, I. *Materials* **2021,** *14,* 4810. doi:10.3390/ma14174810
18. Morita, K.; Morioka, K.; Nakajima, H.; Uchiyama, K.; Yanagida, A.; Shoji, A. *Anal. Sci.* **2021,** *37,* 625–631. doi:10.2116/analsci.20p400
19. Shoji, A.; Nakajima, M.; Morioka, K.; Fujimori, E.; Umemura, T.; Yanagida, A.; Hemmi, A.; Uchiyama, K.; Nakajima, H. *Talanta* **2022,** *240,* 123162. doi:10.1016/j.talanta.2021.123162
20. Hlubina, P.; Ciprian, D.; Kadulová, M. *Proc. SPIE* **2015,** *9450,* 94500A. doi:10.1117/12.2070238
21. Suzuki, H.; Sugimoto, M.; Matsui, Y.; Kondoh, J. *Sens. Actuators, B* **2008,** *132,* 26–33. doi:10.1016/j.snb.2008.01.003
22. Agudelo, D.; Bourassa, P.; Bruneau, J.; Bérubé, G.; Asselin, É.; Tajmir-Riahi, H.-A. *PLoS One* **2012,** *7,* e43814. doi:10.1371/journal.pone.0043814
23. Das, S.; Hazarika, Z.; Sarmah, S.; Baruah, K.; Rohman, M. A.; Paul, D.; Jha, A. N.; Singha Roy, A. *J. Photochem. Photobiol., B* **2020,** *205,* 111825. doi:10.1016/j.jphotobiol.2020.111825
24. Ota, C.; Tanaka, S.-i.; Takano, K. *Molecules* **2021,** *26,* 420. doi:10.3390/molecules26020420
25. Wang, Q.; Ma, X.; He, J.; Sun, Q.; Li, Y.; Li, H. *Spectrochim. Acta, Part A* **2016,** *153,* 612–618. doi:10.1016/j.saa.2015.09.017
26. Mahnik, S. N.; Lenz, K.; Weissenbacher, N.; Mader, R. M.; Fuerhacker, M. *Chemosphere* **2007,** *66,* 30–37. doi:10.1016/j.chemosphere.2006.05.051
27. Nassour, C.; Barton, S. J.; Nabhani-Gebara, S.; Saab, Y.; Barker, J. *Environ. Sci. Pollut. Res.* **2020,** *27,* 1339–1347. doi:10.1007/s11356-019-07045-2
28. Yamanaka, D.; Suzuki, K.; Kimura, M.; Oyama, F.; Adachi, Y. *Carbohydr. Polym.* **2022,** *282,* 119125. doi:10.1016/j.carbpol.2022.119125

License and Terms

This is an open access article licensed under the terms of the Beilstein-Institut Open Access License Agreement (https://www.beilstein-journals.org/bjnano/terms), which is identical to the Creative Commons Attribution 4.0 International License (https://creativecommons.org/licenses/by/4.0). The reuse of material under this license requires that the author(s), source and license are credited. Third-party material in this article could be subject to other licenses (typically indicated in the credit line), and in this case, users are required to obtain permission from the license holder to reuse the material.

The definitive version of this article is the electronic one which can be found at:
https://doi.org/10.3762/bjnano.17.89

BEILSTEIN JOURNAL OF NANOTECHNOLOGY

Nanoscale-enabled cross-scale chemical sensing for underwater monitoring and beyond

Tatsuhiro Fukuba*[1,2], Nicolas Clement[3], Henri Vo Van Qui[3], Yui Sasaki[4], Koji Toma[5] and Tsuyoshi Minami[2]

Perspective

Open Access

Address:
[1]Research Institute for Marine Technology and Engineering, Marine Engineering Science Center, Marine Observational Technology Research Group, Japan Agency for Marine-Earth Science and Technology, Natsushima-Cho 2-15, Yokosuka, Kanagawa, 237-0061, Japan, [2]Institute of Industrial Science, The University of Tokyo, 4-6-1 Komaba, Meguro-ku, Tokyo, 153-8505, Japan, [3]LIMMS/CNRS-IIS, 4-6-1 Komaba, Meguro-ku, Tokyo, 153-8904, Japan, [4]Research Center for Advanced Science and Technology, The University of Tokyo, Komaba 4-6-1, Meguro-ku, Tokyo, 153-8904, Japan and [5]College of Engineering, Shibaura Institute of Technology, 3-7-5 Toyosu, Koto-ku, Tokyo, 135-8548, Japan

Email:
Tatsuhiro Fukuba* - bafuk@jamstec.go.jp

* Corresponding author

Keywords:
cross-scale sensing; lab-on-a-chip (LOC); nanoscale sensing; underwater

Beilstein J. Nanotechnol. **2026,** *17,* 1505–1515.
https://doi.org/10.3762/bjnano.17.103

Received: 27 March 2026
Accepted: 13 October 2026
Published: 30 October 2026

This article is part of the thematic issue "Nanotechnology for cross-scale analysis: comprehensive evaluation of water environments".

Associate Editor: P. Ayala

© 2026 Fukuba et al.; licensee Beilstein-Institut.
License and terms: see end of document.

Abstract

In aquatic environments, such as oceans, lakes, and rivers, molecular-level chemical reactions and the distribution of chemical species are related to global environmental changes through various biogeochemical processes. Understanding this relationship requires addressing cross-scale challenges at two distinct levels: overcoming interfacial physical constraints, such as Debye screening in high-salinity waters, at the sensing level and bridging local microscale measurements with macroscale environmental dynamics at the observational level. In this paper, we describe sensing technologies that can enable cross-scale sensing in aquatic environments. Here, we focus on nanoscale interfacial sensing and molecular recognition technologies, as well as lab-on-a-chip technologies for *in situ* measurements including power-efficient pumping technologies. Additionally, underwater observation platforms that link the local chemical sensing and global processes are overviewed. Beyond environmental applications, these sensing technologies offer a cross-disciplinary approach that can be extended to analyze biological systems facing similar physicochemical constraints.

Introduction

Aquatic environments such as oceans, lakes, and rivers are complex systems with interactions among a variety of biogeochemical processes across a wide range of spatial and temporal scales. Distribution of dissolved chemical species and molecular-level biogeochemical processes affect not only the behavior of individuals, communities, and single ecosystems, but also

global environmental changes. In ocean environments, from the surface to the deep sea, from the coast to the open ocean, environmental parameters such as temperature, salinity, and concentrations of dissolved chemicals change dynamically across various spatiotemporal scales. These variations propagate across the sediment–water and air–water interfaces and connect the processes within the Earth system. Because these variations have a wide temporal range, it is difficult to capture the whole picture only with a single sensor technology. Moreover, appropriate observation platforms are necessary in addition to sensing devices for practical *in situ* measurements. For example, slight fluctuations in the proton concentration, which affect the equilibrium of the carbonate system in seawater, can be described as acid–base reactions at the molecular level. However, such small changes influence coral calcification rates and plankton community structure and may ultimately affect the marine carbon cycle and global climate change [1]. To measure variations of proton concentration, generally expressed as pH, reliably *in situ*, sensing devices that can capture pH variations with high spatiotemporal resolution are necessary. Furthermore, bridging localized chemical sensing to global monitoring requires a scalable approach that integrates miniaturized sensor devices with autonomous and distributed observation platforms. The international Argo program, which utilizes thousands of profiling floats across the ocean environment, is a representative example of such scalable global observation networks [2]. Recently, this program was expanded to Biogeochemical Argo (BGC-Argo) for the measurement of biogeochemical processes on individual floats with sensors for dissolved oxygen, pH, and nutrients [3]. These advances show the importance of integrating highly miniaturized and reliable chemical sensors and scalable autonomous platforms to realize large-scale environmental monitoring. To address this issue, we propose a cross-scale sensing approach based on molecular-scale sensing, microfluidics to support the sensing, and observation platforms capable of local and global environmental monitoring. Furthermore, this approach may also become a technological foundation for future biological and in vivo sensing applications because aquatic and biological environments share several physicochemical constraints.

Perspective

Field-proven sensor technologies

Ion-sensitive field-effect transistors (ISFETs)

In aquatic environments, a variety of chemical sensors and biosensors have been developed and utilized for the rapid detection and quantification of dissolved chemical species [4]. For example, glass electrodes are widely used for underwater potentiometric pH measurements [5]. However, glass electrodes have limitations in terms of mechanical robustness and potential for further miniaturization due to their structure. Moreover, periodic maintenance and calibration are required due to the presence of a liquid junction. When such maintenance is not feasible, signal drift results in a decrease in measurement reliability [6]. Alternatively, ion-sensitive field-effect transistors (ISFETs) [7,8] have been noted as robust devices suitable for long-term *in situ* underwater measurements [9-14]. ISFETs are solid-state devices composed of silicon and dielectric materials, and their cavity-free structure provides resistance to hydrostatic pressure changes [9]. The sensitive area of ISFETs used for underwater applications is typically made of dielectric materials such as tantalum pentoxide (Ta_2O_5), aluminum oxide (Al_2O_3) [9], or silicon nitride (Si_3N_4) [14]. The dielectric layer is deposited under high-temperature conditions in clean-room environments, resulting in highly dense, defect-free, and thus mechanically robust and chemically stable crystalline or amorphous structures. Their low output impedance and CMOS compatibility have made ISFETs one of the most established underwater chemical sensors. In particular, pH-ISFETs have been evaluated *in situ*, including deep-sea environments, and their effectiveness has been successfully demonstrated [13]. In subsequent studies, their application has been expanded to the measurement of important carbonate system parameters such as the partial pressure of CO_2 (pCO_2) [10,14] and total alkalinity [15]. The response of the pH-ISFET arises from protonation and deprotonation reactions occurring at the metal oxide surface [7,8]. Because these reactions occur within the Debye screening length at the solid–liquid interface, the electric potential changes remain detectable even under high-ionic-strength conditions. However, when a functional layer is introduced onto the gate surface for the detection of specific target molecules, Debye screening can limit sensitivity in high-ionic-strength liquids such as seawater. A similar challenge exists in sensor operation within biological systems, which also exhibit high ionic strength comparable to that of seawater [16,17]. The variation in ionic strength from freshwater rivers (<10 mM) to brackish estuaries and marine environments (0.6–0.7 M) [18] makes the design of electrostatic sensing platforms increasingly challenging and complex (Figure 1). Therefore, overcoming the limitations of sensitivity caused by Debye screening is expected to be a key issue in advancing cross-scale sensing, which aims to link molecular-level information with macroscopic environmental processes.

Emerging technologies

Surface plasmon polariton-based optical sensing

To overcome the Debye screening limitation in high-ionic-strength environments, using functional layers with short-range molecular recognition mechanisms (e.g., aptamers) or employing transistor devices with nanoscale channel thickness are promising strategies. Alternatively, sensing modalities that detect signals beyond the Debye screening length are another

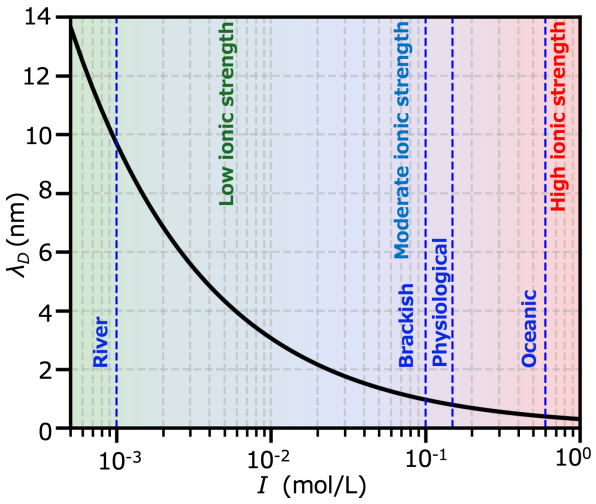


Figure 1: Debye length variation with typical ionic strength across river, brackish, physiological, and oceanic environments.

promising way to overcome this limitation. One of the representative examples is surface plasmon polaritons (SPPs) [19]. SPPs are waves formed by the collective motion of electrons at a metal surface, which create a localized electromagnetic field that extends slightly into the surrounding medium. The evanescent electromagnetic field typically extends about 100 to 200 nm into the medium, depending on the wavelength of the incident light and the dielectric properties of the material. Molecular binding events at the metal surface can be detected by SPPs based on changes in the local refractive index, because the sensing field extends beyond the Debye screening length even in environments with high ionic strength. Recent advances in multimodal interfacial characterizations further emphasize the utility of SPR-based sensing platforms for evaluating molecular adsorption and binding kinetics at solid–liquid interfaces [20]. In particular, integrating functional bio-interfaces onto optical fiber-based SPR platforms has emerged as a practical approach for real-time monitoring of molecular interactions and adsorption dynamics at solid–liquid interfaces [19,21]. This architecture provides a compact and flexible optical sensing platform suitable for marine applications. Indeed, SPR-based platforms have demonstrated practical utility in oceanography; for instance, portable SPR devices have been deployed for direct, sensitive detection of hazardous proteins in raw seawater [19]. Integrating such biorecognition platforms into optical fiber configurations further offers a direct-immersion approach for real-time, *in situ* biochemical sensing.

Nanoscale transistors (Nano-FETs)

NanoFET-based sensing devices are characterized by nanoscale channels and interfacial structures [22-24]. The application of nanoFETs is one of the promising approaches for chemical sensing under Debye screening constraints as they efficiently transduce surface potential modulation into electrical signals. The key significance of nanoFETs lies in nanoscale structures that directly translate molecular-scale phenomena into electrical signals. Therefore, transistor technologies based on nanomaterials and nanoscale interfacial design become a crucial technological foundation for advancing cross-scale sensing under high-ionic-strength conditions, including marine environments. In underwater environments, some metal ions show toxic effects on ecosystems, while certain kinds of trace metals, such as iron, also function as essential factors for biological activity [25]. Therefore, the highly sensitive and quantitative determination of dissolved metal ions is important not only for assessing ecosystem impacts but also for understanding material cycling in the ocean and for exploring underwater mineral resources. As one of the examples, nanoFET-based sensors with selective membranes have been studied for the detection of heavy metal ions in aqueous environments [26].

To address Debye screening limitations, cross-scale target conversion strategies, wherein molecular recognition events are transformed into localized secondary chemical or ionic signals, offer an effective approach for high-salinity sensing. For example, Ono et al. integrated a graphene FET with femtoliter microfluidic droplets to detect pathogens captured by antibodies beyond the Debye screening length. In this system, a target-associated enzyme converts the substrate into diffusible ammonia, which accumulates in the microdroplet and directly adsorbs onto the graphene channel to yield an electrical signal [27]. Furthermore, adopting CRISPR-Cas enzymatic reactions serves as a powerful signal conversion strategy to indirectly detect target DNA that is otherwise challenging to capture directly in high-salinity environments. This approach effectively broadens the applicability of electrical and optical sensing devices for marine biosensing [28].

In recent years, a new approach has been proposed in which ion-specific interfacial interactions are directly converted into electrical signals using a nanoFET. Sivakumarasamy et al. demonstrated the detection of multiple ion species in serum at physiological ionic strength, without the use of selective membranes, by employing nanotransistor-based ion sensors [29]. Furthermore, our recent work demonstrated the quantitative detection of lanthanum (La^{3+}), a representative rare-earth element, using a liquid-gated nanoFET without selective recognition layers [30]. This approach presents a sensing mechanism distinct from conventional Debye screening-limited sensing by exploiting differential interfacial interactions of ions (non-coulombic ion-specific interactions) at the nanoscale channel surface. The limitation of this approach is the need to imple-

ment the standard addition calibration method. However, it has the advantage of suppressing long-term drift as the calibration is inherently embedded within the measurement process. Furthermore, such calibration procedures can be integrated and automated using lab-on-a-chip (LOC) technology, making them effective for *in situ* environmental sensing.

Molecular recognition at the nanoscale

In cross-scale sensing, target molecules and ions exhibit diverse geometries, sizes, and charges; therefore, appropriate recognition materials should be designed on principles of molecular recognition chemistry. In this context, detection mechanisms can be classified into two types, namely, selective and cross-reactive detection. The specificity of recognition materials based on the lock-and-key principle enables selective detection through high binding affinity. Meanwhile, as observed in the mammalian olfactory system, simultaneous detection is achieved through combinatorial responses of multiple cross-reactive receptors exhibiting moderate binding affinities. For example, aptamers represent one of the possible recognition elements due to their small size, structural tunability, and compatibility with high-ionic-strength conditions; they have been applied to FET-based chemical sensors for selective detection [31]. Under Debye screening conditions, aptamers are practical recognition elements because their flexible three-dimensional structure allows bonding events and the resulting charge redistribution to occur in the vicinity of the semiconductor surface. Localized rearrangements of the structure of the molecular backbone can still induce detectable changes of the interfacial potential at the sensing surface, even when the molecular length exceeds the Debye length under physiological conditions [17,32]. Actually, notable results have been reported where organic FETs functionalized with DNA aptamer-modified gold nanoparticles successfully achieved selective target detection even in undiluted seawater [33].

As another example, enzyme-based reaction sensing mechanisms also represent a promising approach. Enzymatic reactions induce local changes in proton concentration and other ionic species at the sensor interface, enabling effective signal transduction via ISFETs even under Debye-screened conditions [34]. For applications in extreme environments, such as the deep sea, characterized by high pressure and low temperature, it is necessary to carefully assess possible changes in enzyme activity and stability prior to deployment of the sensor devices based on enzymatic reactions. As outlined above, nanoscale molecular design of recognition elements is essential not only for selectivity but also for effective electrical readout. The integration of molecular recognition mechanisms with transistors has utilized a variety of approaches for clinical applications [35].

In contrast to recognition materials based on the lock-and-key principle, molecular self-assembly systems have been investigated as effective recognition platforms for simultaneous detection in aqueous environments [36]. Such systems are attractive because they utilize reversible interactions to construct cross-reactive chemical sensors without requiring complex synthetic processes. For example, Sasaki et al. reported a molecular self-assembled chemical sensor array based on the reversible formation and substitution reactions of boronate esters between target molecules and building blocks of chemical sensors. Spontaneous association and dissociation governed by dynamic covalent bonds generate distinct response patterns, enabling the qualitative identification and quantitative estimation of multiple metal ions, even under competitive ion conditions, using machine learning methods [37]. Furthermore, the concept of molecular self-assembly was expanded to a coordination binding-based sensor array utilizing catechol dyes and zinc(II) ions for oxyanion detection [38]. This chemical sensor array achieved both qualitative identification and quantitative measurement in natural water samples without any sample treatment. Currently, these sensor devices are being actively developed as simple and disposable paper-based technologies for rapid on-site analysis [39]. To apply this approach to marine environments, translating these self-assembled sensing chemistries into LOC-based colorimetric device formats or optodes represents a promising strategy for multiparameter underwater sensing. A systematic overview of these field-proven and emerging cross-scale sensing technologies is summarized in Table 1.

Enabling technologies

Lab-on-a-chip technology for fluid handling

As discussed earlier, nanoscale transistor technologies, functionalized sensing interfaces, and molecular recognition strategies have expanded the scope of *in situ* chemical measurements. Notably, some of these technologies have demonstrated sensing capability even under high-ionic-strength conditions, suggesting their relevance for challenging environments such as marine environments. However, practical implementation of these novel sensing technologies in real-world environments needs strategic design of the entire measurement system, including fluid handling for sample and reagent delivery and pretreatment. Analytical assays including sample pretreatment, reagent mixing, and chemical reactions fundamentally require integration with precise fluid handling systems integrated on sensor devices. In addition, a flow system is often required to enable sensor calibration for drift compensation, which can become significant during long-term continuous operation. Integrated flow systems may also enable periodic cleaning procedures to mitigate biofouling of the sensing interface, thereby reducing sensor drift during long-term operation [12]. Moreover, the inte-

Table 1: Overview of field-proven and emerging sensing technologies for cross-scale marine environmental monitoring.

Technology	Major target	Core sensing principle	Advantages	Current limitations	Ref.
Field-proven technologies					
pH-ISFETs	carbonate system parameters (pH, pCO_2, total alkalinity)	gate potential change via surface protonation/deprotonation	high stability, fast response, high pressure tolerance, CMOS compatibility	reference electrode drift, biofouling, need for periodic calibration	[7-15]
Emerging technologies					
surface plasmon polaritons	biomolecules (e.g., hazardous proteins), dissolved gases	surface plasmon resonance at metal–dielectric interfaces	label-free detection, non-coulombic sensing	temperature and salinity cross-sensitivity, surface biofouling	[19-21]
nanoscale transistors	specific ions (e.g., trace/heavy metals), nucleic acids	charge sensitivity and non-coulombic ion interactions at nanoscale interfaces	ultrahigh sensitivity, high miniaturization, low power consumption	severe Debye screening in seawater, complex nanofabrication	[22-26,29, 30]
molecular recognition at the nanoscale	small molecules, trace metals, biomarkers	conformational changes bringing charges within the Debye length, dynamic self-assembly and competitive ligand/ion displacement	can mitigate Debye screening limitations through conformational/charge-redistribution mechanisms	challenges in instrumentation and system integration, biofouling, receptor/enzyme instability	[17,31-39]

gration of flow systems with optical components is essential for analytical measurements based on molecular recognition strategies utilizing colorimetric principles, which require controlled mixing of samples and reagents. In label-free nanoFET sensor devices based on ion-specific interfacial interactions, a series of standard solutions, in principle, must be introduced quantitatively to obtain corresponding sensor responses. LOC technologies have been increasingly developed as an essential approach for implementing flow-based systems in field applications [40,41]. For example, LOC technology has been applied to continuous measurements [42,43] to achieve miniaturization of *in situ* spectrophotometric pH measurement systems. By integrating microfluidic channels, mixers, pumps, and valves, *in situ* calibration and automated measurement sequences become possible for long-term operation of chemical sensors.

In marine LOC devices, achieving efficient reagent mixing under high Péclet number (Pe) conditions without excessive pressure drop is a key design challenge. To prevent measurement errors caused by Taylor–Aris dispersion during *in situ* calibration, microfluidic handling must minimize boundary mixing between chemicals and samples or calibration standards. Droplet microfluidics is a powerful tool offering rapid internal convection. For optical or rapid colorimetric LOC systems, segmented microfluidics using droplet or gas-plug boundaries can effectively reduce axial dispersion [40]. However, oil-phase contamination may interfere with FET sensing and affect sensor performance. Single-phase continuous microfluidics with low-resistance passive mixing may therefore be advantageous for simple and robust *in situ* sensing devices. Passive mixing structures, such as curved microchannels inducing Dean flow or grooved channels generating chaotic advection [44], can promote mixing while maintaining relatively low hydrodynamic resistance. Furthermore, for long-term monitoring where rapid sample switching is not required, stop-flow operation [40] can be leveraged to enable passive diffusive mixing while reducing flow-induced dispersion and continuous pumping power consumption.

While LOC technologies enable the miniaturization of sensors and *in situ* analysis devices, the power consumption of pumping systems remains a major challenge for long-term deployment. It is a critical issue especially for the deployments using well-miniaturized ocean observation platforms with limited electric power supply. Furthermore, stable fluid flow with minimal pulsation is needed for nanoscale sensing particularly in freshwater or low-ionic-strength solutions because streaming potentials may influence the electrical response of nanoscale transistor sensors [45]. Therefore, the successful field deployment of nanoscale sensing technologies depends on the practical implementation of power-efficient and stable pumping technologies. In recent years, low-power or passive pumping technologies have been explored for LOC systems as alternatives to mechanically actuated pumps and valves, which typically require substantial electrical power [46]. Recent advances and practical integrations of power-efficient and power-free pumping technologies specifically targeted for *in situ* underwater measurements have also been discussed in a previous review [47]. One

example of a stable and energy-efficient pumping technology is the electroosmotic pump (EOP), which is based on electroosmosis. By applying an electric field along a microchannel with charged walls, the motion of counterions within the electric double layer is induced. Through viscous coupling, this ionic motion results in bulk fluid flow [48]. One of the advantages of EOPs is the ability to generate a stable flow with minimal pulsation, owing to the absence of mechanically moving parts. However, in high-ionic-strength solutions, such as physiological fluids or seawater, the efficiency of EOPs may decrease due to increased electrical conductivity and Joule heating [48]. Although high conductivity can make the direct pumping of certain samples challenging, it has also motivated the development of advanced indirect pumping approaches that utilize working fluids to maintain efficiency. EOPs can also serve as effective pressure sources for actuating integrated microvalves and other fluidic components that operate intermittently during measurements. For example, the applicability of an *in situ* LOC chemical analyzer with EOPs as actuators for on-chip valves and a flow-rate regulator within a microfluidic device was shown through chemiluminescence-based quantitative determination of manganese in seawater [49].

A power-free pumping technology already in practical use in the medical field is the infusion balloon pump [50]. This medical device, driven by the elastic contraction of a balloon, is used for the continuous delivery of medicine that is filled into an expandable balloon to a patient. It offers the advantage of continuous flow through a simple structure without requiring an external power supply. This mechanism generates no pulsation because it relies on the steady contraction of the inflatable balloon. The practical applicability of balloon pumps has been demonstrated through their integration into LOC-based *in situ* biochemical analyzers. Their pumping performance remained stable even under elevated hydrostatic pressure of up to 20 MPa (corresponding to a depth of approximately 2,000 m), demonstrating their robustness for deep-sea applications [51]. Pumping mechanisms based on the expansion of elastomer membranes can also be integrated into LOC devices, providing a simple and power-free approach for fluid handling [52].

Osmotic pumps, generally used for continuous drug delivery in living animals, are another off-the-shelf power-free pumping solution. They rely on osmotic pressure across a semipermeable membrane to drive fluid flow and maintain a nearly constant drug release rate [53]. The Osmo pump is a small pump with no moving parts other than a semipermeable membrane, enabling long-term fluid delivery; however, its flow rate is relatively limited when used alone. Furthermore, it requires a long time for the flow rate stabilization during the initial stage of operation. This technology has already been applied to LOC devices for the quantitative analysis of metal ions [54] and for sampling [55] in deep-sea environments. These power-free pumping technologies may be well suited for housekeeping fluidic operations that support long-term observations, such as the continuous cleaning of sensor devices.

Hydrostatic pressure rises by approximately 0.1 MPa for each 10 m of depth in aquatic environments. Therefore, in most cases, analytical instruments, electronics, and batteries deployed underwater must be placed in pressure-tight housings to protect them from hydrostatic pressure. In recent years, a method for pumping that utilizes the hydrostatic pressure difference between the inside and outside of a pressure-tight housing has been proposed [30,56,57]. By connecting the inside and outside of a pressure-tight housing via an appropriate flow resistance, such as a capillary tube, power-free pumping driven by hydrostatic pressure can be achieved. According to the Hagen–Poiseuille equation, the flow rate is determined by pressure difference, liquid viscosity, and capillary dimensions. In deep-sea environments, long or narrow capillary tubes are required to decrease large pressure differences, which makes miniaturization challenging. A compact and practical system can be realized by integrating microfluidic channels as a microfluidic pressure reducer (MPR). Power-free pumping using a glass-based MPR has demonstrated stable delivery of both pure water and natural seawater up to 10 MPa of hydrostatic pressure [57]. Furthermore, a mechanism enabling stepwise flow-rate adjustments using MPR devices with branched microchannels has been proposed and is currently under evaluation (Figure 2). By combining this power-free pumping technology with an indirect pumping platform, practical fluid control operations can be realized. For example, integrating a 3D-printed fluidic platform designed for indirect pumping with a pH-ISFET enables the delivery of multiple pH standard solutions, and *in situ* calibration capability has also been demonstrated [56]. As discussed above, the integration of LOC tech-

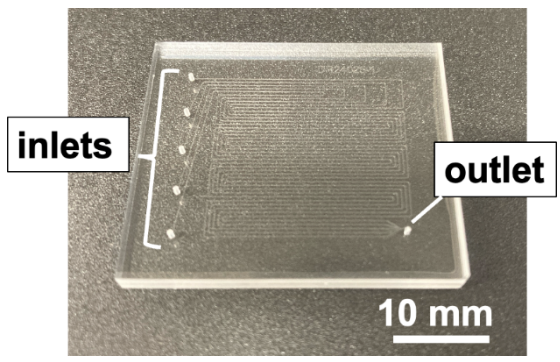


Figure 2: Microfluidic pressure reducer (MPR) with a branched microchannel.

nologies, power-free or power-efficient pumping strategies, and nanoscale sensors enables the deployment of advanced analytical methodologies in harsh field environments.

Extended-gate FET (EG-FET) technology

Considering the high ionic strength and harsh physicochemical conditions of marine environments, the development of appropriate recognition materials significantly expands the potential of chemical sensor platforms as discussed in the previous section. In addition to molecular design, device-level engineering is equally critical for the practical deployment of nanoscale sensing technology in marine environments. To date, ISFETs have shown effectiveness in chemical sensing under marine environments; however, robust device architectures are required to ensure operational stability and practical deployment in such extreme environments. The extended-gate FET (EG-FET) architecture is particularly well suited for implementing surface functionalization with molecular recognition layers, including enzymes [34]. The EG-FET configuration is designed to physically separate the transistor from the sensing element, allowing only the functionalized sensing surface to be exposed to the surrounding environments. This separation allows the transistor circuitry to be housed and protected within a pressure-tight housing while maintaining direct environmental interaction of the sensing surface. As a result, the configuration improves operational stability and protects the FET circuitry under high pressure and corrosive conditions, while also facilitating easy replacement of the sensing element. With the growing demand for mineral resource exploration and associated environmental impact assessment missions, sensing performed at depths of thousands of meters is becoming increasingly important. While such conditions remain largely unexplored for Nano-FET technologies, significant changes in operating mechanisms are expected under deep-sea conditions, which must be studied in the future.

Deploying thin-film NanoFETs with microfluidics in deep-sea environments presents material challenges, particularly interfacial delamination under shear stress and high pressure. To improve layer stability and prevent pinhole leakage, possible fabrication strategies include combining high-density deposition methods (e.g., atomic layer deposition or sputtering) with adhesion layers, such as Ti or Cr [8,15]. Post-deposition thermal annealing may also help relieve internal stress and densify the dielectric matrix, depending on the materials and fabrication process [8].

Connecting nanoscale sensors to macroscale fluidic packaging requires a hierarchical fabrication approach to prevent dead volume and sample dispersion. While 3D printing provides robust macroscale manifolds, its spatial resolution cannot interface directly with nanochannels at present. Therefore, intermediate microfluidic interfaces can be fabricated using photolithography and soft lithography with polydimethylsiloxane (PDMS) to form micrometer-scale channels [58]. Elastomeric PDMS serves a dual purpose by functioning as a flow cell and acting as a gasket that seals rigid sensor chips against 3D-printed housings, which may help reduce pressure-induced mechanical stress and fluid leakage.

Observation platform technology

To deploy sensor devices in environments such as the ocean, appropriate mounting platforms are indispensable. In particular, for spatiotemporally resolved deployments aimed at cross-scale sensing, the use of scalable platform technologies is essential. In recent years, uncrewed observation platforms have gained increasing importance as alternatives to conventional ocean observation systems based on crewed research vessels [59]. This section provides an overview of platform technologies that link nanoscale sensing techniques and global environmental monitoring.

A moored observatory is one of the most fundamental platforms for long-term, continuous observation of the marine environment at fixed locations. By deploying sensor devices from the surface to the seafloor, long-term observation of biogeochemical parameters with high temporal resolution becomes possible. Installation and retrieval of observation buoys require costly shipboard operations, sensor calibration, maintenance, and biofouling prevention measures. Therefore, to achieve long-term and sustainable observations, it is important to design cost-effective observation systems and establish effective operational procedures [60]. In the future, more efficient observation systems will need to be developed by miniaturizing moored buoys and introducing technologies that enable automated deployment, recovery, maintenance, and sensor replacement, thereby supporting sustained ocean observations.

Another approach is the use of virtual mooring technology based on various autonomous surface vehicles (ASVs) or autonomous underwater gliders [61]. Deploying a miniaturized virtual mooring platform using an aircraft or other means could enable timely deployment of observation tools and is expected to become a promising approach for future ocean observation [62,63]. In terms of power supply, a certain amount of electricity can be generated using solar panels mounted on a surface float. Furthermore, some ocean platforms can harvest multiple forms of renewable energy, including wind, waves, and ocean currents. For example, some unmoored platforms integrate wave-induced turbines or subsurface wave energy harvesters to achieve long-term, self-sustained operations [62]. Drifting buoys, especially profiling floats, are representative ex-

amples of the successful realization of a global ocean observation network. Thousands of autonomous profiling floats are deployed throughout the oceans to continuously observe basic physical parameters such as water temperature and salinity [2]. Recent expansions through the BGC-Argo program have enabled observations of additional parameters [3] (Figure 3). These profiling floats are subject to strict constraints on size, power consumption, and payload weight; therefore, the integration of small, low-power sensing devices is essential [64]. In recent years, deployment of profiling floats in coastal areas has also been reported. While traditional drifting buoys can lead to unexpected operational conflicts in coastal environments due to their unpredictable trajectories, certain advanced floats have been studied and developed to minimize these risks by temporarily anchoring to the seabed [65]. However, the operational scope of these drifting platforms remains constrained by their reliance on environmental conditions or specific seabed characteristics. To overcome these limitations, platforms capable of more flexible movement underwater and on the sea surface will become increasingly important. In recent years, compact remotely operated vehicles [66], autonomous underwater vehicles [67], underwater gliders [61], and ASVs [68] have become available off-the-shelf for practical missions.



Figure 3: Argo float (left) and BGC Argo float (right), © JAMSTEC. Reproduced with permission. This content is not subject to CC BY 4.0.

For the rapid transport and deployment of sensor devices to remote places, unmanned aerial vehicles are also useful ocean observation platforms [69]. They also support simultaneous optical sensing using onboard imaging sensors [59], allowing *in situ* measurements to be complemented with high-resolution spatial observations of the surrounding marine environment. However, there is a bottleneck on payload weight and power capacity. Therefore, further miniaturization and reduced power consumption of sensor devices are essential. While *in situ* sensing platforms provide detailed local measurements, airborne and satellite remote sensing technology play an important complementary role by enabling observations across broader spatial scales. Active optical sensing technologies, such as lidar, can also be used to estimate biogeochemical parameters of water columns based on laser backscatter signals [70]. These approaches emphasize the potential of remote sensing to capture large-scale environmental variability. In contrast, *in situ* chemical sensing technologies provide direct measurements of dissolved chemical species and molecular-scale processes in aquatic environments. The integration of *in situ* nanoscale sensing and remote sensing offers a complementary strategy for linking molecular-level processes with global environmental dynamics across scales.

Future Directions

As outlined here, nanoscale sensing technologies are steadily expanding the potential for sensing in high-ionic-strength environments, such as oceans and biological systems. The pH-ISFET, already in practical use for pH measurement in aquatic environments, can be regarded as a pioneering success story that links nanoscale interfacial phenomena to macroscopic oceanic observations, and ultimately, to global environmental issues. However, the direct electrical detection of specific targets using FET-based sensors is constrained by Debye screening, which continues to pose a fundamental challenge. The integration of nanoscale transistors, molecular recognition technologies, extended-gate structures, and power-efficient pumping technologies, as outlined here, offers a pathway towards underwater *in situ* sensing technologies while addressing these limitations. For example, the convergence of LOC technology and 3D printing enables the incorporation of power-efficient pumping systems, indirect pumping architectures, and protective packaging (pressure-tight housing) functionalities into compact, field-deployable sensing platforms (Figure 4). Despite promising technological advances, several fundamental limitations remain to be addressed before cross-scale marine sensing becomes fully operational. Debye screening in high-salinity seawater still restricts direct electrical detection of larger biomolecules or non-proton target ions, which motivates the use of short conformational receptors (e.g., aptamers) or non-coulombic sensing mechanisms. Potential

drift in solid-state and liquid-junction reference electrodes over multimonth deployments remains an important challenge, highlighting the need for practical *in situ* calibration strategies. Surface biofouling impairs gate sensitivity and clogs microchannels; approaches such as non-fouling surface chemistry [71], deep-UV irradiation [72], or periodic microfluidic washing [12] may help mitigate these effects.

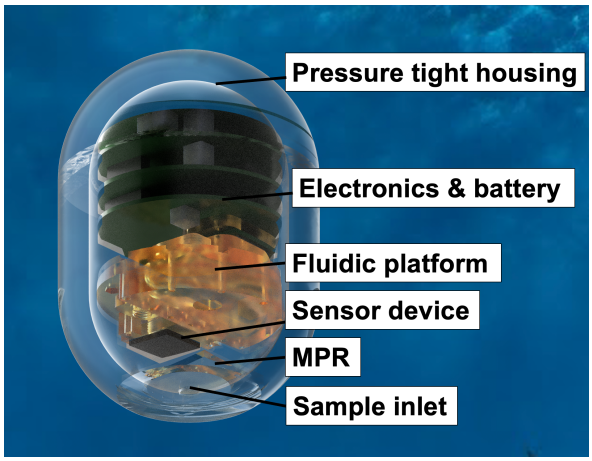


Figure 4: Concept of compact and field-deployable sensing platform.

Both marine and physiological environments share a common physical constraint, that is, high ionic strength. On this shared foundation, nano-interface sensing technology has the potential to become a cross-disciplinary, cross-scale sensing platform for both fields. In the future, further miniaturization and higher levels of packaging, along with increasingly stringent demands for safety and ultralow-power operation, may be necessary to enable the application of nanoscale sensing technologies in continuous in vivo monitoring. Consequently, in addition to LOC technologies, pumping methods that operate with minimal or no power consumption are expected to become increasingly important. Historically, "bioanalytical-originated" devices such as ISFETs have been applied in marine environmental sensing. In contrast, "ocean-originated" miniaturized sensing technologies integrating nanoscale sensing and LOC technologies are expected to evolve into next-generation platforms in biomedical and healthcare fields, enabling bidirectional cross-disciplinary innovation in the future.

Acknowledgements

AI-based tools (ChatGPT, OpenAI; Gemini and NotebookLM, Google) were used for language editing, structural improvement, and to provide suggestions on manuscript organization. The authors reviewed and validated all content and take full responsibility for the article. No AI tools were used for data generation, analysis, or image creation/editing.

Funding

This work was supported by the Japan Society for the Promotion of Science (JSPS) KAKENHI Grant Number JP23H03866, JP23H03864, and JP23H03865.

Author Contributions

Tatsuhiro Fukuba: conceptualization; project administration; visualization; writing – original draft; writing – review & editing. Nicolas Clement: writing – original draft; writing – review & editing. Henri Vo Van Qui: visualization; writing – original draft; writing – review & editing. Yui Sasaki: writing – original draft; writing – review & editing. Koji Toma: writing – original draft; writing – review & editing. Tsuyoshi Minami: conceptualization; funding acquisition; project adminis-tration; supervision; writing – original draft; writing – review & editing.

ORCID® iDs

Tatsuhiro Fukuba - https://orcid.org/0000-0002-0484-2577
Nicolas Clement - https://orcid.org/0000-0002-4924-4087
Henri Vo Van Qui - https://orcid.org/0009-0000-8417-6350
Yui Sasaki - https://orcid.org/0000-0003-4185-569X
Koji Toma - https://orcid.org/0000-0002-1683-1496
Tsuyoshi Minami - https://orcid.org/0000-0001-8331-378X

Data Availability Statement

Data sharing is not applicable as no new data was generated or analyzed in this study.

References

1. Doney, S. C.; Fabry, V. J.; Feely, R. A.; Kleypas, J. A. *Annu. Rev. Mar. Sci.* **2009,** *1,* 169–192. doi:10.1146/annurev.marine.010908.163834
2. Wong, A. P. S.; Wijffels, S. E.; Riser, S. C.; Pouliquen, S.; Hosoda, S.; Roemmich, D.; Gilson, J.; Johnson, G. C.; Martini, K.; Murphy, D. J.; Scanderbeg, M.; Bhaskar, T. V. S. U.; Buck, J. J. H.; Merceur, F.; Carval, T.; Maze, G.; Cabanes, C.; André, X.; Poffa, N.; Yashayaev, I.; Barker, P. M.; Guinehut, S.; Belbéoch, M.; Ignaszewski, M.; Baringer, M. O.; Schmid, C.; Lyman, J. M.; McTaggart, K. E.; Purkey, S. G.; Zilberman, N.; Alkire, M. B.; Swift, D.; Owens, W. B.; Jayne, S. R.; Hersh, C.; Robbins, P.; West-Mack, D.; Bahr, F.; Yoshida, S.; Sutton, P. J. H.; Cancouët, R.; Coatanoan, C.; Dobbler, D.; Juan, A. G.; Gourrion, J.; Kolodziejczyk, N.; Bernard, V.; Bourlès, B.; Claustre, H.; D'Ortenzio, F.; Le Reste, S.; Le Traon, P.-Y.; Rannou, J.-P.; Saout-Grit, C.; Speich, S.; Thierry, V.; Verbrugge, N.; Angel-Benavides, I. M.; Klein, B.; Notarstefano, G.; Poulain, P.-M.; Vélez-Belchí, P.; Suga, T.; Ando, K.; Iwasaska, N.; Kobayashi, T.; Masuda, S.; Oka, E.; Sato, K.; Nakamura, T.; Sato, K.; Takatsuki, Y.; Yoshida, T.; Cowley, R.; Lovell, J. L.; Oke, P. R.; van Wijk, E. M.; Carse, F.; Donnelly, M.; Gould, W. J.; Gowers, K.; King, B. A.; Loch, S. G.; Mowat, M.; Turton, J.; Rama Rao, E. P.; Ravichandran, M.; Freeland, H. J.; Gaboury, I.; Gilbert, D.; Greenan, B. J. W.; Ouellet, M.; Ross, T.; Tran, A.; Dong, M.; Liu, Z.; Xu, J.; Kang, K.; Jo, H.; Kim, S.-D.; Park, H.-M. *Front. Mar. Sci.* **2020,** *7,* 700. doi:10.3389/fmars.2020.00700

3. Roemmich, D.; Alford, M. H.; Claustre, H.; Johnson, K.; King, B.; Moum, J.; Oke, P.; Owens, W. B.; Pouliquen, S.; Purkey, S.; Scanderbeg, M.; Suga, T.; Wijffels, S.; Zilberman, N.; Bakker, D.; Baringer, M.; Belbeoch, M.; Bittig, H. C.; Boss, E.; Calil, P.; Carse, F.; Carval, T.; Chai, F.; Conchubhair, D. Ó.; d'Ortenzio, F.; Dall'Olmo, G.; Desbruyeres, D.; Fennel, K.; Fer, I.; Ferrari, R.; Forget, G.; Freeland, H.; Fujiki, T.; Gehlen, M.; Greenan, B.; Hallberg, R.; Hibiya, T.; Hosoda, S.; Jayne, S.; Jochum, M.; Johnson, G. C.; Kang, K.; Kolodziejczyk, N.; Körtzinger, A.; Traon, P.-Y. L.; Lenn, Y.-D.; Maze, G.; Mork, K. A.; Morris, T.; Nagai, T.; Nash, J.; Garabato, A. N.; Olsen, A.; Pattabhi, R. R.; Prakash, S.; Riser, S.; Schmechtig, C.; Schmid, C.; Shroyer, E.; Sterl, A.; Sutton, P.; Talley, L.; Tanhua, T.; Thierry, V.; Thomalla, S.; Toole, J.; Troisi, A.; Trull, T. W.; Turton, J.; Velez-Belchi, P. J.; Walczowski, W.; Wang, H.; Wanninkhof, R.; Waterhouse, A. F.; Waterman, S.; Watson, A.; Wilson, C.; Wong, A. P. S.; Xu, J.; Yasuda, I. *Front. Mar. Sci.* **2019,** *6,* 439. doi:10.3389/fmars.2019.00439
4. Liu, Y.; Lu, H.; Cui, Y. *J. Mar. Sci. Eng.* **2023,** *11,* 1469. doi:10.3390/jmse11071469
5. Dickson, A. G.; Sabine, C. L.; Christian, J. R., Eds. *Guide to Best Practices for Ocean CO2 Measurements;* North Pacific Marine Science Organization: Sidney, BC, Canada, 2007; Vol. PICES Special Publication 3. https://www.ncei.noaa.gov/access/ocean-carbon-acidification-data-system/oceans/Handbook_2007.html
6. Seiter, J. C.; DeGrandpre, M. D. *Talanta* **2001,** *54,* 99–106. doi:10.1016/s0039-9140(00)00635-4
7. Bergveld, P. *Sens. Actuators, B* **2003,** *88,* 1–20. doi:10.1016/s0925-4005(02)00301-5
8. Sinha, S.; Pal, T. A. *Electrochem. Sci. Adv.* **2022,** *2,* e2100147. doi:10.1002/elsa.202100147
9. Le Bris, N.; Birot, D. *Anal. Chim. Acta* **1997,** *356,* 205–215. doi:10.1016/s0003-2670(97)00533-3
10. Shitashima, K.; Maeda, Y.; Koike, Y.; Ohsumi, T. *Int. J. Greenhouse Gas Control* **2008,** *2,* 95–104. doi:10.1016/s1750-5836(07)00092-8
11. Jimenez-Jorquera, C.; Orozco, J.; Baldi, A. *Sensors* **2010,** *10,* 61–83. doi:10.3390/s100100061
12. Bresnahan, P. J., Jr.; Martz, T. R.; Takeshita, Y.; Johnson, K. S.; LaShomb, M. *Methods Oceanogr.* **2014,** *9,* 44–60. doi:10.1016/j.mio.2014.08.003
13. Johnson, K. S.; Jannasch, H. W.; Coletti, L. J.; Elrod, V. A.; Martz, T. R.; Takeshita, Y.; Carlson, R. J.; Connery, J. G. *Anal. Chem. (Washington, DC, U. S.)* **2016,** *88,* 3249–3256. doi:10.1021/acs.analchem.5b04653
14. Hemming, M. P.; Kaiser, J.; Heywood, K. J.; Bakker, D. C. E.; Boutin, J.; Shitashima, K.; Lee, G.; Legge, O.; Onken, R. *Ocean Sci.* **2017,** *13,* 427–442. doi:10.5194/os-13-427-2017
15. Briggs, E. M.; Sandoval, S.; Erten, A.; Takeshita, Y.; Kummel, A. C.; Martz, T. R. *ACS Sens.* **2017,** *2,* 1302–1309. doi:10.1021/acssensors.7b00305
16. Stern, E.; Wagner, R.; Sigworth, F. J.; Breaker, R.; Fahmy, T. M.; Reed, M. A. *Nano Lett.* **2007,** *7,* 3405–3409. doi:10.1021/nl071792z
17. Nakatsuka, N.; Yang, K.-A.; Abendroth, J. M.; Cheung, K. M.; Xu, X.; Yang, H.; Zhao, C.; Zhu, B.; Rim, Y. S.; Yang, Y.; Weiss, P. S.; Stojanović, M. N.; Andrews, A. M. *Science* **2018,** *362,* 319–324. doi:10.1126/science.aao6750
18. Langmuir, D. *Aqueous Environmental Geochemistry;* Prentice Hall: Upper Saddle River, NJ, USA, 1997.
19. Homola, J. *Chem. Rev.* **2008,** *108,* 462–493. doi:10.1021/cr068107d
20. Yamada, S.; Urano, H.; Toma, K. *Beilstein J. Nanotechnol.* **2026,** *17,* 1223–1256. doi:10.3762/bjnano.17.85
21. Kitaya, N.; Yamanaka, D.; Morita, K.; Naito, R.; Suhara, H.; Suzuki, K.; Nakajima, H.; Moriiwa, Y.; Morioka, K.; Yanagida, A.; Shoji, A. *Beilstein J. Nanotechnol.* **2026,** *17,* 1290–1301. doi:10.3762/bjnano.17.89
22. Cui, Y.; Wei, Q.; Park, H.; Lieber, C. M. *Science* **2001,** *293,* 1289–1292. doi:10.1126/science.1062711
23. Ohno, Y.; Maehashi, K.; Yamashiro, Y.; Matsumoto, K. *Nano Lett.* **2009,** *9,* 3318–3322. doi:10.1021/nl901596m
24. Sarkar, D.; Liu, W.; Xie, X.; Anselmo, A. C.; Mitragotri, S.; Banerjee, K. *ACS Nano* **2014,** *8,* 3992–4003. doi:10.1021/nn5009148
25. Morel, F. M. M.; Price, N. M. *Science* **2003,** *300,* 944–947. doi:10.1126/science.1083545
26. Liu, C.; Ye, Z.; Wei, X.; Mao, S. *Electrochem. Sci. Adv.* **2022,** *2,* e2100137. doi:10.1002/elsa.202100137
27. Ono, T.; Kanai, Y.; Inoue, K.; Watanabe, Y.; Nakakita, S.-i.; Kawahara, T.; Suzuki, Y.; Matsumoto, K. *Nano Lett.* **2019,** *19,* 4004–4009. doi:10.1021/acs.nanolett.9b01335
28. Kim, N.; Collins, D. S.; Donghia, N. M.; Miller, B. S.; Sallum, H. M.; Lybbert, S. R.; Perini, E.; Niemi, J. B.; Collins, J. J.; Nguyen, P. Q. *Nat. Sustainability* **2026,** *9,* 51–64. doi:10.1038/s41893-025-01752-0
29. Sivakumarasamy, R.; Hartkamp, R.; Siboulet, B.; Dufrêche, J.-F.; Nishiguchi, K.; Fujiwara, A.; Clément, N. *Nat. Mater.* **2018,** *17,* 464–470. doi:10.1038/s41563-017-0016-y
30. Fukuba, T.; Fujiwara, A.; Nishiguchi, K.; Bergaud, M.; Grall, S.; Li, S.; Kim, S.-H.; Clément, N. Application of Ambient Pressure-Driven Pumping Technology Towards Ultra Low-Power Underwater Sensing. In *2023 IEEE Underwater Technology (UT),* Tokyo, Japan, March 6–9, 2023; IEEE, 2023; pp 1–5. doi:10.1109/ut49729.2023.10103205
31. Song, S.; Wang, L.; Li, J.; Fan, C.; Zhao, J. *TrAC, Trends Anal. Chem.* **2008,** *27,* 108–117. doi:10.1016/j.trac.2007.12.004
32. Maehashi, K.; Katsura, T.; Kerman, K.; Takamura, Y.; Matsumoto, K.; Tamiya, E. *Anal. Chem. (Washington, DC, U. S.)* **2007,** *79,* 782–787. doi:10.1021/ac060830g
33. Knopfmacher, O.; Hammock, M. L.; Appleton, A. L.; Schwartz, G.; Mei, J.; Lei, T.; Pei, J.; Bao, Z. *Nat. Commun.* **2014,** *5,* 2954. doi:10.1038/ncomms3954
34. Sarcina, L.; Macchia, E.; Tricase, A.; Scandurra, C.; Imbriano, A.; Torricelli, F.; Cioffi, N.; Torsi, L.; Bollella, P. *Electrochem. Sci. Adv.* **2023,** *3,* e2100216. doi:10.1002/elsa.202100216
35. Poghossian, A.; Schöning, M. J. *Electroanalysis* **2014,** *26,* 1197–1213. doi:10.1002/elan.201400073
36. Sasaki, Y.; Kubota, R.; Minami, T. *Coord. Chem. Rev.* **2021,** *429,* 213607. doi:10.1016/j.ccr.2020.213607
37. Sasaki, Y.; Minamiki, T.; Tokito, S.; Minami, T. *Chem. Commun.* **2017,** *53,* 6561–6564. doi:10.1039/c7cc03218h
38. Hamedpour, V.; Sasaki, Y.; Zhang, Z.; Kubota, R.; Minami, T. *Anal. Chem. (Washington, DC, U. S.)* **2019,** *91,* 13627–13632. doi:10.1021/acs.analchem.9b02822
39. Sasaki, Y.; Minami, T. *Beilstein J. Nanotechnol.* **2026,** *17,* 828–838. doi:10.3762/bjnano.17.59
40. Nightingale, A. M.; Beaton, A. D.; Mowlem, M. C. *Sens. Actuators, B* **2015,** *221,* 1398–1405. doi:10.1016/j.snb.2015.07.091
41. Fukuba, T.; Fujii, T. *Lab Chip* **2021,** *21,* 55–74. doi:10.1039/d0lc00871k
42. Rérolle, V. M. C.; Floquet, C. F. A.; Mowlem, M. C.; Connelly, D. P.; Achterberg, E. P.; Bellerby, R. R. G. J. *TrAC, Trends Anal. Chem.* **2012,** *40,* 146–157. doi:10.1016/j.trac.2012.07.016

43. Yin, T.; Papadimitriou, S.; Rérolle, V. M. C.; Arundell, M.; Cardwell, C. L.; Walk, J.; Palmer, M. R.; Fowell, S. E.; Schaap, A.; Mowlem, M. C.; Loucaides, S. *Environ. Sci. Technol.* **2021,** *55,* 14968–14978. doi:10.1021/acs.est.1c03517
44. Suh, Y. K.; Kang, S. *Micromachines* **2010,** *1,* 82–111. doi:10.3390/mi1030082
45. Newaz, A. K. M.; Markov, D. A.; Prasai, D.; Bolotin, K. I. *Nano Lett.* **2012,** *12,* 2931–2935. doi:10.1021/nl300603v
46. Luo, X.; Yang, L.; Cui, Y. *Sens. Actuators, A* **2023,** *363,* 114732. doi:10.1016/j.sna.2023.114732
47. Fukuba, T. *Bunseki Kagaku* **2025,** *74,* 265–272. doi:10.2116/bunsekikagaku.74.265
48. Li, L.; Wang, X.; Pu, Q.; Liu, S. *Anal. Chim. Acta* **2019,** *1060,* 1–16. doi:10.1016/j.aca.2019.02.004
49. Provin, C.; Fukuba, T.; Okamura, K.; Fujii, T. *IEEE J. Oceanic Eng.* **2013,** *38,* 178–185. doi:10.1109/joe.2012.2208849
50. Skryabina, E. A.; Dunn, T. S. *Am. J. Health-Syst. Pharm.* **2006,** *63,* 1260–1268. doi:10.2146/ajhp050408
51. Fukuba, T.; Nakasa, A.; Tsukada, O.; Fujii, T. Application of Drug Infusion Balloons to Microfluidic Systems for In Situ Measurement. In *Proceedings of the 22nd International Conference on Miniaturized Systems for Chemistry and Life Sciences (μTAS 2018),* 2018; pp 815–817.
52. Morimoto, Y.; Mukouyama, Y.; Habasaki, S.; Takeuchi, S. *Micromachines* **2016,** *7,* 39. doi:10.3390/mi7030039
53. Herrlich, S.; Spieth, S.; Messner, S.; Zengerle, R. *Adv. Drug Delivery Rev.* **2012,** *64,* 1617–1627. doi:10.1016/j.addr.2012.02.003
54. Chapin, T. P.; Jannasch, H. W.; Johnson, K. S. *Anal. Chim. Acta* **2002,** *463,* 265–274. doi:10.1016/s0003-2670(02)00423-3
55. Jannasch, H. W.; Wheat, C. G.; Plant, J. N.; Kastner, M.; Stakes, D. S. *Limnol. Oceanogr.: Methods* **2004,** *2,* 102–113. doi:10.4319/lom.2004.2.102
56. Fukuba, T. Application of Ambient Pressure-Driven Pumping Technology for Underwater pH Measurement. In *2025 IEEE Underwater Technology (UT),* IEEE, 2025; pp 1–4. doi:10.1109/ut61067.2025.10947281
57. Fukuba, T. Development of Power-Free Pumping Technology Utilizing Water Pressure in the Marine Environment. In *Proceedings of the 41st Sensor Symposium on Sensors, Micromachines and Applied Systems,* 2024. (in Japanese).
58. Duffy, D. C.; McDonald, J. C.; Schueller, O. J. A.; Whitesides, G. M. *Anal. Chem. (Washington, DC, U. S.)* **1998,** *70,* 4974–4984. doi:10.1021/ac980656z
59. Yuan, S.; Li, Y.; Bao, F.; Xu, H.; Yang, Y.; Yan, Q.; Zhong, S.; Yin, H.; Xu, J.; Huang, Z.; Lin, J. *Sci. Total Environ.* **2023,** *858,* 159741. doi:10.1016/j.scitotenv.2022.159741
60. Venkatesan, R.; Ramesh, K.; Kishor, A.; Vedachalam, N.; Atmanand, M. A. *Front. Mar. Sci.* **2018,** *5,* 469. doi:10.3389/fmars.2018.00469
61. Petritoli, E.; Leccese, F. *Drones* **2025,** *9,* 21. doi:10.3390/drones9010021
62. Ticona Rollano, F.; Hume, D.; Martinez, J.; Deng, D.; Rose, D.; Weicht, L.; Kenny, C.; McNally, J.; Fogarty, M. *Powering the Blue Economy: A Survey of Station-Keeping Methods for Mooringless Platforms; Technical Report PNNL-31719*; Pacific Northwest National Laboratory (PNNL): Richland, WA, USA, 2021.
63. Wu, D.; Zhou, R.; Xia, Q.; Zhou, P.; Zhang, X.; Jin, Z.; Zhang, Y.; Yang, C. *Ocean Eng.* **2025,** *328,* 121053. doi:10.1016/j.oceaneng.2025.121053
64. Johnson, K. S.; Coletti, L. J.; Jannasch, H. W.; Sakamoto, C. M.; Swift, D. D.; Riser, S. C. *J. Atmos. Oceanic Technol.* **2013,** *30,* 1854–1866. doi:10.1175/jtech-d-12-00221.1
65. Andre, X.; Dutreuil, V.; Le Reste, S. *Sea Technol.* **2016,** *57,* 21–26.
66. Singh, R.; Sarkar, P.; Goswami, V.; Yadav, R. *Ocean Eng.* **2022,** *266,* 112796. doi:10.1016/j.oceaneng.2022.112796
67. Pairaud, I.; Petton, S.; Sellet, H.; Helleringer, C.; Le Bihan, C.; Charria, G. Using a micro-AUV for monitoring coastal river plume areas. In *Proc. IEEE OCEANS 2025 Brest,* IEEE, 2025; pp 1–10. doi:10.1109/oceans58557.2025.11104618
68. Bolbot, V.; Sandru, A.; Saarniniemi, T.; Puolakka, O.; Kujala, P.; Valdez Banda, O. A. *J. Mar. Sci. Eng.* **2023,** *11,* 2387. doi:10.3390/jmse11122387
69. Burnett, M.; Abdelwahab, M.; Satme, J. N.; Downey, A. R. J.; Barahona Smith, G.; Fonce, A.; Imran, J. *Sensors* **2026,** *26,* 1158. doi:10.3390/s26041158
70. Chen, W.; Chen, P.; Zhang, H.; He, Y.; Tang, J.; Wu, S. *Intell. Mar. Technol. Syst.* **2023,** *1,* 10. doi:10.1007/s44295-023-00007-y
71. Gokaltun, A.; Yarmush, M. L.; Asatekin, A.; Usta, O. B. *Technology* **2017,** *5,* 1–12. doi:10.1142/s2339547817300013
72. Bueley, C.; Olender, D.; Bocking, B. *J. Ocean Technol.* **2014,** *9,* 48–67.

License and Terms

This is an open access article licensed under the terms of the Beilstein-Institut Open Access License Agreement (https://www.beilstein-journals.org/bjnano/terms), which is identical to the Creative Commons Attribution 4.0 International License (https://creativecommons.org/licenses/by/4.0). The reuse of material under this license requires that the author(s), source and license are credited. Third-party material in this article could be subject to other licenses (typically indicated in the credit line), and in this case, users are required to obtain permission from the license holder to reuse the material.

The definitive version of this article is the electronic one which can be found at:
https://doi.org/10.3762/bjnano.17.103